

# Simple Book Example

TeXstudio Team

January 2013

ii

thesis

# Contents

<b>Introduction</b>	<b>1</b>
<b>1 Theory and methods of plenoptic imaging</b>	<b>9</b>
1.1 Introduction . . . . .	9
1.2 Plenoptic function and the light field . . . . .	11
1.3 Plenoptic camera . . . . .	14
1.4 Plenoptic Camera 1.0 . . . . .	16
1.4.1 Phase space in plenoptic 1.0 . . . . .	22
1.4.2 Light Field Parametrization . . . . .	24
1.5 Plenoptic 1.0 rendering . . . . .	29
1.6 Plenoptic Camera 2.0 . . . . .	32
1.7 Plenoptic camera 2.0: a geometrical optics analysis . . . . .	40
1.8 Plenoptic 2.0 rendering . . . . .	44
<b>2 Fresnel Simulation Toolbox</b>	<b>47</b>
2.1 Introduction . . . . .	47
2.2 Scalar Theory of diffraction . . . . .	49
2.2.1 Helmholtz equation . . . . .	52
2.2.2 Solutions of Helmholtz Equations . . . . .	53
2.2.3 The Fresnel Approximation . . . . .	54
2.3 Operator Free space propagation: Fresnel Approximation approach . . . . .	55
2.3.1 Multi-Step Fresnel propagation operator . . . . .	57
2.4 Operator Free space propagation: Angular spectrum of plane waves approach . . . . .	59
2.4.1 Angular spectrum of plane waves . . . . .	59
2.4.2 Band Limited Angular Spectrum . . . . .	63
2.4.3 Corrected Band Limited Angular Spectrum Method . . . . .	71
2.4.4 Performances of the Angular spectrum methods . . . . .	73
2.5 Operator Thin Lens . . . . .	76
2.5.1 Aliasing in phase sampling . . . . .	82

2.6	Comparison between the free space propagation operators . . . . .	84
2.6.1	Description of the system . . . . .	85
2.6.2	Image of a point source . . . . .	86
2.7	Coherence . . . . .	91
2.7.1	Temporal coherence . . . . .	92
2.7.2	Spatial Coherence . . . . .	93
2.7.3	Simulation of spatial coherence . . . . .	94
2.7.4	Simulation of temporal coherence . . . . .	100
2.8	Optimization of coherence parameters . . . . .	101
2.8.1	Optimization of Spatial Coherence . . . . .	102
2.8.2	Optimization of temporal coherence . . . . .	105
2.8.3	Coherent imaging vs incoherent imaging . . . . .	108
<b>3</b>	<b>Simulations of a plenoptic 1.0 system</b>	<b>111</b>
3.1	Introduction . . . . .	111
3.2	Description of the system . . . . .	111
3.2.1	Diffraction effects on the System . . . . .	113
3.3	Advanced Rendering Techniques . . . . .	116
3.3.1	Changing Aperture . . . . .	117
3.3.2	Changing the point of view . . . . .	120
3.4	Depth estimation . . . . .	120
3.5	Synthetic refocus . . . . .	126
3.5.1	Synthetic refocus algorithm . . . . .	128
3.5.2	Refocusing Operator . . . . .	131
3.6	Results of the Simulations . . . . .	133
3.7	Focal stack depth estimation . . . . .	139
<b>4</b>	<b>Simulation of a plenoptic 2.0 system</b>	<b>145</b>
4.1	Rendering in Plenoptic 2.0 . . . . .	146
4.1.1	Extracting sub images . . . . .	148
4.1.2	Basic Rendering . . . . .	149
4.1.3	Depth based rendering . . . . .	151
4.2	Description of the system . . . . .	154
4.3	Optical performances of a focused plenoptic system . . . . .	159
4.4	Impulse response of a Focused Plenoptic system . . . . .	163
4.5	Two point resolution . . . . .	167
4.6	Frequency analysis of a focused plenoptic system . . . . .	171
4.7	Conclusions . . . . .	186

<b>5 Light Field Microscope</b>	<b>189</b>
5.1 From simulation to the real system . . . . .	189
5.2 Description of the System . . . . .	191
5.3 Performances of the system . . . . .	197
5.4 Image acquisition protocol . . . . .	198
5.5 Rendering of experimental data . . . . .	203
5.6 Optical Phase Space . . . . .	209
<b>6 Conclusions and Future work</b>	<b>213</b>



# List of Figures

1.1	Differences between a traditional camera and a computational camera [1]. . . . .	10
1.2	Two point representation of light field. Each ray of light is unequivocally defined by the coordinates of two points of interception. . . . .	13
1.3	Point angle representation. A ray of light is unequivocally defined by the coordinates of a point that belongs to a plane perpendicular at the optical axis z and by the angles $\theta_x$ and $\theta_y$ that it forms with the optical axis along the directions x and y. . . . .	13
1.4	Plenoptic camera and its fundamental components. The presence of the micro array allows to record the light field . . . . .	14
1.5	Top: Plenoptic camera 1.0. The main lens is focused on the object and forms and image on the micro array and the micro array. $f$ is the focal length of the main lens and $f_\mu$ the focal length of the micro lens array. Bottom: Plenoptic camera 2.0. The main lens is focused on an object and forms an image on the plane represented by the dashed line. The micro array acts as a relay between the main lens image and the sensor, since it satisfy the lens equation $1/a + 1/b = 1/f_\mu$ . . . . .	16
1.6	Ray diagram of a plenoptic 1.0 system. The main lens is in a 2f configuration and the sensor plane is conjugated with the main lens plane. The micro lens position maps the position (x,y) of the point P, while the sub image maps the directions of the rays coming from that point. The ray with direction $\theta_1$ falls on the pixel 1 (blue), the ray with direction $\theta_2$ falls on the pixel 2 (green) and the ray with direction $\theta_3$ falls on the pixel 3 (red). The sub image $d$ maps the direction of the ray.	18

1.7 Sampling of Light Filed. Each ray is described by a set of four coordinates, two spatial (x,y) and two directional (u,v). The spatial coordinates are sampled by the position of the lens let in the micro array, the directional coordinates are sampled by the pixel under the lens let. Point A, its position is sampled by the lens let number 1(x=1), and three rays are green (1,1), red(1,2), blue(1,3). Each ray is defined by x and v. Point B:for one position (x=5) three rays are sampled green (5,1), red(5,2), blue(5,3), dashed line. . . . .	20
1.8 F-number matching between the main lens and the micro lens in the array. . . . .	21
1.9 When the f-number is matched, all the rays captured by the main lens are mapped on the sub image (yellow). If the f-number is smaller (red), the sub image is smaller and there is an under sampling of the set of rays. If the f-number of the lens let is bigger (green), the sub image is larger and cross talk happens between near sub images . . . . .	22
1.10 Sampling of the light field and phase space representations of the rays. . . . .	23
1.11 Example of a raw plenoptic 1.0 image. . . . .	24
1.12 Zoom on the raw image. Each lens-let is formed by 20 X 20 pixels. Each pixel represents a direction of the rays hitting the lens let that produced the sub image. . . . .	25
1.13 The array view is an array of the different point of view obtained rearranging the pixels according to the directional coordinates. . . . .	26
1.14 The array view is an array of the different points of view obtained by rearranging the pixels according to the directional coordinates. . . . .	27
1.15 Zoom of the central part of the array view showing in detail the different points of views. . . . .	28
1.16 Sampling of the light field and phase space representations of the rays.[2] . . . . .	29
1.17 Rendering an image from plenoptic 1.0 raw data is equal to summing all the directional samples for each position. This process is shown for the the $(x, \theta_x)$ slice of the phase space. [3]	31
1.18 rendered image form the raw data in figure 1.11. Resolution is only 75 X 75 pixel. . . . .	32

1.19 If the main lens image is formed in front of the micro array the configuration is called "Copernican", top, and the focal length of the micro array is smaller then the distance b. If the main lens image is formed behind the micro array the configuration is "Galilean", on the bottom, and the focal length of the micro array is bigger then the distance b. . . . .	34
1.20 Raw data of a point source sampled by a plenoptic 2.0 system with a magnification of the micro array stage equal to 0.3. Data acquired with numerical simulations. . . . .	36
1.21 Zoomed Raw data of a point source sampled by a plenoptic 2.0 system with a magnification of the micro array stage equal to 0.3. Data acquired with numerical simulations. The grid represent the boundaries of each sub image to show how the point of view of the point source changes across the lens lets. The sub images are shifted by a quantity proportional to the position of the lens let in the array. . . . .	36
1.22 Sampling of the light field by a plenoptic 2.0 system. The one dimensional case is shown. Each micro lens has a diameter equal to $d$ , a focal length $f_\mu$ , and images the main lens image on the sensor according to the lens law $1/a + 1/b = 1/f_\mu$ . The total range of directions that can be sampled is given by $d/b$ . Each lens let samples a sub set of directions equal to $d/a$ as a single direction. The range of directions shown in red are sampled by the central micro lens as a single point of view. The angular resolution is therefore $d/a$ and the total number of directional sampled is 3. . . . .	37
1.23 Raw images of a point source simulated with different magnifications. From top left to bottom right: $m = 1$ , $m = 0.5$ , $m = 0.25$ , $m = 0.1$ . . . . .	39
1.24 System formed by a single lens let. The rays at the main lens image plane are transformed into the rays at the sensor plane by the lens let. The transformation can be described by a matrix $A$ . . . . .	42

1.25 Sampling of the light field by plenoptic 2.0 camera. For each of the two points represented, red and green, The total range of directional coordinates are sampled by three different lens lets. For one position three directions are sampled, with a resolution of $d/a$ . Therefore the directional sampling in plenoptic 2.0 is made across many lens lets. This can be seen in the phase space. Lenset B and C sample 2 directions indicated with the same number in the ray diagram and the phase space. Lens let A only samples one direction of the red point. . . . .	44
1.26 Image rendering with the focused plenoptic camera. One pixel of the rendered image is given by the integration on all the directions $d/b$ associated with a given position. The integration takes place across the lens let. . . . .	45
2.1 example . . . . .	55
2.2 To remove the scaling factor between the input and output fields, a multi step Fresnel approach has been developed. The field is propagated by unit of $dz$ , the minimum distance to keep the sampling the same. . . . .	57
2.3 Structure of the operator free space propagation with the angular spectrum of plane waves method. The initial disturbance $U(x, y; 0)$ is transformed into the angular spectrum $A(f_x, f_y; 0)$ with a Fourier transform implemented by a FFT algorithm. The angular spectrum is multiplied by the propagation transfer function $H(f_x, f_y)$ and the resultant angular spectrum is inverse transformed into the output disturbance $U(x, y; z)$ . .	63
2.4 example . . . . .	65
2.5 example . . . . .	69
2.6 Structure of the operator free space propagation with the angular spectrum of plane waves method in its band limited version. The initial disturbance $U(x, y; 0)$ is transformed into the angular spectrum $A(f_x, f_y; 0)$ with a Fourier transform implemented by a FFT algorithm. The angular spectrum is multiplied by the propagation transfer function $H(f_x, f_y)$ whose bandwidth has been limited according to equation 2.63. The bandwidth of the transfer function depends on the sampling of the input field, the wavelength of the light $\lambda$ and the propagation distance. The resultant angular spectrum is inverse transformed into the output disturbance $U(x, y; z)$ . $N$ is the sampling of the input field, $z$ the propagation distance and $\lambda$ the wavelength. . . . .	70

2.7	The maximum spatial frequency is linked to the dimension of the sampling window of the output field $w$ and the propagation distance $z$ . . . . .	72
2.8	example . . . . .	75
2.9	Comparison between the Signal to Noise ratio (SNR) as a function of the propagation distance for the three propagation method seen in section 2.4.1. The BL and the corrected BL methods improve the SNR, that instead drops with the increasing of the propagation distance when the normal AS method is used. . . . .	76
2.10	Thickness of a lens as a function of position along x coordinate. It can be defined in the same way along the y coordinate . . . . .	77
2.11	example . . . . .	79
2.12	A thin lens converts a plane wave into a spherical wave. . . . .	81
2.13	Phase profile of a computer generated lens. The blue line shows the quadratic phase term and the red line shows the same phase term wrapped every $2\pi$ . This wrapping is the source of the aliasing. . . . .	82
2.14	Schematic of the 2f system simulated. f is the focal lenght, z the propagation distances, D is the aperture of the lens, w the field of view and N the sampling resolution. . . . .	85
2.15	Operator sequence for the 2f system. . . . .	86
2.16	From top to Bottom: Image and intensity cross section of a point source according to multi step method, angular spectrum method, band limited angular spectrum method and corrected band limited angular spectrum method. . . . .	88
2.17	From top left to bottom right: Power spectrum of the image of a point source obtained with the multi step Fresnel method, the Angular spectrum method, the band limited angular spectrum method and the corrected band limited angular spectrum method . . . . .	90
2.18	Young experiment setup. . . . .	94
2.19	A random phase mask is generated propagating light coming form an array of sources, each one with a random phase value in the interval $[-\pi, \pi]$ . . . . .	96
2.20	Process of the creation of the phase mask. Top: array of point sources with a random phase value; centre: array of the areas of coherence at source after the convolution with $K$ ; bottom: randomized areas of coherence at object plane after the propagation of $d_c$ . . . . .	98

2.21	Final random phase mask generated by 10, 50, 100 and 200 sources. . . . .	99
2.22	Emission spectrum of the LED considered in our simulations and real image system. . . . .	101
2.23	example . . . . .	102
2.24	Signal to noise ratio of the image of a USAF resolution target plotted as a function of the coherence index $C$ . . . . .	103
2.25	Images of the USAF resolution target with different values of $\iota$ . Increasing the number of point sources generating the phase mask creates improves the resolution and the contrast . . . . .	104
2.26	Noise due to the speckles in an image of a USAF resolution target after only 5 iterations. . . . .	105
2.27	Images of the USAF resolution target obtained adding an increasing number of snapshot. this is equivalent to increase the integration time of the sensor. The noise due to the speckles caused by the phase mask decreases with increasing number of iterations. . . . .	106
2.28	Signal to noise ratio as a function of the number of iterations. The threshold has been calculated looking at the variance of the previous five data. . . . .	107
2.29	Comparison between the coherent and an incoherent response of a simple 2f system to a sharp edge. . . . .	109
3.1	The parameters that characterize the micro lens array are: the pitch $p$ , defined as the distance between the centres of two lens lets, the diameter $d$ , the number of lens lets per raw $N$ and the size of the micro array $W$ . . . . .	112
3.2	The parameters that characterize the micro lens array are: the pitch $p$ , defined as the distance between the centres of two neighbouring lens lets, the diameter $d$ , the number of lens lets per row $N$ and the size of the micro array $W$ . . . . .	113
3.3	Values of acceptable lens let diameter to avoid diffraction induced cross talk. . . . .	114
3.4	Raw image of a point source. The grid represents the edges of the sub images. If the point source is in focus, it should be represented by only one lens let. Because of diffraction some light goes also on the neighbouring sub images. . . . .	115

- 3.5 Phase space of the light field of a point object: on the left when the condition 3.3 is respected; on the right when diffraction induces cross talk arise between neighbours lens lets. Cross talk introduces a blur in the rendered image whose width is  $\Delta x$ . . . . . 116
- 3.6 Rendering seen from the  $(x, \theta_x)$  slice of the phase space. The directional pixels not considered for the integration are shown in grey. . . . . 118
- 3.7 Raw plenoptic 1.0 image obtained from Levoy *et al.* The microscope was a Zeiss Axiovert with a 20x/0.5NA (dry) objective. The micro lens array was 24mm x 36mm, with square 125-micron x 125-micron f/20 micro lenses, held in front of the Axiovert's side camera port using an optical bench mount. The camera was a Canon 5D full-frame digital SLR. The specimen was the thin silky skin separating two layers of an onion, immersed in oil to improve transparency [4]. . . . . 119
- 3.8 Rendered Images from the raw data in figure 3.7. On the left there is the full aperture imagea, obtained integrating along all the directional coordinates while on the right there is the all in focus image obtained taking onli the central pixel of the each sub image, that corresponds to rays with the direction parallel to the optical axis. . . . . 120
- 3.9 Sampling of the light field of a point source in focus, on the top, closer to the main lens, centre, and further away, bottom. When the source is out of focus, both position and directions are sampled by more than one lens let since the main lens image is not formed any more on the lens let plane. . . . . 123
- 3.10 Information on the depth of a point source imaged by a plenoptic 1.0 system. As explained in section 1.4.1 If the point source is in focus, on the top, it's position is sampled by one lens let as well as the whole set of directions . . . . . 124
- 3.11 Physical meaning of the slope in the phase space. If the point source is further then the camera focal plane, the phase space line has a negative slope. If the point source is closer then the focal plane, the slope of the phase space line is positive. . . . . 125

3.12 Numerical simulation of a point source imaged by a plenoptic 1.0 imaging system. The point source was placed at three different distances from the main lens. The top three figures show the focused image. In the centre ones a defocus of 0.125 m is added and the point source is further away from the main lens. In the bottom ones the point source is closer to the main lens of .25 m. In all the three cases the raw data image is on the left, the rendered image is on the centre and the phase space line is on the right. . . . .	126
3.13 The synthetic camera refocusing method is based on the fact that it is always possible to define a virtual aperture that is focused on the lens let plane. . . . .	127
3.14 Changing the focal plane of the camera is equal to re parametrize the light field according to the new coordinates. The re parametrization is basically a shift proportional to the ratio between the refocused plane and the original camera plane $\alpha$ . . . . .	129
3.15 Changing the position of the focal plane is equal to shear the light field in the phase space. The total area remains the same since the total light field is conserved. . . . .	132
3.16 Flow chart of the operator shearing. . . . .	133
3.17 Set up simulated. . . . .	134
3.18 Position of the point sources imaged inside the volume V simulated. . . . .	135
3.19 Raw image on the left and rendered image on the right. Intensity is shown in false colour in order to appreciate variations in energy distribution. . . . .	136
3.20 Values of the refocusing factor $\alpha$ as a function of the defocus. A positive defocus means that the object is further away with respect to the main lens, a negative defocus indicates an object that is closer. . . . .	137
3.21 Refocused Images of the three point sources in image 3.19. In the top one the point A is refocused, in the bottom one the point B is refocused. The colour bar indicates the how the intensity is distributed. When the point source is refocused, the intensity distribution is higher with respect to the out of focus points. . . . .	138
3.22 Refocused images... . . . .	140
3.23 Refocused images... . . . .	142
3.24 Estimated values of $\alpha$ represented by blue stars and the theoretical values represented with the blue line. . . . .	143

3.25 Distance between the estimated values of alpha and thje actual theoretical values. . . . .	143
4.1 Top: the point <b>A</b> is imaged by the main lens into the point <b>A'</b> . <b>A'</b> is imaged by the lens let array into a number of sub images depending by the magnification of the micro array stage, in this case $m=0.333$ . Bottom: particular of the raw image at the point source A and phase space diagram. The three sub images 1,2 and 3 are three different points of view of the object. . . . .	147
4.2 Relation between the position of the centre of a lens let $x$ and the position of the centre of the correspondent sub image $x + x'$ . . . . .	149
4.3 Basic rendering algorithm. The Rendered image is composed tiling together patches extracted by each sub image. The patch size is dependent by the magnification of the micro array stage. . . . .	150
4.4 The points that belongs to the object plane represented in red are imaged on a virtual main lens image plane. This plane is relayed on a virtual sensor plane by a virtual micro array whose parameters are $a'$ and $b'$ and $m' = b'/a'$ . . . . .	152
4.5 . . . . .	153
4.6 Ray diagram of the system simulated. . . . .	154
4.7 Values of the parameter $b$ correspondent to values of magnification varying from 0.1 to 0.5. . . . .	156
4.8 Values of the parameter $b$ corresponding to values of magnification varying from 0.1 to 0.5. . . . .	157
4.9 Aperture of the main lens as a function of the magnification in order to respect the f-number matching condition. . . . .	158
4.10 Aperture of the main lens as a function of the magnification in order to respect the f-number matching condition. . . . .	160
4.11 lateral resolution as a function of the magnification. . . . .	162
4.12 optical cut-off frequency as a function of the magnification. . . . .	162
4.13 Left: raw sensor image, Right: rendered image. Artifacts are present. Magnification: 0.5 . . . . .	164
4.14 Left: raw sensor image, Right: rendered image. Artifacts are present. Magnification: 0.3. . . . .	164
4.15 Left: raw sensor image, Right: rendered image. Artefacts are present. Magnification: 0.25 . . . . .	165

- 4.16 From top to bottom: comparison between the main lens image profile, in blue, and the rendered image profile, in red, for magnification values of 0.5,0.3 and 0.25. The central lobe of the rendered image increase with the magnification, as well as the number of artefacts. . . . . 166
- 4.17 On the top left there is the main lens image of two point sources separated by the Rayleigh distance  $\delta x$ . On the top right its corresponded rendered plenoptic image obtained with a magnification of 0.5. As expected from the theory, the resolution of the rendered image is half the one of the main lens image, and the two points are no more distinguishable as confirmed by the intensity profiles of the two images on the bottom. . . . . 169
- 4.18 The image on the top left shows the main lens image of two point sources separated by the Rayleigh distance  $2\delta x$ . On the top right there is its corresponded rendered plenoptic image obtained with a magnification of 0.5. Doubling the Rayleigh distance the rendered image is at the limit of resolution, where the maximum of the Airy pattern of one point falls on the first zero of the second point. . . . . 170
- 4.19 Modulation transfer functions of the main lens (green) and the overall imaging system (red) for a magnification value of  $m = 0.5$ , top,  $m = 0.3$ , central, and  $m = 0.25$ , bottom. . . . . 173
- 4.20 The object imaged in this simulation is a sinusoidal grating containing five different frequencies. . . . . 175
- 4.21 Top: on the left it is shown the raw sensor image, on the right the main lens image. Bottom: On the left there is the rendered image, on the right the same image has been low pass filtered to remove some of the rendering artefacts. Magnification was 0.5 . . . . . 176
- 4.22 On the left: intensity profiles of the main lens image, top and of the rendered image, bottom. On the right the spatial frequencies modulated according to the MTF as shown by the power spectra of the main lens image on the top right and of the rendered image on the bottom right. The magnification of the lens let array is  $m = 0.5$  and cut-off frequency of the system is  $f_{cut-off} = 10^4 m - 1$  . . . . . 177

4.23 Evolution of the spectrum of the optical field as it propagates through the imaging system. First step the field is propagated through the main lens and its frequency content is modulated by its MTF whose bandwidth is $\Delta\nu_1$ . Then modulated field passes through the lens let array stage and because of the magnification that is less than zero its bandwidth is reduced further to $\Delta\nu_2$ . Since $\nu_1 < \nu_2$ the imaging system is modelled as a linear low pass filter with a bandwidth $\Delta\nu_1$ defined by the magnification of the micro array stage. . . . .	179
4.24 Top: on the left it is shown the raw sensor image, on the right the main lens image. Bottom: On the left there is the rendered image, on the right the same image has been low pass filtered to remove some of the rendering artefacts. Magnification was 0.3. . . . .	181
4.25 On the left: intensity profiles of the main lens image, top and of the rendered image, bottom. On the right: spatial frequency modulation done by MTF. The cut-off frequency of the system is $0.756 \times 10^4 m^{-1}$ . . . . .	182
4.26 Aliased frequencies transmitted to the rendered image. . . . .	183
4.27 Top: raw sensor image, on the right the main lens image. Bottom: On the left there is the rendered image, on the right the same image has been low pass filtered to remove some of the rendering artefacts. Magnification was 0.3. . . . .	184
4.28 On the left: intensity profiles of the main lens image, top and of the rendered image, bottom. On the right there are the spatial frequencies modulated according to the MTF. The cut-off frequency of the system is $0.6 \times 10^4 1/m$ . . . . .	185
5.1 Emission spectrum of the LED light source used in the system .	192
5.2 Schematics of the light field microscope. The values of the distances are: $z_c=27$ mm, $z_k=120$ mm, $z_1=z_2=120$ mm. . . . .	193
5.3 Schematics of the light field recording stage. . . . .	194
5.4 Lens let array parameters. . . . .	195
5.5 Optical resolution as a function of the magnification. . . . .	197
5.6 Common causes of bad alignment between the micro lens array and the sensor. . . . .	199
5.7 Calibration image with f-number not matched. . . . .	200
5.8 Calibration image with matched f-number. . . . .	200
5.9 Raw plenoptic 2.0 image of the USAF resolution target obtained by the real system built in lab. The top image has a magnification of 0.5, the bottom 0.4. . . . .	201

5.10	Raw plenoptic 2.0 image of the USAF resolution target obtained by the real system built in lab. The top image has a magnification of 0.3, the bottom 0.25. . . . .	202
5.11	The sub images grid generated selecting a row and a column from the calibration image and setting a threshold to that allows the software to know when a sub image ends and the other end. . . . .	205
5.12	Rendered images of a 1951 USAF resolution target. the raw data shown in figures 5.9 and 5.10.Magnifications are from top left to bottom right: 0.25 0.3 0.4 and 0.5. . . . .	206
5.13	Top: Rendered image obtained from the same raw data used to render the image on the bottom right in figure 5.12. In this case the grid used to select the micro images is not correctly set, presenting an offset of 15 pixel for every sub image and errors in detecting the sub image as the bottom figure shows. .	207
5.14	The optical momentum correspond to the direction of the ray of light. . . . .	209
5.15	. . . . .	210

# Introduction

The information contained in the light surrounding the environment we live in is captured by the different living being according to the structure and the nature of their visual systems. The human eye is a single lens imaging system whose retina is composed by three different types of photosensitive cells [5]. For this reasons cameras have always been designed to capture light in the same way the human eye works, single lens with three colour pixels producing two dimensional images based on three colours [6]. This way of designing cameras produce a loss of information respect the all sets of information included into the light reaching the imaging system. Adelson *et al.* in 1991 proposed a to describe the whole set of information contained in the light defining the plenoptic function [7], ray based a seven dimension function describing intensity, direction and wavelength of rays propagating in the space. According to Adelson a conventional imaging device captured projections of this function. For example a photo is obtained integrating along the directional variables the function, obtaining a two dimensional intensity pattern of the object imaged loosing information on its three dimensional structure. If the integration is performed also along the wavelength the image will be in black and white and also the information on the wavelength will be lost, while adding a polariser we can obtain information on the state

of polarization of the optical field coming from the object. [8, 2]. The reality we see and measure with the instruments and the senses we have is just a projection of a more complex reality and great part of the information carried by the electromagnetic field is lost. This situation is similar to the one described in Plato's "Allegory of the cave" where a group of people are being chained for all their life inside a cave and facing a blank wall on which shadows of different objects are projected. For them the shadows produced by the objects passing in front of the fire are the only reality they know since they are limited in their perception by their situation[9] . The same happen with human perception and with the camera that imitates human visual system. All conventional imaging instruments are limited and the images they produce is a projection of a more complex quantity containing all information that light carries. Even the most advanced imaging instrument will always produce data that are close to reality, but that does not reach it, both for intrinsic properties of light, such as diffraction, and because they have been designed to collect only a small set the reality. The role of scientific research is to push further this limit and understand how close to reality an measuring instrument can go. In this work will be described a new set of instruments that are able to sample the plenoptic function and the post processing methods to access all the information it carries. The character of this thesis will be mostly computational, and numerical simulations will be used as an instrument to explore the potential and define the limitations of this class of instruments.

The first idea that more information were carried by the light contained in a scene was made by Leonardo da Vinci who understood that described the

volume containing the light as filled by a dense array of light rays, called by him "radiant pyramids" [7]. The plenoptic function described by Adelson and Wang *et al.* is the formalization of this concepts of "radiant pyramids" adding to the directions and positions of the rays information on the wavelength. The problem now, once it has been defined the extra information contained in the scene, is to define a method to measure it. The first work about capturing the plenoptic function was done by Yves in 1903 on his works on parallax panorama-grams [10, 11] and by Lippmann in 1908 [12] who proposed an array of pinhole cameras. The key to capture the plenoptic function is to have multiple views of the object to image. This can be done translating a single camera to different positions over a spherical or planar surface[13, 14, 15], method known as time sequential sampling, or by using an array of cameras [16, 17, 18] that is the multi-sensor sampling. Multi -sensor techniques give high performances in term of resolution but are extremely complicated and expensive, while time-sequential techniques suffer the loss of the capability to capture dynamic scenes [6]. The solution between costs and resolution is given by single-shot plenoptic sampling techniques based on a space multiplexing of the plenoptic function [6], as proposed by Ives [11] and Lippmann [12]. This single-shot space multiplexing method produces an array of elemental images on the sensor and this introduces several trade-offs between spatial and directional resolution [6, 19] as well optical resolution trade-offs [20]. Several families of devices has been developed. In this work will be described those who sample the plenoptic function using an array of micro lenses in front of the sensor as described by Adelson and Wang *et.al* [8], Ng *et al.* [21, 2], Ueda *et al.* [22] and Georgiev *et al.* [3]. In particular Ng

*et al.* developed the first generations of plenoptic imaging systems, known as plenoptic 1.0, then improved by Georgiev *et al.* who modified them giving birth to the second generations, or plenoptic 2.0. This two class of instruments will be treated in this work. Other methods to capture the plenoptic function are based on creating a mask patterns that enables frequency domain multiplexing of the plenoptic function [23, 24], compressive imaging techniques [25] or exotic solution such as a slit camera [26]. The resulting image obtained with all this different methods contains all the extra information contained in the plenoptic function, but they are codified. Therefore the final image is obtained implementing post processing algorithms in order to decode these information. For this reason the process of capturing plenoptic images is also called computational photography [6, 1]. Along with the image rendering several post processing features can be performed once the information captured are decoded. This features includes digital refocus [2], changing the point of view, estimating depth [26, 6, 27, 28] and super-resolution imaging [29, 30, 31, 32].

The purpose of this work is to analyse the optical performances of micro lens array based plenoptic imaging systems. When this project started all existing work on this kind of instruments has been done using a ray optics approach. This work uses a wave optics approach so the behaviour of a plenoptic imaging system at its diffraction limit. This is the first work that quantifies the effects of diffraction on the quality of raw sensor images and rendered images, defining a new trade-off between spatio-angular resolution and optical resolution. This facts has not been investigated in other work because they most of the applications of plenoptic imaging regards photogra-

phy and imaging of macroscopic objects. When the attention is moved to the microscopic world, diffraction effects become important. The first thing that has been done was to develop an home made simulation platform for wave propagation in a generic optical system. Existing method to implement free space propagation has been investigated and a variant of one of the existing methods has been proposed in order to make it more efficient. It has also defined a new empirical method to simulate light in any state of coherence based on the true physical nature of coherence and it has been proven to give realistic results. Once the simulation platform has been properly tested it has been used to simulate a plenoptic imaging system. Different parameters have been changed in order to investigate their influence on the optical properties of the system. At the same time post processing algorithms to extract information from the raw sensor data have been developed following the guidelines present in literature. Some innovative custom made solutions have been also applied. Different configurations of plenoptic setup have been compared, with particular attention to the optical performances of plenoptic 2.0 imaging systems. The information collected have then been used to build an home made plenoptic microscope.

In the first chapter an introduction of plenoptic imaging will be given. It will be explained in a rigorous way how to pass from a seven dimensional plenoptic function to a four dimensional function called light field. A definition of light field will be given and it will be explained how the light field carries information regarding the 3D structure of the scene imaged properties and how it is sampled by the two different configurations, plenoptic 1.0 and plenoptic 2.0. A rigorous theoretical description of both class of system

will be given using geometrical optics, with particular attention to the post processing methods to decode the information in it.

The second chapter is a description of the home made simulation platform developed. The platform has been written in MATLAB and implements wave propagation of light under the Fresnel approximation. It has been designed to be a versatile and modular platform composed by operators that applied to an input optical field give an output field. The first operator to be described is the free space propagation based on Fresnel approximation of diffraction. The scalar theory of diffraction will be treated from a theoretical point of view starting from Maxwell equations to end with the expression of Fresnel diffraction integral. Then different method to implement Fresnel propagation will be analysed highlighting advantages and disadvantages of each one of them in term of resolution, signal to noise ratio and computational effort. These methods are: the direct Fresnel integral application, the multi step propagation, the angular spectrum method and the band-limited angular spectrum method. It will also be presented an original variation of the band limited angular spectrum method to optimize the trade-off between the signal to noise ratio and digital aliasing. Then the lens operator will be described. Once the lens has been defined there will be shown some results of simulation of simple optical systems with the purpose of comparing the performances of the five different free space propagation operators. This chapter is concluded by the exposition of the method to simulate partially coherent light.

The third chapter is a complete description of a plenoptic 1.0 system. It will be explained how to design and run simulations and how the to implement in

MATLAB existing post processing algorithms to render the final image from the raw sensor data. Digital refocus principles and methods will be described as well as the change the point of view. An original home made method to estimate the depth of point sources will be also proposed.

Chapter four is about the simulations performed to define the optical properties of a plenoptic 2.0 system. It will be calculated the impulse response of the system together with its modulation transfer function. A frequency analysis of the system will be done as well, and it will be explained how the different parameters of the system influence the optical resolution of the final rendered image. Such a detailed optical analysis of a plenoptic system has never been done using wave optics simulations.

Chapter five contains the description of the real setup built in the laboratory to verify the conclusions achieved with the simulations. A full description of the system will be given, as well as a description of the protocol to follow to capture light field images. Few results will be presented.

The final chapter is about the conclusions and the future possibilities of development of plenoptic imaging systems.



# **Chapter 1**

## **Theory and methods of plenoptic imaging**

### **1.1 Introduction**

A camera is a device that captures light in a scene [33]. The main constituents of a conventional camera are the detector and lens. The rays of light passing through the aperture of the lens are recorded on the sensor as a two dimensional irradiance map of the scene imaged. Therefore a traditional camera performs a limited sampling of the complete set of rays, and in general of the amount of information, contained in the scene [1]. It is interesting to define the total amount of information contained in the light captured by a camera and if there is an effective way to record and extract it. The space is filled with a dense array of light with various intensities [7]. From each point of the object imaged a cone of rays departs and fills the whole space while propagating. If a traditional camera is placed at a certain position from the object it will sample only the rays passing through its aperture. The set of information contained in this cone of rays will than be recorded on a two dimensional plane. This process of recording light coming

## 10CHAPTER 1. THEORY AND METHODS OF PLENOPTIC IMAGING

from a three dimensional scene on a two dimensional plane causes loss of information. Following Adelson *et al.* [7] all the information carried by the light propagating into space can be described by a function, called plenoptic function. Different parametrizations of the plenoptic are possible. One of these is a four dimensional function called Light Field that will be described in more detail in the next sections. It will also be described a new class of optical instruments, are called computational cameras, that are able to record and extract information from the light field. Computational cameras differ from a conventional camera in the way they sample the light coming from the object using a non conventional new optics that codifies the light that hits the detector. This coded information is then decoded by a computational stage, in order to extract an image [1]. Schematics of the difference between a conventional and a computational camera can be found in figure 1.1

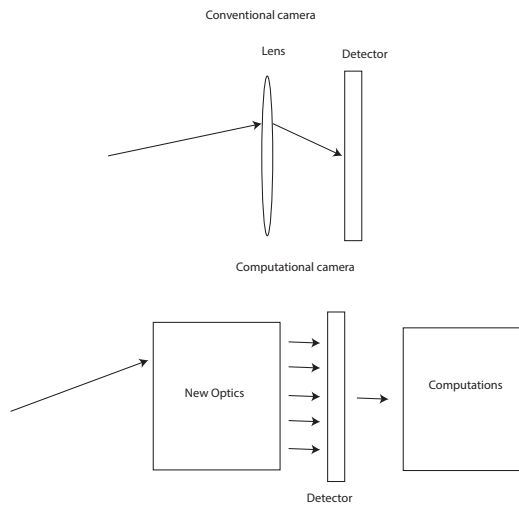


Figure 1.1: Differences between a traditional camera and a computational camera [1].

## 1.2 Plenoptic function and the light field

A black and white photograph taken by a conventional camera represents the intensity of light seen by a single viewpoint, at a single time, averaged and weighted over the wavelengths of the visible spectrum [7]. For each point of the sensor, the intensity can be represented as function of the position  $P(x, y)$ . A colour photograph adds information about the wavelength  $\lambda$  of the light adding a third variable,  $P(x, y, \lambda)$ . If several photos are taken in succession forming a movie the time dependence is added,  $P(x, y, \lambda, t)$  and if the movie is captured using holographic techniques, i.e. saving phase and amplitude at of the optical field, all the information regarding the light intensity observable from any viewpoint  $\vec{V} = (V_x, V_y, V_z)$  is recorded. Therefore to describe all the information that is potentially available from the light coming from the object a seven dimensional function is needed. It takes the name of plenoptic function and its name comes from Latin *plenum* that means full [8, 7, 6]. The plenoptic function implicitly contains a description of every possible photograph that can be taken of a particular scene from any possible point of view. To record the plenoptic function, one should move the camera along all the possible positions  $\vec{X}$  around the object and take a snapshot or have an array of cameras surrounding the object taking snapshots simultaneously. The plenoptic function is an idealized concept and it is impossible to record it completely. However it is possible to acquire samples of it or projection along one dimension. For example a conventional black and white picture is a two dimensional slice along the coordinates  $x$  and  $y$  of the seven dimensional plenoptic function taken from a single point of view, av-

## 12CHAPTER 1. THEORY AND METHODS OF PLENOPTIC IMAGING

eraging the wavelength and integrating over the exposure time. A plenoptic camera is able to record a section of the plenoptic function [7]. In particular, it records the part of the plenoptic function whose rays pass through the aperture of the camera, hence all the possible viewpoints contained in the lens aperture. Final images are constructed by sectioning the plenoptic function along certain coordinates. The process of extracting information from the plenoptic function is called rendering [13, 3] and it is where the computational stage operates. Before proceeding in describing a plenoptic camera in detail it is useful to define another parametrization of the plenoptic function derived by Levoy *et al.* that is more useful to implement the computational algorithms in the following sections. This parametrization is called light field and is defined as the radiance as a function of position and direction [13]. It is described by a set of four coordinates, two spatial coordinates and two directional coordinates and for this reason is often referred to as the 4D Light Field. There are two possible representation of the light field: the two point representation and the point-angle representation. With reference to figure 1.2 in the two point parametrization a ray of light is propagating in the free space form the point  $(x,y)$  to the point  $(u,v)$ . Its direction of propagation in three dimensional space is defined by the couple of points where it crosses two parallel planes. Therefore the set of coordinates  $(x,y)$  and  $(u,v)$  defines only one ray of light [13]. The point angle parametrization instead uses the coordinates of the point where the ray intercept a plane perpendicular to the optical axis, and the angles that it forms with the optical axis along the directions  $x$  and  $y$ , namely  $\theta_x$  and  $\theta_y$ , as shown in figure 1.3 [28]. In both cases the intensity is a function of four coordinates.

The 4D light field is therefore:

$$L(x, y, u, v) = L(x, y, \theta_x, \theta_y) \quad (1.1)$$

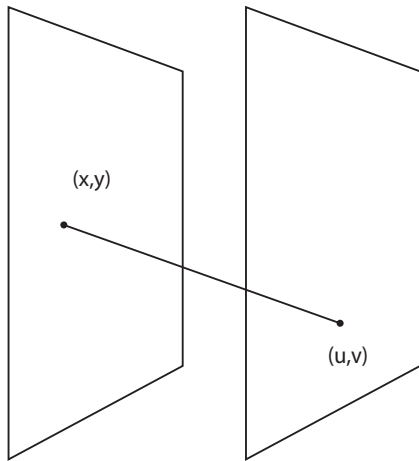


Figure 1.2: Two point representation of light field. Each ray of light is unequivocally defined by the coordinates of two points of interception.

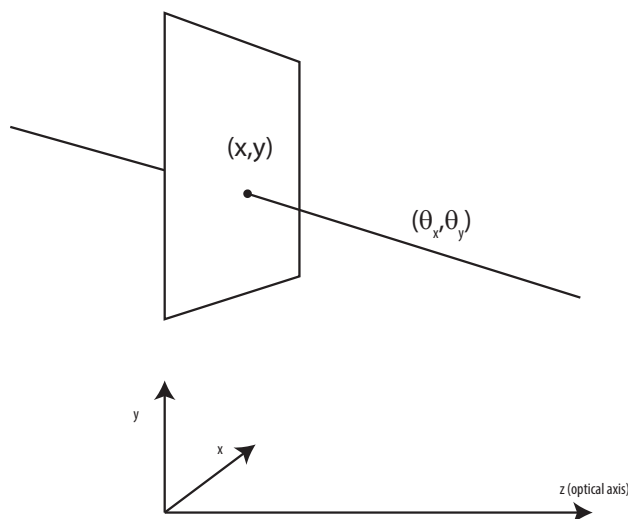


Figure 1.3: Point angle representation. A ray of light is unequivocally defined by the coordinates of a point that belongs to a plane perpendicular at the optical axis  $z$  and by the angles  $\theta_x$  and  $\theta_y$  that it forms with the optical axis along the directions  $x$  and  $y$ .

For each pixel of the sensor of a plenoptic camera it is possible to determine these four coordinates. The information provided by the two extra directional coordinates enables a set of computational features such as 3D reconstruction, synthetic refocus, full depth of field and aberration correction [2]. Each of these features is possible after having decoded the light field with the computational stage as shown in figure 1.1.

### 1.3 Plenoptic camera

A plenoptic camera is a camera that records the 4D light field as described in equation 1.1. The version proposed and built by Adelson and Wang in 1992 [8] is composed of a main lens, a sensor and a micro lens array placed in front of the sensor [8]. The presence of the micro array enables the codification of the directional information on the sensor. This coded image represents the raw data of the plenoptic camera. This kind of camera can be seen in figure 1.4:

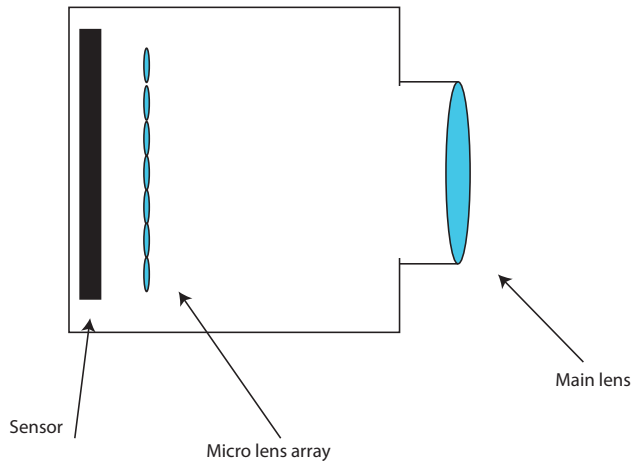


Figure 1.4: Plenoptic camera and its fundamental components. The presence of the micro array allows to record the light field .

The optical performance of the camera depends on the array's design characteristic. The main issue with the micro lens array is its position with respect to the main lens and the sensor. Depending on where it is placed two types of cameras are possible:

- if the main lens forms its image on the micro array and the sensor plane is conjugated with the main lens it is the first generation plenoptic camera, or plenoptic 1.0 [21]
- if the main lens forms its image on a plane that is different from the micro array plane and the micro lenses image the main lens image plane on the sensor it is the focused plenoptic camera, or plenoptic 2.0 [3]

The two different kinds of cameras can be seen in figure 1.5. In the next sections both configurations will be extensively analysed and the way in which they capture the light field will be explained with particular attention to the differences in the raw data they produce. Their performances in term of lateral and directional (or angular) resolution will be detailed. The computational algorithms to render images from the raw data will also be extensively explained.

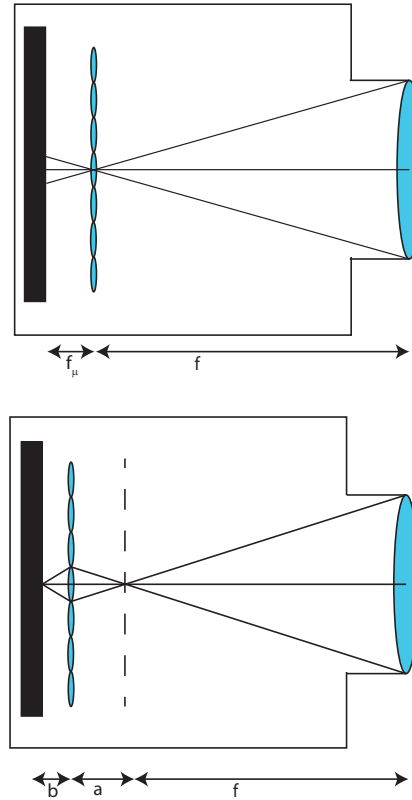


Figure 1.5: Top: Plenoptic camera 1.0. The main lens is focused on the object and forms and image on the micro array and the micro array.  $f$  is the focal length of the main lens and  $f_\mu$  the focal length of the micro lens array. Bottom: Plenoptic camera 2.0. The main lens is focused on an object and forms an image on the plane represented by the dashed line. The micro array acts as a relay between the main lens image and the sensor, since it satisfy the lens equation  $1/a + 1/b = 1/f_\mu$ .

## 1.4 Plenoptic Camera 1.0

The first version of the plenoptic camera has been proposed and realised by Adelson and Wang in 1992 [8] and then improved by Ng *et al.* in 2006 [21, 2]. The purpose of Ng was to design a camera that can use ray tracing techniques to compute synthetic photographs after the acquisition of the four dimensional light field. The main difference between Ng camera and Adelson

and Wang camera is that the latter was a prototype that utilized a system of relay lenses from the main lens image plane and the micro lens array [21] while in Ng camera the array of micro lenses is placed directly in front of the sensor. Each micro lens forms an elemental sub image on the sensor and the directional information is inside the sub images. The main lens focuses the rays coming from one point on the object plane on a single point in the image plane. If an array of micro lenses is placed at this image plane all the rays will end up on a single micro lens. The micro lens will then split this bundle of rays on the sub image underneath it, separating the rays according to their direction. This is explained in figure 1.6 where the plenoptic camera is modelled a simple 2 f system. Since the sensor plane is conjugate with the main lens image under each micro lens there will be an image of the main lens aperture. For simplicity in figure 1.6 the system is composed by only five micro lenses and each sub image is composed of only three pixels. The rays departing from a single point in the object plane shown in blue, red and green, are transferred by the main lens on a single micro lens. As an effect of the micro lens, each ray ends on a different pixel of the micro image.

18 CHAPTER 1. THEORY AND METHODS OF PLENOPTIC IMAGING

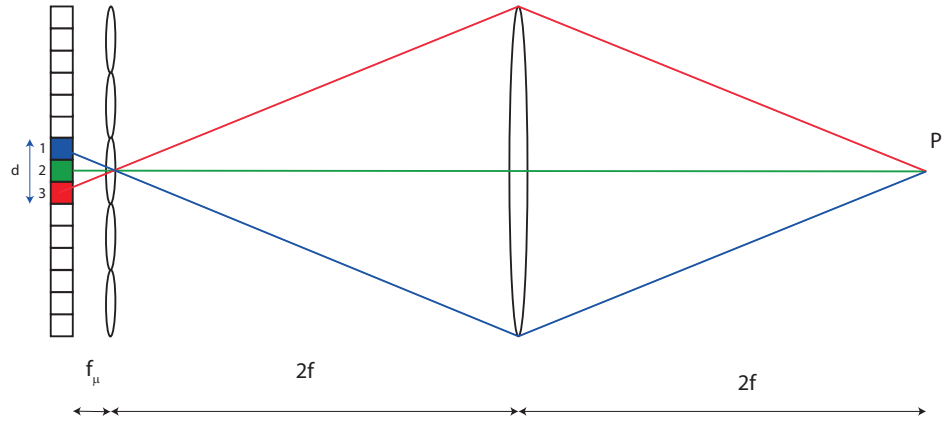


Figure 1.6: Ray diagram of a plenoptic 1.0 system. The main lens is in a  $2f$  configuration and the sensor plane is conjugated with the main lens plane. The micro lens position maps the position  $(x,y)$  of the point  $P$ , while the sub image maps the directions of the rays coming from that point. The ray with direction  $\theta_1$  falls on the pixel 1 (blue), the ray with direction  $\theta_2$  falls on the pixel 2 (green) and the ray with direction  $\theta_3$  falls on the pixel 3 (red). The sub image  $d$  maps the direction of the ray.

Since in figure 1.6 there are only three pixels per micro lens, the maximum number of directions that can be sampled is three. A plenoptic camera samples as many directions as the number of pixels under each lens let, therefore the directional resolution is given by the sub image resolution. Regarding spatial resolution, looking again at figure 1.6 can be noticed that the spatial position of the point  $P$  is recorded at the micro array plane and the sampling of the position is linked to the number of lenses in the micro array. This leads to a trade-off between directional and spatial resolution since due to the finite dimension of the sensor, when more pixels are used to record the direction the same amount of pixel is lost to record the position. A further and more detailed explanation of this will be given in the next paragraph. Now look how the light field is recorded. With reference to figure 1.7 two points are shown at two different positions but on the same focal plane. The

task now is to find a link between Levoy's definition of Light Field, the two point representation [13, 4], and the output data of the plenoptic 1.0 camera. Each sub image under each lens-let is an image of the main lens aperture, while the main lens image is formed on the micro array plane. To define the direction of a ray two points are needed. One point is its origin, the second is where it crosses the main lens. These two points are sampled by the lens let array and by the sub images on the sensor, as shown in figure 1.7. Therefore it is possible to refer to the micro lens position on the array with spatial coordinates  $(x,y)$ , and to the pixels of the sub images as the directional co-ordinates  $(u,v)$ . With an array of  $5 \times 5$  micro lenses and a sensor of  $15 \times 15$  pixel, the 4D light field recorded will be a  $5 \times 5 \times 3 \times 3$  function. Each point of this function is an intensity value identified by four coordinates, 2 spatial and 2 directional. the sampling of the spatial coordinates is  $5 \times 5$ , the sampling of the directional coordinates is  $3 \times 3$ .

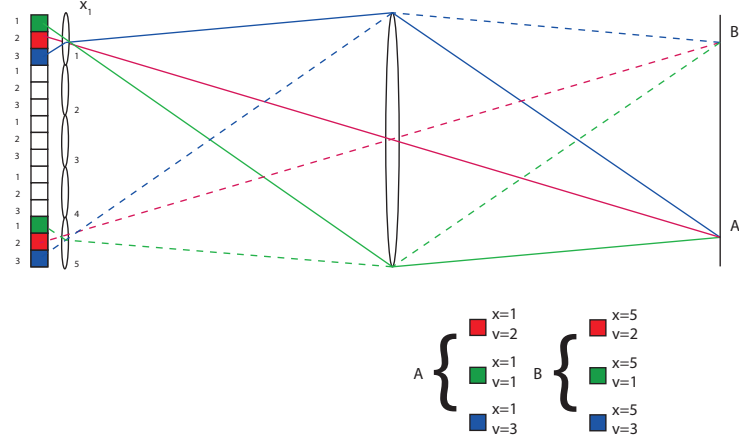


Figure 1.7: Sampling of Light Filed. Each ray is described by a set of four coordinates, two spatial ( $x,y$ ) and two directional ( $u,v$ ). The spatial coordinates are sampled by the position of the lens let in the micro array, the directional coordinates are sampled by the pixel under the lens let. Point A, its position is sampled by the lens let number 1( $x=1$ ), and three rays are green (1,1), red(1,2), blue(1,3). Each ray is defined by  $x$  and  $v$ . Point B:for one position ( $x=5$ ) three rays are sampled green (5,1), red(5,2), blue(5,3), dashed line.

This sampling used in the example above is of course very low. The amount of light captured by a lens is defined by its f-number that is the ratio between the focal length and the aperture. The f-number is proportional to the number of rays with different directions that enter into the main lens aperture. We can also define the relative f-number as the ratio between the distance between the lens and its image, and the aperture.

$$f_{\#} = \frac{z}{d} \quad (1.2)$$

where  $z$  is the distance from the main lens and the image plane and  $d$  its aperture diameter. Another useful quantity to describe the amount of directions sampled by a lens is its numerical aperture, defined, referring to figure

1.8 as:

$$NA = n \sin(\theta) \simeq n\theta = \frac{2}{f_{\#}} \quad (1.3)$$

Where  $n$  is the index of refraction, and  $\theta$  is half the total range of direction sampled by the lens. In air  $n=1$ , therefore the relation between the f-number and the range of directions is given by:

$$\Delta\theta = 2\theta = \frac{4}{f_{\#}} \quad (1.4)$$

To be sure that all the directions sampled by the main lens are mapped into the light field, the f-number of the lens let should match the f-number of the main lens [21] as shown in figure 1.8. This condition known as f-number matching is very important in plenoptic imaging. If the f-number of the lens let is smaller than the one of the main lens then there is an under sampling of the rays intercepted by the main aperture, since some of the pixels remain dark. If the f-number of the lens let is bigger on the other hand there is cross-talk between the sub images. In both cases directional information is in part lost (figure 1.9) .

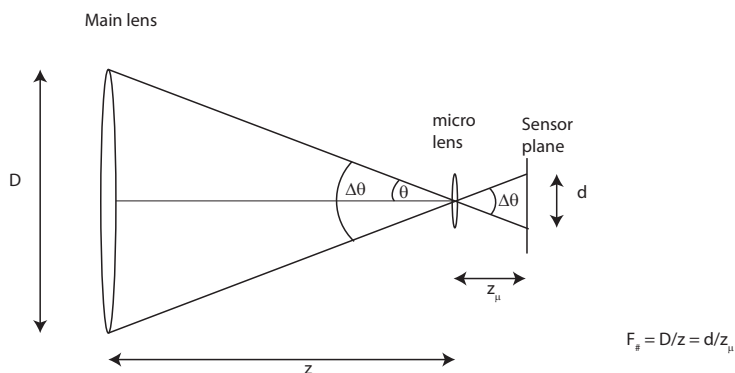


Figure 1.8: F-number matching between the main lens and the micro lens in the array.

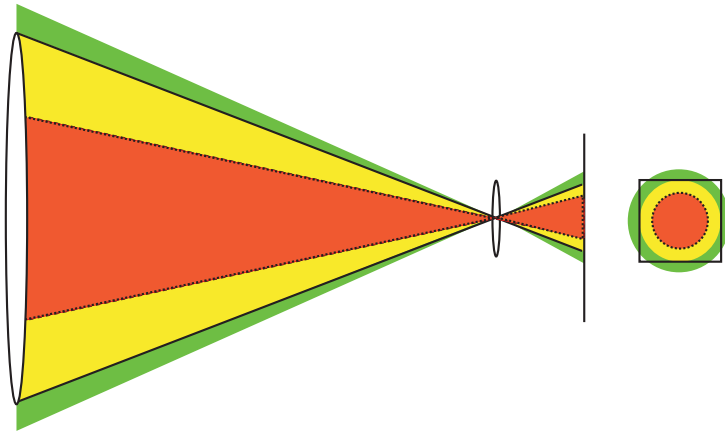


Figure 1.9: When the f-number is matched, all the rays captured by the main lens are mapped on the sub image (yellow). If the f-number is smaller (red), the sub image is smaller and there is an under sampling of the set of rays. If the f-number of the lens let is bigger (green), the sub image is larger and cross talk happens between near sub images .

#### 1.4.1 Phase space in plenoptic 1.0

It is very useful to analyse the sampling of the light field under a phase space point of view. In figure 1.10 a point source is sampled by the lens let array. Here it is considered the mono dimensional case for simplicity. The single ray departing form the point  $P$  on the focal plane of the main lens is refracted by the optical system and is captured by a pixel on the sensor that belong to the sub image of a lens let. The sub image position on the array gives the coordinate  $x$ . The pixel of the sub image gives the direction  $\theta_x$ . Therefore in the phase space a single ray is represented by a point with coordinates  $(x, \theta_x)$ . Considering all the rays departing from the point  $P(x)$  captured by the main lens, they will all be focused on a single lens let and then split on the sub image. Each pixel of the sub image corresponds to a different direction (ray). In the phase space this is equivalent to a vertical line. The

physical meaning is that to single spatial position  $x$  corresponds a range of  $\Delta\theta_x$  possible different directions, defined by the numerical aperture of the main lens matched with the one of the lens let.

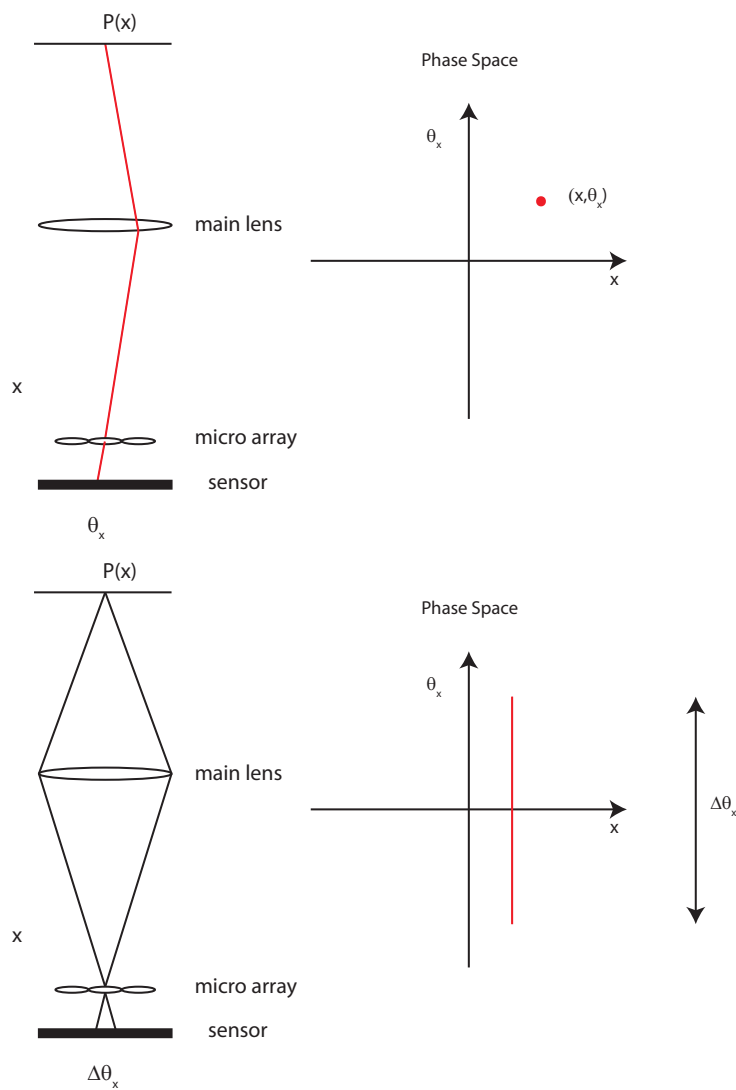


Figure 1.10: Sampling of the light field and phase space representations of the rays.

### 1.4.2 Light Field Parametrization

Before discussing the rendering procedures for plenoptic 1.0 light field data there will be described the three different parametrizations of the light field from the raw image. A plenoptic 1.0 raw image looks like an array of sub images, each sub image contains samples of direction. An example of a plenoptic raw image can be seen in figure 1.11, while in figure 1.12 it is shown in detail how a sub image appears. The raw image has been generated simulating light propagating into a plenoptic camera, using a Matlab toolbox developed as part of this work which is described in detail in chapter 2. The camera is composed of a 60 mm lens, with an aperture of 7 mm, and a sensor with a resolution of 1500 by 1500 pixel. The micro array is composed of 75 by 75 lens let with a focal length of 5 mm. The object imaged is a flat two dimensional image, therefore no depth information is stored.

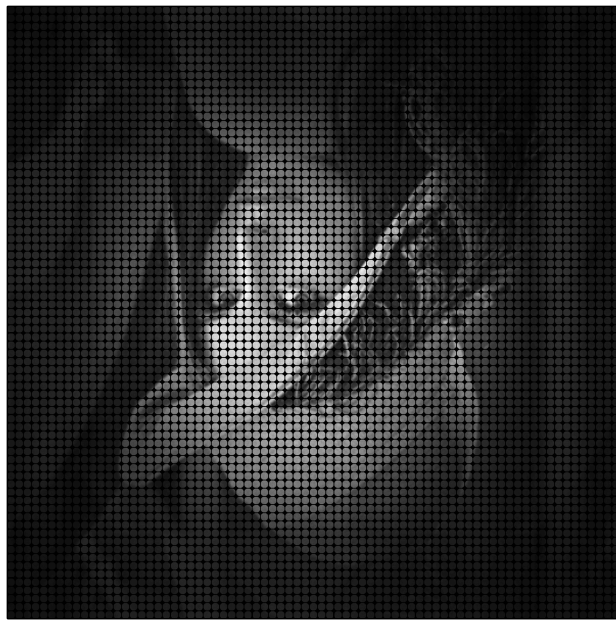


Figure 1.11: Example of a raw plenoptic 1.0 image.

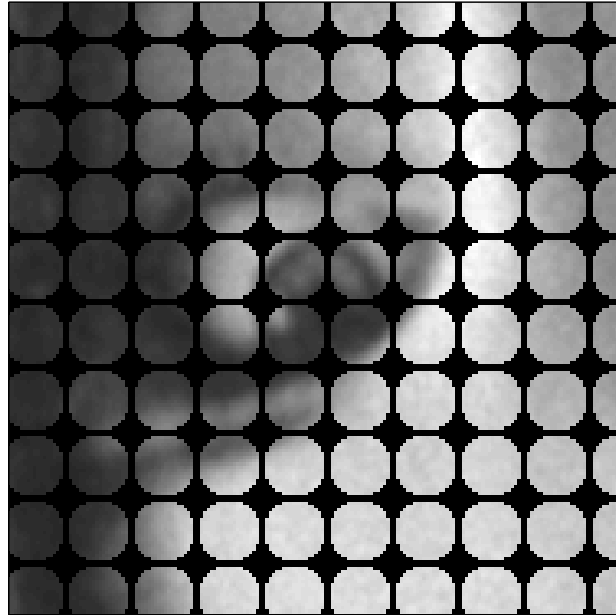


Figure 1.12: Zoom on the raw image. Each lens-let is formed by  $20 \times 20$  pixels. Each pixel represents a direction of the rays hitting the lens let that produced the sub image.

This raw image is the first parametrization of the light field and it is called camera view. Pixels are arranged according to the positional coordinates, and each sub image contains the directional coordinates as shown in figures 1.11 and 1.13. A second parametrization, known as array view, is obtained by rearranging the pixels according the directional coordinates [2]. The result is an array of  $N \times N$  sub images, where  $N$  is the number of samples of the directional coordinates. Each sub image represents the point of view linked with a direction  $(\theta_x, \theta_y)$ . The array view can be seen in figure 1.14 and 1.15 while the method to pass from the camera view to the array view is illustrated in figure 1.13.

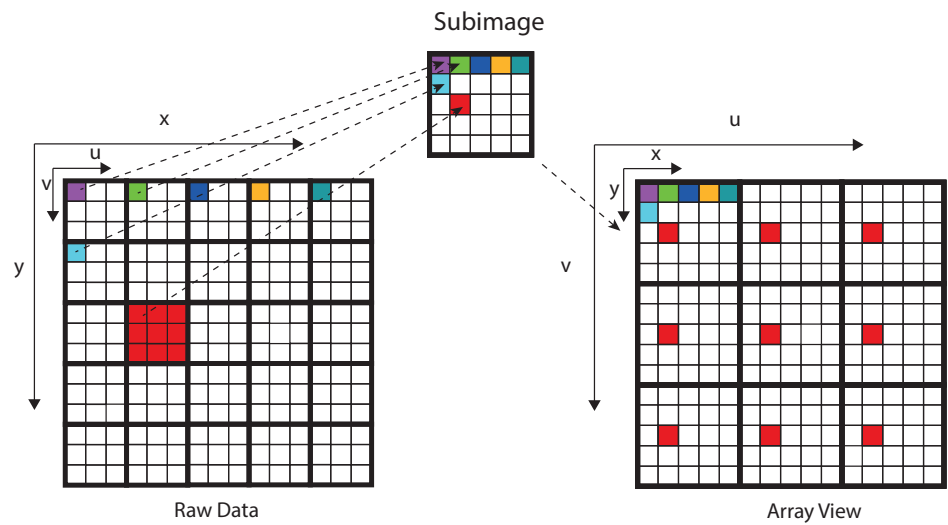


Figure 1.13: The array view is an array of the different point of view obtained rearranging the pixels according to the directional coordinates.

An example of the array view parametrization of the raw image in figure 1.11 is shown in figure 1.14.

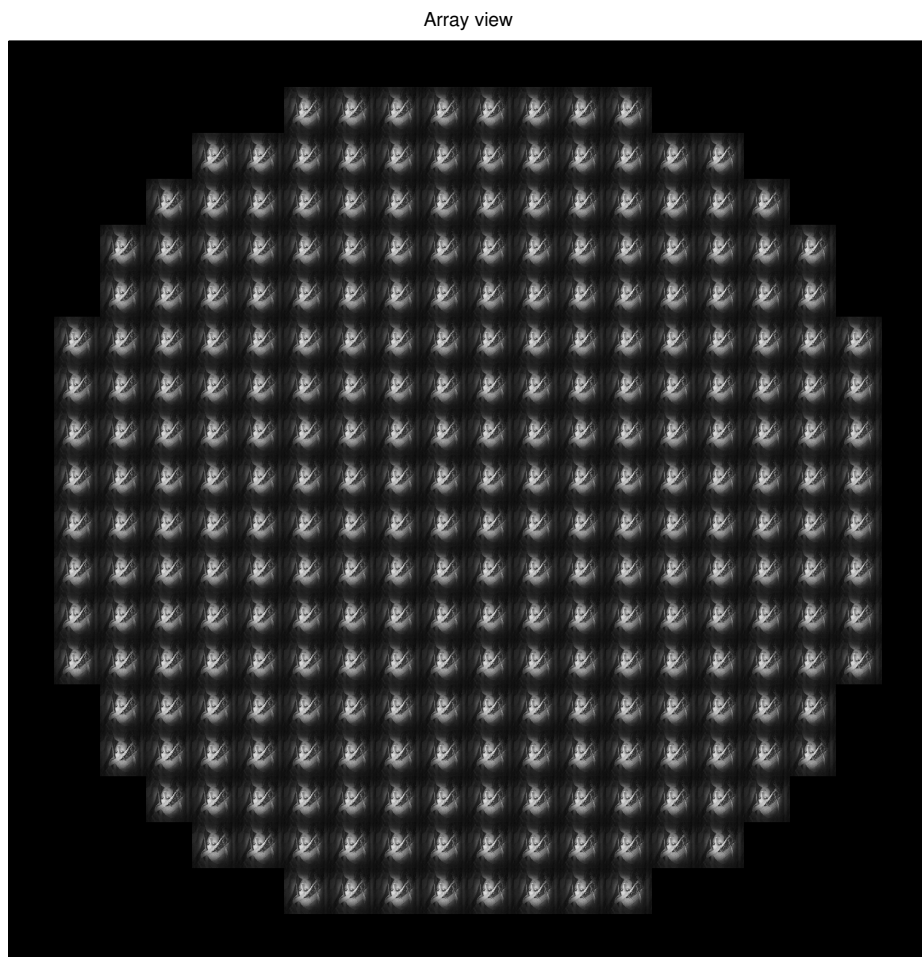


Figure 1.14: The array view is an array of the different points of view obtained by rearranging the pixels according to the directional coordinates.



Figure 1.15: Zoom of the central part of the array view showing in detail the different points of views.

The third and last parametrization of the light field, is the 4 D radiance, a four dimensional function that represents radiance as a function of position and direction. [13]. This third parametrization is less intuitive but is very useful from a computational point of view since it is a four dimensional array, and every ray can be addressed by a set of four coordinates, or indices, as will be explained in detail in chapter 3.

## 1.5 Plenoptic 1.0 rendering

The act of de-codifying the information present on the sensor of the plenoptic camera in order to get an image is called rendering. In a conventional 2D image the intensity of each single pixel, corresponding to a position, is obtained summing the contributions of all the rays of light converging to that point of the sensor [3] as shown in figure 1.16. This is equivalent to integrate for each position all the possible directions of the light field.

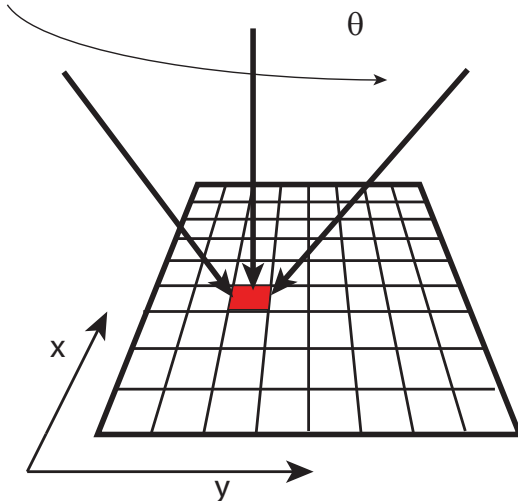


Figure 1.16: Sampling of the light field and phase space representations of the rays.[2]

The same is valid for a computational image, where the integration are made in post processing from the raw plenoptic data captured. If  $L(x, y, u, v)$  is the sampled 4D light field, the radiance  $E(x, y)$  on a pixel  $(x, y)$  of the final rendered image will be given by integrating all the rays coming from all the sampled directions  $(u, v)$  for any fixed point  $(x, y)$ . Following the work of Ng

*et al.* [2] we have:

$$I(x, y) = \frac{1}{z^2} \iint L(x, y, u, v) A(u, v) \cos^4 \theta dudv \quad (1.5)$$

Where  $z$  is the distance between the main lens and the sensor,  $\Theta$  is the angle formed by the rays and the sensor normal and  $\cos^4 \Theta$  is the vignetting factor that takes into account the reduced effects of the rays striking the sensor from oblique directions.  $A(u, v)$  is an aperture function that limits the directions upon which integration takes place to the ones included in the aperture of the main lens. In the paraxial approximation, the  $\cos^4 \Theta$  term can be dropped as well as the  $1/z^2$  term and equation 1.5 becomes:

$$I(x, y) = \iint L(x, y, u, v) A(u, v) dudv \quad (1.6)$$

From a computational point of view, since the samples are discrete, the double integral becomes as a sum along the directional coordinates  $u$  and  $v$ . The total intensity of each pixel of the rendered image is then the sum of the intensities of the pixels that form the correspondent sub image divided by the number of pixels in the sub image. For a light field with  $N \times N$  directional samples, the intensity  $I(x, y)$  is given by:

$$I(x, y) = \frac{1}{N^2} \sum_{i=0}^N \sum_{j=0}^N L(x, y, i, j) \quad (1.7)$$

This can be seen very clearly in the phase space where each pixel of the final image is made by the mean of all  $N$  directional samples [3], as shown in figure 1.17.

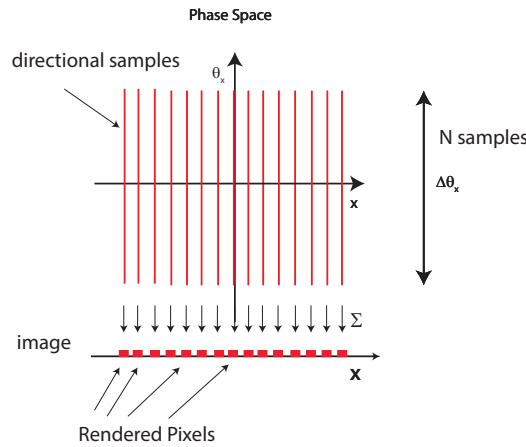


Figure 1.17: Rendering an image from plenoptic 1.0 raw data is equal to summing all the directional samples for each position. This process is shown for the the  $(x, \theta_x)$  slice of the phase space. [3]

Looking at figure 1.17 can be noted that rendering an image from a light field captured by a plenoptic 1.0 camera causes a loss of resolution if compared with the image collected by a conventional camera using the full sensor. Each pixel of the final image correspond to one lens let. Considering a plenoptic camera composed by a sensor with a resolution of  $1000 \times 1000$  pixels and a micro lens array of  $100 \times 100$  lens lets, each sub image will contain  $10 \times 10$  directional samples. All these samples will contribute in computing the intensity of a single pixel, therefore there will be only one pixel per lens let in the final image whose resolution is  $100 \times 100$  pixels. This is the main limitation to plenoptic 1.0 cameras, the better the directional information are sampled, the more spatial resolution is lost. [3, 2]. An example of a rendered image from a computer generated light field is shown in figure 1.18



Figure 1.18: rendered image form the raw data in figure 1.11. Resolution is only  $75 \times 75$  pixel.

This loss of resolution arises from the fact that the lenslet array is not focused on the sensor and it produces on the sensor a blurred image [3].

## 1.6 Plenoptic Camera 2.0

A new kind of plenoptic camera, named focused plenoptic camera or plenoptic camera 2.0, has been proposed by Georgiev and Lumsdaine *et al.* [34, 35]. As shown in figure 1.5 the plenoptic camera 2.0 is based on an array of micro lenses focused on the image plane of the main lens. In this configuration the sensor plane becomes conjugated with the main lens image plane. As will be discussed in the next sections, in a plenoptic 2.0 camera exists a flexible trade-off between angular and spatial resolution [3] leading a full sensor resolution

in the final image [36, 37]. There are two possible configurations of the plenoptic 2.0 camera, as shown in figure 1.19. In both configurations each micro lens forms on the sensor a relay image of part of the main lens image. The position of the micro array is determined to satisfy the lens equation  $1/a + 1/b = 1/f_\mu$ , where  $a$  is the distance from the main lens image plane to the micro array,  $b$  is the distance from the micro array to the sensor plane and  $f_\mu$  is the focal length of each micro lens. If  $b$  is bigger than the focal length  $f_{mu}$  the camera is in a "Copernican configuration" where the main lens image is a real image in front to the micro array, while if  $b$  is smaller than  $f_{mu}$ , the distance  $a$  happens to be negative and the main lens image is formed behind the sensor plane. This is called "Galilean configuration" and the micro array images on the sensor a virtual main lens image.1.19[3].

## 34CHAPTER 1. THEORY AND METHODS OF PLENOPTIC IMAGING

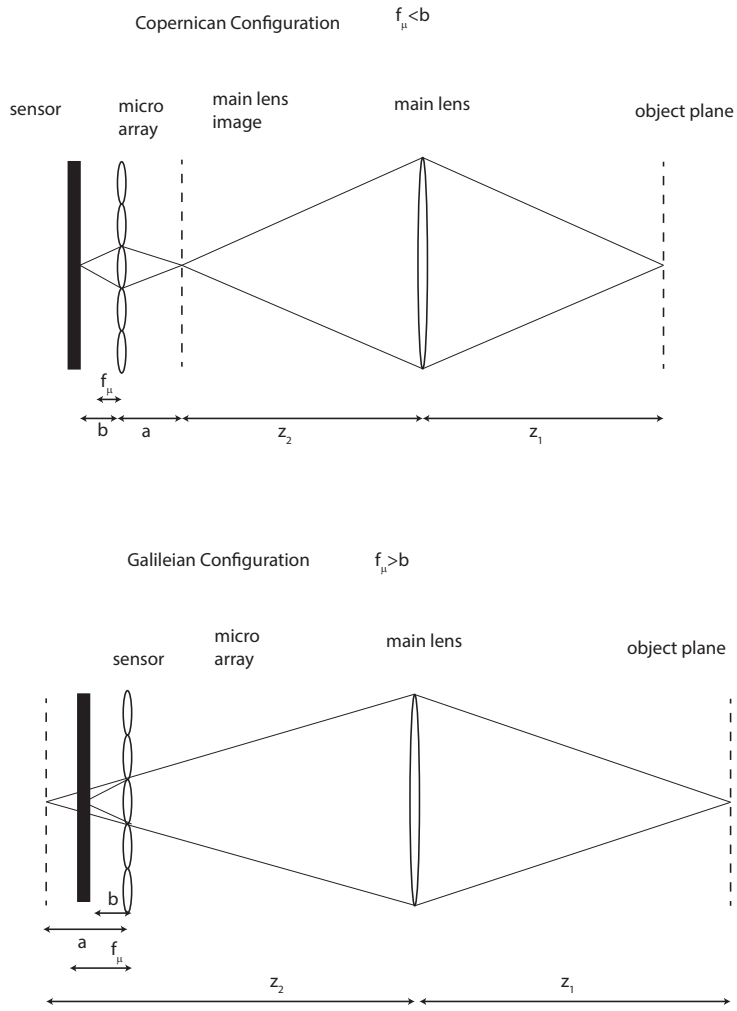


Figure 1.19: If the main lens image is formed in front of the micro array the configuration is called "Copernican", top, and the focal length of the micro array is smaller than the distance  $b$ . If the main lens image is formed behind the micro array the configuration is "Galilean", on the bottom, and the focal length of the micro array is bigger than the distance  $b$ .

For both configurations the magnification of micro array stage is:

$$m = \frac{b}{a} \quad (1.8)$$

The ratio between the distances  $a$  and  $b$  plays a crucial role in sampling the light field in the plenoptic camera 2.0. Figure 1.20 shows a raw plenoptic 2.0

image of a point source acquired simulating a system as it will be explained in chapter 2. The system is composed by a main lens with a focal length of 60 mm, in a 2f configuration and a micro array made of  $150\mu m$  diameter lens lets with focal length of 5.3 mm. The distances  $a$  and  $b$  are set in order to have a magnification  $m$  of 0.3. In this configuration each point of the main lens image is sampled by three lens lets and each sub image corresponds to a point of view of the object. The number of points of view depends on the magnification of the micro array stage. Hence, in order to have more than one point of view recorded it is necessary that the magnification  $m$  is less than one. Looking at figure 1.20 the raw image is composed by a  $3 \times 3$  matrix of sub images, three points of view in the x direction and three along the y direction. Figure 1.21 shows central  $5 \times 5$  sub images in the raw data. The central sub image records the direction corresponding to the central point of view, indicated in both figures with the number 2. The lens lets respectively on the left and on the right of the central one record the directions corresponding to the point of views to from the left, indicated with 1 in figure 1.22, and right, indicated with 3. We can see how the sub images 1 and 3 are shifted towards the outer edge of the sub image. This happens as an effect of the change in the point of view as well as because the sub images are flipped upside down as an effect of the imaging law.

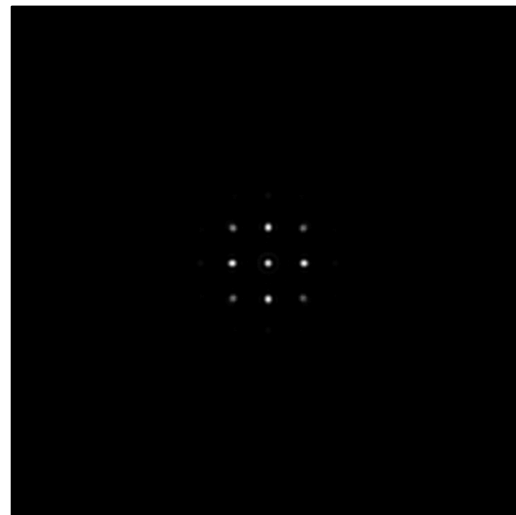


Figure 1.20: Raw data of a point source sampled by a plenoptic 2.0 system with a magnification of the micro array stage equal to 0.3. Data acquired with numerical simulations.

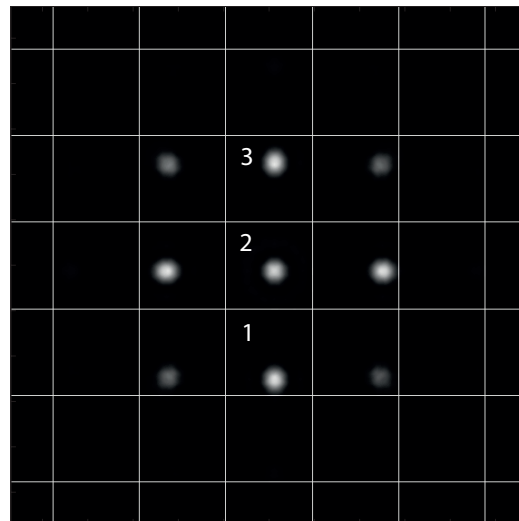


Figure 1.21: Zoomed Raw data of a point source sampled by a plenoptic 2.0 system with a magnification of the micro array stage equal to 0.3. Data acquired with numerical simulations. The grid represent the boundaries of each sub image to show how the point of view of the point source changes across the lens lets. The sub images are shifted by a quantity proportional to the position of the lens let in the array.

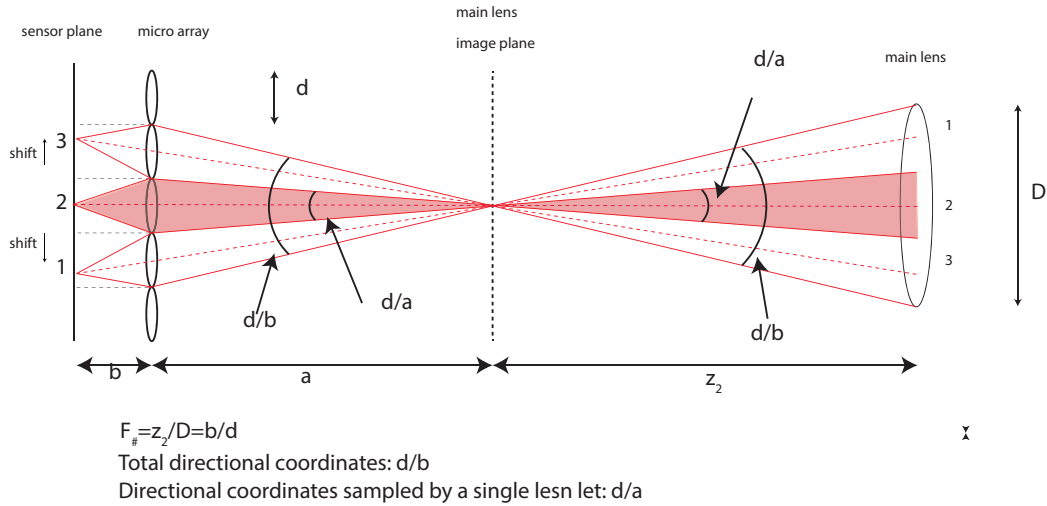


Figure 1.22: Sampling of the light field by a plenoptic 2.0 system. The one dimensional case is shown. Each micro lens has a diameter equal to  $d$ , a focal length  $f_\mu$ , and images the main lens image on the sensor according to the lens law  $1/a + 1/b = 1/f_\mu$ . The total range of directions that can be sampled is given by  $d/b$ . Each lens let samples a sub set of directions equal to  $d/a$  as a single direction. The range of directions shown in red are sampled by the central micro lens as a single point of view. The angular resolution is therefore  $d/a$  and the total number of directional sampled is 3.

As in the 1.0 case, the f-number of the micro lenses matches the f-number of the main lens. Referring to figure 1.22, because of the f- number matching condition, the total number of directions captured by the main lens is defined as  $P = D/z_2 = d/b$  where  $D$  is the aperture of the main lens,  $z_2$  the distance of the main lens image,  $d$  is the diameter of the lens let and  $b$  is the distance between the lens let and the sensor. The amount of directions captured by a single lens let is equal to  $p = d/a$ . Hence the range sampled by the single lens let with respect to the total range of directions in the light field is:

$$\frac{p}{P} = \frac{d}{a} \frac{b}{d} = m \quad (1.9)$$

Hence:

$$p = \frac{b}{a}P = mP \quad (1.10)$$

Therefore the magnification of the lens let array determines the angular resolution of the plenoptic 2.0 system. In the case illustrated in figures 1.23 and 1.22 for each position  $x$  on the main lens image plane, 3 directions are sampled. Regarding the spatial resolution of the rendered image, since the main lens image is scaled by the lens lets by a factor of  $m$ , the resolution of the rendered image will be  $b/a$  times the resolution of the full sensor. This fact implies that the spatio-angular trade off of the plenoptic 2.0 camera is not fixed by the number of micro lenses, but it is determined by the optical geometry of the micro lens stage, and is fully determined by the magnification  $m = b/a$ . The more samples of the directional coordinates, the less will be the spatial resolution of the rendered image. In section 1.7 a more rigorous proof of this will be given. Figure 1.23 shows the effect of magnification on the raw image of a point source. If the magnification is 1, the main lens image is replicated on the sensor under only one lens let. No further information is given by the micro array stage. The whole range of directions is sampled by a single lens let and with only one point of view it is not possible to recover the directional information. In order to have more than one point of view,  $m$  should be at least 0.5. In this case the point source is replicated under a total of four lens lets giving 2 by 2 points of view to render the image. If the magnification decreases further, the number of points of view increases. We can state that the directional information in plenoptic 2.0 is recorded not by a single lens let like in the 1.0 case, but across many lens lets, since each point of the object plane is imaged by a number of lens lets proportional

to the inverse of the magnification 1.8. Each of this lens samples a part of the directional coordinates contained into the light field equal to  $d/a$ . The more point of view are presents, the smaller will be the quantity  $d/a$ , and therefore, the better will be the angular resolution. [35]

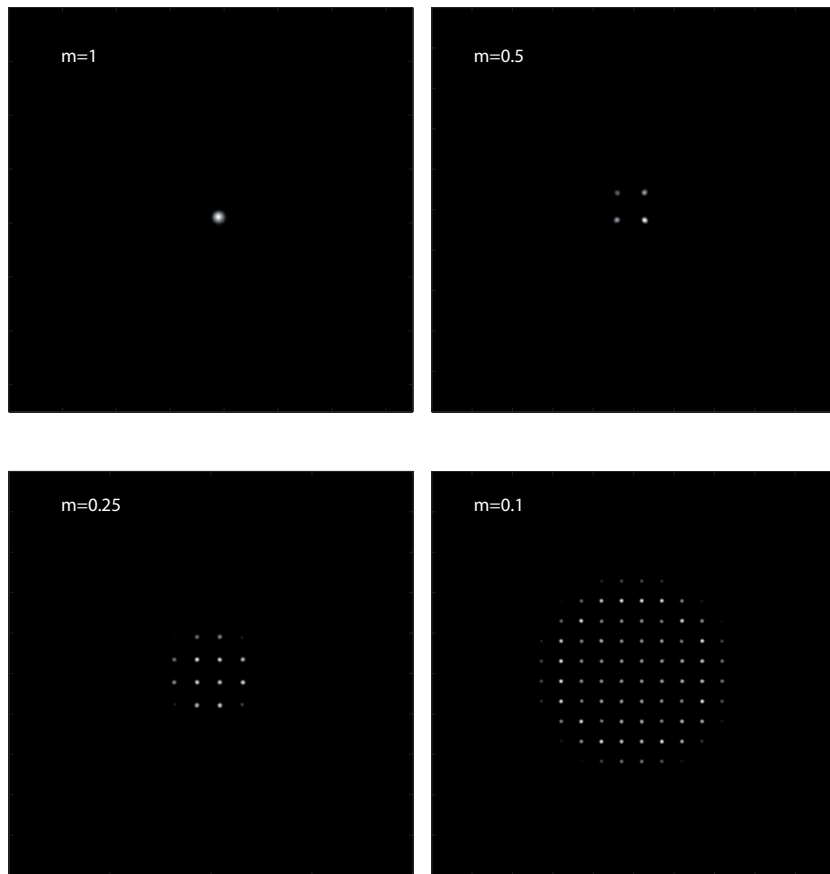


Figure 1.23: Raw images of a point source simulated with different magnifications. From top left to bottom right:  $m = 1$ ,  $m = 0.5$ ,  $m = 0.25$ ,  $m = 0.1$ .

## 1.7 Plenoptic camera 2.0: a geometrical optics analysis

This section provides a mathematical proof of the concepts introduced in section 1.6. The mathematical model of Light Field sampling in plenoptic 2.0 has been developed by Lumsdaine and Georgiev [35, 34]. The goal of this chapter is to express the intensity profile present on the sensor as a function of the light field at the focal plane of the main lens. The intensity on the sensor is given by integrating along all the rays, or the directions, the light field at the sensor in analogy with what discussed in 1.5:

$$I(x, y) = \iint_{\theta_x, \theta_y} L(x, y, \theta_x, \theta_y) d\theta_x d\theta_y \quad (1.11)$$

For simplicity only one positional coordinate  $x$  is considered, and its corresponding direction will be described by a new coordinated called *momentum*, in analogy with Hamiltonian mechanics, defined as:

$$p_x = n\theta_x \quad (1.12)$$

$n$  is the refractive index of the medium of propagation, assumed to be homogeneous. The reason of this change in coordinates is that using the momentum  $p$  the transformations matrix of the optical elements are invertible, and the calculations are simpler [38]. The one dimensional intensity profile is then equal to:

$$I(x) = \int_{p_x} L(x, p_x) dp_x \quad (1.13)$$

In the phase space the rays composing the light field, will be represented by points with coordinates  $(x, p_x)$ . Given a ray  $\overrightarrow{X_0} = (x, p_x)$ , it is possible to

define an arbitrary matrix  $A$  describing the transformation the ray undergoes while propagating in an optical system as:

$$\vec{X}_1 = A\vec{X}_0 \quad (1.14)$$

Where  $\vec{X}_1$  is a vector representing the ray after the transformation  $A$ . The transformation matrix has been defined with the property of having  $\det(A)=1$ , and being invertible it is possible to express the ray  $\vec{X}_0$  as a function of  $\vec{X}_1$  as:

$$\vec{X}_0 = A^{-1}\vec{X}_1 \quad (1.15)$$

The same considerations can be made for the full set of rays composing the light field. In the hypothesis of zero loss during the propagation, the total light field  $L$  is conserved, and  $L(\vec{X}_0)$  equals  $L(\vec{X}_1)$ . Therefore:

$$L_1(\vec{X}_1) = L_0(\vec{X}_0) \quad (1.16)$$

Because of equation 1.14 the Light Field at the position  $\vec{x}_1$  is :

$$L_1(A\vec{X}_0) = L_0(\vec{X}_0) \quad (1.17)$$

For the ray  $\vec{X}_1 = A\vec{X}_0$ :

$$L_1(\vec{X}_1) = L_0(A^{-1}\vec{X}_1) \quad (1.18)$$

For the generic ray  $\vec{X}$  the light field transformation formula becomes:

$$L_1(\vec{X}) = L_0(A^{-1}\vec{X}) \quad (1.19)$$

Equation 1.19 shows the link between the light field at a plane, with the same light field after an arbitrary optical transformation. Referring to figure 1.24

a single lens let of diameter  $d$  is shown and the light field at the sensor plane  $L_b(x, p_x)$  is expressed as a function of the coordinates of the light field at the main lens image plane  $L_a(x, p_x)$ . The link between the two light fields is given by equation 1.19. According to geometrical optics, and as is explained in [39], the optical transfer matrix  $A_{ab}$  from the main lens image plane and the sensor is the composition of two free space propagation matrix and an lens matrix.

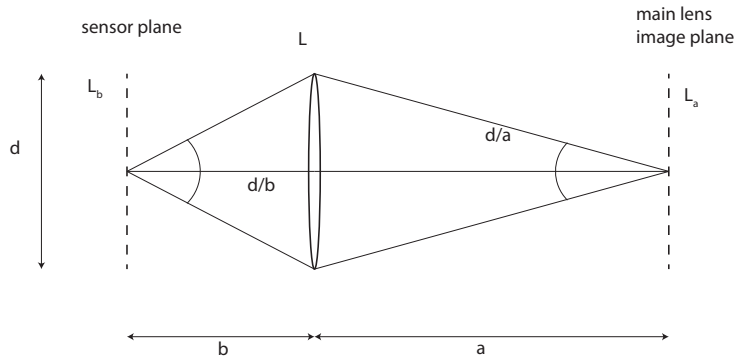


Figure 1.24: System formed by a single lens let. The rays at the main lens image plane are transformed into the rays at the sensor plane by the lens let. The transformation can be described by a matrix  $A$ .

We have:

$$A_{ab} = \begin{bmatrix} 1 & b \\ 0 & 1 \end{bmatrix} \begin{bmatrix} 1 & 0 \\ -\frac{1}{f_\mu} & 1 \end{bmatrix} \begin{bmatrix} 1 & a \\ 0 & 1 \end{bmatrix} = \begin{bmatrix} -\frac{b}{a} & 0 \\ -\frac{1}{f_\mu} & -\frac{a}{b} \end{bmatrix} \quad (1.20)$$

Its inverse is:

$$A_{ab}^{-1} = \begin{bmatrix} -\frac{a}{b} & 0 \\ \frac{1}{f_\mu} & -\frac{b}{a} \end{bmatrix} \quad (1.21)$$

Applying the inverse  $A^{-1}$  matrix in equation to equation 1.19 and substituting into the integral in equation 1.11, the intensity on the sensor behind a single lens let is:

$$I(x) = \int_{p_x} L_a\left(-\frac{a}{b}x, -\frac{b}{a}p_x - \frac{1}{f}x\right) dp_x \quad (1.22)$$

From figure 1.24, for a single spatial coordinate  $x$  on the main lens image plane the integration takes place on a range of directional coordinates  $p_x$  equal to  $d/b$  and the result is:

$$I(x) = \frac{d}{b} L_a\left(-\frac{a}{b}x, -\frac{1}{b}x\right) \quad (1.23)$$

From equation 1.23 the micro lens maps the spatial coordinates on the main lens image plane to the sensor with a scaling factor equal to the magnification  $m = b/a$ . Therefore the resolution of the sampled light field on the sensor is  $b/a$  times the resolution of the sensor. The directional coordinates are mapped as  $x/b$ . If the lens let diameter is  $d$  then the maximum number of directional coordinates sampled by one lens let is equal to the f-number of the lens let  $d/b$ . Figure 1.24 shows how a single micro lens samples the radiance from a single point  $X$  on the main lens image plane. Each pixel of the micro lens image samples a single position  $X$  and a span of  $d/a$  directional coordinates  $p_x$ . The same position  $X$  is sampled also by other micro-lenses as shown in picture 1.25, but since each micro lens only captures  $d/a$  samples of the directional coordinates, each lens let samples a different portion of the total span directional coordinates contained in the light field.

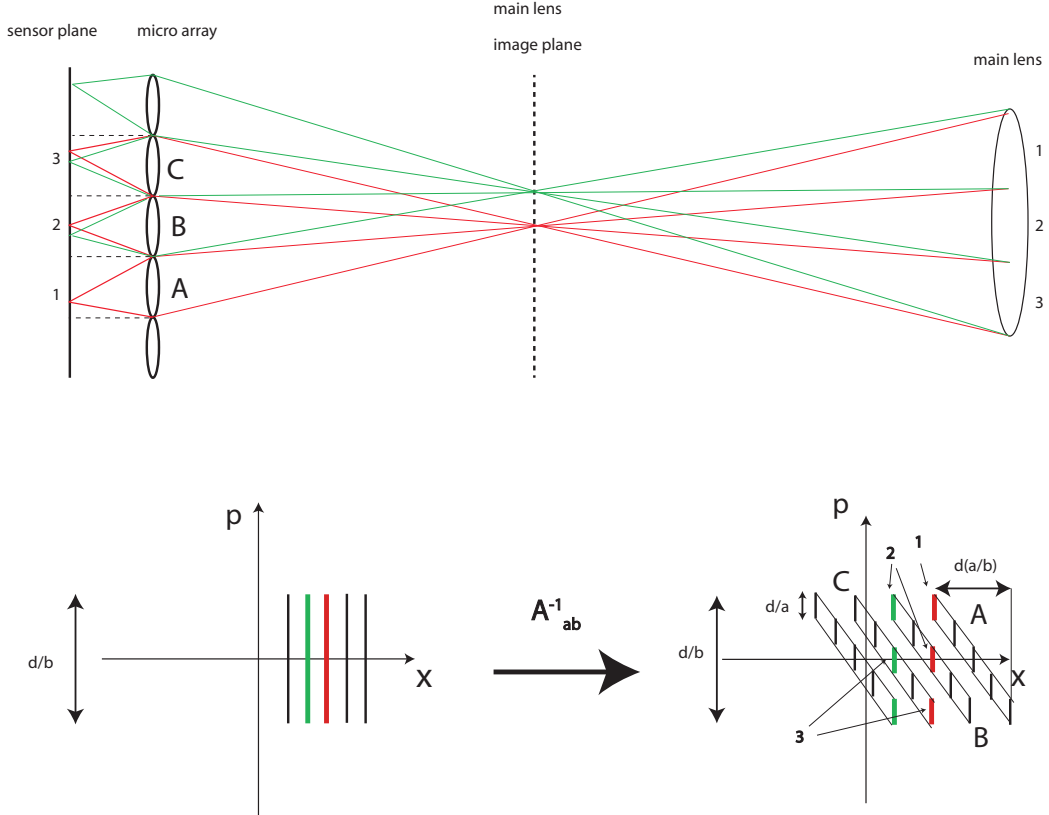


Figure 1.25: Sampling of the light field by plenoptic 2.0 camera. For each of the two points represented, red and green, The total range of directional coordinates are sampled by three different lens lets. For one position three directions are sampled, with a resolution of  $d/a$ . Therefore the directional sampling in plenoptic 2.0 is made across many lens lets. This can be seen in the phase space. Lenset B and C sample 2 directions indicated with the same number in the ray diagram and the phase space. Lens let A only samples one direction of the red point.

## 1.8 Plenoptic 2.0 rendering

The basic rendering in plenoptic 2.0 cameras is still made by integrating all directions associated to a single position, as shown 1.8. The difference with plenoptic 1.0 rendering is that this time the directional coordinates for a single position,  $d/b$ , are recorded across many lens lets, each sampling  $d/a$

coordinates and as a consequence of that, the integration takes place across all of these micro lenses [28]. The basic rendering process is shown in figure 1.26.

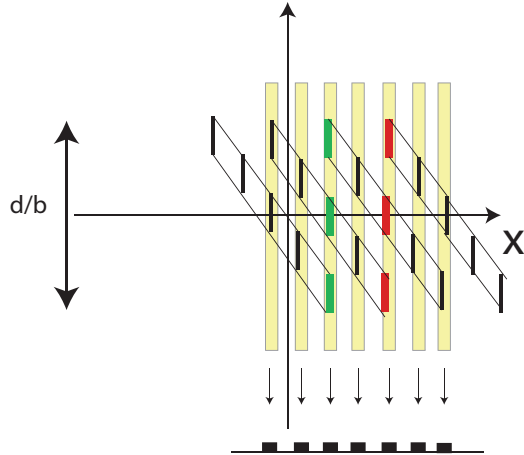


Figure 1.26: Image rendering with the focused plenoptic camera. One pixel of the rendered image is given by the integration on all the directions  $d/b$  associated with a given position. The integration takes place across the lens let.

rendering an image in plenoptic 2.0 is more complicated and less intuitive than the 1.0 case, therefore a more detailed analysis of plenoptic 2.0 rendering will be given in chapter 4.



# Chapter 2

## Fresnel Simulation Toolbox

### 2.1 Introduction

In this chapter will be described a MATLAB simulation toolbox developed as a part of this doctorate project in order to investigate the potentiality of plenoptic imaging for biomedical and microscopy applications with particular interest in its behaviour at the diffraction limit. In literature can be found many works on simulating plenoptic imaging devices. When this project began in 2012 there were few works that analysed the behaviour of a plenoptic camera under a wave optics approach and the majority of the literature treated the plenoptic system under a ray tracing approach. Then in the last years various research groups developed independently Fresnel wave optics analysis of plenoptic 1.0 imaging systems, such as Schroff *et al.* [40, 30] and Trujillo-Servilla *et al.* [41] and a Fourier optics approach of the diffraction limit of a digital camera, Farrell *et al.* [42]. In this work a Fresnel optics approach has been applied to a plenoptic camera with purpose of understanding how the light field is recorded and to define some guidelines to design a working setup. Particular attention has been dedicated to the

behaviour of the system at its diffraction limit, subject that has never been explicitly treated in literature. In this chapter there will be exposed four different methods to simulate light propagation in an optical system and it will be described and compared their performance in term of accuracy of the results, noise and computational effort. A Fresnel optics approach has been chosen because the simulation tool to describe a plenoptic imaging system has to the following requirements:

- It has to preserve the phase of the optical field propagating in order to preserve directional information of the rays of light;
- It has to take into account the effects of diffraction;
- It had to be adaptable in order to easily change the characteristic of the optical system, trying various configurations, keeping the operator based approach of ray tracing.

To address these features, a wave optics simulation toolbox has been designed and developed. Most of the existing literature on simulating plenoptic system are based on ray tracing techniques [43, 44, 45, 2, 13] . The advantages of using ray tracing is that the transformations that rays undergo during the propagation can be described by two basic linear operators and compositions of them. These are the free space propagation and the lens operator. In developing the wave optics simulation this principle has been kept, and two operators have been defined: propagation and lens. four different types of propagation operator have been described and compared. In analogy with ray tracing an optical system has been simulated using composition of the

two simple operators. In developing this platform all the media composing the system has been considered as linear, isotropic, homogeneous and non dispersive. The meaning of this properties in the following section

## 2.2 Scalar Theory of diffraction

The term diffraction has been defined by Sommerfeld as "any deviation of light rays from rectilinear paths which cannot be interpreted as reflection or refraction" [46]. The commplex vectorial equations describing wave propagation in three dimentional space can be simplified into a set of scalar equations using the Scalar Theory of Diffraction as expplained by Goodman [47]. The starting point is given by Maxwell Equations in absence of sources of electrical field of magnetic dipoles:

$$\begin{aligned} \nabla \times \vec{E} &= -\mu \frac{\partial \vec{H}}{\partial t} \\ \nabla \times \vec{H} &= \epsilon \frac{\partial \vec{E}}{\partial t} \\ \nabla \cdot \epsilon \vec{E} &= 0 \\ \nabla \cdot \mu \vec{B} &= 0 \end{aligned} \tag{2.1}$$

where  $\vec{E}$  is the electric field,  $\vec{H}$  is the magnetic field,  $\mu$  and  $\epsilon$  are respectively the magnetic permeability and electrical permittivity of the medium in which the optical wave is propagating. Both  $\vec{E}$  and  $\vec{H}$  are a functions of the position  $x, y$  and  $z$ , as well as the time  $t$ .

The operator  $\nabla$  is defined as:

$$\nabla = \frac{\partial}{\partial x} \hat{i} + \frac{\partial}{\partial y} \hat{j} + \frac{\partial}{\partial z} \hat{k} \quad (2.2)$$

where  $\hat{i}, \hat{j}$  and  $\hat{k}$  are unit vectors along directions  $x, y$  and  $z$ .

Propagation is assumed to happen in a dielectric medium that is linear, isotropic and homogeneous. A medium is linear if its response to a several disturbances acting simultaneously can be decomposed into the sum of the responses to the single disturbances taken individually. It is isotropic if its properties do not depends on the directions of polarization of the wave and is homogeneous if its permittivity is constant along all direction of propagation. The medium is considered also to be non dispersive, that is the permittivity  $\epsilon$  is not dependent on the wavelength.

Applying the operator  $\nabla \times$  to the left and to the right side of the first equation of 2.1 and using the vector identity

$$\nabla \times (\nabla \times \vec{E}) = \nabla(\nabla \cdot \vec{E}) - \nabla^2 \vec{E} \quad (2.3)$$

$$\nabla(\nabla \cdot \vec{E}) - \nabla^2 \vec{E} = \nabla \times (-\mu \frac{\partial \vec{H}}{\partial t}) \quad (2.4)$$

From the third equation in 2.1:

$$\nabla \cdot \epsilon \vec{E} = 0 \quad (2.5)$$

hence equation 2.4 becomes:

$$-\nabla^2 \vec{E} = \nabla \times (-\mu \frac{\partial \vec{H}}{\partial t}) \quad (2.6)$$

since both the operators  $\nabla \times$  and its derivative are linear it is possible to swap them on the right hand side of equation 2.4. Then substituting the second

Maxwell equation 2.1 into the 2.6:

$$-\nabla^2 \vec{E} = -\mu\epsilon \frac{\partial^2}{\partial t^2} \vec{E} \quad (2.7)$$

Where  $\nabla^2$  is the Laplacian operator defined as:

$$\nabla^2 = \frac{\partial^2}{\partial x^2} \hat{i} + \frac{\partial^2}{\partial y^2} \hat{j} + \frac{\partial^2}{\partial z^2} \hat{k} \quad (2.8)$$

We define the refractive index of the medium in which the wave is propagating as:

$$n = \sqrt{\frac{\epsilon\mu}{\epsilon_0\mu_0}} \quad (2.9)$$

where  $\epsilon_0$  is the permittivity of the vacuum and  $\mu_0$  the magnetic permeability in vacuum. Therefore the speed of light in the vacuum is:

$$c = \sqrt{\frac{1}{\epsilon_0\mu_0}} \quad (2.10)$$

Then the wave equation for the electric field becomes:

$$\nabla^2 \vec{E} - \frac{n^2}{c^2} \frac{\partial^2 \vec{E}}{\partial t^2} = 0 \quad (2.11)$$

Similar considerations can be done for the magnetic field, leading to an identical equation:

$$\nabla^2 \vec{H} - \frac{n^2}{c^2} \frac{\partial^2 \vec{H}}{\partial t^2} = 0 \quad (2.12)$$

Since the wave equation is obeyed by both the electric field and magnetic fields, it is possible to define a scalar wave equation, obeyed by the single components of those vectors. The scalar field components are represented as a function  $u(x, y, z, t)$  called field disturbance. The scalar wave equation is then:

$$\nabla^2 u - \frac{n^2}{c^2} \frac{\partial^2 u}{\partial t^2} = 0 \quad (2.13)$$

With this scalar approximation it is possible to treat the propagation of an optical field as a scalar. This is only valid under the assumption of a linear, isotropic, homogeneous and non dispersive medium, since all the component in all the directions of the electric and magnetic fields must behave identically.

### 2.2.1 Helmholtz equation

In the case of monochromatic wave the scalar field  $u$  is a function of time  $t$  and position  $\vec{X}$  defined as:

$$u(\vec{X}, t) = A(\vec{X}) \cos[2\pi\nu t - \phi(\vec{X})] \quad (2.14)$$

$A(\vec{X})$  is the amplitude of the disturbance and  $\phi(\vec{X})$  is its phase at point in the space with coordinates  $\vec{X} = (x, y, z)$ . Separating space and time dependence:

$$u(\vec{X}, t) = \operatorname{Re}\{U(\vec{X})e^{-j2\pi\nu t}\} \quad (2.15)$$

where  $U$  is a complex function of position and includes the a phase term  $e^{j\phi(\vec{X})}$ .

$$U(\vec{X}) = A(\vec{X})e^{j\phi(\vec{X})} \quad (2.16)$$

This field should satisfies the scalar wave equation 2.13. Substituting equation 2.16 into 2.13:

$$\nabla^2[U(\vec{X})e^{-j2\pi\nu t}] - \frac{n^2}{c^2} \frac{\partial^2}{\partial t^2}[U(\vec{X})e^{-j2\pi\nu t}] = 0 \quad (2.17)$$

Expressing the derivatives and simplifying the exponential terms:

$$\nabla^2[U(\vec{X})] + \left(\frac{2\pi\nu n}{c}\right)^2 [U(\vec{X})] = 0 \quad (2.18)$$

The wave number is defined as:

$$k = \frac{2\pi\nu n}{c} \quad (2.19)$$

and expression 2.18 becomes:

$$(\nabla^2 + k^2)U = 0 \quad (2.20)$$

Equation 2.20 is the Helmholtz equation and it describes the behaviour of a complex disturbance propagating in a homogeneous medium.

### 2.2.2 Solutions of Helmholtz Equations

An analytical expression of the complex disturbance  $U$  that satisfies the Helmholtz equation can be found using the green's theorem under particular boundaries condition as explained by Goodman [47]. There are two possible solutions: Fresnel-Kirchhoff and Rayleigh-Sommerfeld. Considering a wave  $U_0$  propagating through a diffracting screen at a point in space with coordinates  $z = 0$  with an aperture  $D$  the boundaries conditions:

- Fresnel-Kirchhoff (FK) conditions

$$U(x, y, 0) = U_0(x, y, 0) \text{ for } (x, y) \in D$$

$$U(x, y, 0) = 0 \text{ for } (x, y) \notin D$$

$$\frac{\partial U}{\partial z} = \frac{\partial U_0}{\partial z} \text{ for } (x, y) \in D$$

$$\frac{\partial U}{\partial z} = 0 \text{ for } (x, y) \notin D$$

- Rayleigh-Sommerfeld (RS) conditions:

$$U(x, y, 0) = U_0(x, y, 0) \text{ for } (x, y) \in D$$

$$U(x, y, 0) = 0 \text{ for } (x, y) \notin D$$

The FK conditions lead to a simple result but they are not physically correct since they imply the field after the screen to be zero outside of the aperture in the immediate proximity of the screen as well as its normal derivative. Results given by the FK condition are accurate only for a distance from the aperture much larger than the wavelength. The RS condition on the other hand is less strict since it does not require the derivatives of the disturbance and leads to a solution of the Helmholtz equation that is:

$$U(x, y, z) = \frac{1}{j\lambda} \iint_{\sigma} U(\xi, \eta, 0) \frac{e^{jkr}}{r} \cos(\theta) d\xi d\eta \quad (2.21)$$

where, with reference to figure 2.1,  $\theta$  is the angle between the  $z$  axis and the direction of propagation,  $r = \sqrt{z^2 + (x - \xi)^2 + (y - \eta)^2}$  is the distance between the point  $P_1 = (x, y, z)$  and  $P_0 = (\xi, \eta, 0)$  and  $\sigma$  is the area of aperture. Since  $\cos(\theta) = \frac{z}{r}$ :

$$U(x, y, z) = \frac{z}{j\lambda} \int \int_{\sigma} U(\xi, \eta, 0) \frac{e^{jkr}}{r^2} d\xi d\eta \quad (2.22)$$

Equation 2.22 is the Rayleigh-Sommerfeld diffraction formula [47], and can be simplified under the Fresnel approximation, as will be explained in section 2.2.3.

### 2.2.3 The Fresnel Approximation

It is possible to approximate the distance of propagation  $r$  between  $P_0$  and  $P_1$  with its Taylor expansion up to the second order:

$$r = \sqrt{1 + \left(\frac{x - \xi}{z}\right)^2 + \left(\frac{y - \eta}{z}\right)^2} \approx z \left[ 1 + \frac{(1)}{2} \left(\frac{x - \xi}{z}\right)^2 + \frac{1}{2} \left(\frac{y - \eta}{z}\right)^2 \right] \quad (2.23)$$

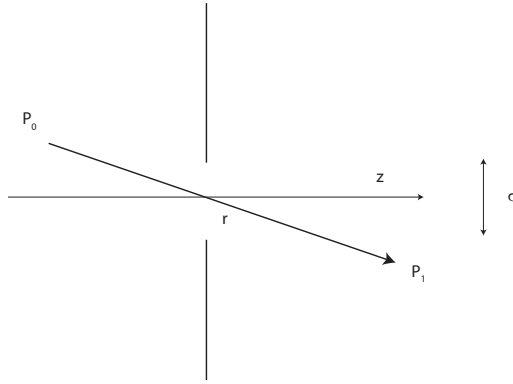


Figure 2.1: example

Therefore for large propagation distances,  $z \gg x, y$ , the diffraction integral becomes:

$$U(x, y) = \frac{e^{jkz}}{j\lambda z} \int \int_{-\infty}^{\infty} U(\xi, \eta) e^{\frac{jk}{2z}[(x-\xi)^2 + (y-\eta)^2]} d\xi d\eta \quad (2.24)$$

Factorizing the exponential term the disturbance becomes:

$$U(x, y) = \frac{e^{jkz}}{j\lambda z} e^{j\frac{k}{2z}(x^2+y^2)} \int \int_{-\infty}^{\infty} U(\xi, \eta) e^{\frac{jk}{2z}(\xi^2+\eta^2)} e^{\frac{-jk}{2z}(x\xi+y\eta)} d\xi d\eta \quad (2.25)$$

This can be seen as the Fourier transform of the disturbance before the aperture  $U(\xi, \eta)$  multiplied by a quadratic phase factor  $e^{\frac{jk}{2z}(\xi^2+\eta^2)}$  [47].

## 2.3 Operator Free space propagation: Fresnel Approximation approach

The first version of the operator free space propagation has been developed using the Fresnel Integral as written in equation 2.25. The input disturbance  $U(\xi, \eta)$  is considered to be illuminated by monochromatic light with wavelength  $\lambda$ . As stated in section 2.2.3 the Fresnel integral can be seen as the two dimensional Fourier transform of the input field  $U(\xi, \eta)$  multiplied

by a quadratic phase factor [47, 48]. This is going to be very useful from a computational point of view since it can be implemented with a fast Fourier transform algorithm (FFT) [49].

We define the function  $U'(\xi, \eta)$  as:

$$U'(\xi, \eta) = U(\xi, \eta) e^{\frac{jk}{2z}(\xi^2 + \eta^2)} \quad (2.26)$$

The optical field at the plane  $z$  is the product of the Fourier transform of  $U'(\xi, \eta)$  with the phase term  $e^{\frac{jk}{2z}(x^2 + y^2)}$ :

$$U(x, y) = \frac{e^{ikz}}{i\lambda z} e^{\frac{ik}{2z}(x^2 + y^2)} \mathcal{F}[U'(\xi, \eta)] \quad (2.27)$$

where the spatial frequencies of the Fourier Transform can be correlated with the spatial coordinates  $x$  and  $y$  by the relation:

$$\begin{cases} \nu_x = \frac{x}{\lambda z} \\ \nu_y = \frac{y}{\lambda z} \end{cases} \quad (2.28)$$

This method is computationally fast since it requires only one Fourier transform, and it is analytically correct. Particular attention should be given to the sampling of the optical field  $U$  and  $U'$ . Because of the presence of the Fourier transform the coordinates of the input and output fields are not sampled in the same way, but are scaled of a factor that is proportional to the distance of propagation, as shown in equation 2.28 [49]. Therefore the input and output planes have different sampling [48]. In addition the multiplicative phase factor:

$$e^{\frac{ik}{2z}(\xi^2 + \eta^2)} \quad (2.29)$$

presents to rapid oscillation of the phase of the optical field for small variations of  $z$ , since  $z$  is at its denominator [48, 50]. In order to avoid aliasing the

input field requires a large sampling and this is achieved by zero padding the sampling window of the input field, with an increase of the digital resolution of the field. It is known that the computational effort of the FFT algorithm increases with the resolution as  $O(n \log n)$ , where  $n$  is the number of samples of the input field and increasing the sampling resolution of the field leads to long a computational time.

### 2.3.1 Multi-Step Fresnel propagation operator

To overcome the scaling of the field and the large computational time required by the Fresnel propagation integral method, a modified method has been developed. We uses a multi step approach as the one explained by Sypek *et al.* [48, 51] and as its shown in figure 2.2 . The reason to adopt the multi-

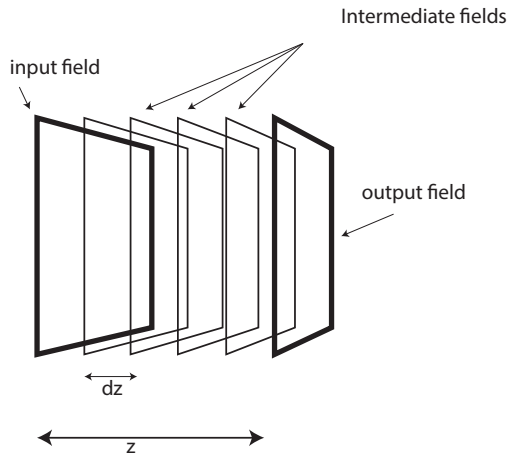


Figure 2.2: To remove the scaling factor between the input and output fields, a multi step Fresnel approach has been developed. The field is propagated by unit of  $dz$ , the minimum distance to keep the sampling the same.

step approach in this project is to remove the scaling factor between the input field and the output field that arise from the Fourier transform as shown in

equation 2.28, while Sypek developed a multi step propagation model to minimize the oscillations of the Fourier spectrum and to avoid large zero paddings.

In the Fourier domain, an optical field sampled by a  $N \times N$  pixels window, and with squared pixels that are  $dx$  wide the spatial frequency resolution is:

$$d\nu = \frac{1}{Ndx} \quad (2.30)$$

Therefore the pixel size in the image plane is according to equations 2.28:

$$d\xi = d\nu\lambda z \quad (2.31)$$

where  $z$  is the propagation distance and  $\lambda$  is the wavelength of the monochromatic wave. The condition to keep the same resolution both in the input field and the output field is:

$$d\xi = d\nu\lambda z = dx \quad (2.32)$$

Substituting the 2.30 into the 2.28:

$$\frac{1}{Ndx} = \frac{dx}{\lambda z} \quad (2.33)$$

Then resolving for  $z$  the minimum propagation distance  $dz$  to keep the same sampling both in the input and output fields is:

$$dz = \frac{W^2}{N\lambda} \quad (2.34)$$

and:

$$z = \sum_{i=1}^N dz_i \quad (2.35)$$

$W = Ndx$  is the dimension in meters of the input field. Equation 2.34 gives the length of the single step in which the propagation distance  $z$  should be

## 2.4. OPERATOR FREE SPACE PROPAGATION: ANGULAR SPECTRUM OF PLANE WAVES APPROACH

divided in order to keep the same resolution.

Although the results obtained with this multi-step approach are correct there are some issues. The propagation distance should be a multiple of  $dz$ , and this is a very significant limitation to the propagation distances that can be set in simulations. In plenoptic imaging systems it is important to know and set the propagation distances with extreme precision and any limitations is not acceptable. Another issue regards the computational time. With the multi step approach the number of FFT performed increases with the steps, leading to a computational time  $N$  times larger than the Fresnel Integral method. For these reasons the angular spectrum method as will be discussed in section 2.4 has been adopted in all the simulations presented in this work.

### 2.4 Operator Free space propagation: Angular spectrum of plane waves approach

The operator free space propagation can be derived considering the is proportional propagation distance [47]. In the Fourier domain the input disturbance can be seen as formed by a set of plane waves travelling in different directions, the *Angular Spectrum of Plane waves* representation of an optical field. In the next section the operator propagation as and its characteristic transfer function will be defined. Three versions of the angular spectrum operator will be presented, and performances of the three versions will be compared.

#### 2.4.1 Angular spectrum of plane waves

The disturbance  $U(x, y; 0)$  describing a monochromatic wave incident a plane  $(x, y)$  at the coordinate  $z=0$  while travelling along the z direction has a Fourier

transform given by:

$$A(f_x, f_y; 0) = \iint_{-\infty}^{\infty} U(x, y; 0) e^{-j2\pi(f_x x + f_y y)} dx dy \quad (2.36)$$

and  $U(x, y; 0)$  is equal to the inverse Fourier transform of its spectrum:

$$U(x, y; 0) = \iint_{-\infty}^{\infty} A(f_x, f_y; 0) e^{j2\pi(f_x x + f_y y)} df_x df_y \quad (2.37)$$

The physical meaning of the equation 2.37 is that the disturbance  $U(x, y; 0)$  can be decomposed in the sum of elemental plane waves propagating in directions given by the wave vector  $\vec{k}$  whose magnitude is  $2\pi/\lambda$  and direction is given by its direction cosines  $(\alpha, \beta, \gamma)$  [47, 50]. Dropping the temporal dependence the plane wave is then:

$$p(x, y, z) = e^{-j\vec{k} \cdot \vec{r}} \quad (2.38)$$

where

$$\vec{r} = x\hat{i} + y\hat{j} + z\hat{k} \quad (2.39)$$

and

$$\vec{k} = \frac{2\pi}{\lambda}(\alpha\hat{i} + \beta\hat{j} + \gamma\hat{k}) \quad (2.40)$$

The exponential becomes:

$$p(x, y, z) = e^{-j\frac{2\pi}{\lambda}(\alpha x + \beta y)} e^{-j\frac{2\pi}{\lambda}(\gamma z)} \quad (2.41)$$

The terms,  $\alpha, \beta$  and  $\gamma$  are the direction cosines of the wave vector  $\vec{k}$  and they are related as:

$$\gamma = \sqrt{1 - \alpha^2 + \beta^2} \quad (2.42)$$

Therefore the complex exponential function in equation 2.36 can be seen as a plane wave with direction cosines

$$\alpha = \lambda f_x, \quad \beta = \lambda f_y, \quad \gamma = \sqrt{1 - (\lambda f_x)^2 + (\lambda f_y)^2} \quad (2.43)$$

## 2.4. OPERATOR FREE SPACE PROPAGATION: ANGULAR SPECTRUM OF PLANE WAVES A

The angular spectrum of plane waves of the disturbance  $U(x, y : 0)$  is the function:

$$A\left(\frac{\alpha}{\lambda}, \frac{\beta}{\lambda}; 0\right) = \iint_{-\infty}^{\infty} U(x, y; 0) e^{-j2\pi(\frac{\alpha}{\lambda}x + \frac{\beta}{\lambda}y)} dx dy \quad (2.44)$$

After a prorogation of  $z$  the disturbance  $U(x, y; z)$  can be written in the form of the angular spectrum in analogy with equation 2.37:

$$U(x, y; z) = \iint_{-\infty}^{\infty} A(f_x, f_y; z) e^{j2\pi(f_x x + f_y y)} df_x df_y \quad (2.45)$$

where  $f_x = \alpha/\lambda$  and  $f_y = \beta/\lambda$ . To be a propagative disturbance, equation 2.45 should satisfy Helmholtz equation 2.20:

$$(\nabla^2 + k^2)U = 0 \quad (2.46)$$

Substituting equation 2.45 into 2.46:

$$\frac{d^2}{dz^2} A(f_x, f_y, z) + \left(\frac{2\pi}{\lambda}\right) [1 - (\lambda f_x)^2 + (\lambda f_y)^2] A(f_x, f_y, z) = 0 \quad (2.47)$$

A solution of the differential equation 2.47 is:

$$A(f_x, f_y, z) = A(f_x, f_y, 0) e^{j\frac{2\pi}{\lambda} \sqrt{1 - (\lambda f_x)^2 + (\lambda f_y)^2}} \quad (2.48)$$

The propagative solution is the one where the spatial frequencies satisfy the condition:

$$(\lambda f_x)^2 + (\lambda f_y)^2 < 1 \quad (2.49)$$

in this case the exponential term in equation 2.48 remains complex and the wave can propagate since it is an oscillating term. For the values of spatial frequencies that satisfy the condition:

$$(\lambda f_x)^2 + (\lambda f_y)^2 > 1 \quad (2.50)$$

the exponent in the equation 2.48 becomes real, and the exponential is a decay term. The solution is no longer propagative and waves are called evanescent waves. It is interesting to see how the angular spectrum theory is more complete than the Fresnel approximation since it includes evanescent components too.

Finally, the disturbance after a propagation in  $z$  can be expressed as a function of the disturbance  $U(x, y; 0)$  at the plane  $z=0$ :

$$U(x, y; z) = \int \int_{-\infty}^{\infty} A(f_x, f_y, 0) e^{j \frac{2\pi}{\lambda} \sqrt{1 - (\lambda f_x)^2 - (\lambda f_y)^2}} e^{j 2\pi (f_x x + f_y y)} df_x df_y \quad (2.51)$$

The last equation enables a calculation of the output field  $U(x, y; z)$  in terms of the input field and the propagation distance, under the approximation of a linear, isotropic, homogeneous and non dispersive medium.

Because of the linearity of the problem, the propagation is considered as a linear system that maps the input disturbance  $U(x, y; 0)$  into the a new field distribution  $U(x, y; z)$ [47]. This linear system is characterized by a transfer function whose bandwidth is limited to the case of the propagative solution of equation 2.47, excluding the evanescent waves. The angular spectrum of the output field can be rewritten as the product of the angular spectrum of the input field multiplied by the transfer function  $H(f_x, f_y)$ :

$$A(f_x, f_y; z) = A(f_x, f_y; 0) \cdot H(f_x, f_y; ) \quad (2.52)$$

The propagation is fully described by the transfer function:

$$H(f_x, f_y) = \begin{cases} e^{j \frac{2\pi z}{\lambda} \sqrt{1 - (\lambda f_x)^2 - (\lambda f_y)^2}} & \text{if } \sqrt{f_x^2 + f_y^2} < \frac{1}{\lambda} \\ 0 & \text{otherwise} \end{cases} \quad (2.53)$$

The bandwidth can be represented as a circle in Fourier space. For frequencies smaller than  $1/\lambda$  the transfer function introduces a shift in the spatial

## 2.4. OPERATOR FREE SPACE PROPAGATION: ANGULAR SPECTRUM OF PLANE WAVES A

domain that is responsible for diffraction [47]. Results obtained with the angular spectrum method are similar to the ones obtained with the Fresnel approximation, but no scaling factor between the input and output field is introduced. From a computational point of view, the angular spectrum operator is composed by 3 steps:

1. Fourier transform of the input field
2. Multiplication of the Fourier transform of the input field with the propagation transfer function in equation 2.53
3. Inverse Fourier transform of the product at step 2. The resultant field is the output disturbance after the propagation in free space.

The process can be seen in figure 2.3

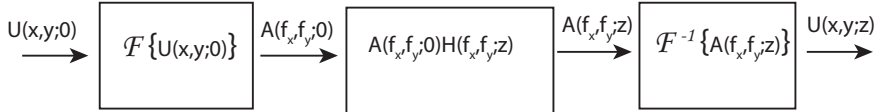


Figure 2.3: Structure of the operator free space propagation with the angular spectrum of plane waves method. The initial disturbance  $U(x, y; 0)$  is transformed into the angular spectrum  $A(f_x, f_y; 0)$  with a Fourier transform implemented by a FFT algorithm. The angular spectrum is multiplied by the propagation transfer function  $H(f_x, f_y)$  and the resultant angular spectrum is inverse transformed into the output disturbance  $U(x, y; z)$

### 2.4.2 Band Limited Angular Spectrum

The transfer function of the propagation in equation 2.53 is a complex exponential oscillating with a frequency depending by the propagation distance  $z$ . Figure 2.4 shows four different profiles of the transfer function for four

propagation distances,  $1\text{ mm}$ ,  $2\text{ mm}$ ,  $10\text{ mm}$  and  $20\text{ mm}$ . Aliasing effects are evident since even for a propagation distance of  $2\text{ mm}$ . When the  $z$  becomes large, the aliasing arises at low spatial frequencies, narrowing the useful bandwidth of the transfer function [50].

## 2.4. OPERATOR FREE SPACE PROPAGATION: ANGULAR SPECTRUM OF PLANE WAVES A

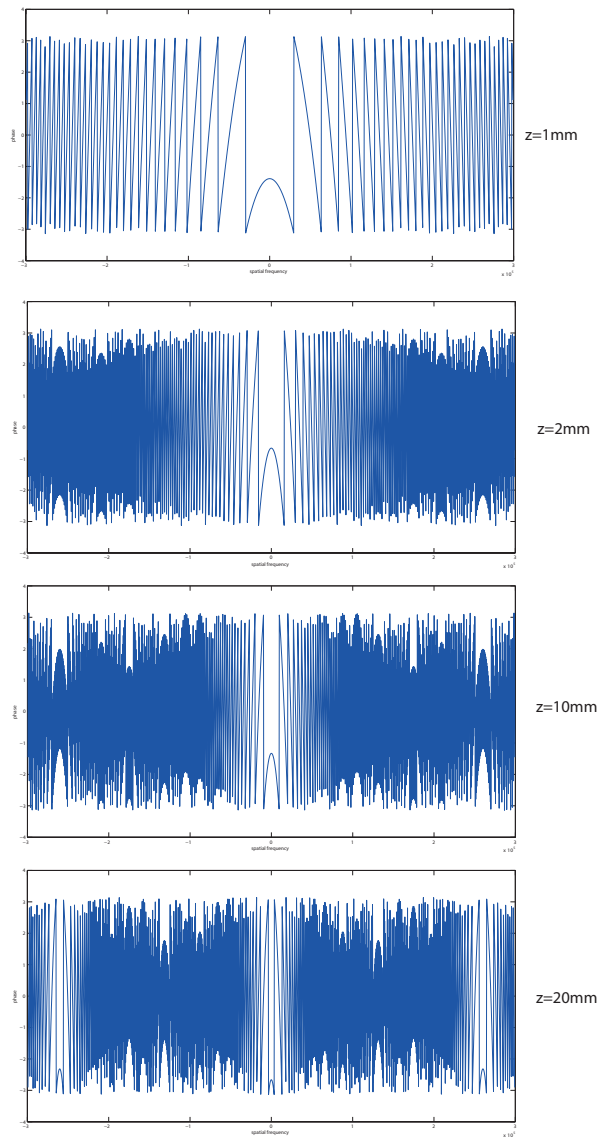


Figure 2.4: Cross section along of the phase of the transfer function of the angular spectrum. It is evident how increasing the propagation distance the oscillation frequency become larger and aliasing arise.

The transfer function can be rewritten as:

$$H(f_x, f_y) = e^{j\phi(f_x, f_y)} \quad (2.54)$$

where  $\phi$  is the oscillating phase term as:

$$\phi(f_x, f_y) = \frac{2\pi}{\lambda} \sqrt{1 - \lambda f_x^2 - \lambda f_y^2} \quad (2.55)$$

Defining the local spatial frequencies of the transfer function [47, 50] as the frequency of the phase oscillation  $\nu_x$  and  $\nu_y$  along  $f_x$  and  $f_y$ :

$$\begin{cases} \nu_x = \frac{1}{2\pi} \frac{\partial}{\partial f_x} \phi(f_x, f_y) \\ \nu_y = \frac{1}{2\pi} \frac{\partial}{\partial f_y} \phi(f_x, f_y) \end{cases} \quad (2.56)$$

the local spatial frequencies become:

$$\begin{cases} \nu_x = -\frac{z}{\lambda} \frac{\lambda^2 f_x}{\sqrt{1 - (\lambda f_x)^2}} \\ \nu_y = -\frac{z}{\lambda} \frac{\lambda^2 f_y}{\sqrt{1 - (\lambda f_y)^2}} \end{cases} \quad (2.57)$$

As stated by Matsushima *et al.* [50], if the input optical disturbance is sampled by an  $N \times N$  sampling window with pixel size  $dx$ , the transfer function is sampled by unit of spatial frequency equals to  $df = 1/(Ndx)$ . To satisfy the Nyquist condition the sample frequency should be at least the double of the bandwidth of the transfer function. For one direction in the local frequency space:

$$\frac{1}{df} \geq 2|\nu_x| \quad (2.58)$$

Modifying the sampling of the transfer function, and of the input field, can lead to huge sampling windows and long computational times. In addition to that in practical applications the sampling interval is usually fixed. Therefore the condition on the maximum frequency range for which the transfer

## 2.4. OPERATOR FREE SPACE PROPAGATION: ANGULAR SPECTRUM OF PLANE WAVES A

function is not aliased:

$$\frac{1}{df_x} \geq 2z \frac{|f_x|}{|\sqrt{(\frac{1}{\lambda^2} + f_x)^2}|} \quad (2.59)$$

Resolving the equation for  $|f_x|$  :

$$|f_x| \leq \frac{1}{\sqrt{(2df_x z)^2 + 1\lambda}} = f_{max} \quad (2.60)$$

Where  $f_{max}$  is the maximum frequency of the transfer function without generating errors due to aliasing. Assuming the sampling of the optical field to be the same in both x and y direction the maximum bandwidth for the sampling in  $f_y$  is equal to the bandwidth in  $f_x$ . Therefore:

$$\frac{1}{df_y} \geq 2|\nu_y| \quad (2.61)$$

$$\frac{1}{df_y} \geq 2z \frac{|f_y|}{|\sqrt{\frac{1}{\lambda^2} + f_y)^2}|} \quad (2.62)$$

$$|f_y| \leq \frac{1}{\sqrt{(2df_y z)^2 + 1\lambda}} = f_{max} \quad (2.63)$$

To avoid aliasing then, the two dimensional transfer function should be limited to a range of frequencies defined by equation 2.62. The expression of the output field will then be:

$$U(x, y; z) = \mathcal{F}^{-1} [A(f_x, f_y; 0)H'(f_x, f_y; z)] \quad (2.64)$$

where

$$H_{BL}(f_x, f_y; z) = H(f_x, f_y; z) \text{rect} \left( \frac{f_x}{f_{max}} \right) \text{rect} \left( \frac{f_y}{f_{max}} \right) \quad (2.65)$$

The MATLAB algorithm to implement the band limitation consists in multiplying the phase term of the propagation transfer function by a phase mask

with the shape of a circle function of radius  $f_{max}$  in the plane of the spatial frequencies. A circular phase mask has been chosen instead of the rectangular phase mask of equation 2.65 because it follows the geometry of the lens aperture, without introducing new spatial features that could effect the diffraction.

The resultant phase of the transfer function is shown in figure 2.5, with the bandwidth for three different propagation distances.

## 2.4. OPERATOR FREE SPACE PROPAGATION: ANGULAR SPECTRUM OF PLANE WAVES A

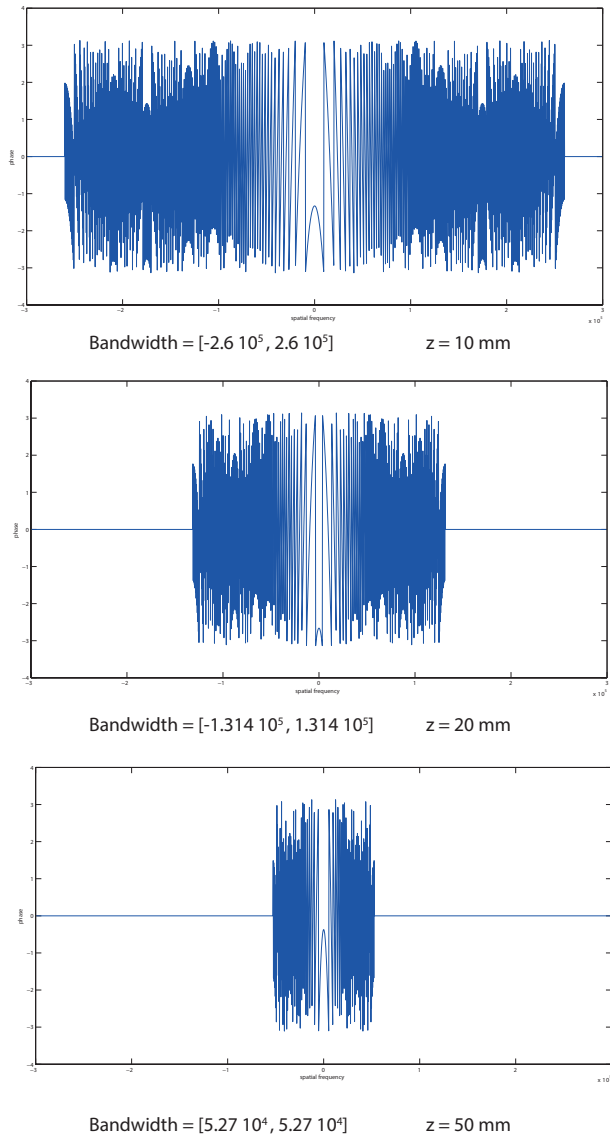


Figure 2.5: Bandwidth of the transfer function for three different propagation distances.

From a computational point of view the algorithm to implement the band limited angular spectrum method can be summarized in the following steps:

1. Computation of the angular spectrum of the input disturbance via a Fourier transform as shown in equation 2.37.

2. Estimation of the maximum bandwidth of the transfer function in order to avoid aliasing error using equations 2.60.
3. Multiplication of the phase of the transfer function for a circular phase mask with radius equal to the frequency obtained in the previous step.
4. Multiplication of the angular spectrum for the band limited transfer function.
5. Inverse Fourier transform of the product at step 4

The structure of the operator free space propagation implemented by the band limited angular spectrum can be seen in figure 2.6

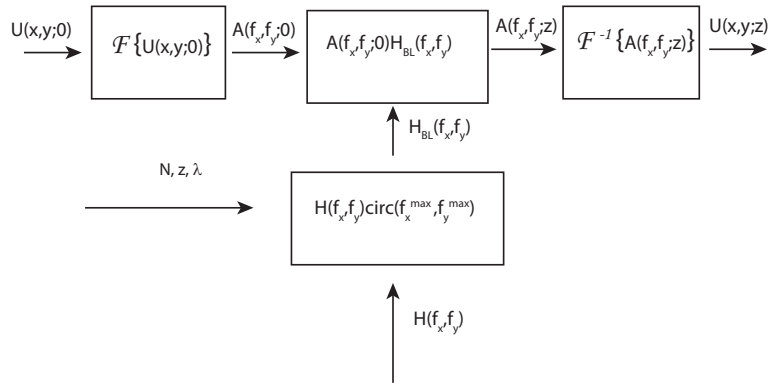


Figure 2.6: Structure of the operator free space propagation with the angular spectrum of plane waves method in its band limited version. The initial disturbance  $U(x, y; 0)$  is transformed into the angular spectrum  $A(f_x, f_y; 0)$  with a Fourier transform implemented by a FFT algorithm. The angular spectrum is multiplied by the propagation transfer function  $H(f_x, f_y)$  whose bandwidth has been limited according to equation 2.63. The bandwidth of the transfer function depends on the sampling of the input field, the wavelength of the light  $\lambda$  and the propagation distance. The resultant angular spectrum is inverse transformed into the output disturbance  $U(x, y; z)$ .  $N$  is the sampling of the input field,  $z$  the propagation distance and  $\lambda$  the wavelength.

### 2.4.3 Corrected Band Limited Angular Spectrum Method

The third method to implement the propagation operator with the angular spectrum is the corrected band limited angular spectrum method. It differs from the band limited angular spectrum presented in section 2.4.1 the bandwidth of the transfer function is truncated to the value of cut-off frequency of the free space propagation in case the Nyquist criterion requires a bandwidth too narrow. For long propagation distances the propagation transfer function acts as a low pass filter on the spatial frequency components of the input signal. When its bandwidth is bigger than the cutoff frequency calculated with the band limited method to avoid digital aliasing there is a loss of resolution in the final image. A trade-off should therefore be found between the error due to the aliasing and the error due to the excessive band limitation. For imaging applications this is not an issue since usually the numerical aperture of the optical elements in the imaging system give already a limitation in the band passing from the input field to the output field. However it is useful to estimate the bandwidth of the free space propagation defining the maximum spatial frequency that is transferred from the object plane to the image plane. This value defines the amount of information transferred from the input field to the image plane. With reference to figure 2.7 for a point in the input field, the range of spatial frequencies that are transferred to the output field are the ones whose direction cosines are contained into the angle that includes the sampling window of the output field. In the hypothesis of the propagation distance much bigger than the sampling window,  $z \gg W$  like in most of the applications of this simulation toolbox the angle  $\theta$  is equal

to:

$$\theta \simeq \frac{W}{z} \quad (2.66)$$

The link between the direction cosine and the spatial frequency is, according

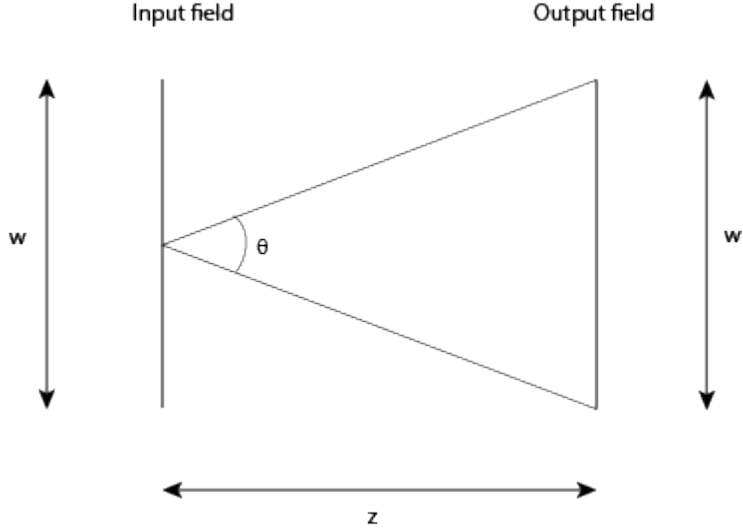


Figure 2.7: The maximum spatial frequency is linked to the dimension of the sampling window of the output field  $w$  and the propagation distance  $z$

to equation 2.43

$$\theta = \lambda f_{cutoff}, \quad (2.67)$$

The cutoff frequency of a field sampled by a sampling window  $W$  and after a propagation distance of  $z$  is defined as:

$$\nu_{cutoff} = \frac{W}{\lambda z} \quad (2.68)$$

Therefore the bandwidth of the transfer function should be bigger than  $\nu_{cutoff}$  in order not to introduce error in the reconstruction of the diffraction pattern due to loss in resolution.

$$f_{max} \geq \nu_{cutoff} \quad (2.69)$$

## 2.4. OPERATOR FREE SPACE PROPAGATION: ANGULAR SPECTRUM OF PLANE WAVES A

If the propagation distance limits the bandwidth of the output field too much, the transfer function can be improved by increasing the sampling of the input field. This condition is equal to having a smaller pixel size. Dealing with bigger sampling windows however increases the computational effort.

### 2.4.4 Performances of the Angular spectrum methods

To evaluate the differences in resolution of the three variants of the angular spectrum methods, Normal Angular spectrum (AS), Band Limited angular spectrum (BL), and Corrected Band Limited Angular Spectrum (corrected BL), it has been implemented a simulation of a free space propagation of an input field that consisted in a circular pupil of diameter 5 mm, sampled with a resolution of  $3000 \times 3000$  pixels with a sampling window of 1 cm. The propagation distances  $z$  varied from 1 m to 10 m. Results are shown in figure 2.8 where the cross section of the diffraction patterns are shown. The BL method shown in the central column gives smooth diffraction patterns. Increasing the propagation distance though the intensity profile lose part of the information because of the excessive low pass filtering action on the propagation transfer function, leading the the complete loss of the diffraction fringes. A comparison with the normal method (AS) can be seen in figure 2.8, where the diffraction fringes are presents with the superimposition of the noise due to aliasing in transfer function sampling. This affects the resolution of the diffraction pattern and the signal to noise ration drops with  $z$  as shown in figure 2.9. A good compromise is found using as bandwidth of the transfer function the one of the propagation obtained with the corrected BL method as explained in section 2.4.3 and as it is shown in figure 2.8 on the

far right column. fringes are clearly present in the diffraction pattern even for large propagation distances and the noise is removed. In figure figure 2.9 the signal to noise ratio (SNR) of the diffraction patterns in figure 2.8 is plotted as a function of the propagation distance for the three examined cases. The band limited angular spectrum method gives a better especially for short propagation distances, where the bandwidth of the transfer function is not low passing the signal but only avoiding the aliasing. It stays in general above the SNR of the corrected BL method, indicated in red of almost 15dB even in the case of large propagation distances. This is due to the excessive smoothing action that brings to the loss of resolution. On the other hand without any limitation of the band (AS), green line, the aliasing generated noise becomes dominant for long propagation distances and the SNR approach the 0 dB value. The best results in terms of resolution and noise reduction are given by the corrected BL method where the information on the diffraction is entirely kept.

## 2.4. OPERATOR FREE SPACE PROPAGATION: ANGULAR SPECTRUM OF PLANE WAVES A

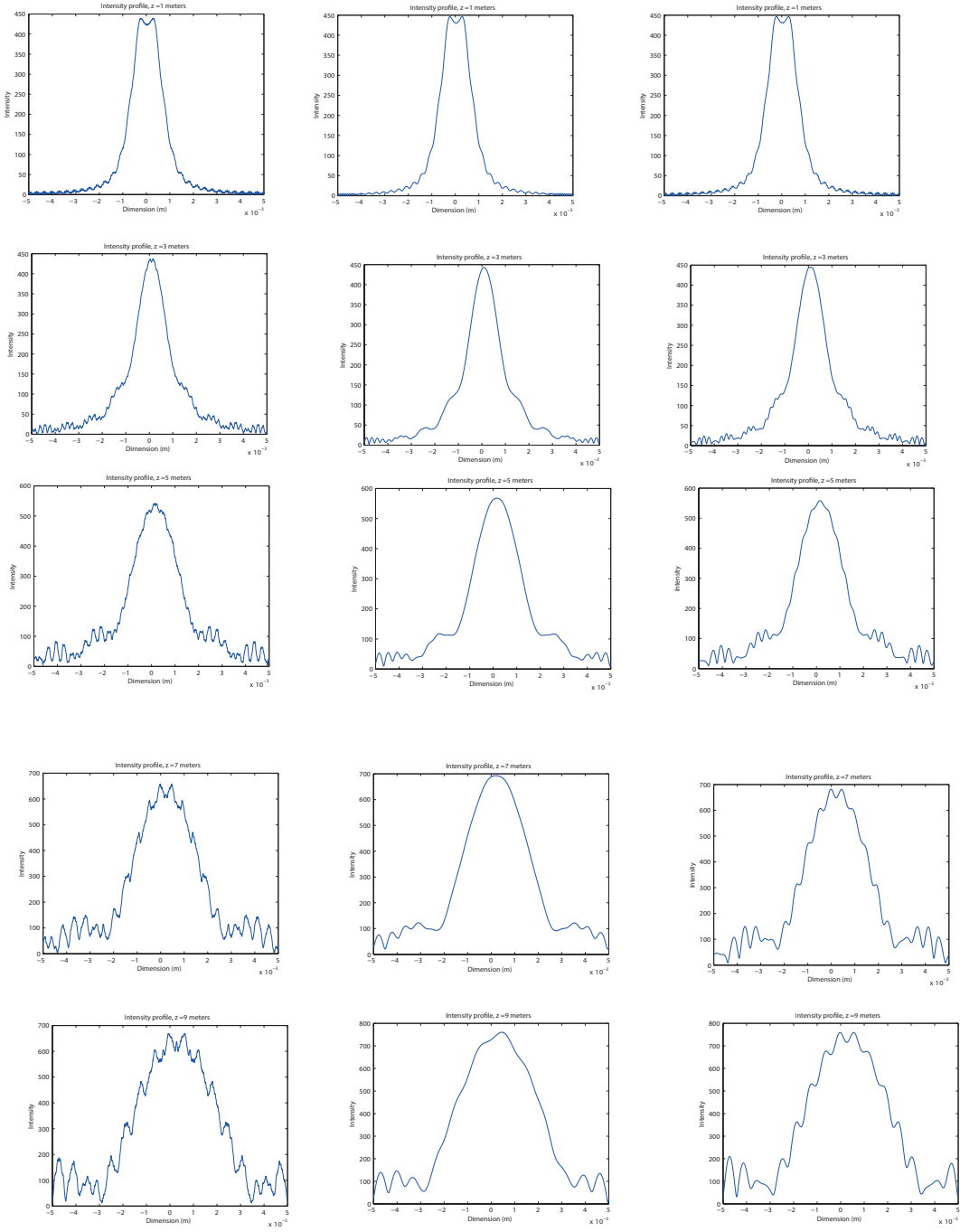


Figure 2.8: Comparison of the performances of the three angular spectrum propagation operator. On the left column are shown diffraction pattern cross section obtained using the angular spectrum method (AS). In the central column the pattern for the same propagation distances have been obtained using the band limited method (BL) and in the right column the same patterns have been obtained using the correct band limited method (corrected BL).

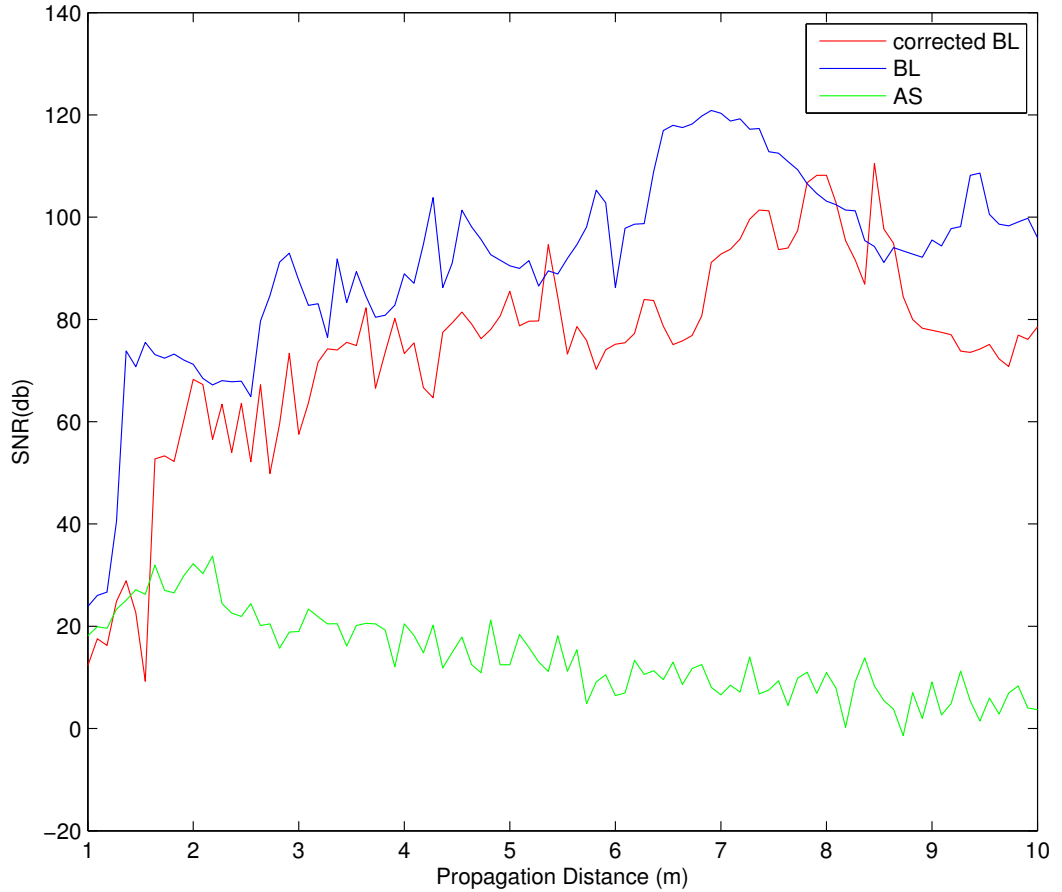


Figure 2.9: Comparison between the Signal to Noise ratio (SNR) as a function of the propagation distance for the three propagation method seen in section 2.4.1. The BL and the corrected BL methods improve the SNR, that instead drops with the increasing of the propagation distance when the normal AS method is used.

## 2.5 Operator Thin Lens

In this section will be described how the operator thin lens has been designed and implemented in the simulation toolbox. For the theory behind the main reference is Goodman [47]. A lens is composed of a material with a refractive

index different from the one of air, normally 1.5, that causes the propagation velocity of the optical field to drop. In the approximation of a thin lens, the translation of the ray of light inside the lens is negligible and if a ray enters the lens at the coordinate  $(x, y)$  on one face, it exits at the same coordinates at the other side. A thin lens delays an incident wave-front by an amount proportional to its thickness. These delays can be modelled introducing a phase factor to the incident field. The thickness function is:

$$\Delta(x, y) \quad (2.70)$$

as the thickness of the lens at the coordinates  $(x, y)$  as shown in figure 2.10, where  $\Delta_0$  is the lens maximum thickness at the coordinates  $(0, 0)$ . The phase

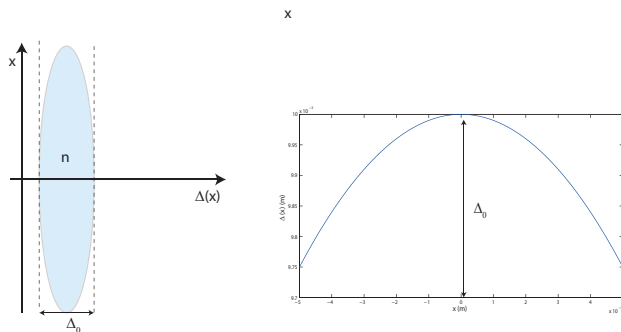


Figure 2.10: Thickness of a lens as a function of position along x coordinate. It can be defined in the same way along the y coordinate

delay introduced by the lens is proportional to its thickness:

$$\phi(x, y) = kn\Delta(x, y) + k[\Delta_0 - \Delta(x, y)] \quad (2.71)$$

where  $n$  is the refractive index of the lens material and  $k = 2\pi/\lambda$  is the wave number. With reference to figure 2.10 the quantity  $kn\Delta(x, y)$  is the phase

delay introduced by the different material of the lens, and  $k[\Delta_0 - \Delta(x, y)]$  is the phase delay introduced by the free space propagation between the two planes represented with dashed line. This phase delay can be seen as a multiplicative phase term defined as:

$$t_{lens} = \exp[jk\Delta_0] \exp[jk(n - 1)\Delta(x, y)] \quad (2.72)$$

The complex field  $U'(x, y)$  immediately after the lens is therefore given by the product of the field entering the lens  $U_0(x, y)$  with the phase delay in equation 2.72.

$$U'(x, y) = t_{lens}(x, y)U_0(x, y) \quad (2.73)$$

The sign convention used in the following derivation is: for a ray of light travelling from left to right:

- any convex surface encountered has positive radius of curvature
- any concave surface encountered had negative radius of curvature

The lens can be split into three elements such that the total thickness function is the sum of three functions: From figure 2.11:

$$\Delta(x, y) = \Delta_1(x, y) + \Delta_2(x, y) + \Delta_3(x, y) \quad (2.74)$$

Where the three components of the thickness are:

$$\Delta_1(x, y) = \Delta_{01}(x, y) - R_1 \left(1 - \sqrt{1 - \frac{x^2 + y^2}{R_1^2}}\right) \quad (2.75)$$

$$\Delta_2(x, y) = \Delta_{02} \quad (2.76)$$

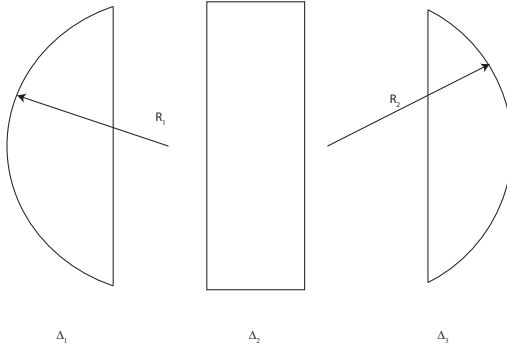


Figure 2.11: The thickness function can be decomposed into the sum of three contributions.

$$\Delta_3(x, y) = \Delta_0(x, y) - R_2 \left( 1 - \sqrt{1 - \frac{x^2 + y^2}{R_2^2}} \right) \quad (2.77)$$

$R_1 > 0$  and  $R_2 < 0$  are respectively the radius of curvature of the right-hand surface and the radius of curvature of the left-hand side of the lens surface. Then total thickness function is given by:

$$\Delta(x, y) = \Delta_0(x, y) - R_1 \left( 1 - \sqrt{1 - \frac{x^2 + y^2}{R_1^2}} \right) + R_2 \left( 1 - \sqrt{1 - \frac{x^2 + y^2}{R_2^2}} \right) \quad (2.78)$$

where  $\Delta_0$  is:  $\Delta_0 = \Delta_{01} + \Delta_{02} + \Delta_{03}$ . In the paraxial approximation it is possible to approximate  $\Delta(x, y)$  with its first element of the Taylor series:

$$\sqrt{1 - \frac{x^2 + y^2}{R_1^2}} \approx 1 - \frac{x^2 + y^2}{R_1^2} \quad (2.79)$$

$$\sqrt{1 - \frac{x^2 + y^2}{R_2^2}} \approx 1 - \frac{x^2 + y^2}{R_2^2} \quad (2.80)$$

Substituting 2.79 and 2.80 into equation 2.78:

$$\Delta(x, y) = \Delta_0(x, y) - \frac{x^2 + y^2}{2} \left( \frac{1}{R_1} + \frac{1}{R_2} \right) \quad (2.81)$$

and substituting 2.81 into equation 2.71 the result is the expression of the phase shift in the exponential form:

$$t_l(x, y) = \exp[jkn\Delta_0] \exp[-jk(n-1) \frac{x^2 + y^2}{2} \left( \frac{1}{R_1} + \frac{1}{R_2} \right)] \quad (2.82)$$

The focal length of the lens  $f$  is the quantity containing the information on the physical properties of the lens and it is defined as:

$$\frac{1}{f} \equiv (n-1) \left( \frac{1}{R_1} + \frac{1}{R_2} \right) \quad (2.83)$$

Finally after dropping the constant phase factor the effects of a thin lens under par-axial approximation as a quadratic phase transformation are described by equation 2.84:

$$t_l(x, y) = \exp[-j \frac{k}{2f} (x^2 + y^2)] \quad (2.84)$$

This equation can represent the effects of any lens, since the sign of  $f$  will define whether the lens is positive or negative. The physical meaning of this expression can be understood examining figure 2.12 When a plane wave, represented by the complex field  $U(x, y)$ , is normally incident on the lens, according to equation 2.73, the field coming out of the lens will be:

$$U'(x, y) = \exp[-j \frac{k}{2f} (x^2 + y^2)] \quad (2.85)$$

The thin lens is introducing a phase term on the incident field, and the resulting field is a quadratic approximation of a spherical wave. As shown

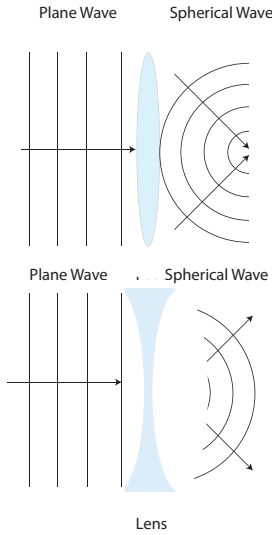


Figure 2.12: A thin lens converts a plane wave into a spherical wave.

in figure 2.12 when  $f$  is positive, the wave is converging towards a point on the optical axis at distance  $f$  from the lens. If  $f$  is negative the wave is diverging from a point on the optical axis placed at a distance  $|f|$  in front of the lens. The lens therefore transforms a plane wave into a spherical wave. The operator thin lens is defined as the product of the quadratic transformation in equation 2.84 with a function describing the aperture of the lens, called pupil  $P(x, y)$ :

$$L(x, y) = P(x, y) \exp[-j \frac{k}{2f} (x^2 + y^2)] \quad (2.86)$$

where the pupil function is defined as:

$$P(x, y) = \begin{cases} 1 & \sqrt{x^2 + y^2} < r \\ 0 & \text{elsewhere} \end{cases} \quad (2.87)$$

where  $r$  is the the radius of the lens aperture.

### 2.5.1 Aliasing in phase sampling

The quadratic phase factor of the thin lens operator is a complex function whose modulus is constant and equal to the unity, and its argument is an oscillating function in the interval  $(0, 2\pi]$ . The argument of the phase factor is shown in figure 2.13

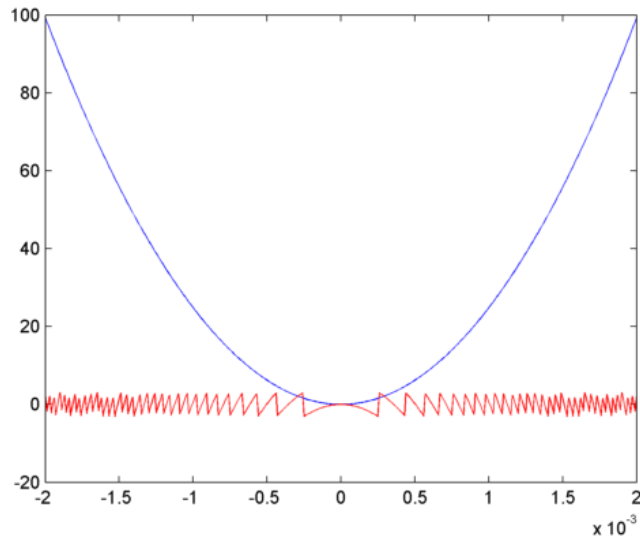


Figure 2.13: Phase profile of a computer generated lens. The blue line shows the quadratic phase term and the red line shows the same phase term wrapped every  $2\pi$ . This wrapping is the source of the aliasing.

The parabolic phase profile gets wrapped since the argument of a complex function varies between 0 and  $2\pi$ . This wrapping of the phase can cause aliasing as the distance from the centre of the lens increases. For high values of  $x$  and  $y$ , the quadratic term becomes too steep and the frequency of oscillation between 0 and  $2\pi$  of the phase factor might become too high to be correctly sampled. With analogy of what has been said in section 2.4, for

a parabolic phase profile:

$$\Phi(x, y) = \frac{k}{2f}(x^2 + y^2) \quad (2.88)$$

The instantaneous frequencies of the phase  $\nu_x$ ,  $\nu_y$  in  $x$  and  $y$  respectively are defined as:

$$\begin{cases} \nu_x = \frac{1}{2\pi} \frac{\partial \Phi}{\partial x} = \frac{1}{2\pi} \frac{k}{f} x \\ \nu_y = \frac{1}{2\pi} \frac{\partial \Phi}{\partial y} = \frac{1}{2\pi} \frac{k}{f} y \end{cases} \quad (2.89)$$

In order to recover all the components of a periodic signal, the sampling frequency should be at least twice the bandwidth of the signal. According to the Nyquist criterion:

$$f_{Nyquist} = 2\nu_{max} \quad (2.90)$$

The maximum instantaneous frequency  $\nu_{max}$  of the phase factor is the one that correspond to the edge of the lens. We consider for brevity the one dimensional case along the  $x$  direction, but the conclusions are valid for the  $y$  direction because of the rotational symmetry of the pupil function in equation 2.87. In this case  $x_{max} = y_{max} = r$  where  $r$  is the radius of the pupil function. Defining the pixel size  $\Delta x$  along  $x$ , and assuming the pixels as squared, so that the sampling frequency  $1/\Delta x$  is the same along both axis, the Nyquist condition to avoid aliasing is:

$$\frac{1}{\Delta x} \geq \frac{1}{2\pi} \frac{k}{f} x_{max} \quad (2.91)$$

Since in general the sampling rate cannot be modified because of the fixed pixel size of the sensor this expression leads to a condition for the radius of the pupil function:

$$r = x_{max} \leq \frac{2\pi f}{k \Delta x} \quad (2.92)$$

Substituting  $k = \frac{2\pi}{\lambda}$  into 2.92:

$$r \leq \frac{\lambda f}{\Delta x} \quad (2.93)$$

The more powerful is the lens,  $f$  will have a smaller value and hence the aperture should be smaller. Since the simulation platform is flexible, in case a particular value of the aperture is needed the equation 2.93, in order to get a condition on the focal length:

$$f \geq \frac{r \Delta x}{\lambda} \quad (2.94)$$

And considering that the digital resolution of a lens with aperture equal to  $2r$  is given by:

$$N = \frac{2r}{\Delta x} \quad (2.95)$$

The minimum resolution of a lens of radius  $r$  and focal length  $f$  is therefore:

$$N \geq \frac{2r^2}{f\lambda} \quad (2.96)$$

Applying these conditions will assure that no aliasing will be introduced by the lens operator.

## 2.6 Comparison between the free space propagation operators

In this section the differences in performance between the Fresnel approximation and the angular spectrum of plane waves approach will be shown, with particular attention to the computational time required by the different methods, the optical resolution and the error. Results will be used to evaluate the characteristic of the different propagation operators.

### 2.6.1 Description of the system

The system simulated is a simple imaging system composed of a single lens with focal length  $f = 158\text{mm}$ , in a  $2f$  configuration, as shown in figure 2.14. The field of view is a square of  $1\text{cm} \times 1\text{cm}$ , and the resolution of the input field is  $2000 \times 2000$  pixels. The aperture of the lens is  $D = 5\text{mm}$  and its f number, defined as:

$$F_{\#} = \frac{z}{D} \quad (2.97)$$

is equal to  $F_{\#} = 63$ , where  $z$  is the distance from the lens to the image plane, that in a  $2f$  configuration is equal to  $z = 2f = 316\text{mm}$ . The optical cut-off

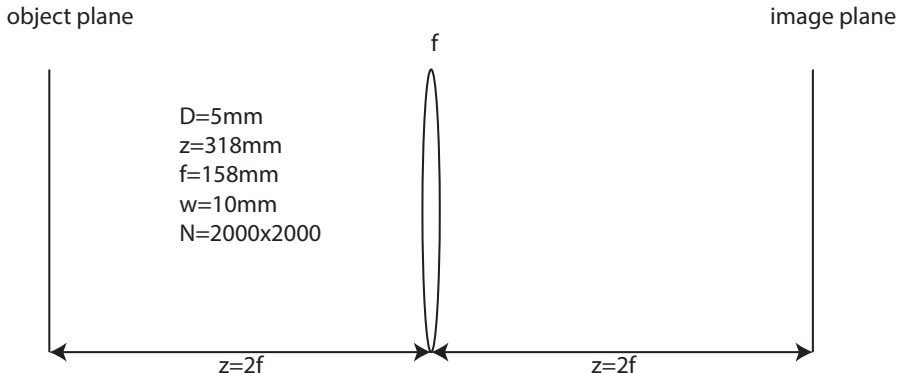


Figure 2.14: Schematic of the  $2f$  system simulated.  $f$  is the focal length,  $z$  the propagation distances,  $D$  is the aperture of the lens,  $w$  the field of view and  $N$  the sampling resolution.

frequency of this system is given by the relation [47]:

$$\nu_c = \frac{1}{\lambda F_{num}} \quad (2.98)$$

and for the system simulated, illuminated with monochromatic light with wavelength  $\lambda = 633\text{nm}$ , it is  $\nu_c = 2.5 \cdot 10^4 \text{cycles/m}$ .

### 2.6.2 Image of a point source

The first experiment simulated is the image of a point source, realized with a pinhole of  $10\mu m$  of diameter placed at the object plane indicated in figure 2.14. The image has been taken using four different methods to propagate the light into the system. Those are:

- Multi step Fresnel method (MSF), section 2.3.1
- Angular spectrum method (AS), section 2.4
- Band Limited Angular Spectrum method (BL), section 2.4.1
- corrected Band Limited Angular Spectrum method (cBL), section 2.4.3

Using as an input field a point source it will be computed the impulse response of each of these different methods. The sequence of operators used to simulate the system is shown in figure 2.15

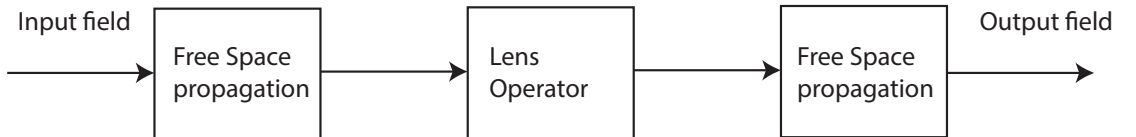


Figure 2.15: Operator sequence for the 2f system.

In the assumption of having a lens with a circular aperture and no aberrations, the impulse response of an optical system is an Airy Disk, that is the Fourier transform of the pupil of the system at the image plane. The fact that the theoretical output of the experiment is well known allows to determine the quality of the simulations tools. In addition to that, the Fourier

## 2.6. COMPARISON BETWEEN THE FREE SPACE PROPAGATION OPERATORS87

transform of the impulse response of an optical system gives information on the frequencies content of the image, hence the band pass of the imaging system and its quality. Figure 2.16 shows the sensor image at the image plane together with intensity profiles of the image.

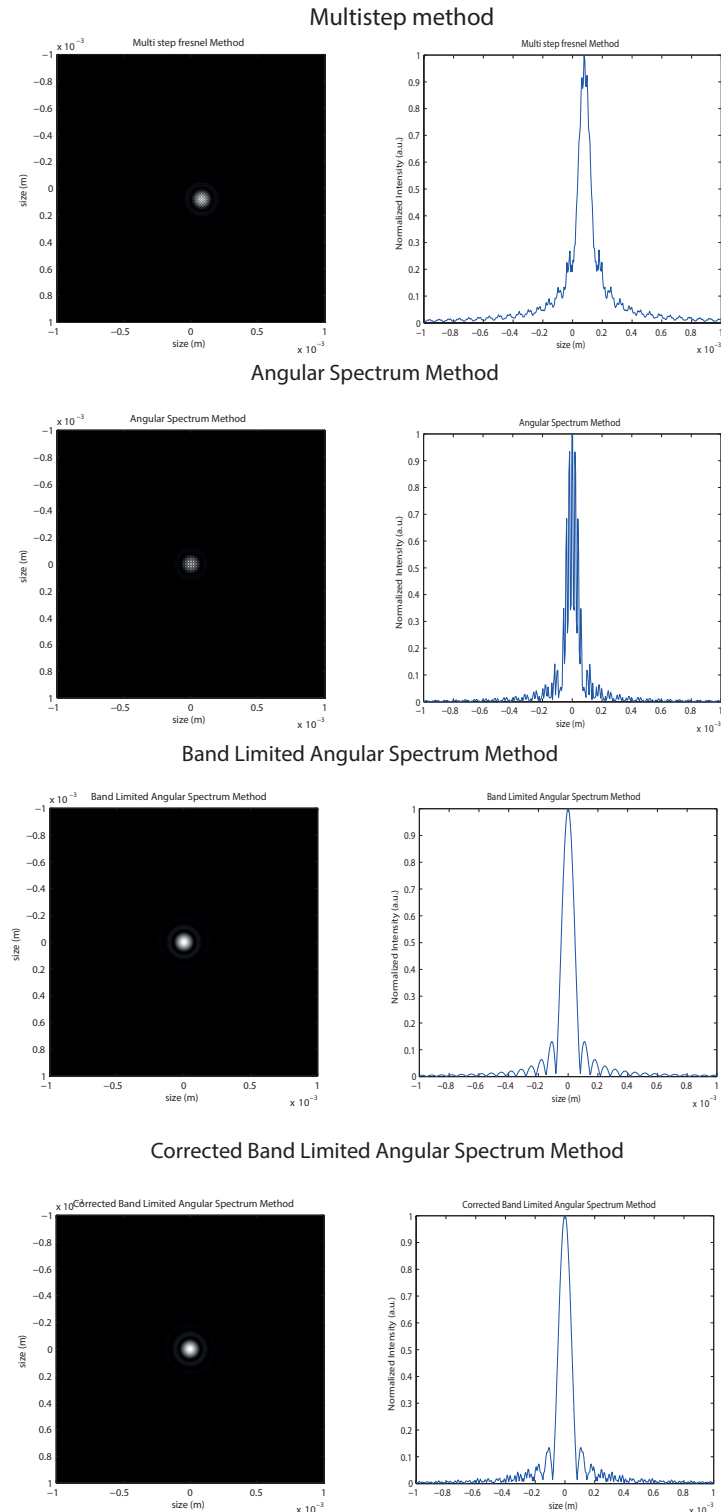


Figure 2.16: From top to Bottom: Image and intensity cross section of a point source according to multi step method, angular spectrum method, band limited angular spectrum method and corrected band limited angular spectrum method.

From figure 2.16 it can be seen that in the case of the Multi-step method the cross section of the impulse response does not go to zero because of additive background noise. The response of the angular spectrum method has a high frequency noise components superimposed to the diffraction pattern, while the band limited angular spectrum method reduces the noise due to aliasing of the transfer function in the angular spectrum case as can be seen comparing the two cross sections. Both the band limited and the corrected band limited methods present no background noise present in the multi step case and in the high frequency noise in the direct angular spectrum case. Another parameter to evaluate the accuracy of these methods is the position of the Airy disk first minimum. It is given by [47, 52]:

$$x_{min} = 1.22 \frac{\lambda z}{D} \quad (2.99)$$

where  $\lambda$  is the wavelength of the light propagating,  $D$  is the aperture of the lens and  $z$  the propagation distance. According to the values in section 2.6.1 the Airy disk should have its first minimum at  $x_{min} = 67\mu m$ . Without considering the multi step case that is too noisy and does not present zeros, the position of the first minimum in the other cases are:

AS	$67.5 \mu m$
BL	$77.5 \mu m$
cBL	$77.5 \mu m$

As expected for both the band limited angular spectrum the Airy Disk is slightly wider due to the low pass filtering action that transfer function has undergone. However noise is reduced sensibly with the band limitation. To better understand how the resolution changes with the different methods,

it is worth to have a look at the Fourier transform of the images shown in figure 2.16. The Fourier transform of the impulse response of a system give its frequency response. The shape of the frequency response gives information about how the frequencies components of the input signal are modulated and transferred to the output signal. When this function goes to zero the correspondent frequency value is called cutoff frequency. For frequencies higher than the cutoff frequency, all the information included in the input signal is lost. For the Results are shown in figure 2.17. The graphs are symmetric with respect to the zero frequency, therefore only the positive frequencies are shown.

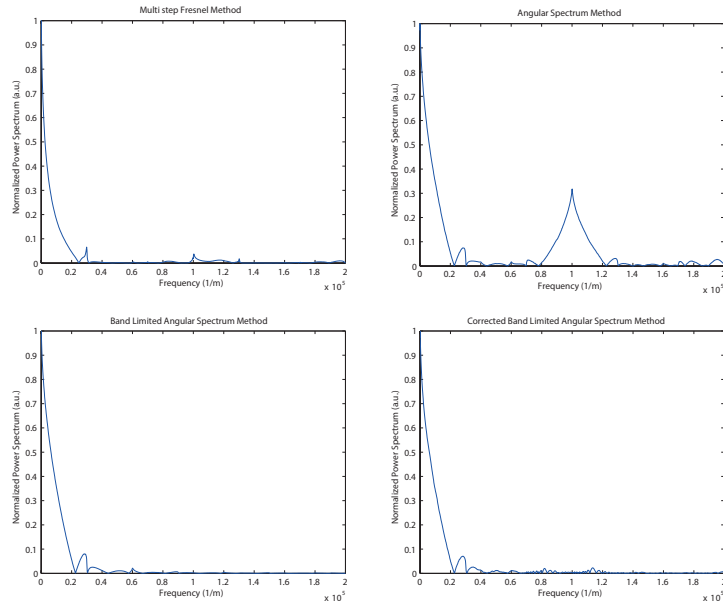


Figure 2.17: From top left to bottom right: Power spectrum of the image of a point source obtained with the multi step Fresnel method, the Angular spectrum method, the band limited angular spectrum method and the corrected band limited angular spectrum method .

From a comparison of the power spectra in figure 2.17 it is possible to note the difference in shape of the power spectrum of the multi step method, that goes to zero slower than the angular spectrum methods spectra. These three figures present as expected the same shape since for low frequency the three angular spectrum methods are identical, with the difference of the frequency components after the cutoff frequency due to the fact that the band limited and the corrected band limited have narrower bandwidths. In the Angular spectrum method graph it is present a strong peak at a frequency of  $10^5 \text{ } 1/m$  due to digital artefacts arisen from aliasing effects. this peak disappears in the other two band limited implementations of the angular spectrum.

## 2.7 Coherence

The Fresnel simulation toolbox has been designed to analyse a light field imaging system. The decision to develop an algorithm to simulate light propagating in a low state of coherence has been made in order too avoid interference pattern cross talk between neighbours lens lets that might decrease the quality of the final image. Diffraction, that is a deterministic property of light [53]. Once the characteristics of the input optical field are known, it is possible to use methods that allows to determine the characteristics of the output optical field completely such as the ones described in sections ??

Coherence is a statistical property of light and is described in terms of second order averages known as coherence function [53, 54]. A full analysis of coherence of optical fields can be found in text books such as Born and Wolf [55] and Goodman [53] and will not be discussed in this work. For the application described in this work coherence will be treated under a less rigorous point

of view, focusing on its practical effects on the optical experiments, and it will be used the physical causes of low coherent light in order to create a model to simulate different degrees of coherence. Before analysing the computational model of coherence it is worth to examine the two different types of coherence. As defined by Goodman [53] :

- **Temporal Coherence** can be defined as the ability of light to interfere with a delayed version of itself
- **Spatial Coherence** can be defined as the ability of light to interfere with a spatially shifted version of itself

The empirical method developed to simulate light propagating at low coherence includes both spatial and temporal coherence.

### 2.7.1 Temporal coherence

Following the explanation of Goodman [53], given a complex disturbance  $U(\vec{X}, t)$  with a finite bandwidth  $\Delta\nu$ , it is expected to remain constant during a time interval  $\tau < 1/\Delta\nu$ . This means that the disturbance taken at two different times in the same spatial position  $U(\vec{X}, t)$  and  $U(\vec{X}, t+\tau)$  are highly correlated if  $\tau < \tau_c$  where  $\tau_c$  is the coherence time. Since the correlation takes place without any spatial shift it is possible to drop the spatial coordinates  $\vec{X}$ . The degree of temporal coherence is therefore given by the autocorrelation function:

$$\Gamma(\tau) = \langle U(t + \tau)U^*(t) \rangle \quad (2.100)$$

The coherence time  $\tau$  is therefore a function of the bandwidth of the light. A perfectly monochromatic plane wave has a very narrow bandwidth and a

long time of coherence, while on the other hand ultra fast laser pulses will have a coherence time that is dependent by the bandwidth of the pulse. The shorter is the pulse, the broader the bandwidth. From the time of coherence it is possible to define the coherence length as  $l_c = v\tau_c$  where  $v = c/n$  is the speed of light in the medium of propagation given by the speed of light in the vacuum  $c$  divided by the refractive index  $n$ .

### 2.7.2 Spatial Coherence

To analyse spatial coherence two complex disturbances  $U(\vec{X}_1, t)$  and  $U(\vec{X}_2, t)$  are observed at the same time in two different position  $\vec{X}_1$  and  $\vec{X}_2$ . When the two points coincide,  $\vec{X}_1 = \vec{X}_2$  the two disturbances are perfectly correlated. When the distance between the two points begin to increase, the correlation degree decreases until they become totally uncorrelated. In order to better understand this concept it is useful to illustrate the Young experiment [56] [56]. With reference to figure 2.18 a squared light source of size  $\Delta x$  emits light towards a screen at a distance  $R$ . On the screen A there are two pinholes  $Q_1$  and  $Q_2$ . In order to have interference fringes on a second screen B the following condition should be satisfied:

$$\Delta x \Delta \theta < \lambda \quad (2.101)$$

Where  $2\theta$  is the angle formed at the source with the two pinholes  $Q_1$  and  $Q_2$  and  $\lambda$  is the wavelength of the light emitted by the source. In order to see the fringes, the two pinholes should be situated in an area  $\Delta A$  of size:

$$\Delta A \sim (R\Delta\theta)^2 = \frac{R^2}{S}\lambda \quad (2.102)$$

$R$  is the distance between the screen A and the source,  $S = \Delta x$  is the area of the source, and equation 2.101 has been used. The area  $\Delta A$  is the coherence area of the light in the plane A around the point  $Q_0$  on the optical axis.

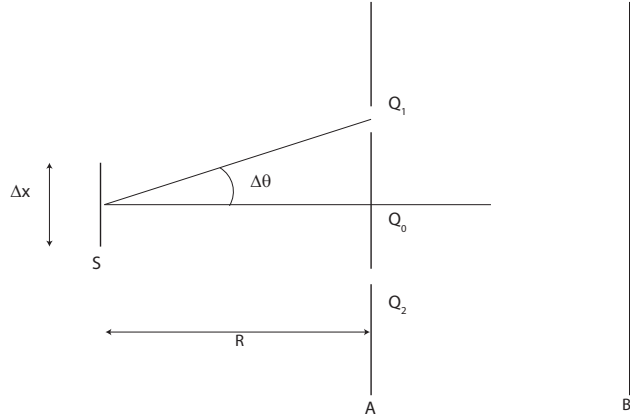


Figure 2.18: Young experiment setup.

The area of coherence quantifies the degree of spatial coherence. It depends on the area of the light source  $S$ , the distance of observation  $R$  and by the wavelength of the light. Interference fringes will be formed in the plane B more likely if the area of coherence is wide since the light remains correlated for even at a large distances  $z$ .

### 2.7.3 Simulation of spatial coherence

A novel method for simulating spatial coherence that generates a source optical field with a degree of coherence defined by the user. An electromagnetic wave is generated by a dipole oscillating at a certain frequency. This dipole can be a molecule, an atom, a group of atoms in a gas. In case of a conventional incandescence light source light is emitted by tungsten atoms exited by the electrical current. Same is valid for other sources of illuminations, like

gas lamps, neon, or solid state light sources like LED, atoms of molecules excited to higher energy level emit light when dropping on the ground energy level. Each dipole emits light with a certain initial phase. Considering a light source of surface  $\Sigma$ , containing oscillating dipoles, the elemental surfaces  $d\Sigma$  is defined as the surfaces on which all the dipoles oscillates with the same phase. The average dimension of the elemental surfaces  $d\Sigma$  is proportional to the degree of spatial coherence of the light source. The more coherent is the light source, the bigger the elemental surfaces will be. From a computational point of view having a light source composed by a mosaic of surfaces with different phases is equivalent to add a phase mask to the input field. This phase mask is composed by areas with a random phase value. The dimension of these areas gives an idea of the degree of spatial coherence. The idea behind the empirical method used to generate the phase mask is shown in figure 2.19:

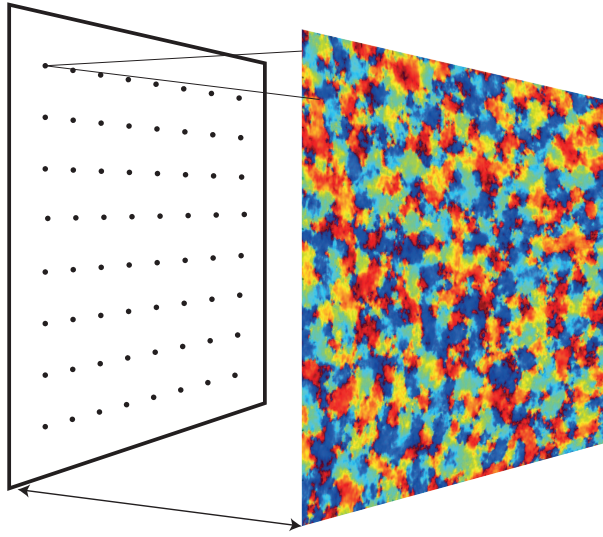


Figure 2.19: A random phase mask is generated propagating light coming from an array of sources, each one with a random phase value in the interval  $[-\pi, \pi]$ .

An array of point sources is displaced on a sampling window of the same dimension as the input field. The sources are placed regularly across the array. If the number of sources is less than 20, the sources are displaced randomly in order not to affect the coherence with their regular structure. The number of point sources used is defined as the coherence index  $C$ . To each of these point sources is assigned a random value of phase in the range  $[-\pi, \pi]$  and an amplitude value of one. Then the array of point sources is convolved with a kernel  $K$  whose size is defined in order to make all the random point sources to merge together. The size of the kernel depends on the resolution  $N$  of the input field and on the coherence index  $C$  and is equal to the ratio  $N/C$ . The result of the convolution is a phase mask that is formed by an array of circular areas with a random phase value. Although this array of sources is already a phase mask, it cannot be used into the

simulation platform, because of its periodicity. In fact it is not a random phase pattern. In order to randomize the shape and the distribution of the coherence areas the array of sources is propagated at a distance bigger than the size of the sources. The distance chosen to propagate the light sources is the one derived in 2.3.1 to keep the same sampling both in the input and output fields using the Fresnel propagation method discussed in section.

From equation 2.34:

$$d_c = \frac{W^2}{N\lambda} \quad (2.103)$$

where  $W$  is the field of view,  $N$  is the sampling and  $\lambda$  is the wavelength of the light. The choice of using the Fresnel propagation as described in section 2.3 has been made because the propagation distance is small and hence aliasing issues do not arise. In addition to that it only requires one Fourier transform, making the random phase generation algorithm faster. The whole process is shown in figure 2.20

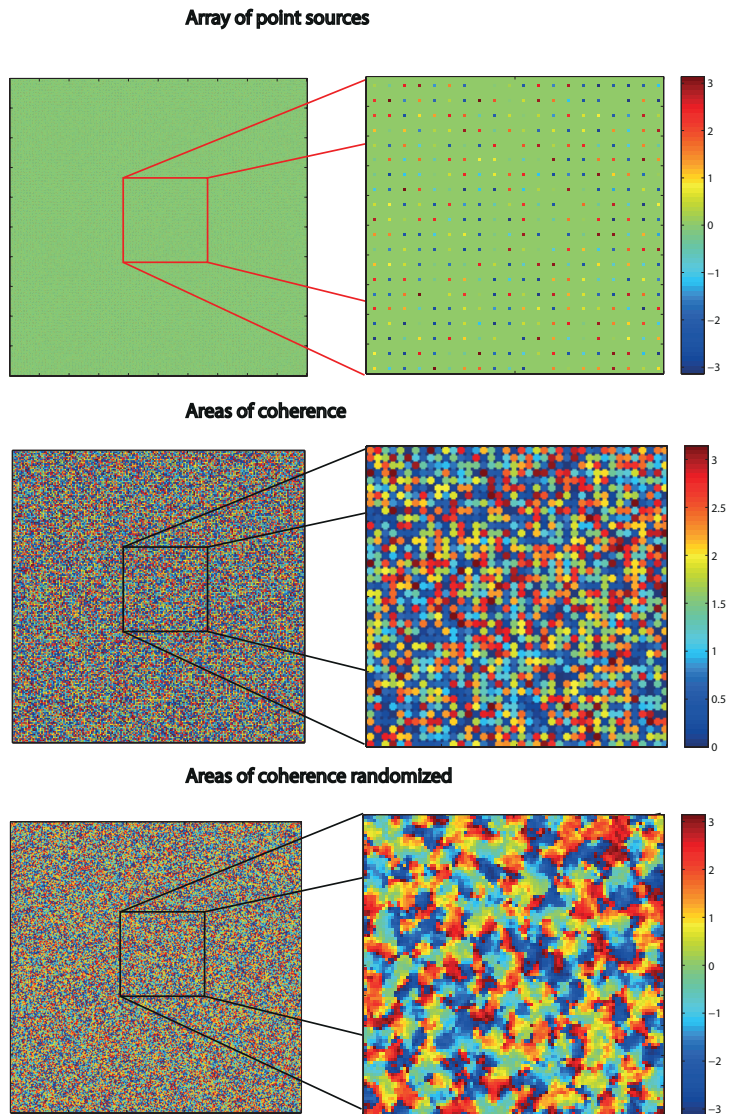


Figure 2.20: Process of the creation of the phase mask. Top: array of point sources with a random phase value; centre: array of the areas of coherence at source after the convolution with  $K$ ; bottom: randomized areas of coherence at object plane after the propagation of  $d_c$ .

Few examples of phase mask generated from different number of sources can be seen in figure 2.21:

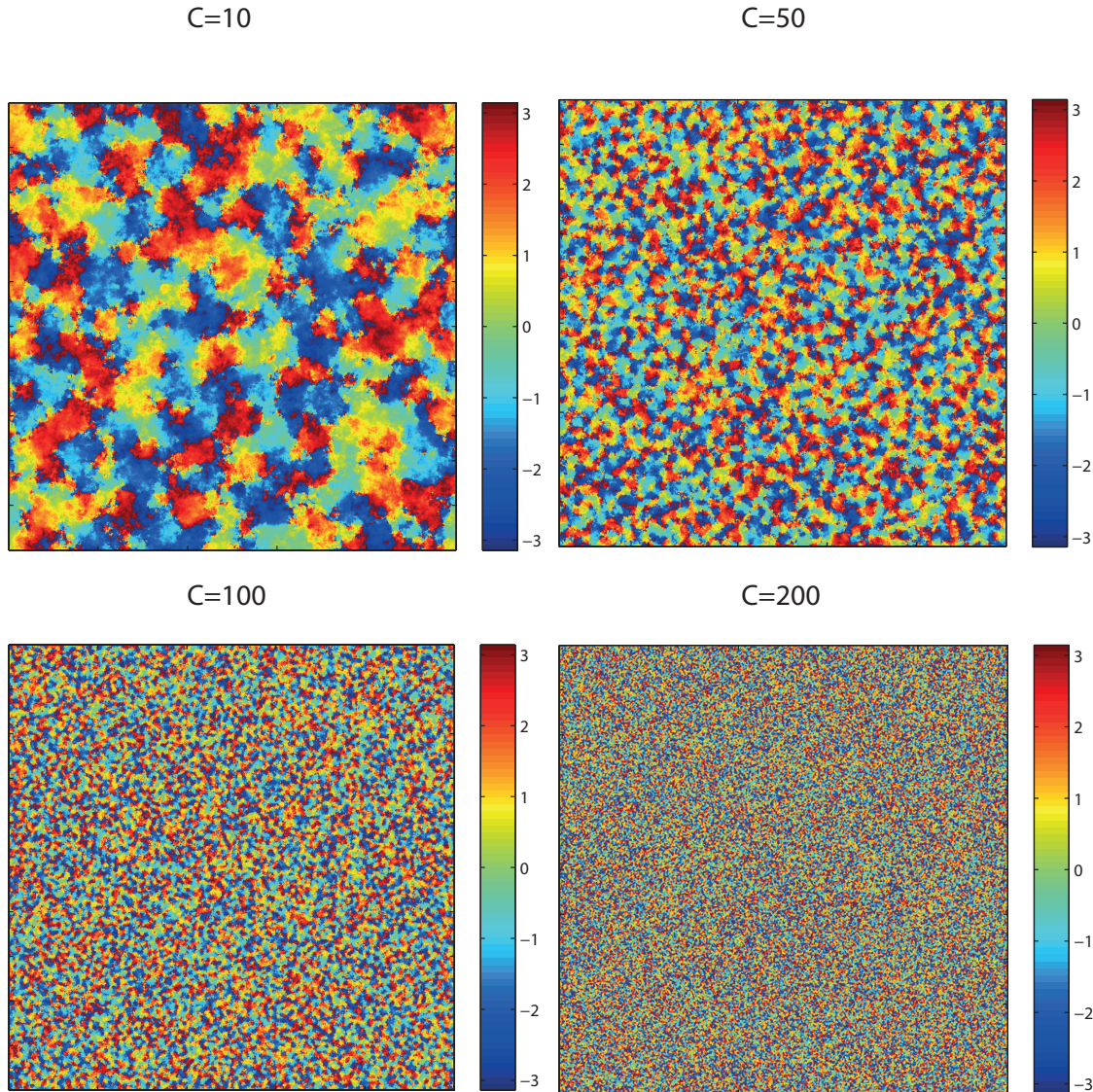


Figure 2.21: Final random phase mask generated by 10, 50, 100 and 200 sources.

The algorithm to generate the random phase mask can be summarized as follow:

- A number of light sources, are defined and arranged in a regular array, and allocated a random phase between  $-\pi$  and  $\pi$ .

- Each source has a size diameter given by:  $N/C$
  
  
  
  
  
  
- This array of sources is then propagated a distance  $d_c$  shown in equation 2.103 in order to randomize the shape of the coherence areas.
  
  
  
  
  
  
- the resultant phase is used as the output phase mask to add the input field.

#### 2.7.4 Simulation of temporal coherence

As discussed in section 2.7.1, temporal coherence is defined by the time  $\tau$  in which the optical wave is correlated with itself. In other words after a time  $t = \tau$ , the optical disturbance  $U(t)$  and  $U(t + \tau)$  are totally uncorrelated and cannot interfere with each other. To simulate this effect many snapshots of the output field are taken each time using a different random distribution phases for the sources. We assume that the time difference between every snapshots is equal to the coherence time  $\tau$ . For the application for which this toolbox has been designed it is not relevant to know the exact value of  $\tau$ . However, the light source used for the real system was a "Thorlabs LED Array Light Source LIU630A", with a wavelength centred on 630 nm and a bandwidth  $\Delta\lambda = 20nm$ . The emission spectrum is shown in figure 2.22.

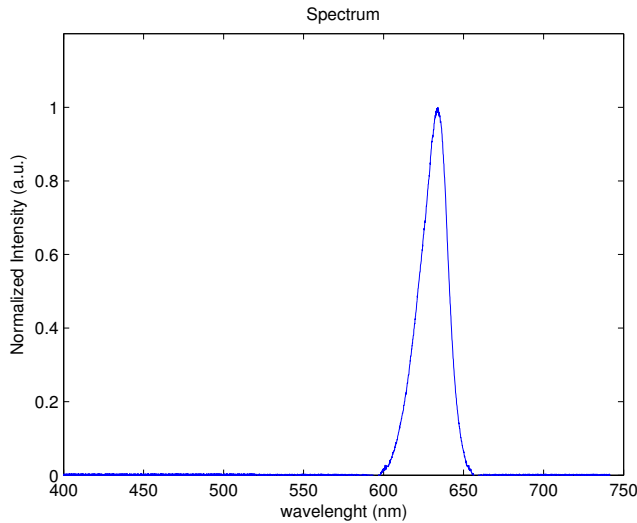


Figure 2.22: Emission spectrum of the LED considered in our simulations and real image system.

Its coherence time is given by:

$$\tau = \frac{1}{\Delta\nu} = \frac{\Delta\lambda}{c} \quad (2.104)$$

That gives a time of coherence  $\tau = 6.6 \times 10^{-17}s$ . Therefore each snapshot is assumed to be taken at the image plane at an interval of  $\tau$ . All the snapshots are then added together, integrating the optical disturbance over time. Longer integration times will give better contrast and less noise as it is shown in the following paragraph.

## 2.8 Optimization of coherence parameters

In the previous sections has been described how to simulate partially coherent light and how to implement an algorithm that produces a certain number of snapshots of the output field each one with a different random phase. The

random phase mask simulates the spatial coherence, the number of iteration instead simulates the effects of temporal coherence.

### 2.8.1 Optimization of Spatial Coherence

In this section will be defined the optimal value of coherence degree  $C$  and evaluating the signal to noise ratio of the outcome images from the 2f system shown in figure 2.14. Simulations have been run propagating an optical disturbance with phase masks generated with different values of the parameter  $C$ . The input field is the USAF resolution target, shown in 2.23

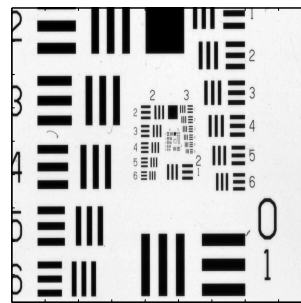


Figure 2.23: USAF resolution target.

The first simulation has been made changing the coherence index  $C$  from a value of 5 (high coherence) to 500 (low coherence) in a sampling window with a resolution of 1765 by 1765 pixels. Figure 2.25 shows how the field at the image plane for different values of  $C$  appears, while figure 2.24 shows a plot of the signal to noise ratio of the images as a function of the coherence index showing an asymptotic behaviour. After a certain threshold value of  $C$ , increasing the coherence index does not improve the image quality. The threshold is defined as the value of  $C$  for which the variance of the previous five values of SNR is less than 0.01.

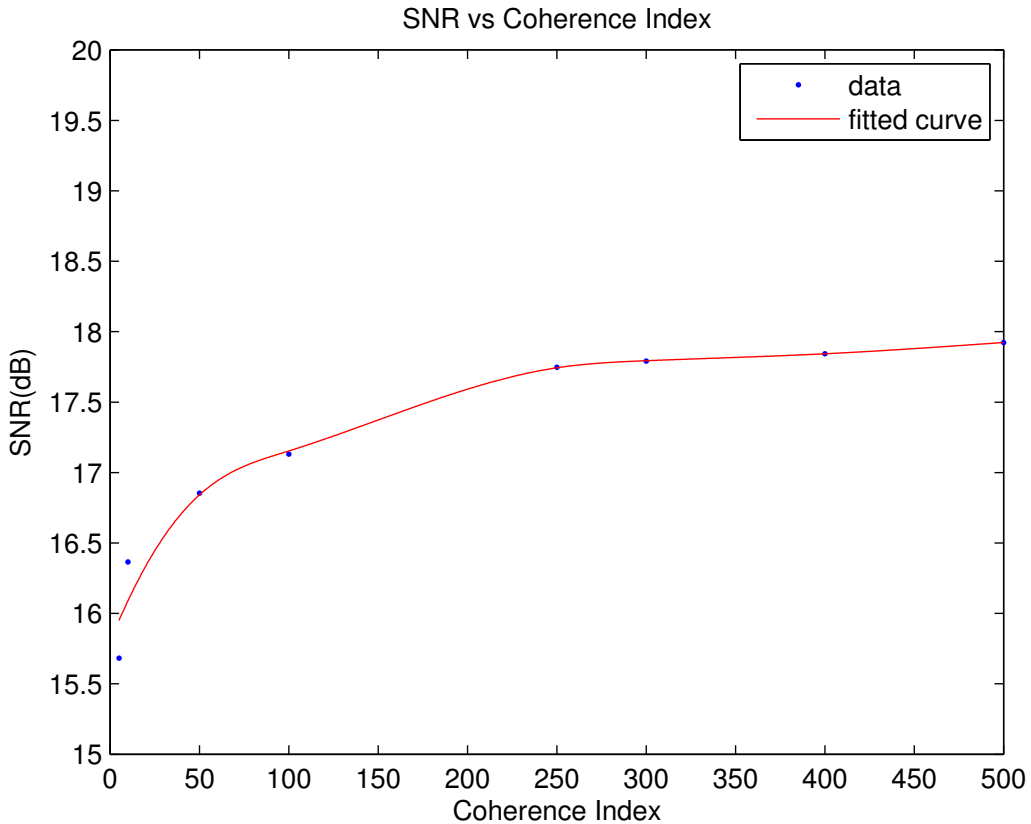


Figure 2.24: Signal to noise ratio of the image of a USAF resolution target plotted as a function of the coherence index  $C$ .

Figure 2.24 shows that for values of  $C$  bigger than 250 the SNR asymptotically tends to 18. In this case the resolution of the input field, and therefore of the phase mask, is 1765 by 1765 pixels, so that the SNR reaches the asymptote when the ratio between the number of sources and the resolution should be 0.14. After this point, there is no gain in making the light source more incoherent in terms of signal to noise ratio improvement. The ratio between the number of sources  $C$  and the resolution of the optical field  $N$  is defined as the incoherence degree  $\iota$ :

$$\iota = \frac{C}{N} \quad (2.105)$$

In figure 2.25 are shown the images of the target shown in 2.23 obtained with different incoherence parameters  $\iota$

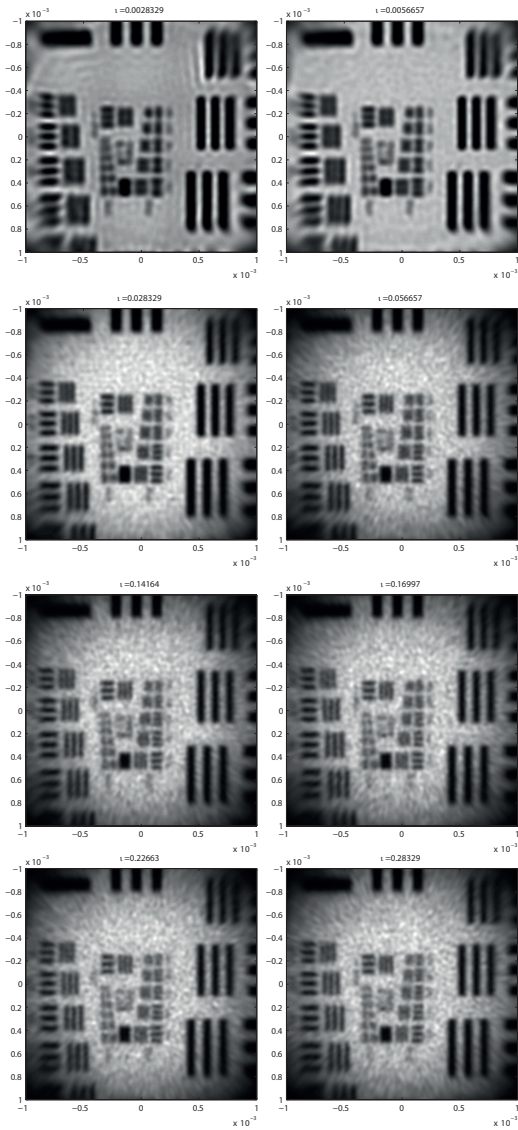


Figure 2.25: Images of the USAF resolution target with different values of  $\iota$ . Increasing the number of point sources generating the phase mask creates improves the resolution and the contrast

### 2.8.2 Optimization of temporal coherence

The second simulation run aimed to define the optimum number of snapshots in order to correctly simulate temporal coherence. The random phase mask acts as a diffuser, and the resultant output field obtained by a single snapshot will present a low signal to noise ratio due to speckles, as shown in figure 2.26

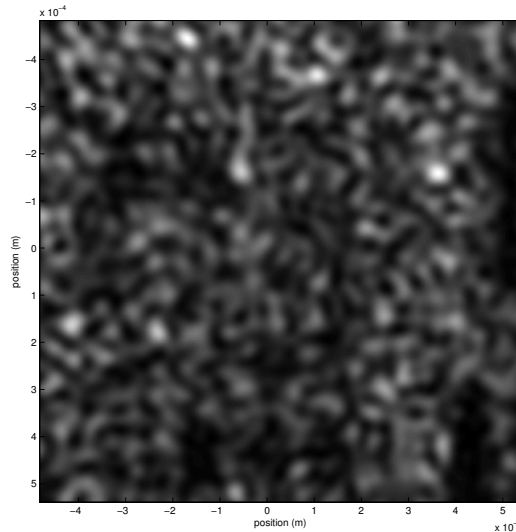


Figure 2.26: Noise due to the speckles in an image of a USAF resolution target after only 5 iterations.

Taking several snapshots and adding them all together is equal to integration over time of the optical field reaching the sensor. While increasing the integration time, the noise due to the speckles drops considerably. Figure 2.27 shows several images of the USAF target in figure 2.23 taken with an incoherence degree of  $\iota = 0.14$ , and with an increasing number of iterations from 5 to 1000.

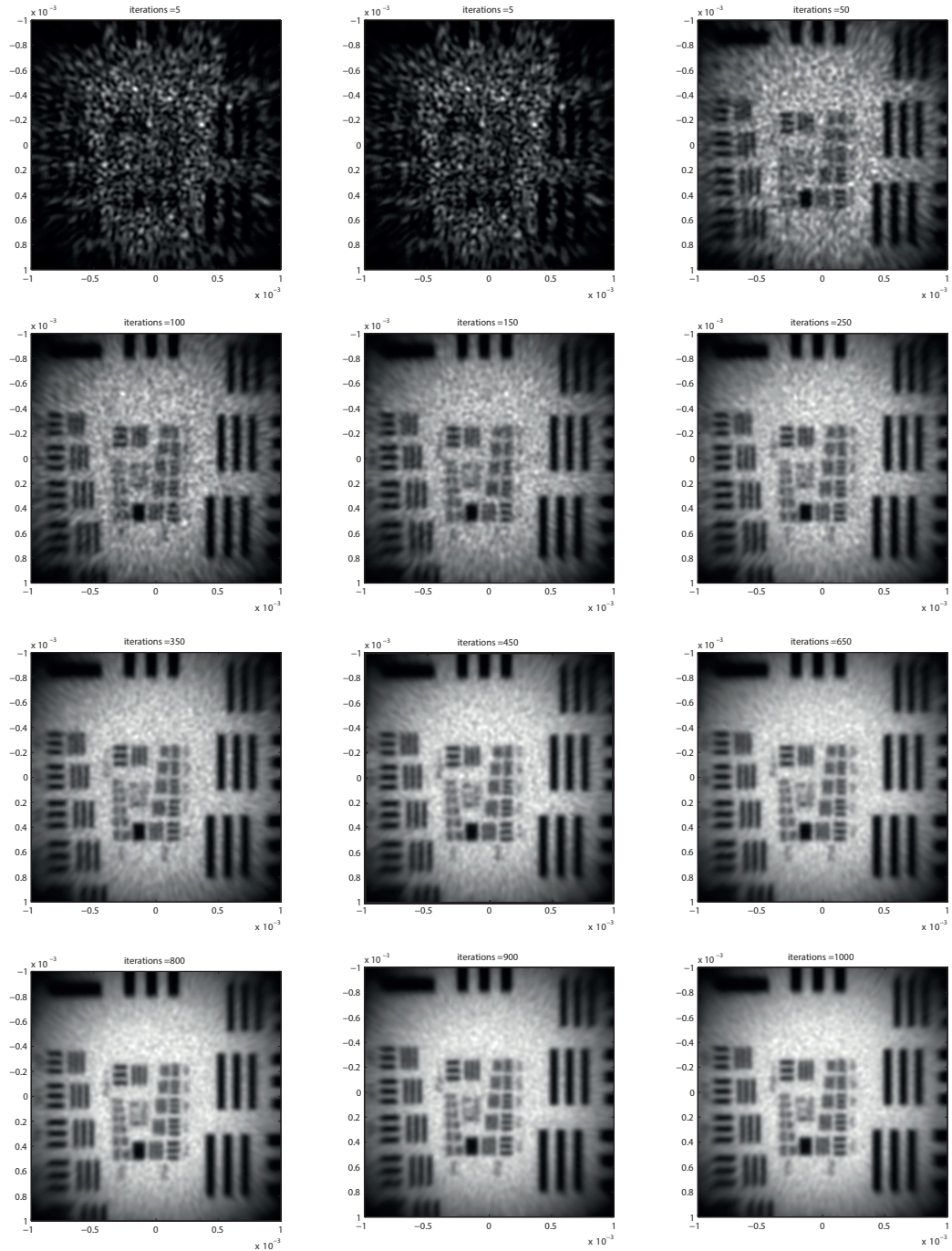


Figure 2.27: Images of the USAF resolution target obtained adding an increasing number of snapshot. this is equivalent to increase the integration time of the sensor. The noise due to the speckles caused by the phase mask decreases with increasing number of iterations.

Since increasing the number of iterations is computationally expensive, the signal to noise ratio of the images in figure 2.27 has been evaluated and plotted as a function of the number of iteration in order to define an optimal parameter. Results are shown in figure 2.28. The threshold is defined as the number of iterations for which the variance of the previous five values of SNR is less than 0.01.

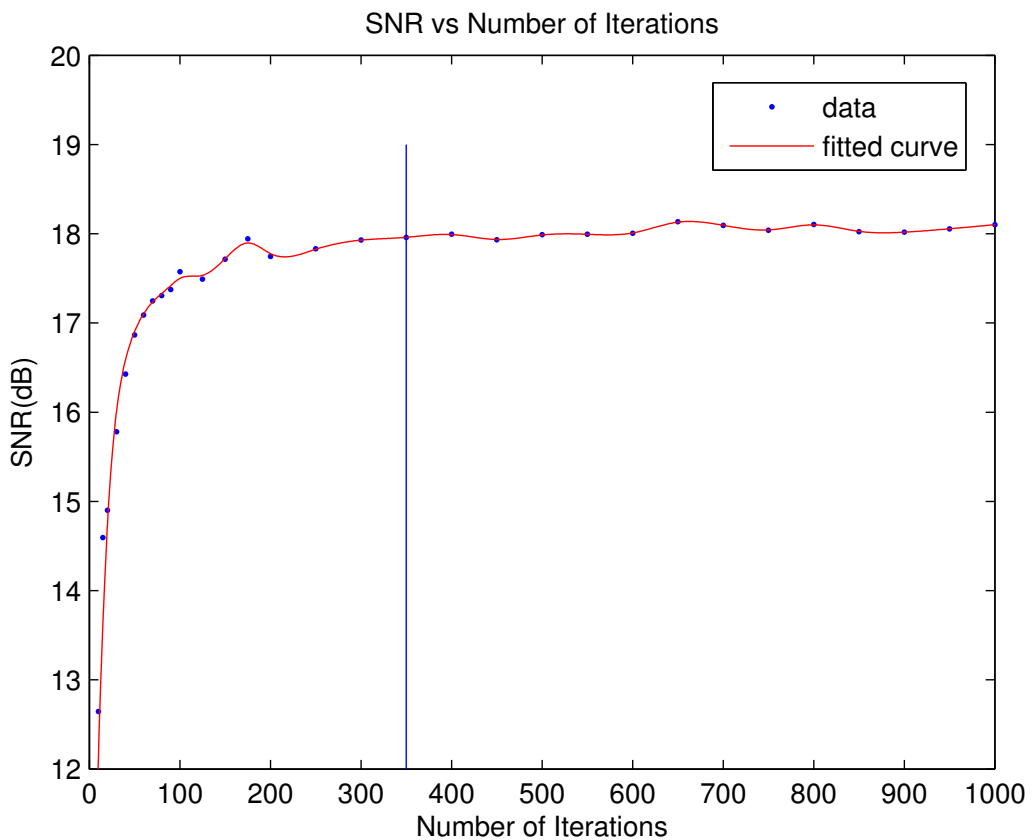


Figure 2.28: Signal to noise ratio as a function of the number of iterations. The threshold has been calculated looking at the variance of the previous five data.

For an image with an incoherence degree of  $\iota = 0.14$  the minimum number of iterations after that the SNR of the image does not improve further is

350. After that value the SNR tends asymptotically to 18 dB in spite of an increased computational effort. Therefore under a SNR point of view the optimal number of iteration to simulate temporal incoherence is 350. All the other simulations presented in this work will be performed with the coherence parameters discussed in this section.

### 2.8.3 Coherent imaging vs incoherent imaging

The image of an edge has been simulated to make a comparison between the coherent and the incoherent response. Data were simulated with the same optical parameters described in section 2.6.1. The intensity profile of an image of an edge is well known both in the case of coherent and incoherent illumination and provides a means of verification for the simulation methodology discussed above. Figure 2.29 shows the response of a coherent and an incoherent imaging systems to a sharp edge. The intensity profile of the edge is shown in green, its coherent image in blue and the incoherent image is shown in red. The two responses are very different. The coherent image presents fringes whose amplitude goes decreasing getting further away from the edge. This effect is known as ringing artefacts, due to the coherent transfer function that usually presents rapid discontinuities [47]. Another property of the coherent image is that it crosses the actual location of the edge at  $1/4$  of its asymptotic value of intensity, while the incoherent image does the same at  $1/2$  of its asymptotic value, as can be seen in figure 2.29 [47]. Both conditions are verified by the simulations run as shown in figure 2.29.

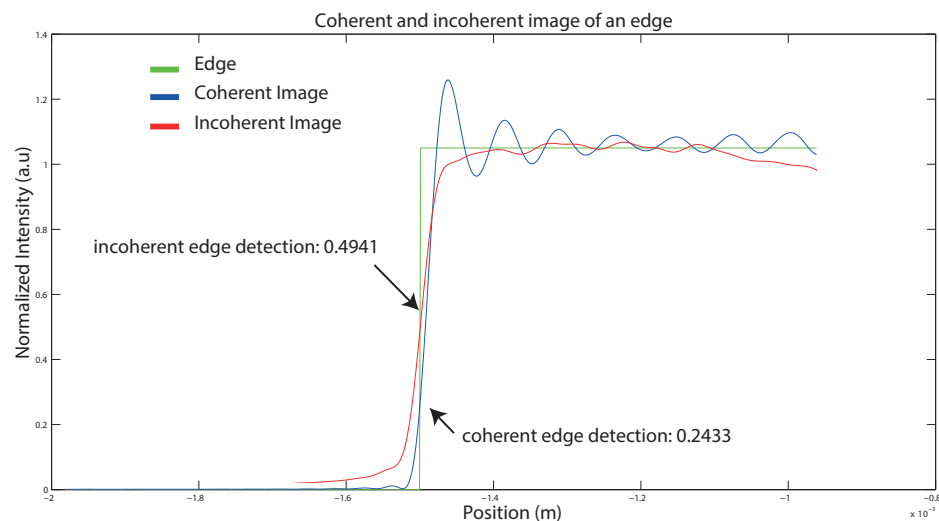


Figure 2.29: Comparison between the coherent and an incoherent response of a simple 2f system to a sharp edge.



# Chapter 3

## Simulations of a plenoptic 1.0 system

### 3.1 Introduction

In this chapter results are presented from simulations of plenoptic 1.0 raw data using the simulation platform described in chapter 2. The methods used to design, develop and test the data processing algorithms, such as rendering, synthetic refocus and depth estimation algorithms, from the digitally generated light fields data are described. All the light field processing algorithms presented in this chapter use the third parametrization of the light field, described in 1.4.2, that is the four dimensional representation of the intensity recorded on the sensor. Each point of this four dimensional array is a ray at the position  $x$  and  $y$  with a direction  $\theta_x$  and  $\theta_y$  [2, 3].

### 3.2 Description of the system

The plenoptic 1.0 camera described in section 1.4 has been modelled as a 2f system composed by a main lens, a micro lens array and a sensor as shown in figure 3.1. The micro lens array is placed at a distance  $z=2f$  from the main

lens, where  $f$  is the focal length of the main lens, and the sensor is placed at a distance  $f_\mu$  from the micro array plane that is also the focal length of the lens lets. In this configuration the lens let array plane is conjugated with the object plane, while the sensor plane is conjugated with the main lens plane. In order to satisfy the f-number matching condition described in section 1.4 once the propagation distances, the micro lens array parameters, the resolution  $N$  of the input field, the wavelength of the light used and the micro array parameters, the software automatically sets the aperture of the main lens.

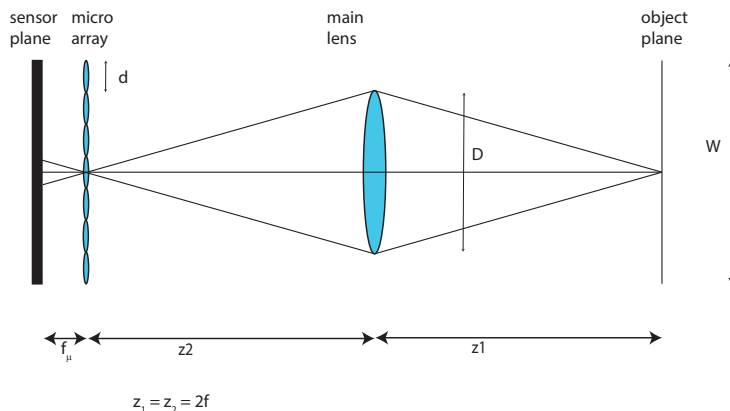


Figure 3.1: The parameters that characterize the micro lens array are: the pitch  $p$ , defined as the distance between the centres of two lens lets, the diameter  $d$ , the number of lens lets per raw  $N$  and the size of the micro array  $W$ .

The micro array parameters are illustrated in figure 3.2 and are the pitch, the diameter of the single lens let, the number of lens let in a row and the size of the array. In all simulations the pitch of the lens lets is taken equal to the size of its diameter and the lens lets are arranged in a square matrix.

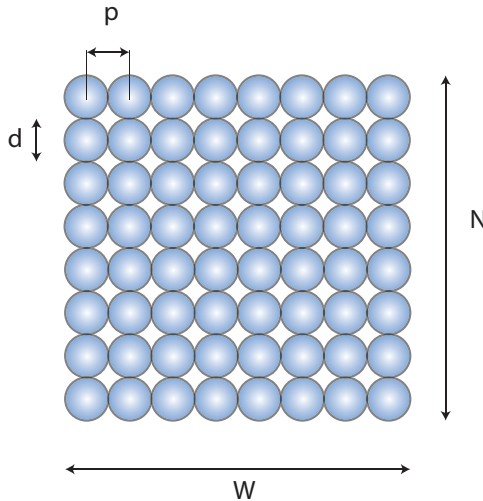


Figure 3.2: The parameters that characterize the micro lens array are: the pitch  $p$ , defined as the distance between the centres of two neighbouring lens lets, the diameter  $d$ , the number of lens lets per row  $N$  and the size of the micro array  $W$ .

### 3.2.1 Diffraction effects on the System

During the development of this work has been noted that diffraction from the lens let circular aperture generates cross talk between neighbouring sub images since the light form a single lens let falls in the sub image of the neighbour lens let. Because of this, blur is present in the rendered image resulting in a loss of spatial resolution. To avoid this loss of resolution the diameter of each lens let should be large enough so that the diameter of the Airy disk is totally smaller than the lens-let diameter. As seen in equation 2.99 for a lens with a circular aperture, the diameter of the Airy disk at its focal plane is

$$d_{\text{Airy}} = 2.44\lambda z/D \quad (3.1)$$

In order to avoid diffraction induced cross talk the lens let diameter should be at least the same diameter as the Airy disk so that the diffraction pattern is included in the sub image until its second zero:

$$D > 2.44 \frac{\lambda z}{D} \quad (3.2)$$

Therefore the condition of  $D$  is:

$$D > \sqrt{2.44 \lambda f_\mu} \quad (3.3)$$

Therefore when choosing a or designing a lens let array for plenoptic imaging, the lens let diameter and the focal length should satisfy equation 3.3. The acceptable values belongs to the area above the blue line in the diagram shown in figure 3.3.

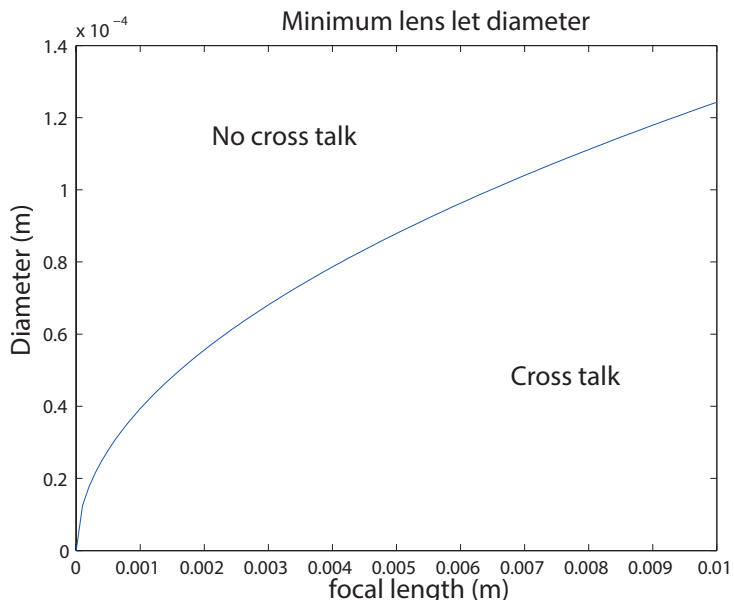


Figure 3.3: Values of acceptable lens let diameter to avoid diffraction induced cross talk.

The effect of cross talk between lens lets on the raw image is shown in figure 3.4.

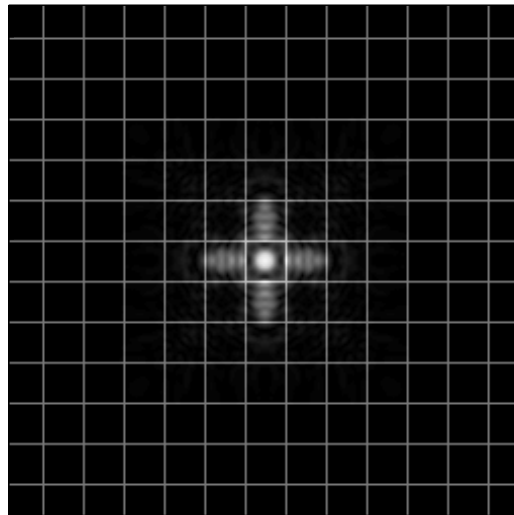


Figure 3.4: Raw image of a point source. The grid represents the edges of the sub images. If the point source is in focus, it should be represented by only one lens let. Because of diffraction some light goes also on the neighbouring sub images.

Figure 3.5 shows what happens in the phase space of point source in presence of cross talk and without cross talk. In the first case there is no blur since all the light coming from a point source in focus is recorded by a single lens let, while in the second case the spreading of the light due to diffraction causes a blur that is proportional to the number of sub images involved.

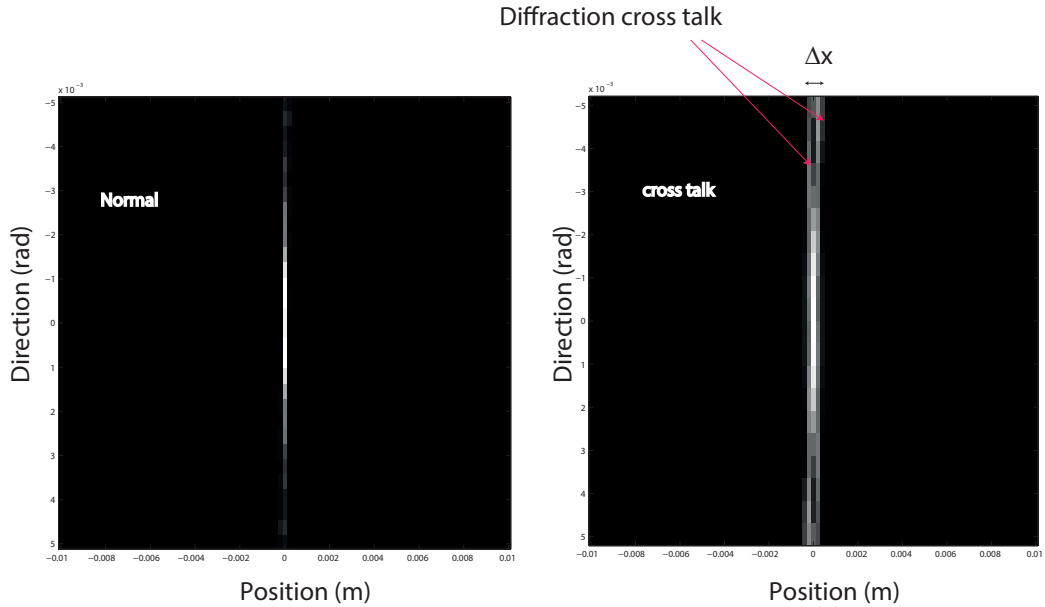


Figure 3.5: Phase space of the light field of a point object: on the left when the condition 3.3 is respected; on the right when diffraction induces cross talk arise between neighbours lens lets. Cross talk introduces a blur in the rendered image whose width is  $\Delta x$ .

### 3.3 Advanced Rendering Techniques

As described in chapter 1.5, one pixel in the rendered image is obtained as a mean of all the pixels of the sub image that corresponds to the position of the pixel in the final image [2]. This method generates an image that is equivalent to the image obtained with a conventional camera without any additional information. Since the final resolution depends on the number of lens lets in the micro array, it will be smaller than the resolution that can be obtained by a conventional camera which instead uses the full sensor resolution [3]. To use the full variety of features enabled by light field imaging, more advanced post processing techniques of the raw data should be used. The first two post processing features presented are the change of aperture

and of point of view. These effects are achieved by integrating each sub image along a sub set of directional coordinates, hence on a smaller number of pixels.

### 3.3.1 Changing Aperture

The quality of the image captured by a conventional camera depends on the combination of shutter speed and aperture chosen in order to get the optimum total exposure [52]. The possibility to change the aperture of the main lens in post processing allows to change the depth of field of the final image. In the simulations presented in this work the shutter speed is not an issue since all the objects imaged where static with constant and uniform illumination. Therefore what determines the exposure is the aperture of the main lens or the f-number. The f-number is proportional to the depth of field of the imaging system that can be defined as the range of depths that appears sharp in the resulting photograph [2]. If the f-number increases and the aperture gets smaller, the depth of field increases. Therefore a plenoptic camera can control the depth of field in post processing. Looking at the raw plenoptic image, each sub image is formed by a number of samples of the directions of the rays. If in equation 1.6 the range of integration along the directional coordinates is reduced, the aperture of the main lens is reduced at the same amount. If the aperture is smaller the rays propagating with an high angle respect the optical axis will not reach the sensor and will be not considered to form the intensity of each pixel. The result is a rendered image that looks like it has been captured with a narrower aperture. Computationally the

algorithm to reduce the aperture is:

$$I(x, y) = \frac{1}{N'^2} \sum_{i=k/2}^{N-k/2} \sum_{j=k/2}^{N-k/2} L(x, y, i, j) \quad (3.4)$$

where  $N' = N - k$  and  $k$  is the range of directional coordinates considered in the sum. This operation in the phase space is shown in figure ??:

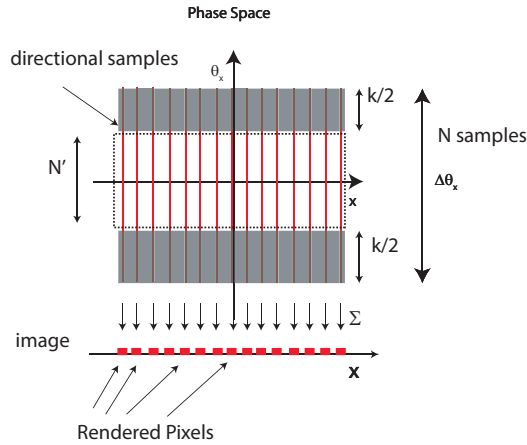


Figure 3.6: Rendering seen from the  $(x, \theta_x)$  slice of the phase space. The directional pixels not considered for the integration are shown in grey.

An effect of reducing the aperture of a camera is to extend its depth of field. Therefore the depth of field can be digitally extended changing the range of directional coordinates included in the sum as explained above. In figure 3.7 is shown the raw image of thin silky skin separating two layers of an onion, immersed in oil to improve transparency obtained by Levoy *et al.* in Stanford University [4].

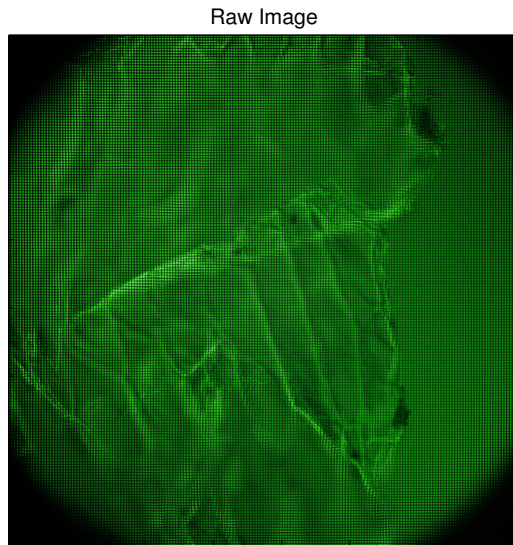


Figure 3.7: Raw plenoptic 1.0 image obtained from Levoy *et al.* The microscope was a Zeiss Axiovert with a 20x/0.5NA (dry) objective. The micro lens array was 24mm x 36mm, with square 125-micron x 125-micron f/20 micro lenses, held in front of the Axiovert's side camera port using an optical bench mount. The camera was a Canon 5D full-frame digital SLR. The specimen was the thin silky skin separating two layers of an onion, immersed in oil to improve transparency [4].

Figure shows 3.8 the differences between the rendered image integrating over the full aperture, and the rendered image obtained using only the central pixel of each sub image. The effect is to reduce the aperture to a pinhole and to have an all-in-focus image. Images has been obtained with home made rendering algorithm written in MATLAB. parating two layers of an onion, immersed in oil to improve transparency.

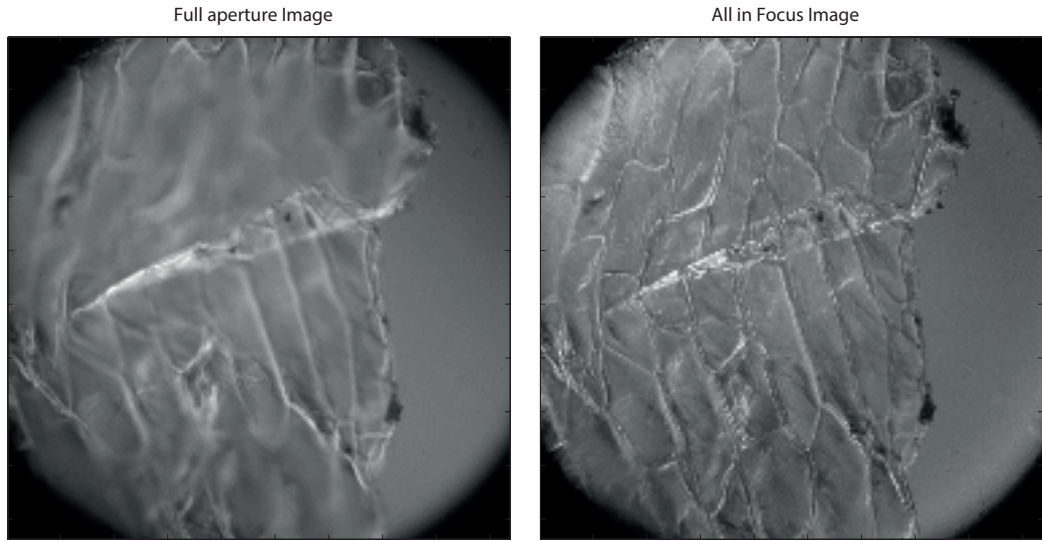


Figure 3.8: Rendered Images from the raw data in figure 3.7. On the left there is the full aperture imagea, obtained integrating along all the directional coordinates while on the right there is the all in focus image obtained taking onli the central pixel of the each sub image, that corresponds to rays with the direction parallel to the optical axis.

### 3.3.2 Changing the point of view

It is possible to change the point of view in the rendered image integrating along a all the directional coordinates in one direction keeping fixed the other direction. For example an image corresponding to a particular point of view can be obtained, with reference to equations 3.5, keeping fixed the

$$\begin{aligned} I(x, y) &= \frac{1}{N} \sum_{i=0}^N L(x, y, i, k_y) \\ I(x, y) &= \frac{1}{N} \sum_{j=0}^N L(x, y, k_x, j) \end{aligned} \quad (3.5)$$

## 3.4 Depth estimation

In this section it will be explained how it is possible to extract depth information from light fields data. In the specific case of plenoptic 1.0 raw

data, depth can be decoded looking at the phase space. In section 1.4.1 is explained that a point source on the focal plane of the main lens looks like a straight vertical line in the phase space. The physical meaning of this is that for a single position, one lens let, all the directional coordinates are sampled[3]. If the point source is out of focus the situation is different. If the source is closer to the main lens with respect to the focal plane, it will be imaged on a plane that is behind the micro array. This situation is shown in figure 3.9. Both directional and positional coordinates are sampled by more than one lens let and each sub image will sample a set of directional coordinates correspondent to the part of the main lens from where the rays come from. Figure 3.10 shows what happens in the phase space. On the lens let plane the spot size will have a width of  $\Delta x$  proportional to the distance, therefore the directions will be sampled by the lens lets included in this interval. Each lens let receives light coming from a particular area of the main lens, its correspondent sub image only records the pixels linked with those coordinates as can be seen comparing figure 3.9 with 3.10. The resultant phase space representation is still a straight line, but with positive slope proportional to the distance of the point source 3.10. If the source is further away from the plane where the main lens is focused, the main lens image is formed before the lens lets plane. The point is still sampled by more than one lens let included in the spot size  $\Delta x$ . The difference with the previous case is that now in the phase space the point source is represented by a straight line with a negative slope. The physical meaning of the slope of the phase space line can be understood by looking at figure 3.11. When the main lens image is formed in front of the micro lens plane the increasing

directions on  $\theta_x$  axis are mapped on decreasing positions on the x axis and the line on the phase space representing the point has a negative slope. If the image is formed behind the micro lens plane increasing directions on  $\theta_x$  axis are mapped on increasing positions on the x axis this inversion is absent and the line in the phase space has a positive slope [2]. This characteristic of the phase space permits to discriminate between points in the scene that are in front or behind the main lens focal plane, giving a first rough depth estimation.

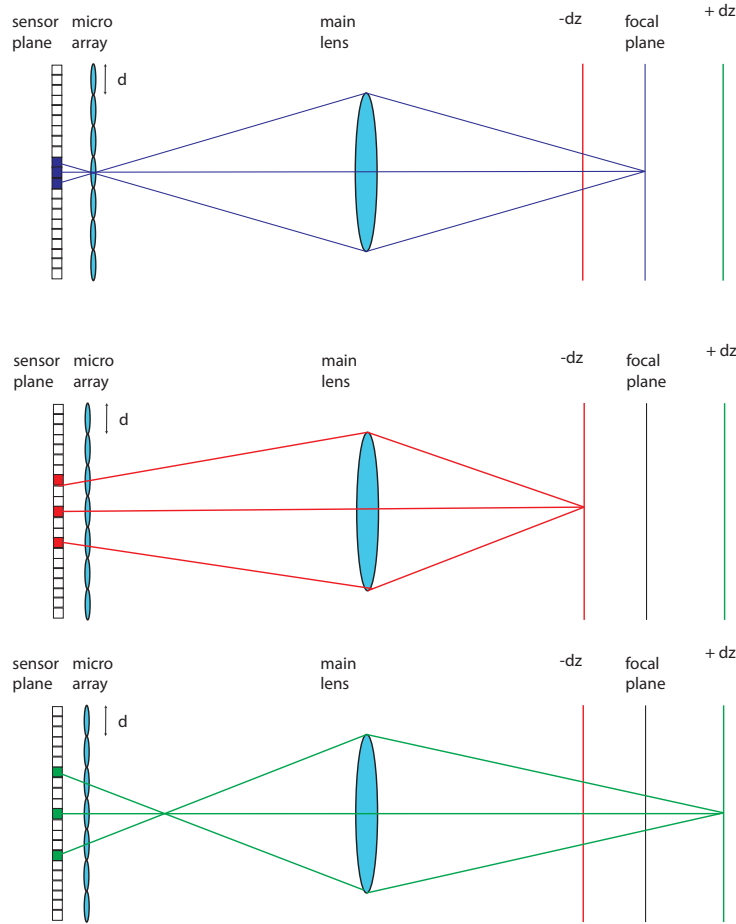


Figure 3.9: Sampling of the light field of a point source in focus, on the top, closer to the main lens, centre, and further away, bottom. When the source is out of focus, both position and directions are sampled by more than one lens let since the main lens image is not formed any more on the lens let plane.

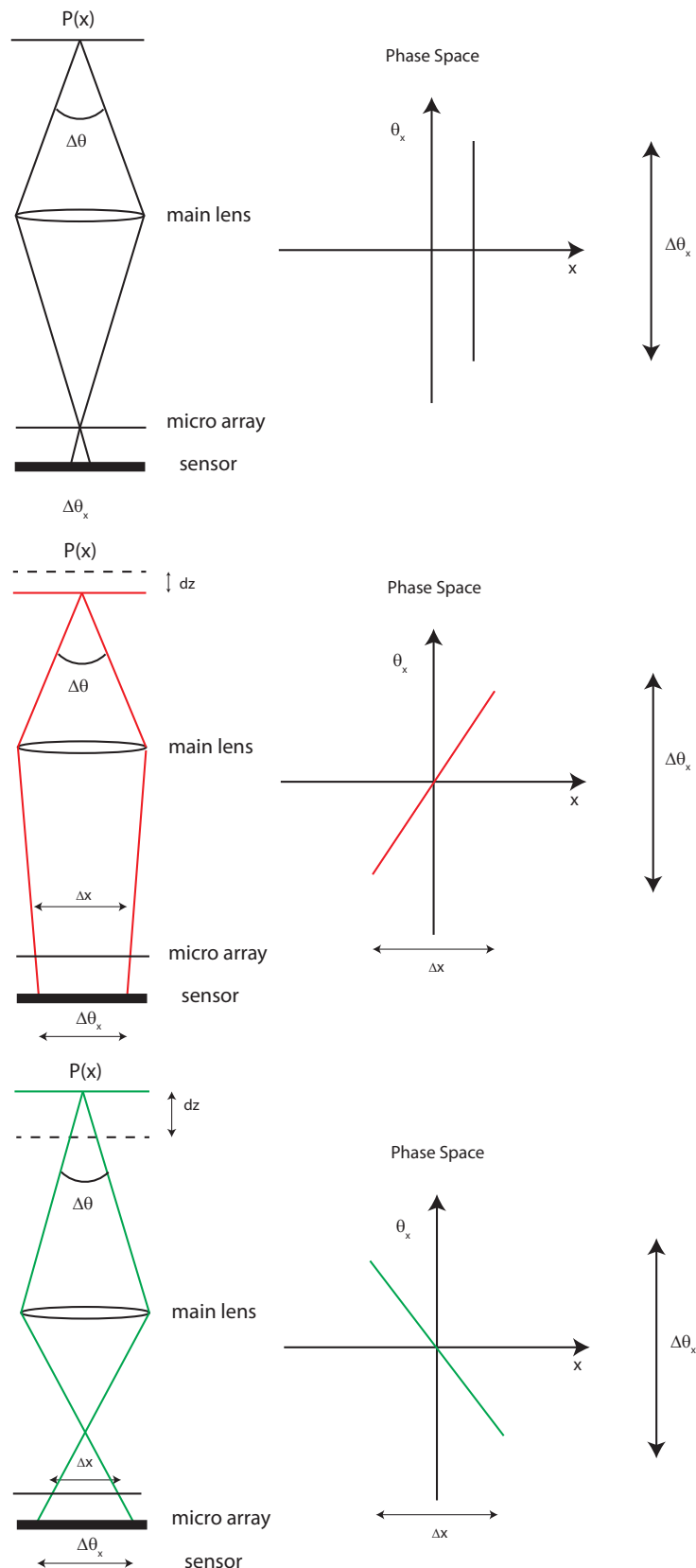


Figure 3.10: Information on the depth of a point source imaged by a plenoptic 1.0 system. As explained in section 1.4.1 If the point source is in focus, on the top, it's position is sampled by one lens let as well as the whole set of directions .

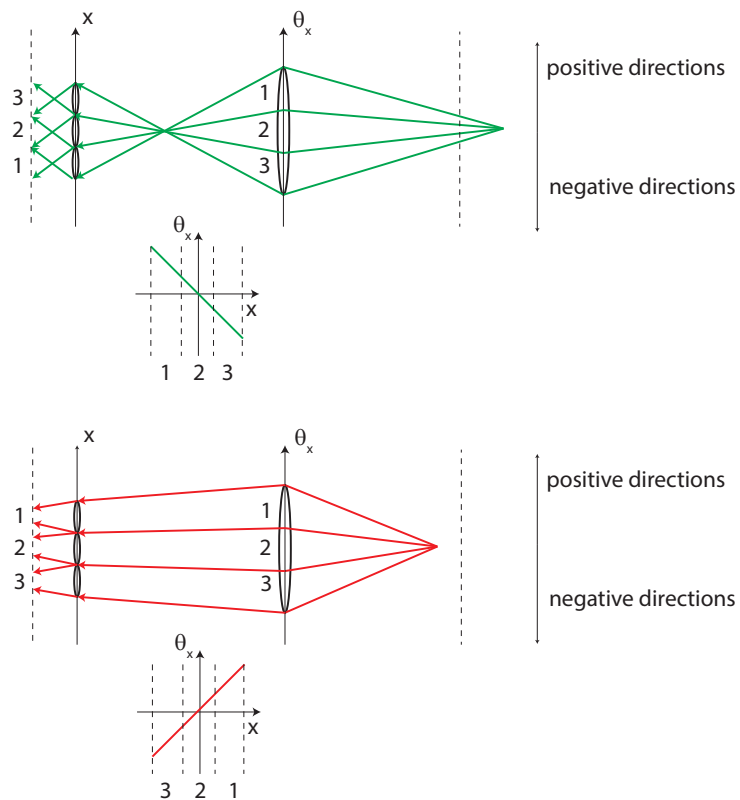


Figure 3.11: Physical meaning of the slope in the phase space. If the point source is further than the camera focal plane, the phase space line has a negative slope. If the point source is closer than the focal plane, the slope of the phase space line is positive.

A simulation of plenoptic 1.0 camera has been made to verify this fact.

The system was composed by a main lens with a focal length of  $120\text{ mm}$ , in a  $2f$  configuration creating an image on the micro array plane. The Micro lens array was composed by a matrix of 101 by 101 lens lets with a diameter of  $100\text{ }\mu\text{m}$  and a focal length of 100

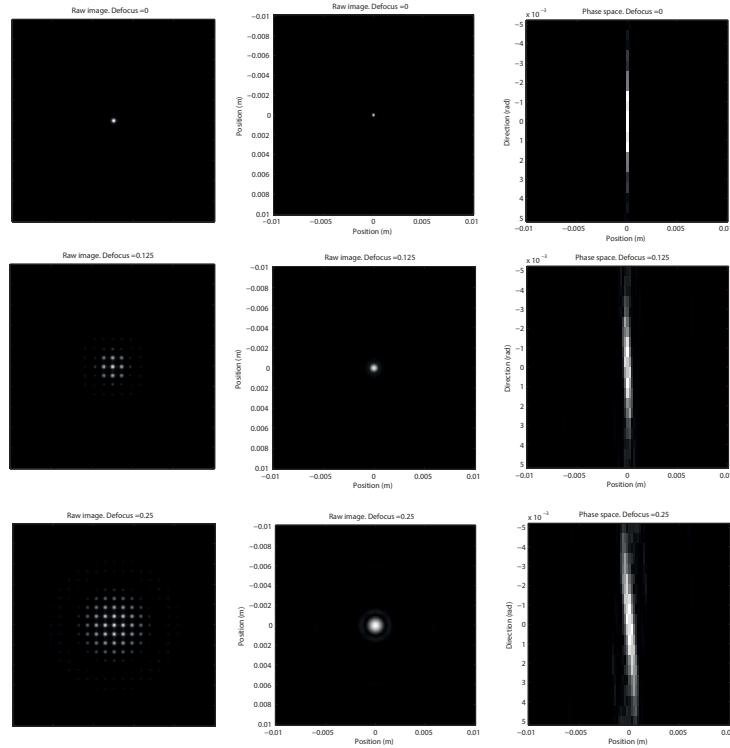


Figure 3.12: Numerical simulation of a point source imaged by a plenoptic 1.0 imaging system. The point source was placed at three different distances from the main lens. The top three figures show the focused image. In the centre ones a defocus of 0.125 m is added and the point source is further away from the main lens. In the bottom ones the point source is closer to the main lens of .25 m. In all the three cases the raw data image is on the left, the rendered image is on the centre and the phase space line is on the right.

### 3.5 Synthetic refocus

Another post processing feature enabled by collecting the light field is the possibility to refocus an image after it has been captured. This feature is called synthetic refocusing and is based on the fact that the recorded light field can be used to compute images as if they were taken by a synthetic camera positioned and focused differently from the actual camera. In this

section the synthetic refocus algorithm is explained according to what is treated in the research work of Ng *et al.* [21, 2]. This method is based on the fact that it is possible to define a synthetic camera composed by an aperture and a sensor plane, for which the defocused object plane results in focus. It will also be explained how this method, based on a synthetic camera model obtained with ray tracing, can be implemented in a wave optics approach using the simulation platform developed in this work and the limitations and the issues arising from a wave approach respect the simple and ideal ray optics approach will be discussed. Figure shows 3.13 a plenoptic 1.0 imaging system whose main lens produces an out of focus image on the micro lens plane. The directional set of coordinates  $\Delta u$  is mapped along the range of spatial coordinates  $\Delta x$ . The light field can be re parametrized in terms of a synthetic light field generated by an aperture on the plane  $u'$  represented by the dashed lens, that focuses the object on a synthetic focal plane,  $x'$ . This second light field is parametrized with the coordinates  $u' v'$  and  $x' y'$ .

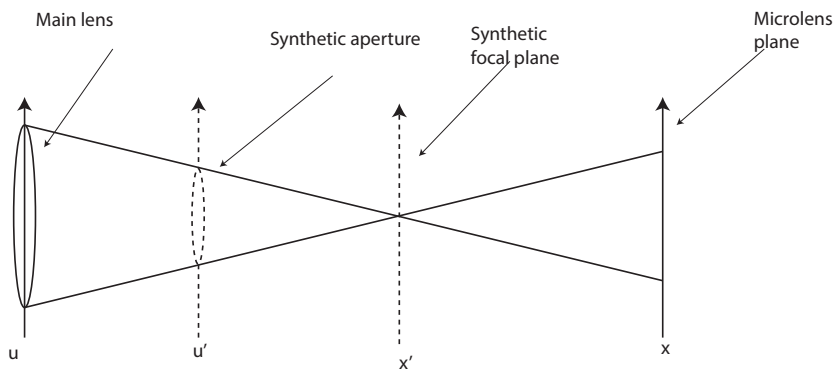


Figure 3.13: The synthetic camera refocusing method is based on the fact that it is always possible to define a virtual aperture that is focused on the lens let plane.

As explained by Ng [21] and in analogy with what was explained in section

1.5 it is possible to define the intensity obtained rendering a synthetic light field  $L'(x', y', u', v')$  at the synthetic focal plane as:

$$I(x, y) = \iint L'(x', y', u', v') A(u', v') du' dv' \quad (3.6)$$

The goal is to express this intensity as a function of the captured light field  $L(x, y, u, v)$  present on the actual sensor plane, finding the relationship that links the set of coordinates  $x, y, u, v$  with  $x', y', u', v'$ .

### 3.5.1 Synthetic refocus algorithm

To find the link between the real and the synthetic light field do the following simplifications are made:

- only the synthetic sensor plane  $x', y'$  will be moved. Therefore the main lens plane  $u', v'$  is at the same position of the plane  $u, v$ , and no transformation is performed on the directional coordinates, therefore  $(u, v) = (u', v')$ .
- the aperture of the main lens will not change,  $A(x', y') = 1$ .

Figure 3.14 shows a two dimensional diagram explaining the re-parametrization under the hypotheses explained above. Only shows the coordinates  $x$  and  $u$  are shown for simplicity.  $F$  is defined as the distance of the main lens from the lens let array plane, and  $F'$  as the distance from the synthetic focal plane. The ratio between these two distances is the refocusing parameter  $\alpha$ , defined as:

$$\alpha = \frac{F}{F'} \quad (3.7)$$

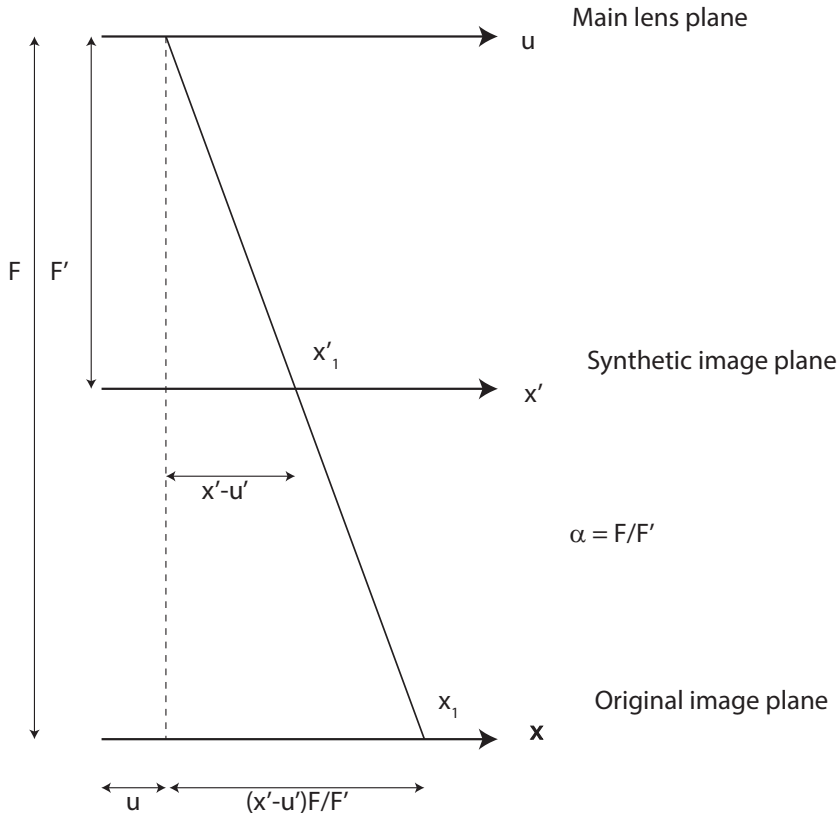


Figure 3.14: Changing the focal plane of the camera is equal to re parametrize the light field according to the new coordinates. The re parametrization is basically a shift proportional to the ratio between the refocused plane and the original camera plane  $\alpha$ .

The refocusing factor can assume the following values:

- $\alpha = 1$  when the synthetic focal plane is at the same position of the main lens focal plane
- $\alpha > 1$  when the distance between the main lens and the synthetic image plane is smaller than the distance between the main lens and its original focal plane. This occurs when the system is refocused on a plane that is further away with respect to the main lens focal plane.

- $\alpha < 1$  when the distance between the main lens and the synthetic image plane is bigger than the distance between the main lens and its original focal plane. This occurs when the refocus takes place on a plane that is closer with respect to the main lens.

Looking at figure 3.14 a ray of light that crosses the main lens plane at the coordinate  $u$  and that then intercepts the synthetic image plane at the point  $x'_1$ , can be represented using the coordinates of the original image plane  $x_1$ . Because of similar triangles, the value of the  $x$  coordinate on the image plane can be expressed as a function of the coordinates  $u, x'$ . We have:

$$x_1 = u + (x'_1 - u) \frac{F}{F'} = u + (x'_1 - u)\alpha \quad (3.8)$$

Therefore extending to the four dimensional case, the points belonging to the synthetic image plane can be expressed as a function of the directional coordinates at the main lens plane and the spatial coordinates at the original image plane as:

$$\begin{aligned} x' &= \frac{x}{\alpha} + u \left(1 - \frac{1}{\alpha}\right) \\ y' &= \frac{y}{\alpha} + v \left(1 - \frac{1}{\alpha}\right) \end{aligned} \quad (3.9)$$

With this change of coordinates the light field at the synthetic focal plane  $x'$  can be written substituting equations 3.9 into equation 3.6.

$$I(x, y) = \iint L \left( \frac{x}{\alpha} + u \left(1 - \frac{1}{\alpha}\right), \frac{y}{\alpha} + v \left(1 - \frac{1}{\alpha}\right), u, v \right) A(x', y') dudv \quad (3.10)$$

Equation 3.10 represents the rendered image obtained integrating along the directional coordinates the light field reparametrized as if it were captured by a camera whose focal plane is the same as the synthetic focal plane.

Focusing at different depths corresponds to changing the separation between the lens and the film plane, shifting it of a quantity proportional to the refocusing factor  $\alpha$ . From equation 3.9 the four dimensional light field at the synthetic plane is obtained from the light field recorded on the sensor by shifting and rescaling its spatial coordinates. The transformation operated on the light field is the composition of two transformations:

- a scaling of a factor  $\alpha$  that depends by the distance of the synthetic focal plane from the main lens.
- a translation term  $u(1 - 1/\alpha)$  that increases with the directional coordinates and with the magnitude of the factor alpha.

Therefore the synthetic refocus can be treated as a linear operator acting on the four dimensional light field that maps the light field recorded on a new set of coordinates. The rendering on this new set of coordinates gives the image focused at a different plane.

### 3.5.2 Refocusing Operator

The synthetic refocus equation 3.10 has been obtained with ray optics considerations only. However, it can be applied to light fields obtained light fields obtained with wave optics simulations. This novel approach to implement the refocusing algorithm to a synthetic generated wave optics is one of the main result of this work. When using wave optics particular attention should be given in the design of the imaging system in order to avoid cross talk effects induced by diffraction, as explained in section 3.2.1. The effects of this operator in the phase space is a change of the slope of the lines

describing the points of the image in the phase space. Since the total light field is conserved, the area in the phase space remains the same, hence the projection of the light field on the phase space results sheared respect the original one.

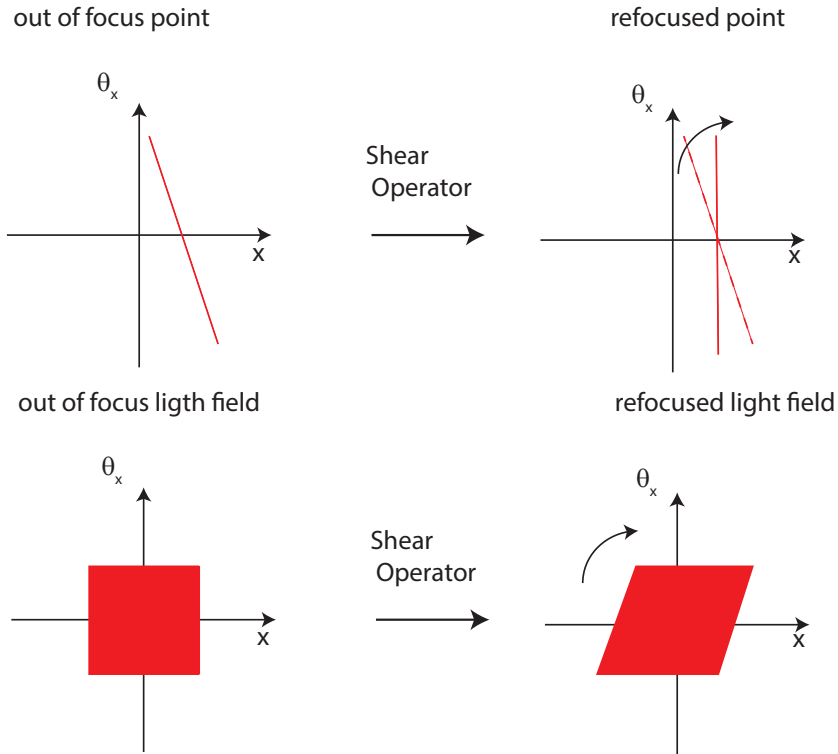


Figure 3.15: Changing the position of the focal plane is equal to shear the light field in the phase space. The total area remains the same since the total light field is conserved.

A MATLAB piece of code has been developed to implement the synthetic refocus operator. The algorithm is composed by two distinct stages. The first stage creates a new set of spatial coordinates shifting and rescaling the the original set of coordinates as shown in equation 3.9. Then the output synthetic light field is created interpolating the input light field using as a base the new set of coordinates. The flow chart can be seen in figure 3.16

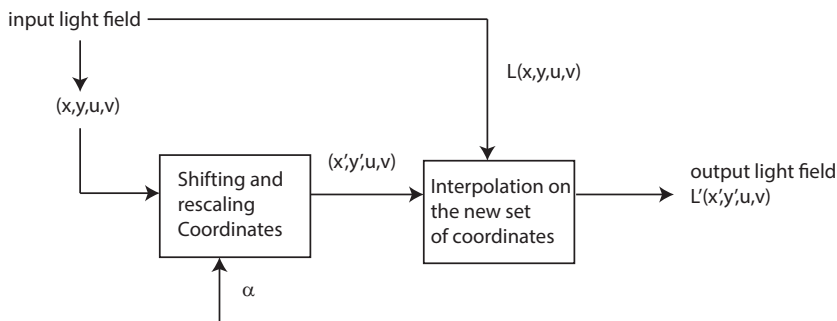


Figure 3.16: Flow chart of the operator shearing.

## 3.6 Results of the Simulations

To test and explore the potentials of the synthetic refocusing algorithm has been used wave optics simulation toolbox described in section ???. The System simulated is the one described in section 2.6.1 and shown in figure 3.17. The optical parameters can be found in the following table.

Main lens focal length f	120mm
Lens aperture D	3.6 mm
Micro lens focal length $f_\mu$	10 mm
Micro lens diameter d	150 $\mu m$
Micro array pitch p	150 $\mu m$
Field of view W	20 mm
f-number	33.6
sensor resolution	3030 by 3030 pixel

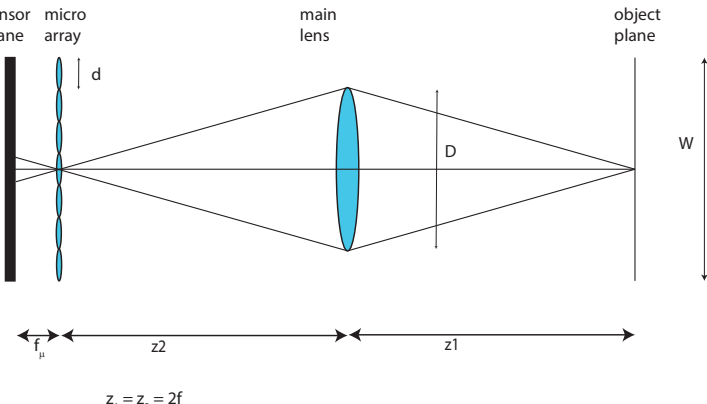


Figure 3.17: Set up simulated.

With this set up the final rendered image resolution is of 101 by 101 pixel. Each pixel of the final image corresponds to a lens let, therefore the spatial resolution the final image is equal to the diameter of the single lens let. Each sub image has 30 by 30 pixels, meaning that the full set of directional coordinates is sampled by  $N_{sub} = 30$  samples. The angular resolution is therefore:

$$\delta\theta = \frac{\Delta\theta}{N_{sub}} = \frac{NA}{N_{sub}} \quad (3.11)$$

and is equal to  $\delta\theta = 2.510^{-4} rad$ .

The first object to be imaged was a volume  $V$  of dimension 20 mm x 20 mm x 100 mm containing three point sources. Each point source has been simulated by a circle of 10  $\mu m$  diameter and are positioned as shown in figure 3.18

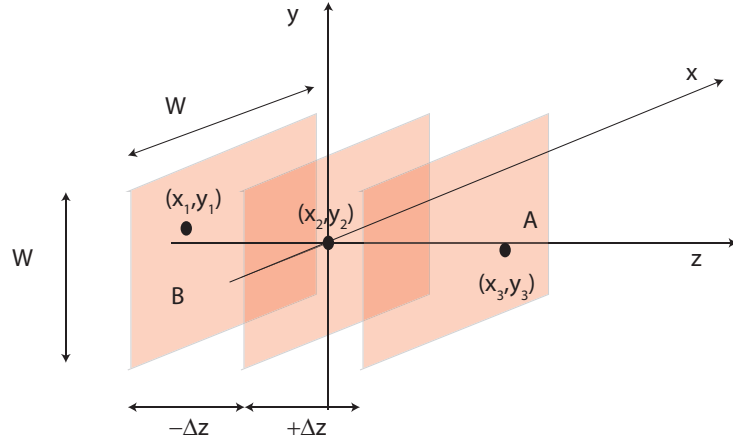


Figure 3.18: Position of the point sources imaged inside the volume  $V$  simulated.

Each plane has been imaged singularly setting the distance  $z_1$  equal to the sum of the distance of the main lens focal plane and the defocus  $\delta z$ . The Coordinates of the points are:

- A:  $x_1 = -3, y_1 = -3, z_1 = -50$
- B:  $x_2 = 0, y_2 = 0, z_2 = 0$
- C:  $x_3 = +3, y_3 = +3, z_3 = +50$

After that the light of the three planes has been propagated into the system, the final raw image has been obtained summing the three separate raw images normalized by the total amount of energy contained. This can be done since the Fresnel simulation toolbox is time independent. Figure 3.19 shows the total raw image and the rendered image integrated without any refocusing.

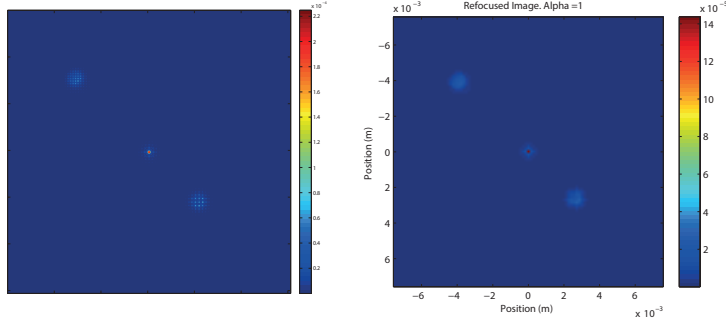


Figure 3.19: Raw image on the left and rendered image on the right. Intensity is shown in false colour in order to appreciate variations in energy distribution.

The central spot is in focus, since the point source is at a distance of  $z = 2f$  on the main lens focal plane. For a defocus of 50 mm the factor  $\alpha$  can be obtained from the lens equation. For the 2f system simulated and referring to figure 3.14 for notations:

$$\frac{1}{f} = \frac{1}{F'} + \frac{1}{z + \Delta z} \quad (3.12)$$

Since  $\alpha = F/F'$ , and in a 2f system  $F=2f=z$ :

$$\frac{1}{f} = \frac{\alpha}{2f} + \frac{1}{2f + \Delta z} \quad (3.13)$$

Resolving for  $\alpha$  becomes:

$$\alpha = \frac{2f + s\Delta z}{2f + \Delta z} \quad (3.14)$$

Figure shows the values of  $\alpha$  obtained by equation 3.14 for defocus varying between plus and minus 10 cm.

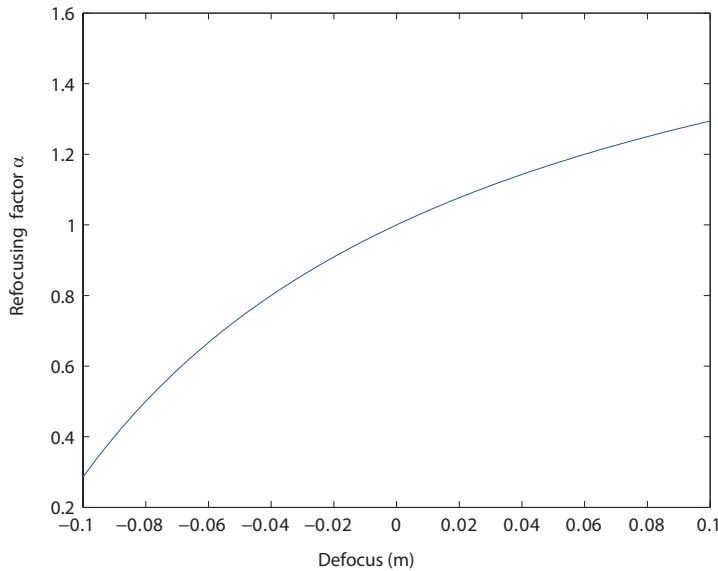


Figure 3.20: Values of the refocusing factor  $\alpha$  as a function of the defocus. A positive defocus means that the object is further away with respect to the main lens, a negative defocus indicates an object that is closer.

We can see from figure 3.20 that, as expected, the refocus factor is not linear with defocus and therefore the axial resolution is not linear. When the object is closer to the main lens, small variations in the defocus give large variations in  $\alpha$  while the opposite happens when the object is further away with respect to the main lens.

Figure 3.21 shows the refocused images obtained from shearing the light field extracted by the raw image in . According to equation 3.14, the point A is refocused for a value of  $\alpha$  equal to 0.7 and point B for  $\alpha = 1.17$ .

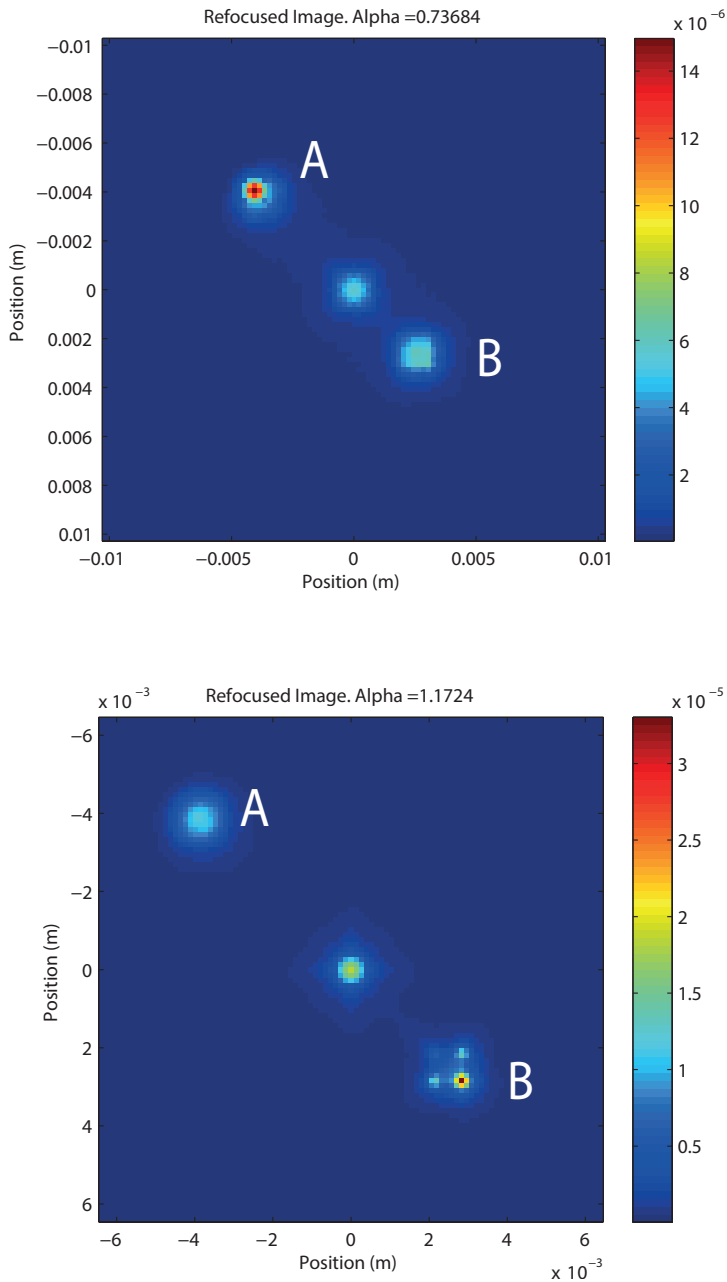


Figure 3.21: Refocused Images of the three point sources in image 3.19. In the top one the point A is refocused, in the bottom one the point B is refocused. The colour bar indicates the how the intensity is distributed. When the point source is refocused, the intensity distribution is higher with respect to the out of focus points.

The effects of the refocusing operator can be appreciated looking the intensity values of the refocused point sources. In the top image of figure 3.21 the point labelled with the letter A is refocused, and the majority of the light present in the photo concentrates on its location. The same happens in bottom figure, where the brightest point, indicated in red according to the colour bar, is the refocused one (B). This is a proof of the fact that the refocusing operator, shearing the four dimensional light field, simply move the intensity from a location to another. The Total energy of the image remains unchanged.

### 3.7 Focal stack depth estimation

The synthetic refocus algorithm provides a method to estimate the depth of a point source in a volume. Looking at the Fourier transform of a rendered image of a point source before and after the refocusing operation can be seen that when the point source is in focus, its spectrum is broader than the blurred one. This fact is true for normal images as well, when the presence of sharp details in the focused image, causes its spectrum to have a larger amount of high spatial frequencies, and therefore a bigger energy distributed on the nigh frequencies. In figure is shown the difference between the spectrum of the out of focus image(blue) and the in focus image(red) for a defocus of 5 cm.

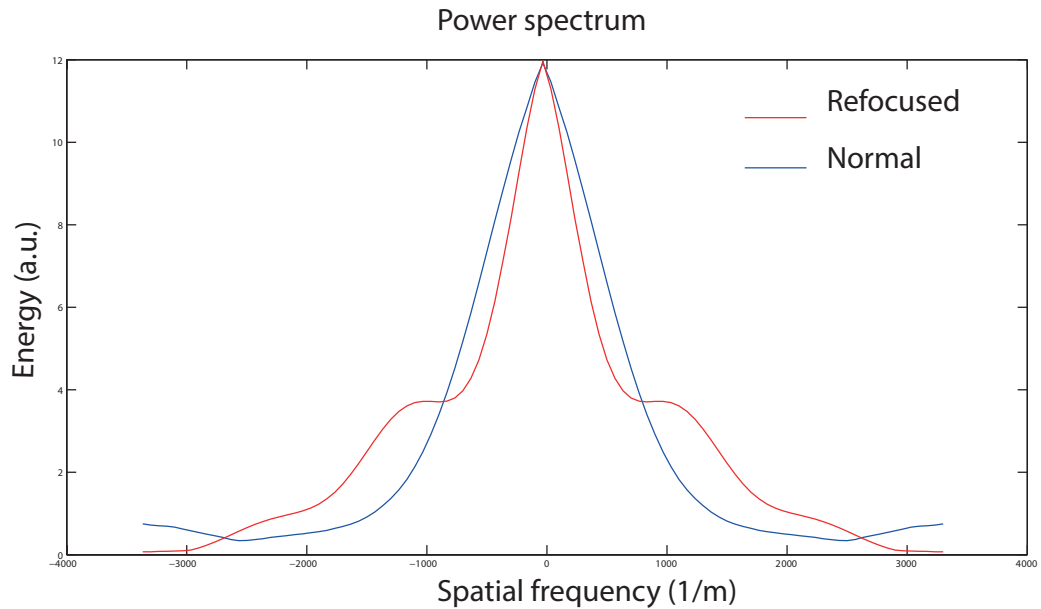


Figure 3.22: Refocused images...

The action of shearing the light field produces a redistribution of the power spectrum of the signal towards high frequency. This effect causes the sharpness of the image and therefore the refocus. This effect can be used to estimate the depth of object imaged just evaluating its level of blur. This blur based depth estimation is an original contribution of this work to light field literature. The method consists in creating a focal stack shearing the light field at different values of the coefficient alpha, that correspond to different focal planes, and rendering the images. After the focal stack is created the power spectrum of each image is calculated using the fast Fourier transform algorithm. The low frequency terms are then removed high pass filtering the images and the total energy contained in the high frequency term is calculated integrating the Fourier spectra. Plotting the values of energy as a function of the different alpha coefficients a curve with a maximum in the

proximity of the most in focus image is obtained. This maximum corresponds to the image in the focal stack that best estimates the actual value of alpha. In figure 3.23 are shown the energy as a function of the refocus parameter alpha for a point source placed at different depths. The vertical red line indicate the position of the maximum. The values of the estimated alpha and the real one are shown in the following table:

Estimated $\alpha$	Real $\alpha$	Error	Defocus
0.85	0.738	0.1132	-0.05 m
0.925	0.8837	0.0413	-0.025 m
1.080	1.0943	-0.0143	+0.025 m
1.105	1.1724	0.0674	+0.05 m

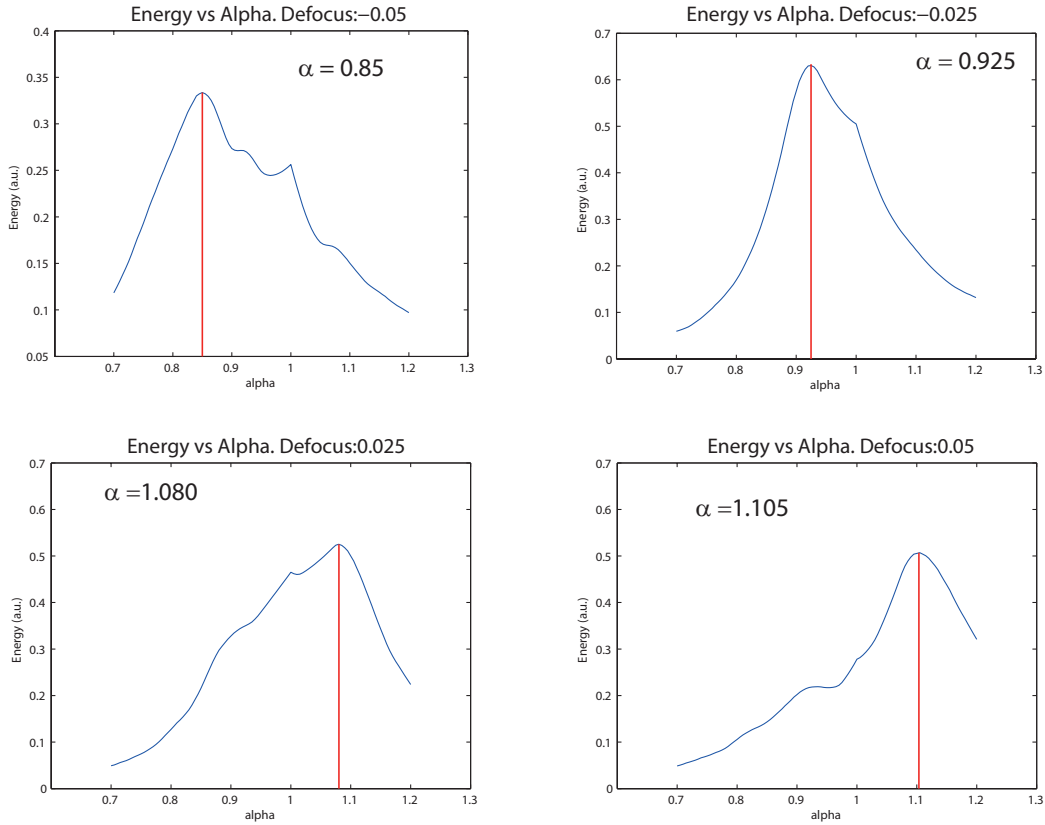


Figure 3.23: Refocused images...

Figure 3.24 shows the distribution of the estimated values of alpha versus the actual values obtained from equation 3.14. The estimated values for a defocus of -0.1 m and - 0.08 m are equal to 1 as if the image would lie on the focal plane. These are clearly wrong estimation and represent a limitation for the method described. It is interesting to see that for negative defocus the parameter  $\alpha$  is over estimated and the error is positive while for positive defocus the error is negative. The minimum error is present for values of defocus corresponding to positions close to the focal plane. The error in the estimation of the refocusing factor is plotted in figure 3.25. Having seen these results the method has a better accuracy in a range of depth around the focal

plane and loses when the absolute value of the defocus increase.

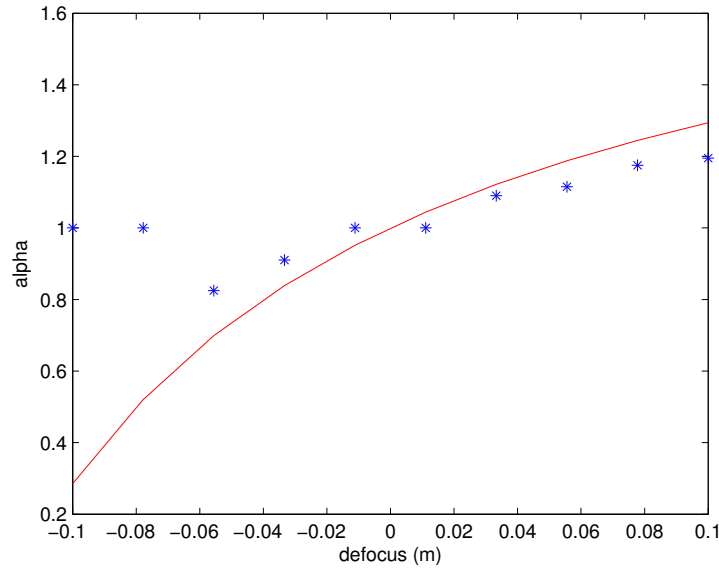


Figure 3.24: Estimated values of  $\alpha$  represented by blue stars and the theoretical values represented with the blue line.

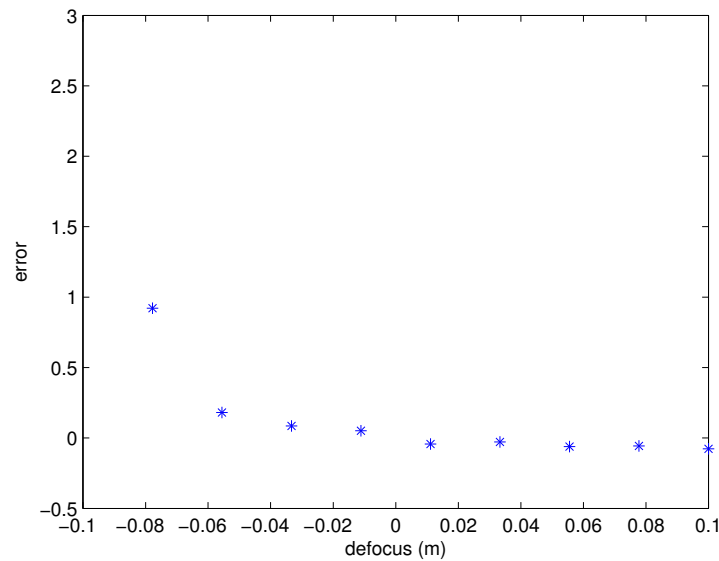


Figure 3.25: Distance between the estimated values of alpha and the actual theoretical values.

These results show that the depth evaluation depends from the distance

of the object from the camera. This is a natural consequence of the non linearity of the lens equation. A way to have a linear dependency of the parameter alpha with the refocusing distance is to have an array of lenslets with variable focal length [6, 27], or changing the focal length of the lenslets dynamically using electro optics effects [57].

# Chapter 4

## Simulation of a plenoptic 2.0 system

In this chapter several simulations performed to characterize the optical performances of a focused plenoptic imaging system will be presented. The scope of this work is to investigate the behaviour of a plenoptic 2.0 imaging system at its diffraction limit under a wave optics approach. All simulations described in this chapter have been run using the Fresnel Simulation Toolbox described in chapter 2. In a plenoptic 1.0 imaging system the resolution is limited by the dimensions of the lens lets [37] and the final rendered image has a much lower resolution than a conventional image. In a focused plenoptic system, as explained in section ??, the resolution of the final rendered image is not linked any more to the number of lens let in the micro array and it is possible to recover the full sensor resolution pushing it even to sub-pixel resolution [34, 35, 31]. This characteristic makes plenoptic systems suitable to a wider range of applications where high spatial resolution is required [6]. In the past years further effort has been made to push plenoptic 2.0 system to achieve super-resolution performances [58, 31, 29]. Here the term super-

resolution is not referred to the achievement of a resolution beyond diffraction limit[32] but to a digital sub pixel resolution only. Especially when applied to microscopy diffraction still is represents a big limitation for plenoptic imaging systems. In this chapter will be explained how diffraction affects the optical resolution of the imaging system and how it is linked to the spatio-angular trade off [19]. Numerical simulations will be used implemented by the platform described in chapter 2.

## 4.1 Rendering in Plenoptic 2.0

As introduced in chapter 1.8, rendering an image from plenoptic 2.0 raw data is based on integrating for each position all the correspondent directional coordinates. While in plenoptic 1.0 each position is sampled by a single lens let, that causes the loss of resolution in the final image, in plenoptic 2.0 each position is sampled by several lens lets. Therefore with reference to figure 4.1, the spatial coordinate (x,y) of point **A** will be sampled by the lens lets 1,2 and 3, therefore **A** is represented by 3 sub images. Each sub image is a different point of view of A and directional coordinates are sampled by these three points of view simultaneously. The number of sub images into which the point *A* is imaged depends by the magnification  $m=b/a$  of the lens let array and is given by:

$$N_{sub} = \frac{1}{m} = \frac{a}{b} \quad (4.1)$$

*a* is the distance of the micro array from the main lens image and *b* is the distance of the from the sensor plane.

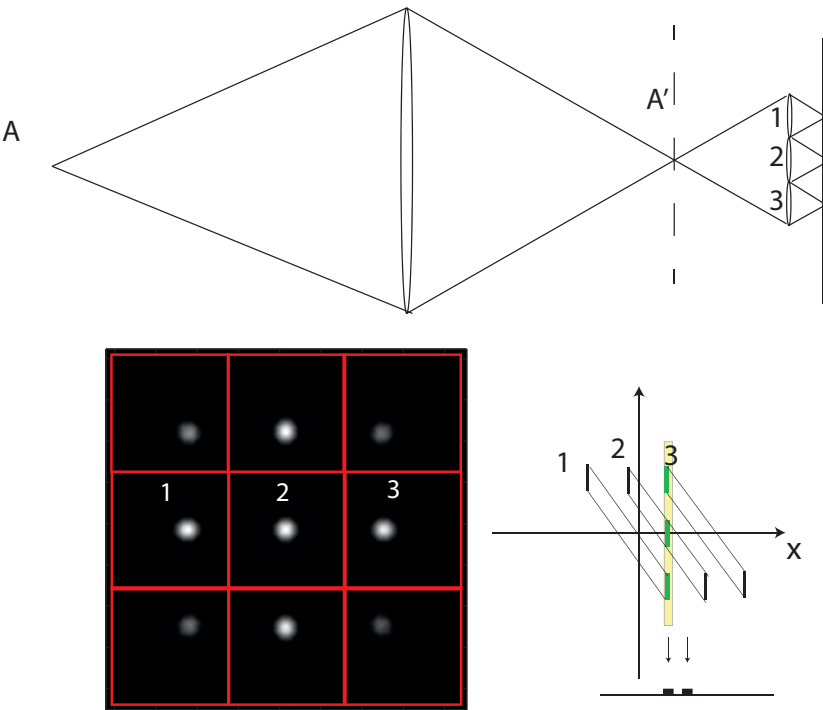


Figure 4.1: Top: the point **A** is imaged by the main lens into the point **A'**. **A'** is imaged by the lens let array into a number of sub images depending by the magnification of the micro array stage, in this case  $m=0.333$ . Bottom: particular of the raw image at the point source **A** and phase space diagram. The three sub images 1,2 and 3 are three different points of view of the object.

From a computational point of view the basic rendering is performed directly on the raw sensor image and has the following steps:

- the single sub images are isolated from each other
- depending on the magnification  $m$  the number of angular samples to be extracted from each sub image is calculated.
- the angular samples are extracted by the sub image and tiled all together forming the rendered image.

### 4.1.1 Extracting sub images

The effect of distortion must be taken into account when extracting the sub images from the raw data. The radial distortion is due to the fact that the sub images are shifted of certain amount because the lens lets are imaging off axis. The shift is proportional to the distance from the centre of the micro array [52] hence the effects of this distortion are larger on the sub images at the edges of the raw data sub images array. These result misaligned with respect to the regular square grid of the micro lens array. With reference to figure 4.2:

$$\frac{x}{z+a} = \frac{x'}{b} \quad (4.2)$$

Therefore each lens let is shifted of a quantity:

$$x' = \frac{xb}{z+a} \quad (4.3)$$

Since  $z \approx z + a$  the centres of each sub image are shifted of a quantity equal to:

$$x' = x \frac{b}{z} \quad (4.4)$$

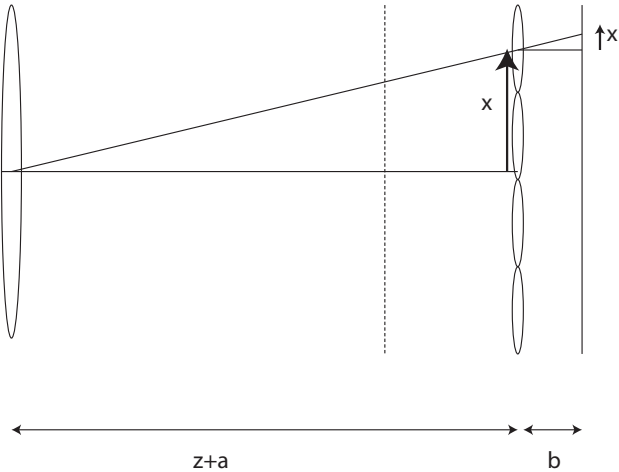


Figure 4.2: Relation between the position of the centre of a lens let  $x$  and the position of the centre of the correspondent sub image  $x + x'$ .

In figure 4.2  $x$  is the position of the centre of a micro lens and its corresponding sub image will be shifted of a quantity  $x'$ : on the distance of the image plane from the main lens  $z$  and the distance of the sensor form the micro lens  $b$ . Once the centres of the sub images have been localized it is possible to extract each sub image of them from the raw data and perform the rendering.

### 4.1.2 Basic Rendering

This section will describe how the basic rendering algorithm works as seen in section 1.8 and as described by Georgiev and Lumsdaine [3, 35]. The raw image on the sensor plane is an image of the main lens image plane [3]. Each sub image represents a single point of view of an area of the main lens image plane. Referring to figure 4.3, if the micro array is composed by  $N$   $x$   $N$  lens lets, the raw sensor image will be composed by an  $N$  by  $N$  array of sub-images. Each sub-image has a dimension of  $P \times P$  where  $P$  is the micro

lens pitch.

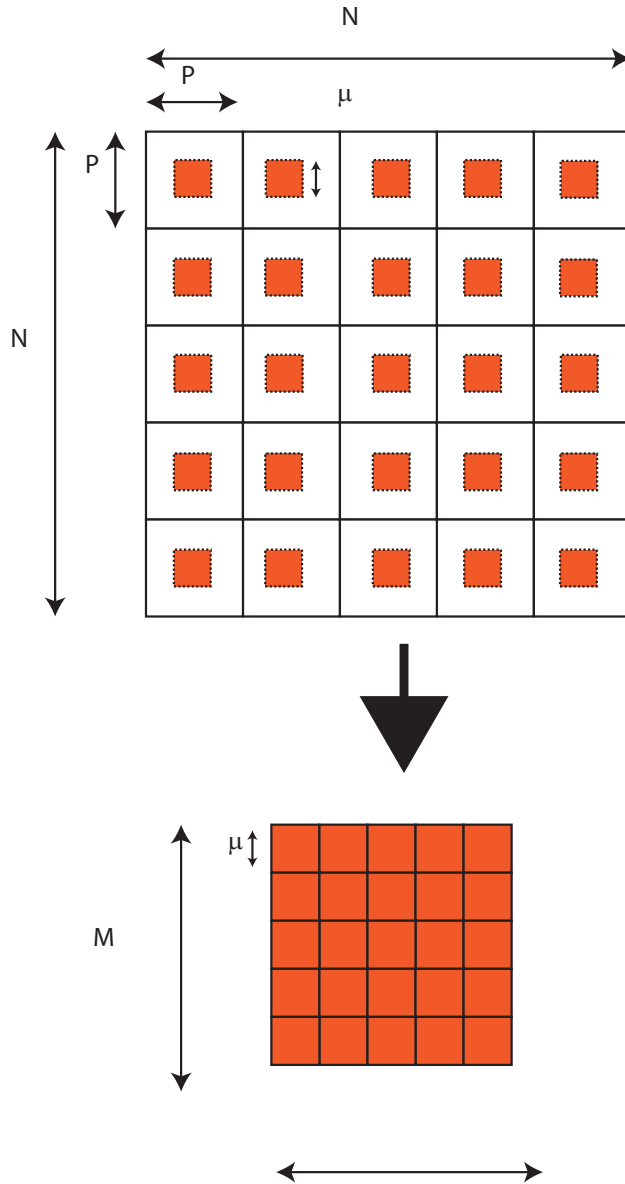


Figure 4.3: Basic rendering algorithm. The Rendered image is composed tiling together patches extracted by each sub image. The patch size is dependent by the magnification of the micro array stage.

The magnification of the micro array is  $m=b/a$  and each micro lens maps the main lens image on the sensor plane on a sub image magnified of a quan-

tity  $m$ . Therefore from each sub image a patch is selected with a dimension equal to:

$$\mu = P \frac{b}{a} = Pm \quad (4.5)$$

The patch size depends on the magnification of the lens lets array. The next section will be shown how this fact can be used to recover depth information from the raw sensor images.

### 4.1.3 Depth based rendering

The patch size  $\mu$  as seen in equation 4.5 depends on the magnification of the micro array stage. If the point imaged is out of focus, its image will be formed on a different plane that is not the main lens image plane. Hence the main lens image will be blurred and so will be the sub images on the sensor. If during the rendering process is taken into account that a point at a different depth with respect to the main lens focal plane will be imaged at a different distance from the micro lens array, it is possible to define a new value of magnification  $m'$  to which will correspond a new patch size  $\mu'$ . With reference to figure 4.4, the points that belong to the plane shown represented by the dashed red line placed at a distance  $d$  from the object plane, will be imaged on a plane in between the main lens and the main lens image plane. It is possible to define a virtual micro array stage with respect to this plane for which its points will be imaged in focused on a virtual sensor plane. The parameters characterizing the virtual micro array stage are the distances  $a'$  and  $b'$  and a magnification  $m' = b'/a'$ .

Copernican Configuration

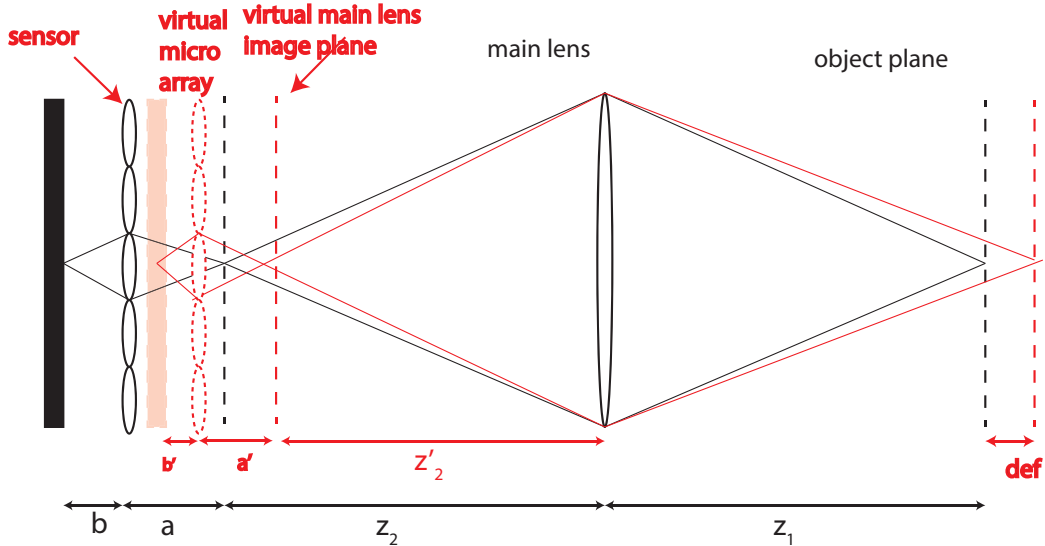


Figure 4.4: The points that belongs to the object plane represented in red are imaged on a virtual main lens image plane. This plane is relayed on a virtual sensor plane by a virtual micro array whose parameters are  $a'$  and  $b'$  and  $m' = b'/a'$ .

The distance between the main lens image plane and the virtual main lens image plane, defined as  $\alpha = a - a'$ , is called virtual depth [59]. It is linked to the actual defocus of the object plane by the lens law referred to the main lens. The magnification of the virtual lens let array defines the patch size to use to rendered the point at that particular depth. The link between the magnification  $m'$  and  $m$  can be defined by applying twice the lens law, once for the main lens and once for the micro array stage. Therefore the virtual main lens plane corresponding to a defocus  $d$  is located at:

$$z'_2 = \frac{(z_1 + d)f}{(z_1 + d) + f} \quad (4.6)$$

$f$  is the focal length of the main lens. The corresponding virtual depth value

is given subtracting the quantities  $z'_2$  and  $z_2$

$$\alpha = z'_2 - z_2 \quad (4.7)$$

Then from the virtual depth  $\alpha$  the values  $a'$  and  $b'$  for the virtual micro array can be obtained.

$$\begin{cases} a' = a - \alpha \\ b' = \frac{a'f}{a' + f} \end{cases} \quad (4.8)$$

And the magnification for the virtual plane is:

$$m' = \frac{b'}{a'} \quad (4.9)$$

Values of the magnification  $m'$  plotted as a function of defocus are shown in figure 4.5

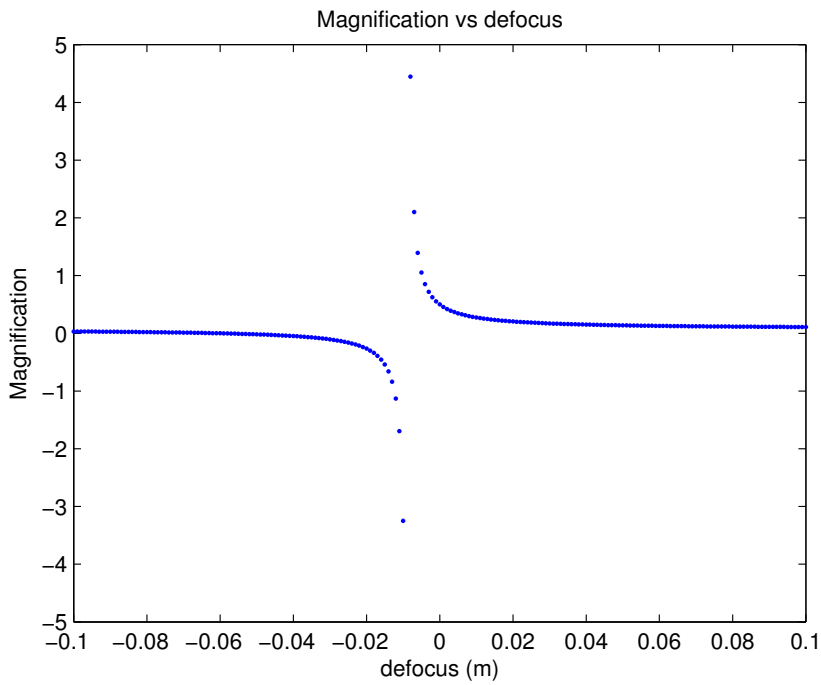


Figure 4.5: .

The patch size corresponding to the new focal plane is therefore:

$$\mu' = Pm' = P \frac{b'}{a'} \quad (4.10)$$

Rendering with the new patch size allows to refocus at a different plane. If the defocus is not known, as it happens in the majority of the cases, is it possible to estimate the depth information of the scene imaged and using this information to render the final image. This algorithms are based on cross correlating each sub image with its closest neighbours in order to evaluate the relative shift due to a change in depth across the lens let[60, 61]. In this way it is possible to determine the patch size that results in the best match with all of its neighbours [3, 34]. The axial resolution of a plenoptic 2.0 system is determined by considering that the minimum shift between neighbouring lens lets is the one equal to one pixel.

## 4.2 Description of the system

The system simulated is shown in figure 4.6. The main lens is in a 2f configuration, therefore  $z_1 = z_2 = z$ .

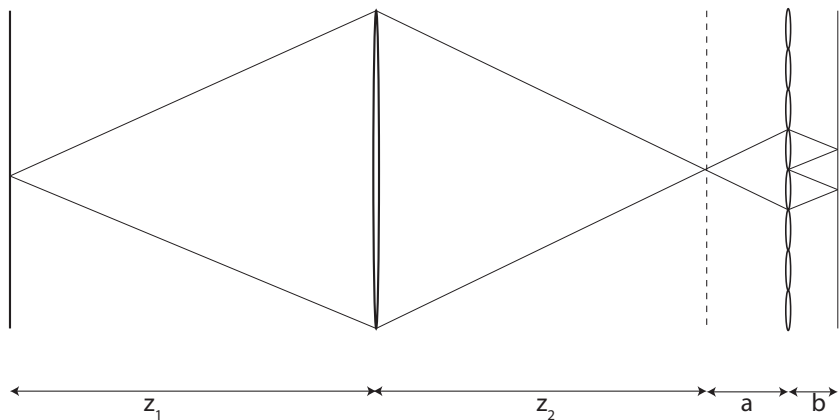


Figure 4.6: Ray diagram of the system simulated.

The main objective of the simulation on a plenoptic 2.0 system was to investigate its behaviour at diffraction limit as well as to better understand the trade-offs in resolution and how the different parameters of the systems affects it. Different combinations of the optical parameters of the system, including main lens aperture, micro array pitch and magnification, have been tested. The modularity of the Fresnel simulation toolbox allows to easily change the simulation parameters independently and collect results. The system parameters are defined; these are the dimension and the number of pixel on the sensor, the pitch and focal length of the lens let array, the focal length of the main lens and the magnification  $m$  aof the micro array stage. The the simulation toolbox is capable of automatically setting all other simulation parameters to respect the f-number matching between the main lens and the lens let array. In a plenoptic 2.0 imaging system the f-number is matched when:

$$\frac{z_2}{d} = \frac{b}{p} \quad (4.11)$$

If the lens let array has a focal length equal to  $f_\mu$  and a pitch equal to  $p$ , the value of the distance from the sensor  $b$  can is obtained by the magnification  $m$  as:

$$b = m f_\mu \left( 1 + \frac{1}{m} \right) \quad (4.12)$$

Equation 4.12 has been obtained substituting the expression of the magnification  $m = b/a$  into the lens equation  $1/a + 1/b = 1/f_\mu$ . Values of the parameter  $b$  as a function of the magnification can be seen plotted in figure 4.7

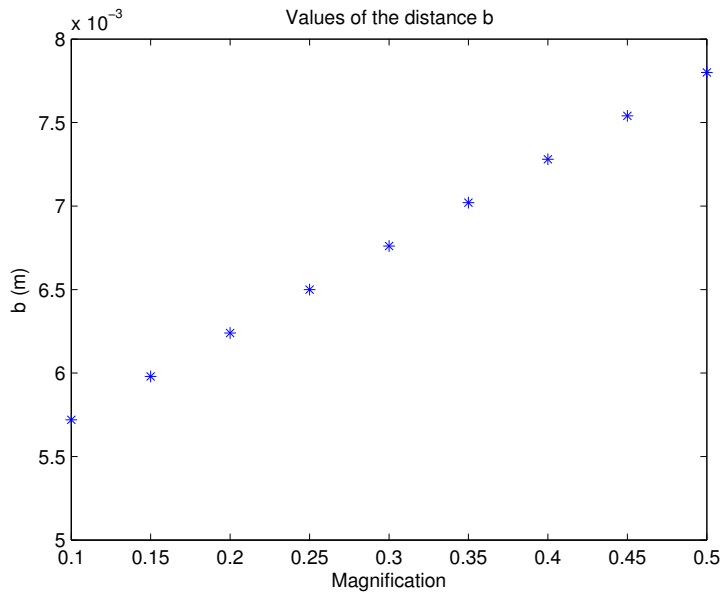


Figure 4.7: Values of the parameter  $b$  correspondent to values of magnification varying from 0.1 to 0.5.

Once  $b$  is defined the distance of the micro lens array from the main lens image is calculated by solving the lens law for  $a$ :

$$a = \frac{bf}{b-f} \quad (4.13)$$

Values of  $a$  as a function of the magnification can be seen in figure 4.8:

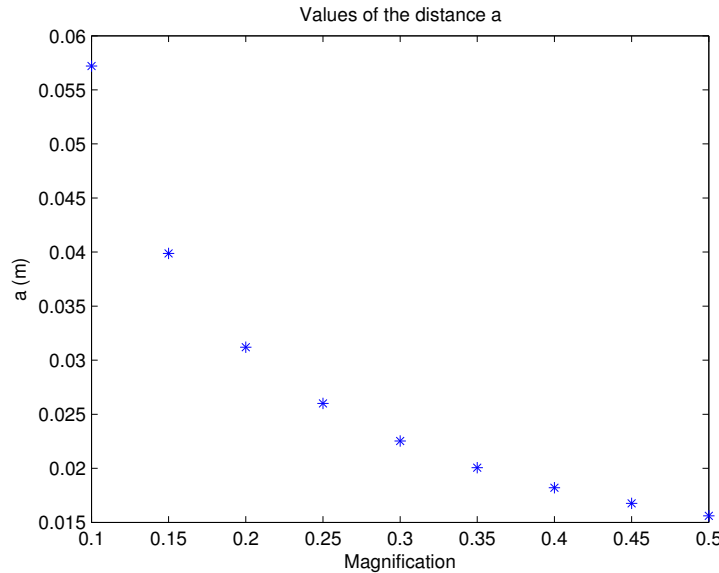


Figure 4.8: Values of the parameter  $b$  corresponding to values of magnification varying from 0.1 to 0.5.

Now that the relay system has been defined, the software defines the aperture of the main lens matching its f-number to the one of the lens let using equation 4.11. We have:

$$r_{lens} = \frac{zp}{2b} \quad (4.14)$$

Values of  $a$  as a function of the magnification can be seen in figure

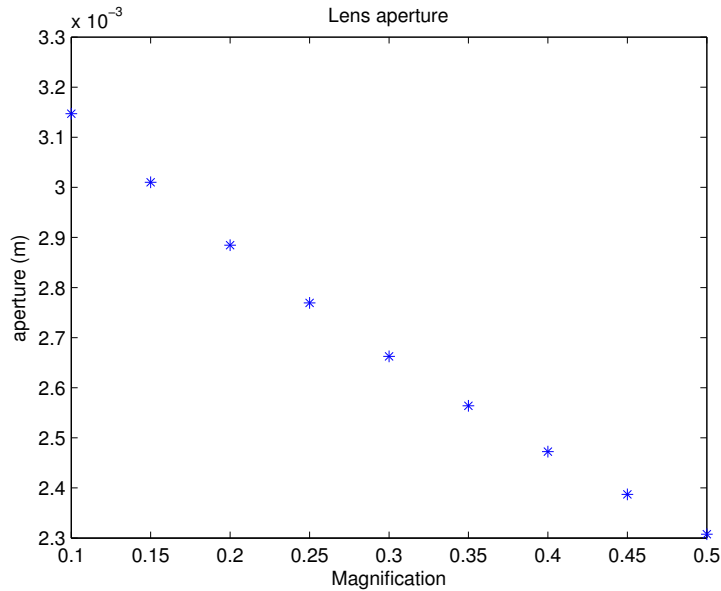


Figure 4.9: Aperture of the main lens as a function of the magnification in order to respect the f-number matching condition.

Therefore the simulation platform is able to set the simulations parameters when some other are given, making the launching procedure of each simulation easy and quick. We set the micro lens array with the following characteristic:

Array size	5.8 x 5.8 mm
Micro lens focal length $f_\mu$	5.3 mm
Micro array pitch p	150 $\mu m$
sensor size	5.8 x 5.8 mm
sensor resolution	3500 by 3500 pixel
pixel size	1.67 $\mu m$
number of lens let	39 x 39 lens lets
main lens focal length	60 mm

And the values obtained for  $a, b$  and the main lens aperture corresponding to the magnification investigated are:

Magnification	<i>a</i>	<i>b</i>	main lens aperture
0.5	15.6 mm	7.8 mm	2.3 mm
0.3	22.5 mm	6.8 mm	2.7 mm
0.25	26 mm	6.5 mm	2.8 mm

### 4.3 Optical performances of a focused plenoptic system

This section shows the results obtained running simulations of the system described in section 4.2 at its diffraction limit. Three different configurations of the micro lens array stage have been tested, corresponding to the parameters  $a$  and  $b$  set in order to have magnification  $m = b/a$  equal to 0.5, 0.3 and 0.25. The first simulation presented is the image of a single focused point source. A comparison between the main lens image and the rendered image will be done to understand the differences in optical resolution and to evaluate the noise induced by the rendering algorithm. The optical resolution of an imaging system is defined by its impulse response, known as point spread function [47, 52]. If the input is a point source in focus, the output image for an unaberrated circular aperture has a well known intensity profile, the Airy disk. The Airy disk defines the broadening that a point source undergo after being imaged by an optical system, hence it is a good estimation of the minimum feature resolvable by the system [47, 62]. The Airy disk is shown in figure 4.10. The position of the first zero of the Airy disk is given by:

$$x_1 = 1.22\lambda F_\# \quad (4.15)$$

and the total extension of the central lobe is defined as the distance between the first two zeros as:

$$\Delta x = 2.44\lambda F_{\#} = 2.44\lambda \frac{b}{p} \quad (4.16)$$

where  $\lambda$  is the wavelength of the radiation,  $b$  is the distance between the lens let and the sensor and  $p$  is the pitch of the micro array and the aperture of the single lens let. The central lobe contains the 90% of the total energy of the optical field, therefore its extension defines the spread that each point undergoes in the final image.

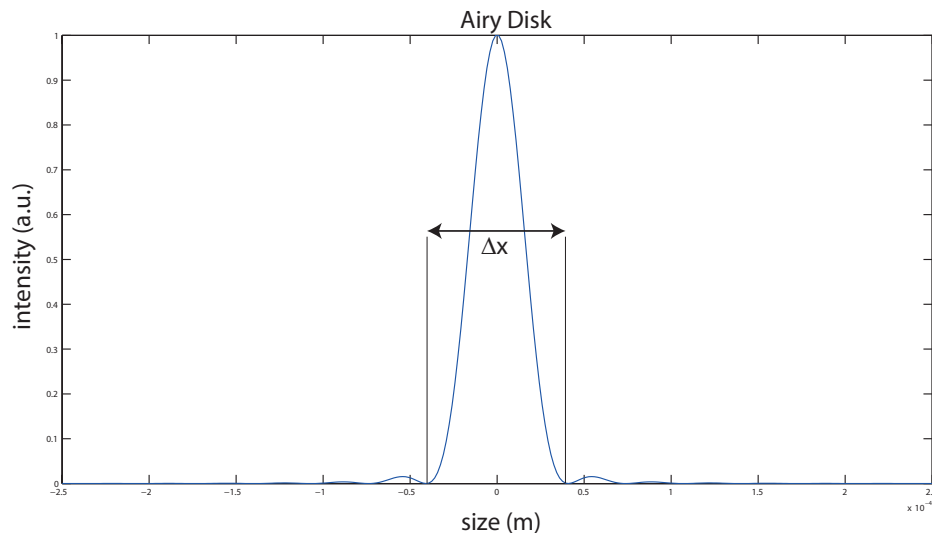


Figure 4.10: Aperture of the main lens as a function of the magnification in order to respect the f-number matching condition.

We define  $\Delta x$  is the optical resolution of the imaging system. In a plenoptic 2.0 system there are two elements that influence the optical resolution, the main lens and the micro lens array. Because of the f-number matching condition, the optical resolution in the two imaging stages should be the same. But because of the magnification present in the micro array stage,

which is different from the magnification of the main lens, the coordinates in the main lens image plane are rescaled by a factor equal to the magnification  $m$  when imaged by the micro array on the sensor [47]. Using the coordinates  $x'$  and  $y'$  of the main lens image plane, the sub image coordinates will be given by:

$$\begin{cases} x = \frac{x'}{m} \\ y = \frac{y'}{m} \end{cases} \quad (4.17)$$

Therefore if a pixel on the main lens image samples a feature size of  $\delta x$ , on the sensor the same pixel will sample a quantity  $\delta x/m$ . Because  $m$  is smaller than 1, the spread of a point on the sensor plane will be bigger than the one on the main lens image plane. The same pixel samples a bigger area of the object in the image. This leads to a loss in optical resolution [20]. The smaller is the magnification, the broader becomes the point spread function and as a consequence the band pass of the micro lens array becomes narrower.

The optical cut off frequency is defined as:

$$\nu_{cutoff} = m \frac{1}{\lambda f_\#} = m \frac{b}{\lambda p} \quad (4.18)$$

Figure 4.11 shows the values of the lateral resolution plotted in function of the magnification of the micro array stage, while in figure 4.12 are plotted the correspondent values of the optical cut off frequency.

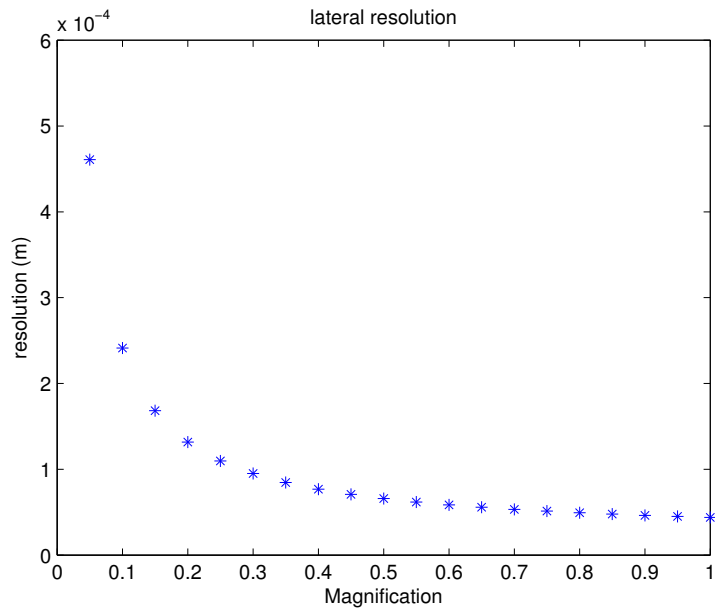


Figure 4.11: lateral resolution as a function of the magnification.

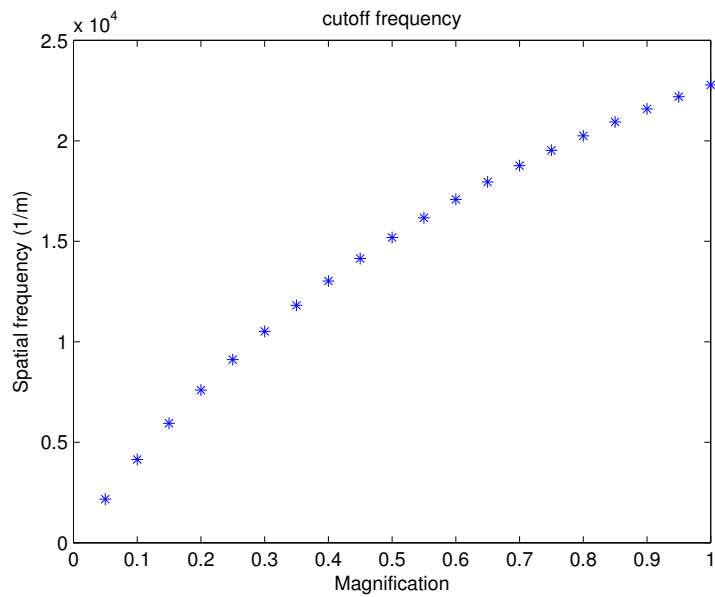


Figure 4.12: optical cut-off frequency as a function of the magnification.

This means that in a plenoptic 2.0 imaging system exists an intrinsic trade-off between optical resolution and spatio-angular resolution. The trade

off between spatial and angular resolution has been described in section 1.6. A further trade off is now present and is it due to diffraction. A low magnification allows to sample very well the direction and therefore to have a finer axial resolution when evaluating depth but a magnification too low will filter out high frequency components of the object. In the next sections will be investigate in detail the optical performances of a focused plenoptic system, performing simulations to better understand the trade off between spatio-angular resolution and optical resolution. This is the first attempt of evaluating the effects of the optical parameters of a focused plenoptic system on the the optical resolution using a wave optics approach.

## 4.4 Impulse response of a Focused Plenoptic system

The first simulation performed was designed to obtain the impulse response of a focused plenoptic system. The point source has been simulated using a pupil with a diameter of  $10 \mu m$ . As explained in section 4.1, the magnification gives the number of points of view that sample an image. To have directional information, a point of the object should be sampled at least by two point of view, therefore by two lets. In this way two set of directional coordinates are captured and on the sensor and each point repeated four times on the raw image, two times horizontally and two vertically. With a magnification of 0.5, the sub images will be 2 per direction, with a magnification of 0.3 each point is expected to be replicated 3 times, and with a magnification of 0.25 four times. Figures 4.13 , 4.14 , and 4.15 show the raw sensor images and the rendered images of a point source when the magnification is 0.5, 0.3 and

0.25.

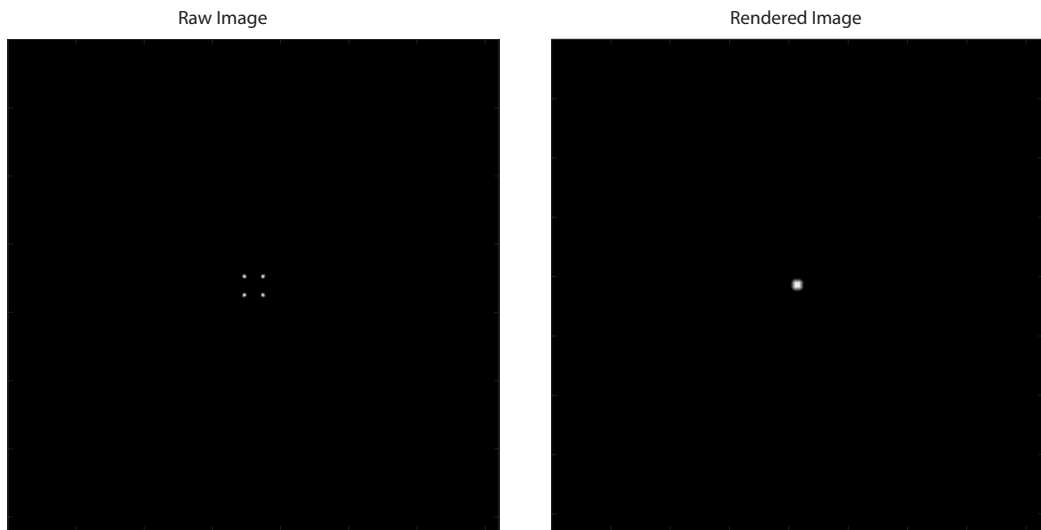


Figure 4.13: Left: raw sensor image, Right: rendered image. Artifacts are present. Magnification: 0.5

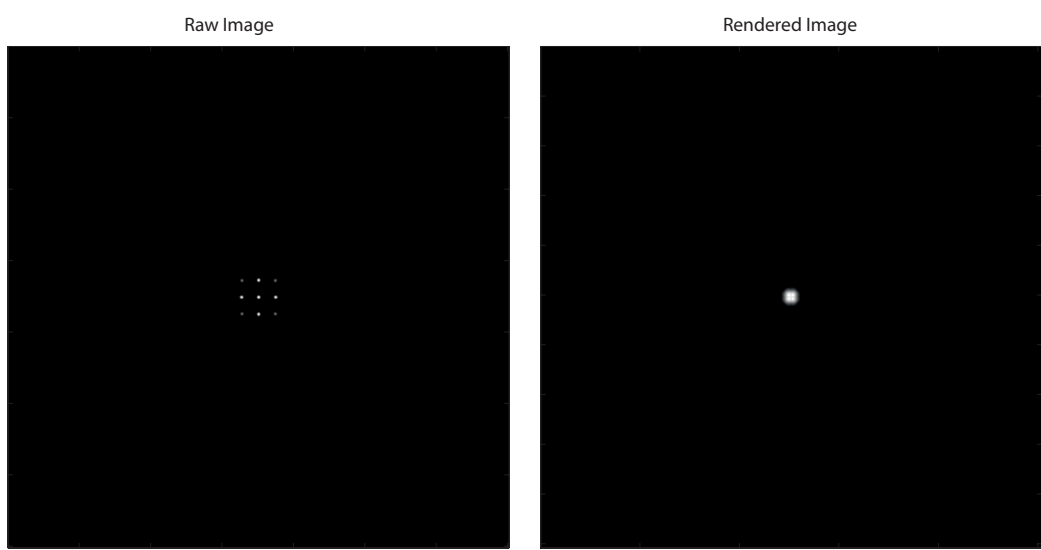


Figure 4.14: Left: raw sensor image, Right: rendered image. Artifacts are present. Magnification: 0.3.

#### 4.4. IMPULSE RESPONSE OF A FOCUSED PLENOPTIC SYSTEM 165

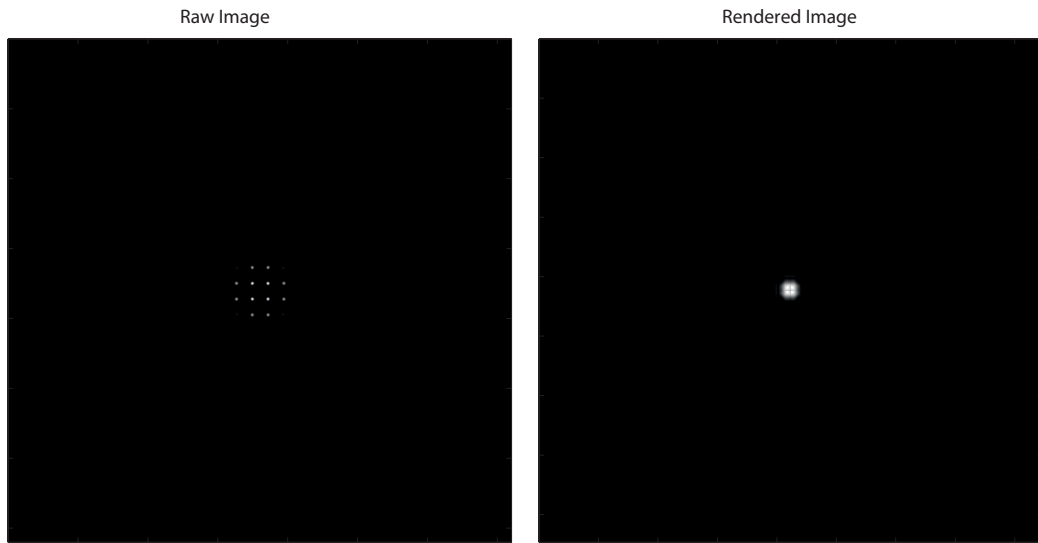


Figure 4.15: Left: raw sensor image, Right: rendered image. Artefacts are present. Magnification: 0.25

Figure 4.16 shows the intensity profiles of the main lens image and of the rendered images. The profiles are obtained by sum all the rows of the matrix of the image and normalizing by its.

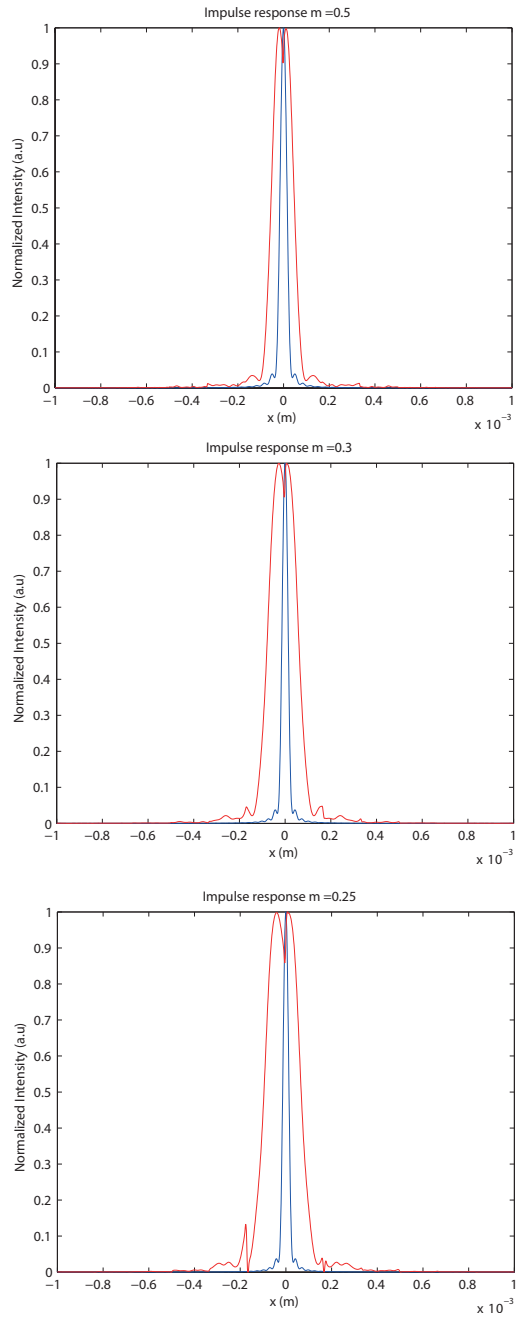


Figure 4.16: From top to bottom: comparison between the main lens image profile, in blue, and the rendered image profile, in red, for magnification values of 0.5, 0.3 and 0.25. The central lobe of the rendered image increase with the magnification, as well as the number of artefacts.

From figure 4.16 it is possible to appreciate the broadening effects of the central lobe of the rendered image intensity profile, in red, with respect to the main lens image. The central lobe size is also dependent on the magnification used as seen in figure 4.11. With a small magnification, the number of sub images that sample a single point source increase, and due to the nature of the rendering process explained in section 4.1.2, the number of artefacts increases, broadening the central lobe and making the lateral resolution worse. Table 4.4 shows the values of the central lobe size of the main lens image,  $\Delta x$ , of the rendered image  $\Delta x'$  and the ratio between them. Error in the ratio is due to the presence of artefacts generated by the rendering algorithm that increases with the decrease of the magnification.

Magnification	$\Delta x$ (m)	$\Delta x'$ (m)	$\Delta x/\Delta x'$
0.5	$7.848 \times 10^{-5}$	$2 \times 10^{-4}$	0.392
0.3	$6.848 \times 10^{-5}$	$2.698 \times 10^{-4}$	0.25
0.25	$6.514 \times 10^{-5}$	$3.574 \times 10^{-4}$	0.18

## 4.5 Two point resolution

Another important instrument to evaluate the resolution of an imaging system is the Rayleigh criterion of resolution. It states that two incoherent point sources are resolved by a diffraction limited imaging system when the centre of the Airy disk intensity pattern generated by one point source falls exactly on the first zero of the Airy disk generated by the other point source [47]. The Rayleigh criterion of resolution states that for two point source of light whose relative phase differs for  $\pi/2$  the minimum distance to resolve them

both in the image plane is given by:

$$\delta x = 1.22\lambda \frac{z}{d} \quad (4.19)$$

Where  $d$  is the lens aperture and  $z$  is the propagation distance. In the simulation the two point sources were placed at distance equal to the Rayleigh distance and they have been imaged by a plenoptic 2.0 system where the micro lens array had a magnification of 0.5. The purpose of this experiment is to prove that the magnification of the micro lenses gives a limits the optical resolution of the system. Figure 4.17 shows the main lens image and the rendered image with their respective intensity profiles, of two point source with a diameter of  $10 \mu m$  separated by a distance  $\delta x = 40\mu m$ . The imaging system simulated is the same described in section 4.2.

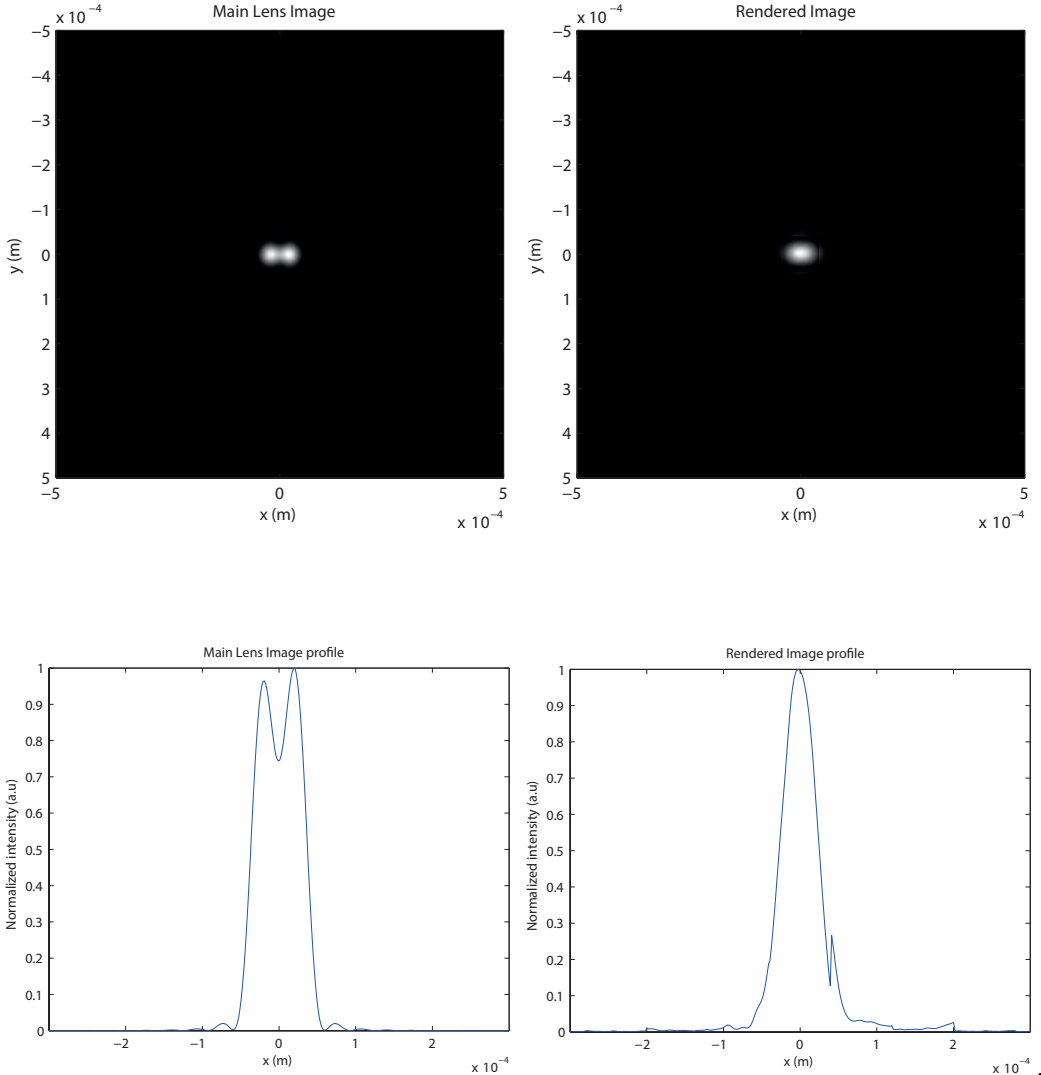


Figure 4.17: On the top left there is the main lens image of two point sources separated by the Rayleigh distance  $\delta x$ . On the top right its corresponded rendered plenoptic image obtained with a magnification of 0.5. As expected from the theory, the resolution of the rendered image is half the one of the main lens image, and the two points are no more distinguishable as confirmed by the intensity profiles of the two images on the bottom.

While in the main lens image the two point sources are at the limit of resolution and the two points are still resolvable, in the rendered image the two spot sizes are merged together and no longer resolvable. If the

separation between the point sources is doubled in the object plane they should be resolve in the rendered image too while keeping the magnification 0.5. Figure 4.18 shows the simulations results for a  $\delta x = 80\mu m$ :

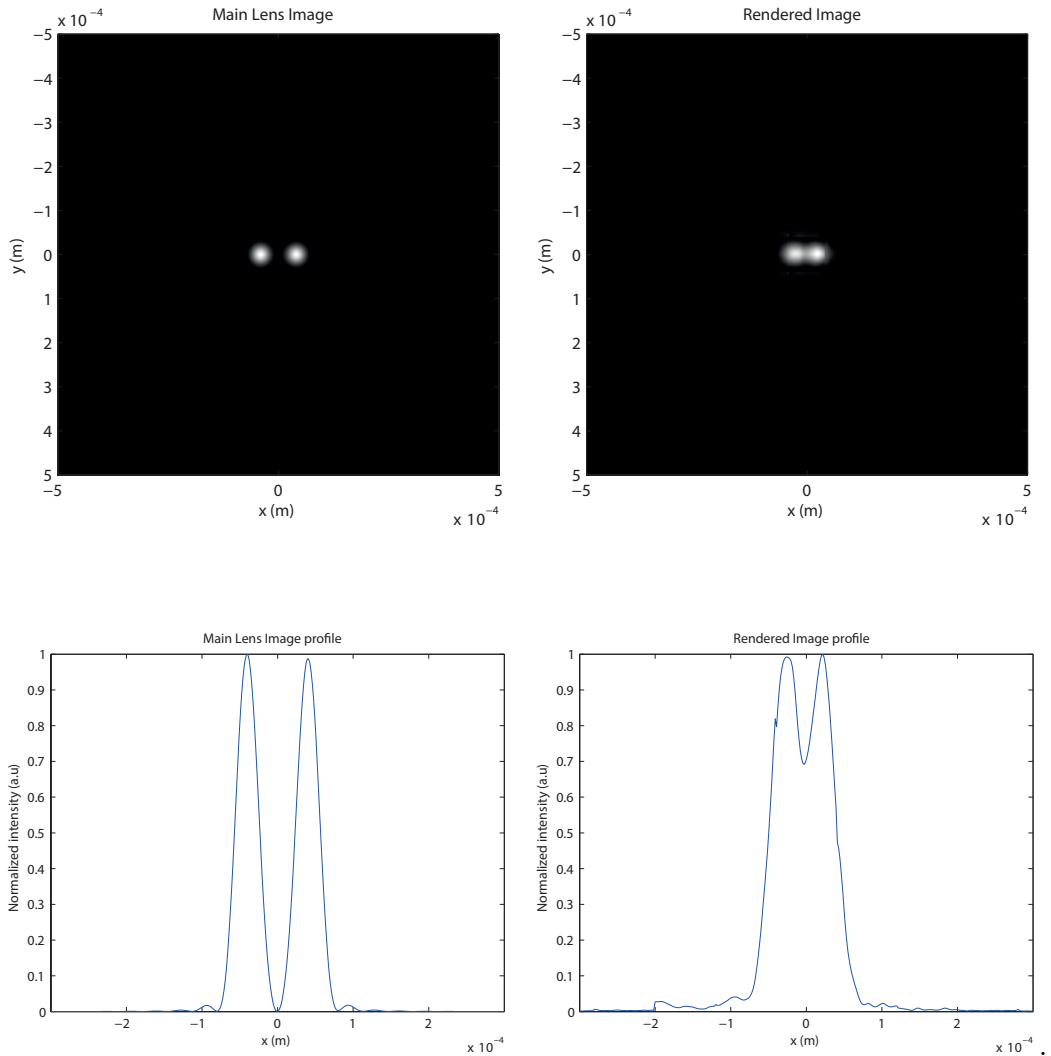


Figure 4.18: The image on the top left shows the main lens image of two point sources separated by the Rayleigh distance  $2\delta x$ . On the top right there is its corresponded rendered plenoptic image obtained with a magnification of 0.5. Doubling the Rayleigh distance the rendered image is at the limit of resolution, where the maximum of the Airy pattern of one point falls on the first zero of the second point.

This results obtained simulating wave optics propagation in the plenoptic imaging system confirm the predictions made in section 4.3 and it is the first experiment of this kind. When imaging an object with a plenoptic 2.0 system the loss of resolution due to the magnification should be taken into account in order not to lose useful information in the sample, or a suitable lens let array configuration should be chosen.

## 4.6 Frequency analysis of a focused plenoptic system

This section will describe the frequency response of a focused plenoptic system and its dependency on the magnification of the lens let array stage. The spatial frequencies that are transferred from the object to the image plane in an optical system are defined by its modulation transfer function (MTF). The MTF is defined as the square modulus of the Fourier transform of the impulse response  $h(x,y)$  of an optical system [47].

It is then:

$$H(f_x, f_y) = |\mathcal{F}\{h(x, y)\}| \quad (4.20)$$

It represents the weighting factor applied by the system to all the frequency components of the optical field coming from the object. The visibility and the contrast of the points corresponding to the different values of spatial frequency changes according to the modulation imposed by the MTF. When it goes to zero, no energy is transmitted for that particular frequency and the detail is no longer present in the image. The value of spatial frequency for which the MTF goes to zero is called optical cut-off frequency. In this section

the effects of the magnification on the location of optical cut-off frequency is investigated. The first result presented is obtained by calculating the modulation transfer function of the plenoptic 2.0 system described in section 4.4, with magnification values of 0.5, 0.3 and 0.25. The MTF for these three cases are shown in figure ??, ?? and ?? and have been obtained applying equation 4.20 to the intensity profiles in figure 4.16. In all the three figures, in green is shown MTF of the single lens imaging system, without the lenslet array stage, and in red the MTF of the plenoptic system.

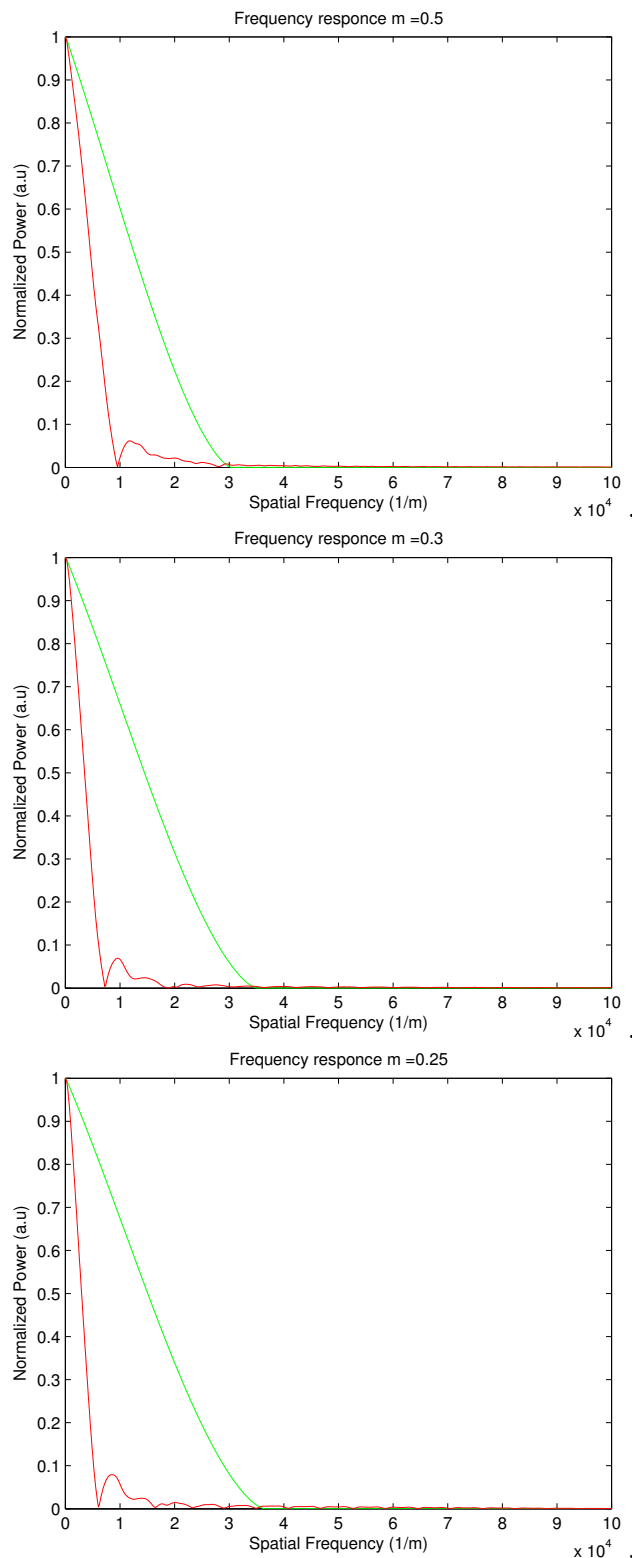


Figure 4.19: Modulation transfer functions of the main lens (green) and the overall imaging system (red) for a magnification value of  $m = 0.5$ , top,  $m = 0.3$ , central, and  $m = 0.25$ , bottom.

From figure 4.19 it is possible to see that the cut off frequency of the single lens system increases with the decreasing of the magnification, while the cut-off frequency decrease with the decreasing of the magnification if the lens let array stage is added. This result is in accord with what seen in sections 4.3 and is a direct consequence of the simulations results shown in section 4.4. The magnification of the micro lens array reduces the optical resolution. this is a direct consequence of the intrinsic trade-of between optical resolution and the spatio-angular resolution. While reducing the magnification of the micro array stage increase the number of directional samples, at the same time makes the optical bandwidth narrower, reducing the lateral resolution. The decrease in the optical cut-off frequency is directly proportional to the decrease of the magnification as predicted in the theory with equation 4.18 and proved by the numerical simulation. This effect will be observed in the images obtained by the real system described in chapter 4). The values of the cut-off frequencies obtained by the simulations are:

Magnification	Rendered $f_{cut-off} m^{-1}$	Main lens $f_{cut-off} m^{-1}$
0.5	$1.00 \times 10^4$	$3.00 \times 10^4$
0.3	$0.76 \times 10^4$	$3.50 \times 10^4$
0.25	$0.63 \times 10^4$	$3.60 \times 10^4$

The second set of simulations done evaluates the effects of the magnification in more detail. A varying frequency sinusoidal grating is imaged incoherently, as explained in chapter 2, by the system with the same three different configurations of the micro array stage. The Grating contains five different frequencies :

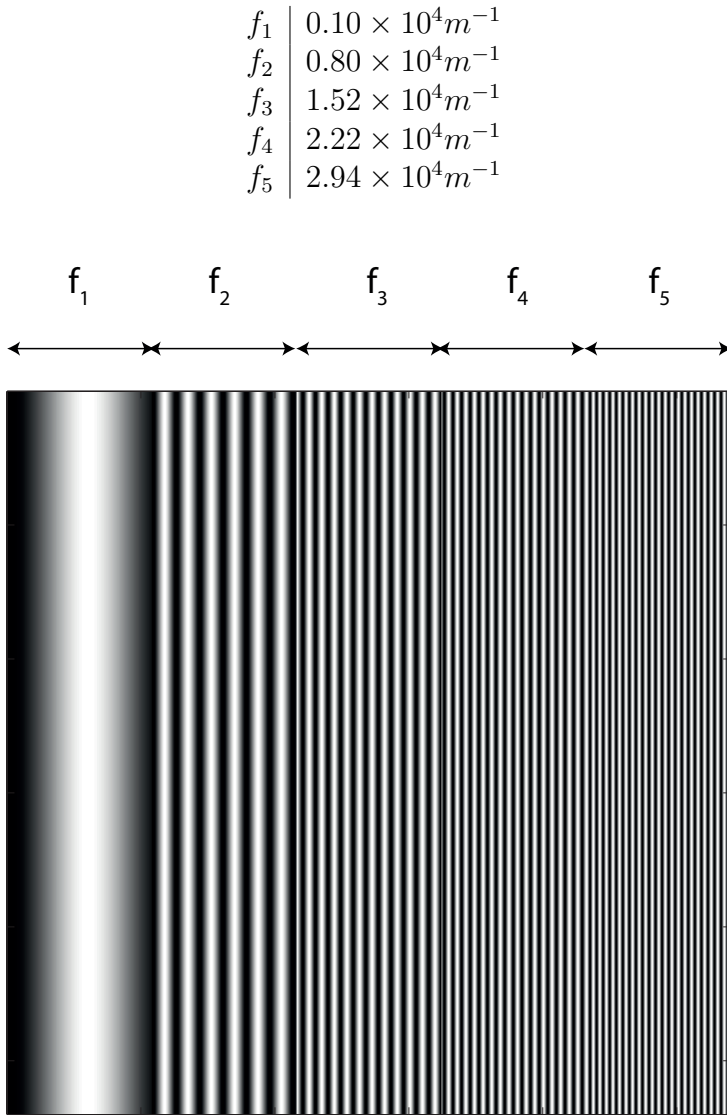


Figure 4.20: The object imaged in this simulation is a sinusoidal grating containing five different frequencies.

Figure 4.21 shows the raw image, the main lens image and rendered images of the sinusoidal grating shown in figure 4.20, imaged with a magnification of  $m = 0.5$ . The two rendered images are obtained with the basic rendering explained in section 4.1. To remove digital artefacts given by the tiling of the sub images patches on the rendered images a low pass Gaussian filter with

$\sigma = 1.162 \times 10^4$  has been applied.

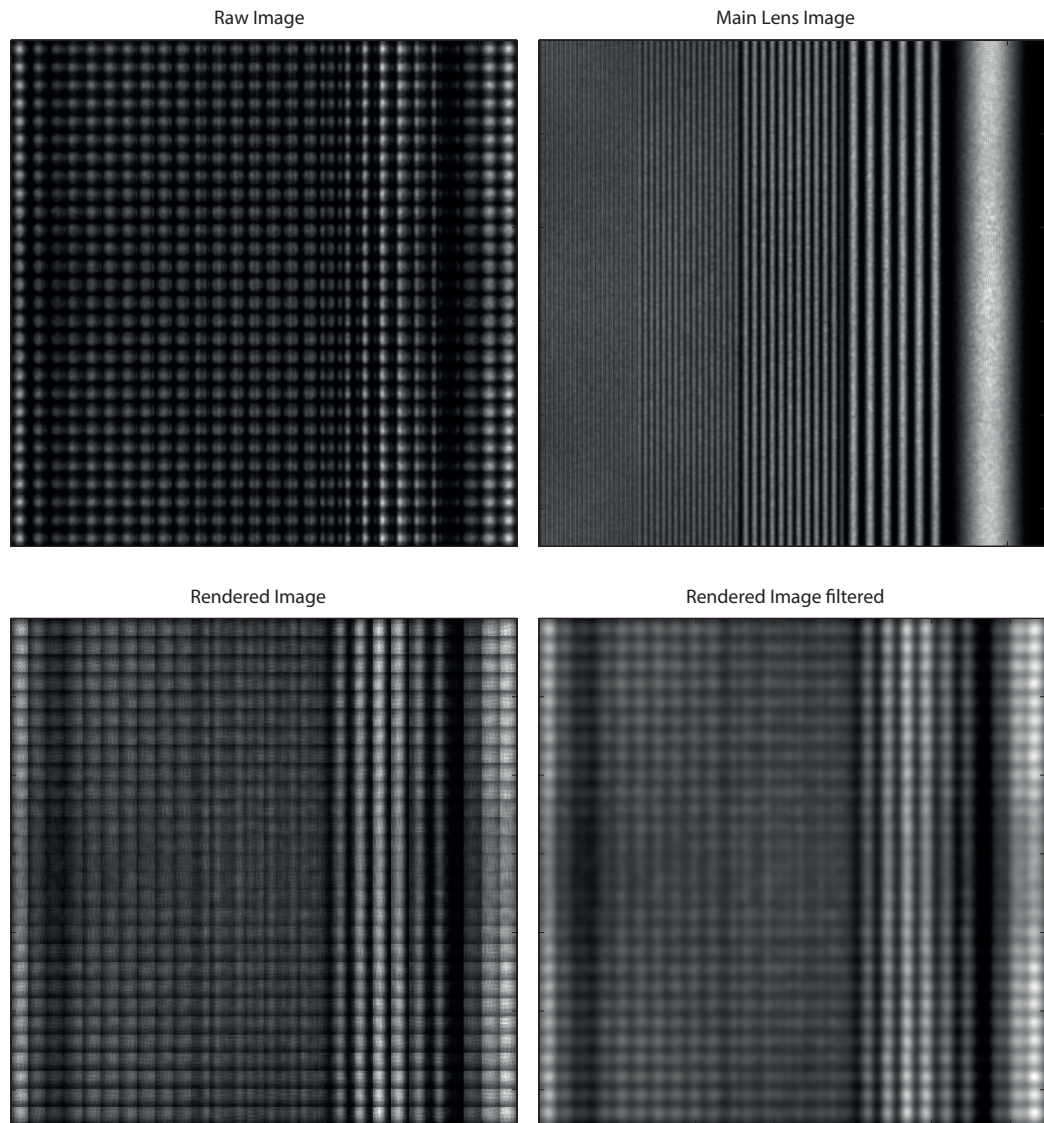


Figure 4.21: Top: on the left it is shown the raw sensor image, on the right the main lens image. Bottom: On the left there is the rendered image, on the right the same image has been low pass filtered to remove some of the rendering artefacts. Magnification was 0.5

The normalized intensity profile of the optical field at the main lens image plane compared with the intensity profile of the rendered image is shown in

figure 4.22 on the left side while on the right the power spectra of the main lens image and of the rendered image is presented. The modulation transfer function of the main lens and of the full plenoptic system has been added in red.

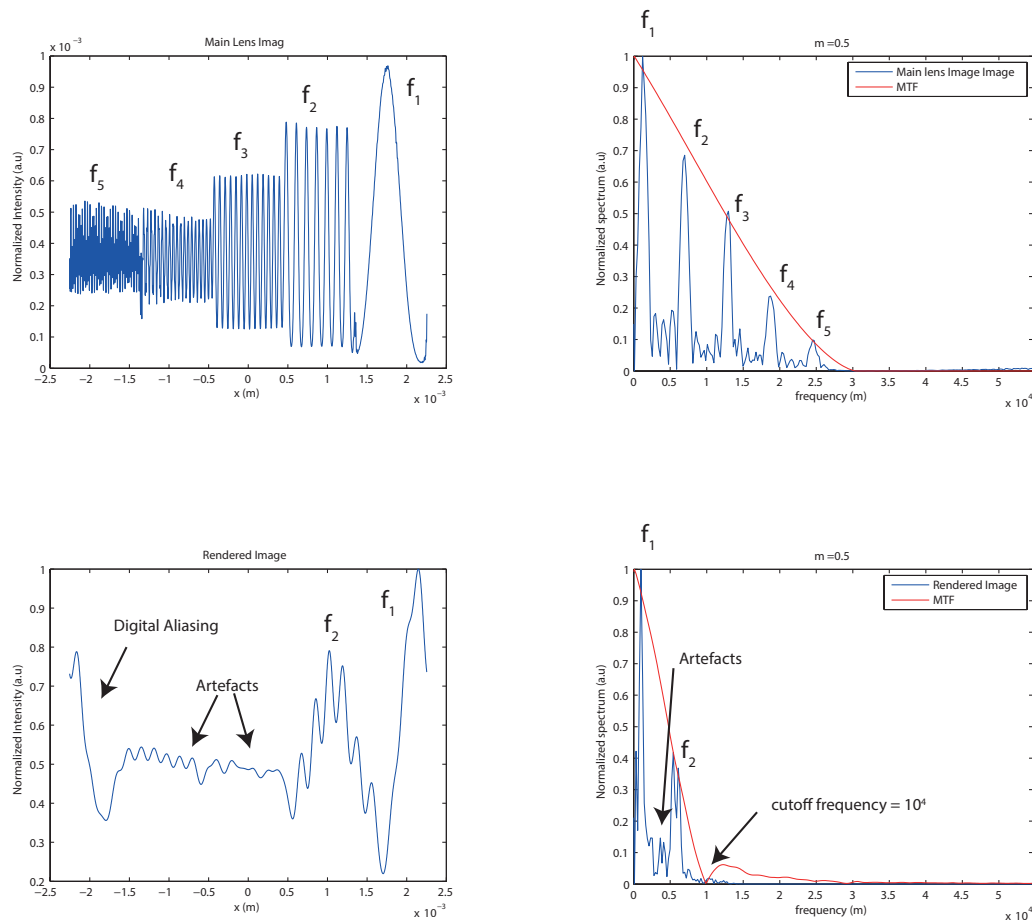


Figure 4.22: On the left: intensity profiles of the main lens image, top and of the rendered image, bottom. On the right the spatial frequencies modulated according to the MTF as shown by the power spectra of the main lens image on the top right and of the rendered image on the bottom right. The magnification of the lens let array is  $m = 0,5$  and cut-off frequency of the system is  $f_{cut-off} = 10^4 m - 1$

As expected the amplitude of the oscillations in both the main lens image and the rendered image follow the profile of the modulation transfer function of the two stages. Not all the frequency components of the object field are transmitted through the different stages of the plenoptic imaging system. In fact it acts as a low pass filter, whose bandwidth depends on the magnification used in the lens let array stage. The low pass filtering action is shown in figure 4.23.

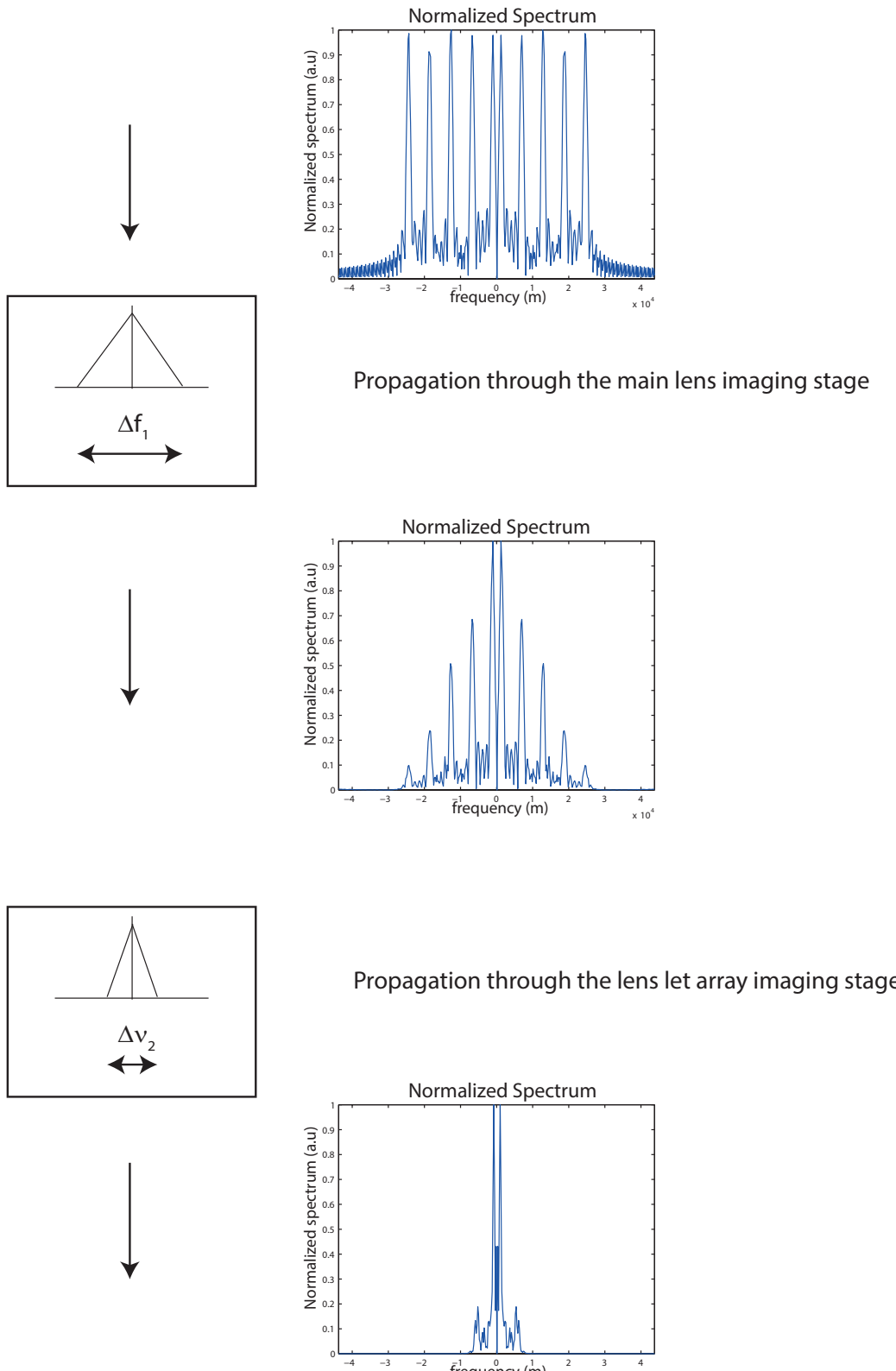


Figure 4.23: Evolution of the spectrum of the optical field as it propagates through the imaging system. First step the field is propagated through the main lens and its frequency content is modulated by its MTF whose bandwidth is  $\Delta\nu_1$ . Then modulated field passes through the lens let array stage and because of the magnification that is less than zero its bandwidth is reduced further to  $\Delta\nu_2$ . Since  $\nu_1 > \nu_2$  the imaging system is modelled as a linear low pass filter with a bandwidth  $\Delta\nu_1$  defined by the magnification of

It is interesting to see also that in the rendered image presents some artefacts which are responsible for some extra frequencies present in the spectrum of the output rendered image. The cut off frequency of the imaging system with a magnification equal to 0.5, is  $10^4/m$ , therefore only the first two frequencies will be transmitted to the rendered image, as shown in figure 4.22. If the magnification drops to  $m = 0.3$  the bandwidth of the system gets narrower, and fewer frequencies are transmitted in the rendered image. Figure 4.24 shows the raw image, the main lens image and rendered images of the sinusoidal grating shown in figure 4.20

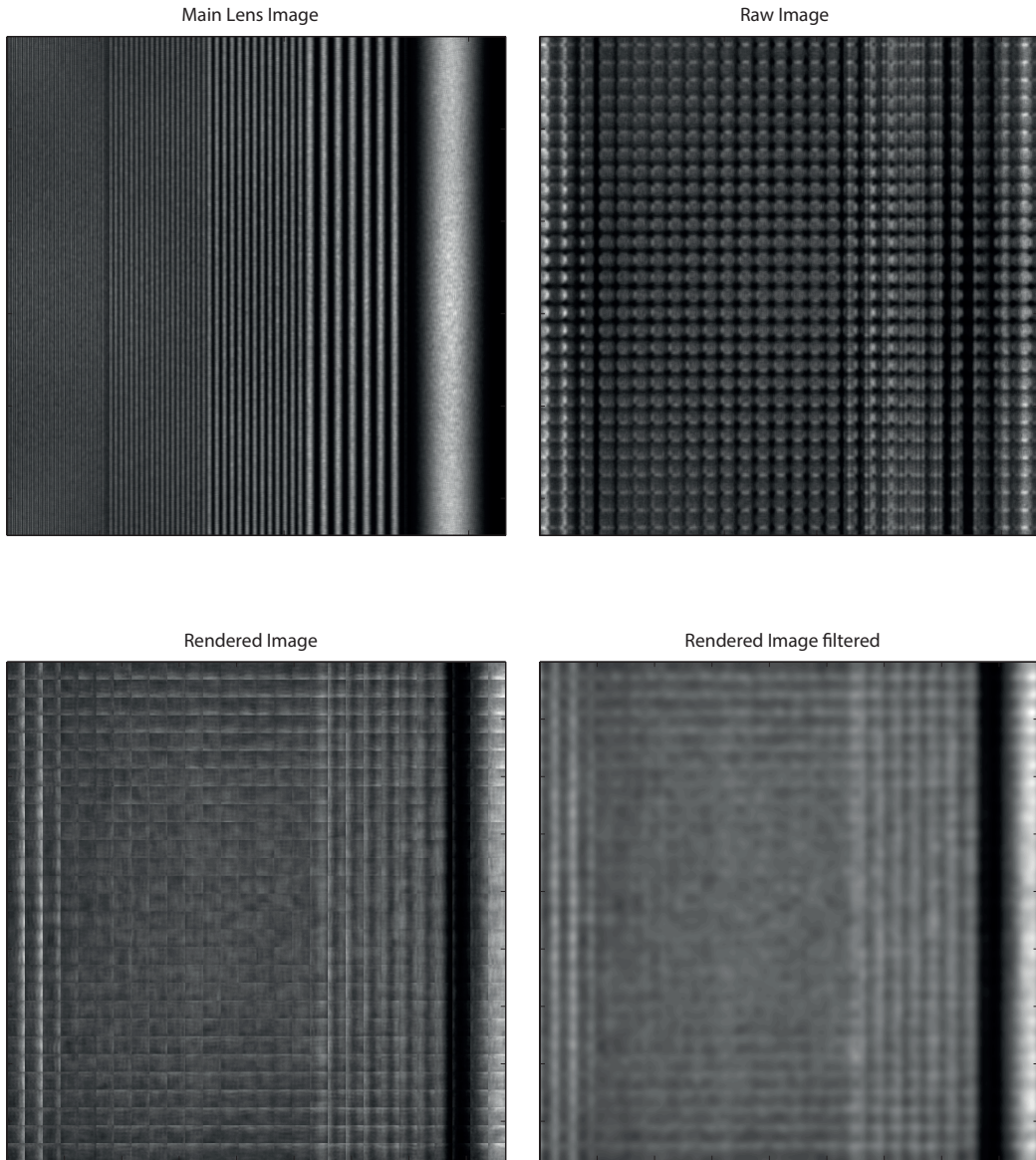


Figure 4.24: Top: on the left it is shown the raw sensor image, on the right the main lens image. Bottom: On the left there is the rendered image, on the right the same image has been low pass filtered to remove some of the rendering artefacts. Magnification was 0.3.

As for the previous case 4.25 shows a comparison of the intensity profile of the main lens image with the rendered image one and of their respective power spectra:

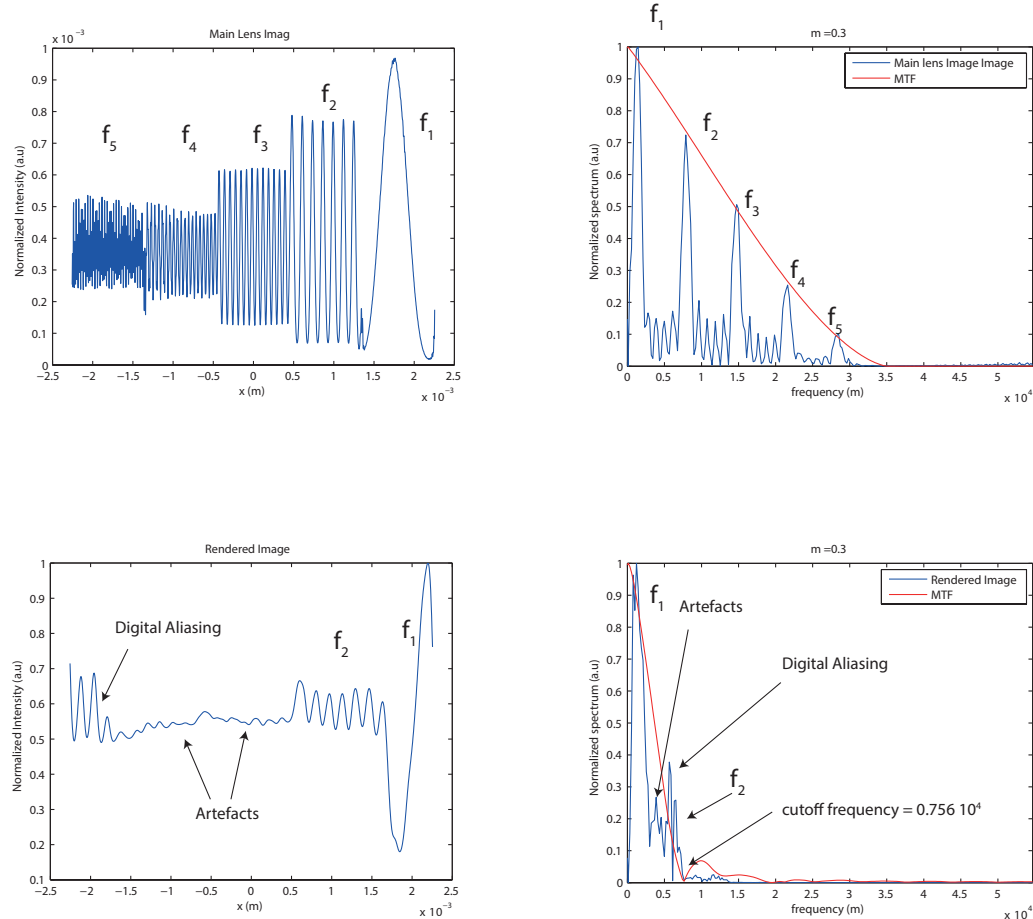


Figure 4.25: On the left: intensity profiles of the main lens image, top and of the rendered image, bottom. On the right: spatial frequency modulation done by MTF. The cut-off frequency of the system is  $0.756 \times 10^4 \text{ m}^{-1}$

From figure 4.25 can be seen that the frequency  $f_2$  gets attenuated more respect the previous case because it is closer to the cut-off frequency of the system. The spectrum of the rendered image allows to discriminate between frequencies due to artefacts and digital aliasing in the rendering process. Their frequency is smaller than the one predicted by the modulation transfer function for that location in the rendered image. These frequencies are

indicated in figure 4.25 with an arrow as artefacts. Low frequencies components generated by digital aliasing in the main lens image, have been picked up by the micro array relay stage and transmitted to the rendered image as indicated in figure 4.25. This effects can be seen in detail in figure 4.26:

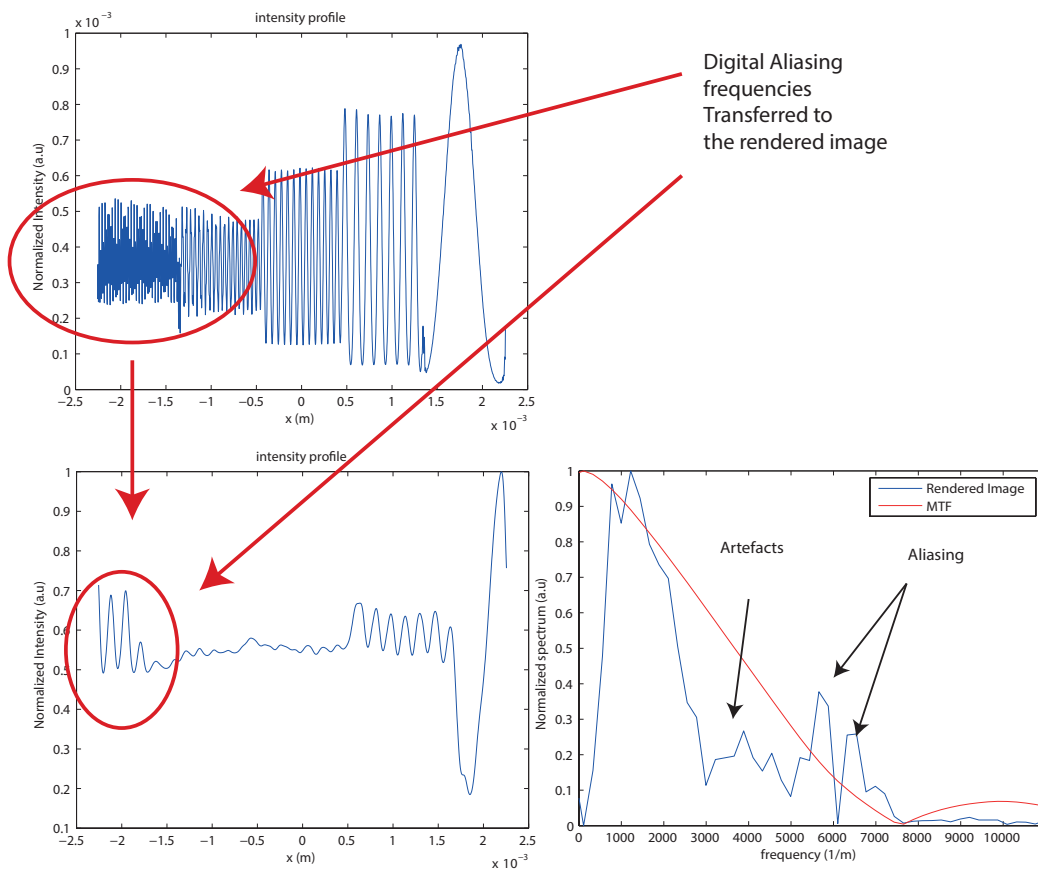


Figure 4.26: Aliased frequencies transmitted to the rendered image.

If the magnification is  $0.25$  the situation becomes the one in figure 4.27 and figure 4.28.

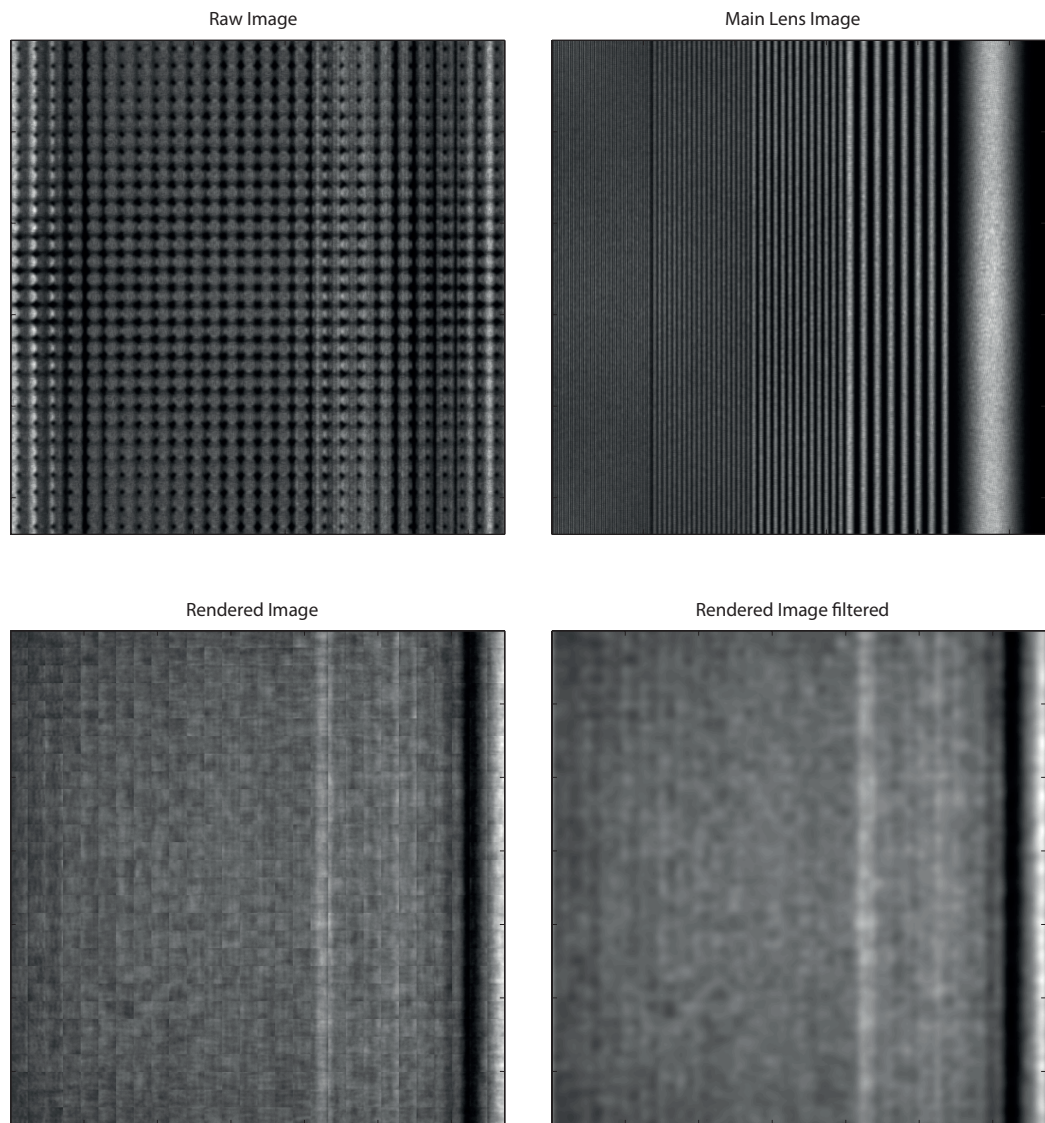


Figure 4.27: Top: raw sensor image, on the right the main lens image. Bottom: On the left there is the rendered image, on the right the same image has been low pass filtered to remove some of the rendering artefacts. Magnification was 0.3.

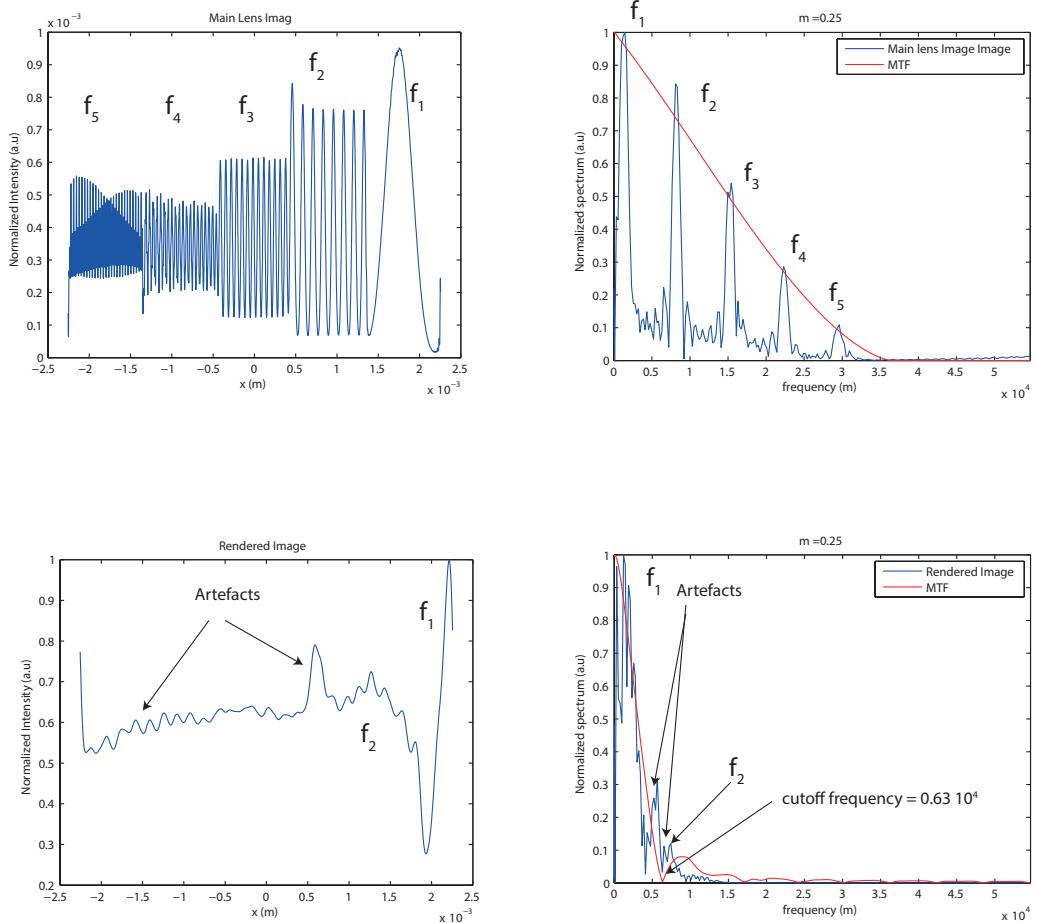


Figure 4.28: On the left: intensity profiles of the main lens image, top and of the rendered image, bottom. On the right there are the spatial frequencies modulated according to the MTF. The cut-off frequency of the system is  $0.6 \times 10^4 1/m$

In the results shown in figure 4.28 there is a lower magnification and the digital aliasing frequencies are no longer transmitted to the rendered image. This is due to the fact that with a narrower bandwidth of the modulation transfer function these frequencies are filtered out of the signal. The same happens to the frequency  $f_2$  of the object field, since the cut off frequency

for a magnification equal to 0.25 is lower than the signal frequency  $f_2$ .

## 4.7 Conclusions

In this chapter has a frequency analysis of a focused plenoptic system has been done to investigate its behaviour at its diffraction limit. We analysed the optical performances of the plenoptic imaging system treating it as a linear system with a finite bandwidth that depends on the magnification of the lens let array. The distances  $a$  and  $b$  not only define the angular resolution of the system and the trade off with spatial resolution, but also allows to quantify the limits of the system in terms of optical resolution. This is a new contribution to the field, first presented in 2014 by Turola *et al.* [20]. Knowing how the optical frequencies are transmitted through the system allows to design its components in order to satisfy the requirements imposed by the practical application encountered. The optical resolution degradation with the increase of the angular resolution represents an intrinsic limitation to plenoptic 2.0 imaging system especially in applications regarding microscopy in which it is the diffraction that limits the resolution.

There are three ways to overcome this limitations: optically, computationally and hybrid one. The first approach consists in improving the basic optical elements of the system, that is choosing low f-number optical elements, larger array of micro lenses and sensors, or improving the optics before the micro array stage in order to deliver pre processed optical frequencies that will not be affected by the loss of resolution in the relay stage. It is also possible to act on the micro lens array, creating an array of lens lets with different focal length [27]. This approach could result in expensive devices, and it

is preferable to approach this issue computationally. Raw plenoptic data can be treated in post processing and can lead to a full sensor resolution rendering, and even a super resolution rendering as done by Georgiev *et al.* [31, 58, 63, 32, 64], by Favaro an Bishop [65, 66, 36, 29] and Shroff *et al.* [40, 30]. Another way to overcome the loss of resolution is to design a hybrid system composed by two branches, a plenoptic branch and and a conventional high resolution branch. This hybrid systems [67, 68], are based on the simultaneously acquisition of a plenoptic and a high resolution image, the latter being used as a base to interpolate the plenoptic data in order to fill the gaps in resolution.

In the next chapter the knowledge and the experience acquired designing and testing simulated plenoptic imaging system through simulation will be used to design a real optical setup, and the results obtained will be discussed.



# Chapter 5

## Light Field Microscope

In this chapter will explained how the experience acquired running the wave optics simulations of a plenoptic imaging system has been used to design and build a working setup of a light field microscope. It is a versatile and flexible instrument with the purpose to test and explore all the potential of light field imaging for microscopy, hence the philosophy was to realize a setup with the maximum number of degrees of freedom possible. In the next sections it will be presented the design parameters and guidelines used to develop the setup. A protocol to acquire and render images will be described and few examples of rendered images will be shown.

### 5.1 From simulation to the real system

The results obtained in the simulation have been used as a guideline in the process of developing a working system. It has been clear since the beginning that a 1.0 system could not be the best option for a practical setup. The reasons for that are:

- A plenoptic 1.0 imaging system, as explained in 1.4, requires the lens

let array to be conjugated to the object plane, and the sensor plane to be conjugated with the main lens. To satisfy this condition along with the f-number matching, the micro array should be placed at a distance to the sensor equal to its focal length with great precision [2, 21, 13, 4]. Advanced machinery and a clean room is needed to fabricate the lens let array with a focal length equal to the substrate thickness and then stick it to the sensor. A solution to bypass this issue is to build a relay system of lenses between the micro lens array and the sensor[8] adding complexity and cost to the system.

- The spatial resolution is limited by the number of lens let in the array. Therefore to achieve high resolution images it is necessary to have an array with a small pitch and a large number of lens let. The sensor should be large with small pixel size, increasing the costs. For example to achieve a resolution of  $1000 \times 1000$  pixel in the final rendered image with lens lets with a diameter of  $150 \mu m$  like the one used in section 3.2, the array should be 15 by 15 cm wide and the sensor should have a resolution of 30000 by 30000 pixel.

Hence from a practical point of view building a proper plenoptic 1.0 system can be quite expensive and complicated considering the performances achieved. A Plenoptic 2.0 it is easier to build and gives better results in terms of spatial and directional resolution trade off. The key variable to control is the distance between the micro lens array and the sensor.

## 5.2 Description of the System

This section will describe the characteristics of the plenoptic 2.0 microscope built. It has been designed following the guidelines given by Georgiev *et al.* [28]. The assembly of the system uses Linos mounts, rods and rails [69]. With reference to figure, a transmission system was built composed of four main parts:

- Illumination: an LED light, a diffuser and a condensing lens are used to concentrate the maximum area of the light source on the sample, A Köhler illumination lens has been added in order to generate a even illumination on the sample removing artefacts generated by imaging the light source on the sensor. [70, 71]
- The main optics: its role is to form an image of the object in front of the micro lens array. A 2f system, with a single lens was built as the simulations described above.
- Micro lens array: The micro lens array is a relay system between the main lens image and the sensor of the microscope. It defines the tradeoff between optical and spatio-angular resolution.
- Sensor plane: it records the light field. It should be large enough to capture all the light coming from the lens let array and it should provide enough resolution to have high resolution sub images.

The illumination system was made by an LED light source, Thorlabs Inc. LED array LIU630, with a central wavelength of 630 nm, an output power

of  $208\text{ mW}$  and an emission spectrum shown in figure 5.1 with a full width half maximum of  $20\text{ nm}$  as already discussed in 2.7.4.

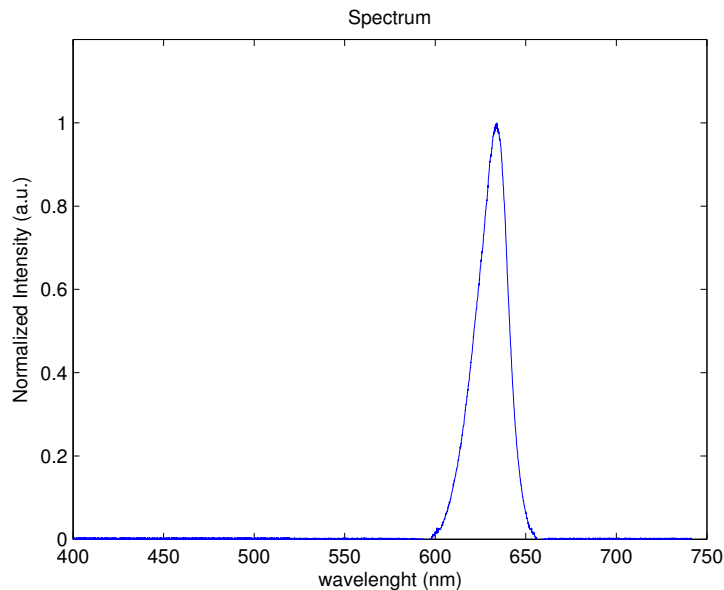


Figure 5.1: Emission spectrum of the LED light source used in the system .

A condensing lens with a focal length of  $27\text{ mm}$  has been placed in front of the light source, in order to maximise the light reaching the sample. The image formed by the condensing lens has been relayed by the Köhler lens on the main lens of the system. In this way the structure of the light source is not affecting the quality of the image [70]. To make it even more uniform a diffuser has been placed between the LED source and the condensing lens, as shown in figure 5.2. The main optics consisted of two plano-convex lenses with a focal length of  $120\text{ mm}$  each placed one next to the other as shown in figure 5.2, in order to give a main lens with a total focal length of  $60\text{ mm}$ . The two lenses have been mounted with the flat surface facing outwards to minimize spherical aberrations. The main lens was in a  $2f$  configuration,

producing an image with a magnification of 1 on the main lens image plane.

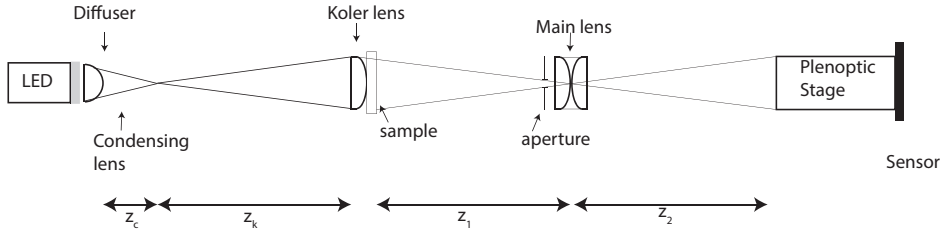


Figure 5.2: Schematics of the light field microscope. The values of the distances are:  $z_c=27$  mm,  $z_k=120$  mm,  $z_1=z_2=120$  mm.

The plenoptic stage is the most complex part of the system. The optical properties are defined by the magnification of the micro array stage [20, 3], therefore in a real system it should be tuned with high accuracy in order to produce a rendered image with the desired resolution. The issue in tuning correctly the magnification is about defining a correct values for the lengths  $a$  and  $b$  in a real system. The technical solution that has been adopted was to use two micro metric mechanical translation stages to move with precision both the whole micro array and sensor block with respect to the main lens and the sensor. The first translation stage moves the whole plenoptic block with respect to the main lens, changing the parameter  $a$ , distance between the main lens image and the micro lens array. Once  $a$  is set a second translation stage moves the sensor with respect to the micro array stage, setting the parameter  $b$ , distance between the micro array and the sensor. In this way the magnification is set. The micro array can also be moved perpendicularly to the optical axis in  $x$  and  $y$ , in order to centre the array with the sensor.

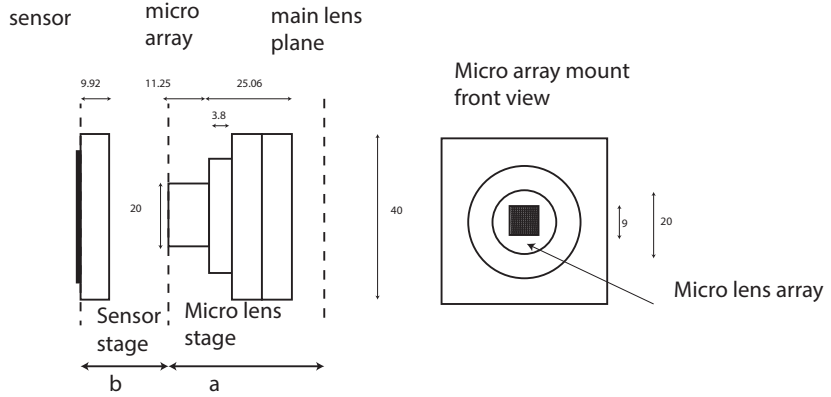


Figure 5.3: Schematics of the light field recording stage.

The micro array used is an MLA150-5c-M by Thorlabs, with a 10 mm by 10 mm square grid made of  $146 \mu\text{m}$  diameter plano-convex lens lets on a substrate of fused silica. The lens let pitch is  $150 \mu\text{m}$ . All the geometric parameters of the lens let array can be seen in figure 5.4 where  $r$  is the radius of curvature of the lens let,  $s$  is the high of the lens let from the substrate,  $p$  is the pitch,  $t$  the thickness of the substrate and  $f$  is the focal length that is linked to the radius of curvature by the relation:

$$f = \frac{r}{n - 1} \quad (5.1)$$

Where  $n$  is the refractive index of the lens let and the substrate, in case of fused silica is 1.5. Assuming the diameter of the lens let almost equal to the pitch, the radius of curvature is linked to the other geometrical parameters by the relation [62]:

$$r = \frac{s^2 + \frac{p^2}{4}}{2s} \quad (5.2)$$

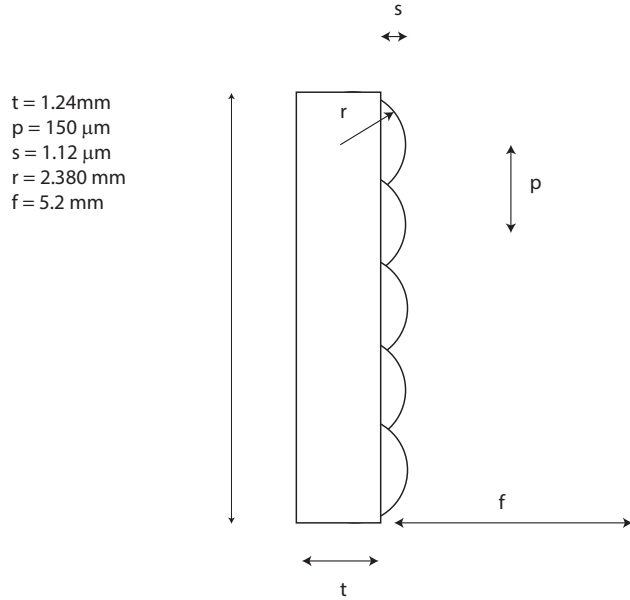


Figure 5.4: Lens let array parameters.

The position of the lens let array respect the sensor and the main lens is controlled by two micro metric translation stages. The parameters to control them of the micro lens array are resumed in table 5.2.  $\alpha$  and  $\beta$  are in this case the amount of shift that the two translation stages should provides in simultaneously in order to obtain the correct position of the micro array stage and therefore the magnification desired. Table 5.2 shows for each couple  $(\alpha, \beta)$  the corresponding optical parameters: the f-number  $F/\#$ , the numerical aperture  $NA$  the cut-off frequencies of the main lens and of the plenoptic stage  $\nu$ . The raw image is recorded using a 10 megapixel CMOS technology sensor with 3840 by 2748 pixels extracted from a UI-1490LE-C-HQ camera from IDS Imaging Development System GmbH. Pixel size is 1.67  $\mu\text{m}$  with a sensor size of 6.413 mm by 4.589 mm mounted at on the back of the translation stage.

Magnification	a (m)	b (m)	NA	F#	$\nu$ Main lens (cycle/m)	$\nu$ Plenoptic (cycle/m)	$\alpha$ (m)	$\beta$ (m)
0	0	0.0052	0.01442	34.6667	22785.2716	0	0.0052	0
0.1	0.05720	0.00572	0.01311	38.1334	20713.8832	2071.3883	0.0057	0.0515
0.15	0.03987	0.0060	0.0125	39.8667	19813.2797	2971.9919	0.0060	0.0339
0.2000	0.0312	0.0062	0.0120	41.6000	18987.7263	3797.5452	0.0062	0.0250
0.2500	0.0260	0.0065	0.0116	43.3334	18228.2173	4557.0543	0.0065	0.0195
0.3	0.02253	0.0068	0.0111	45.0667	17527.1320	5258.1396	0.0068	0.0158
0.35	0.0201	0.0070	0.0107	46.8000	16877.9790	5907.2926	0.0070	0.0130
0.4000	0.0182	0.0073	0.0103	48.5334	16275.1940	6510.0776	0.0073	0.0109
0.45	0.0168	0.0075	0.0099	50.2667	15713.9804	7071.2912	0.0075	0.00922
0.5	0.0156	0.0078	0.0096	52.0000	15190.1811	7595.0905	0.0078	0.0078
0.55	0.0147	0.0081	0.0093	53.7334	14700.1752	8085.0964	0.0081	0.0066
0.6	0.0139	0.0083	0.0090	55.4667	14240.7945	8544.4765	0.0083	0.00555
0.65	0.01320	0.0086	0.0087	57.2000	13809.2555	8976.0160	0.0086	0.0046
0.7	0.0126	0.0088	0.0085	58.9334	13403.1009	9382.1707	0.00834	0.0038
0.75	0.0121	0.0091	0.0082	60.6667	13020.1552	9765.1164	0.0091	0.0030
0.8	0.0117	0.0094	0.0080	62.4000	12658.4842	10126.7874	0.0094	0.0023
0.85	0.0113	0.0096	0.0078	64.1334	12316.3630	10468.9086	0.0096	0.0017
0.9	0.0110	0.0098	0.0076	65.8666	11992.2482	10793.0234	0.0099	0.0011
0.95	0.010673684	0.0104	0.0074	67.6000	11684.7547	11100.5169	0.0101	0.0005
1	0.0104	0.0104	0.0072	69.3334	11392.6358	11392.6358	0.0104	0

Table 5.1: Table containing the parameters of the micro lens array translation stage. a and b are the distances shown in figure 5.4, while  $\alpha$  and  $\beta$  are the shift that the micro metric translator should be moved. In the tables are shown also the optical parameters corresponding to the different positions of the translator.

### 5.3 Performances of the system

With the same methods used for the simulated system in section 4.2 it is possible to define the theoretical performances parameters for the real system designed after the simulated one. Table 5.2 shows the Numerical aperture, and F-number of the system according to the magnification obtained tuning distances  $a$  and  $b$ . It is also shown the corresponding optical resolution for the main lens stage and the plenoptic stage, indicated as  $\nu$ . The values of plenoptic optical resolution are plotted in figure 5.5. Data plotted using the model described in section 4.2.

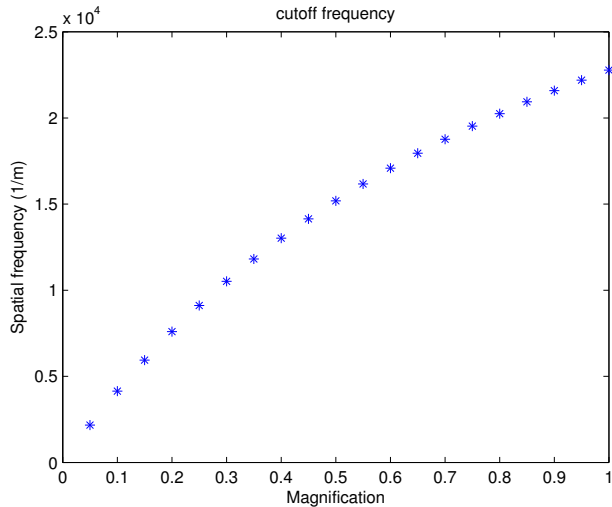


Figure 5.5: Optical resolution as a function of the magnification.

The optical resolution is expected to drop with the decrease of the magnification as proven by the simulations.

## 5.4 Image acquisition protocol

A protocol to capture plenoptic raw data from the system built was developed. It can be summarised as follows:

- according to the magnification required the parameters  $a$  and  $b$  are set by moving the two translation stages by the quantities  $\alpha$  and  $\beta$  indicated in table 5.2.
- the object is removed in order to capture a calibration image using a uniform pattern of monochromatic light.
- the object is put back in place and the raw imaged is captured.
- The final image is rendered using the basic rendering algorithm explained in section 4.1.

The calibration image is required to verify the correct alignment of the lenslet array, that the f-number matching condition is respected and to have a guide to create the sub-images grid to render the final image. The position in  $x$  and  $y$  of the micro lens array can be adjusted moving the mount of the micro array in  $x$  and  $y$  until the round sub images are aligned with the frame of the field of view and rotating the array around the optical axis. These four conditions are shown in figure

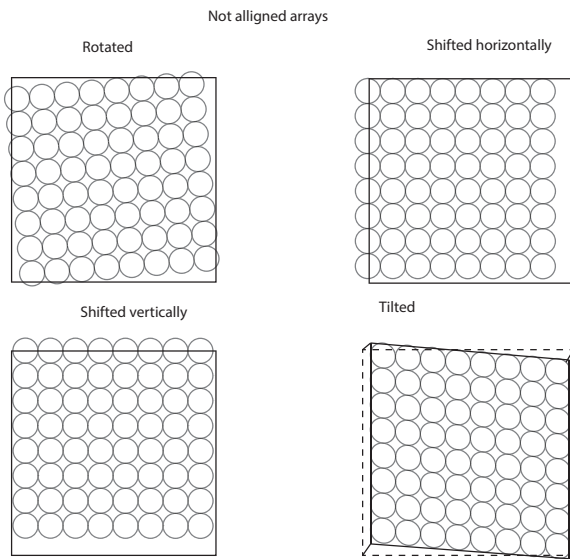


Figure 5.6: Common causes of bad alignment between the micro lens array and the sensor.

The same image can be used to match the f-number of the main lens with the one of the lens let array according to the configuration of  $a$  and  $b$  chosen. This is done manually by changing the aperture placed in front of the main lens until sub images touch each other. Figure 5.7 shows the case where the aperture of the main lens is too small, and the gap between the sub images is too large. Figure 5.8 shows the calibration image obtained with the correct aperture of the main lens.

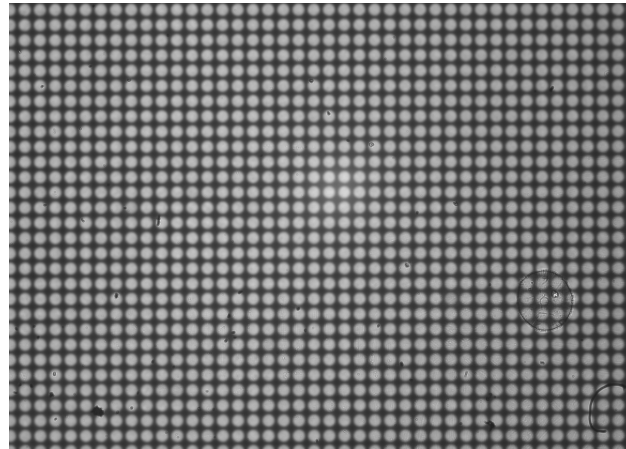


Figure 5.7: Calibration image with f-number not matched.

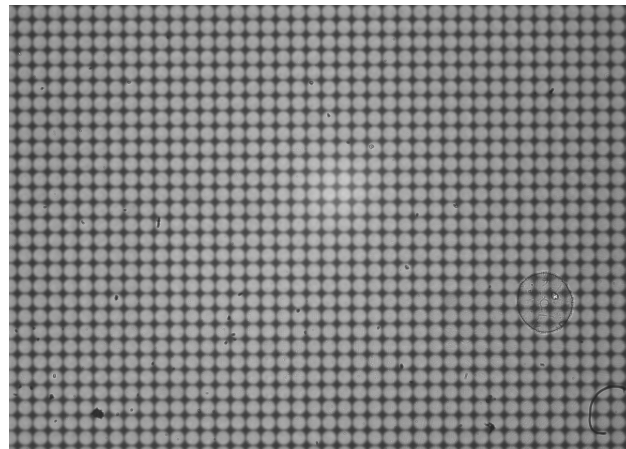
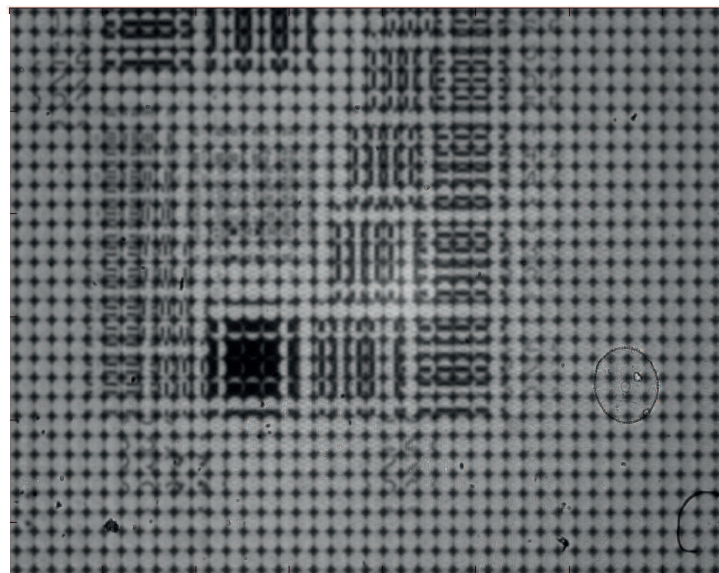


Figure 5.8: Calibration image with matched f-number.

After the f-number is matched, it is possible to proceed with the acquisition of the raw image of the sample. In this case a USAF resolution target has been used as an object. Figure 5.9 shows the raw images obtained with magnifications equal to 0.5 and 0.4, while figure 5.10 shows the raw images obtained with a magnification of 0.3 and 0.25.

Magnification: 0.5



Magnification: 0.4

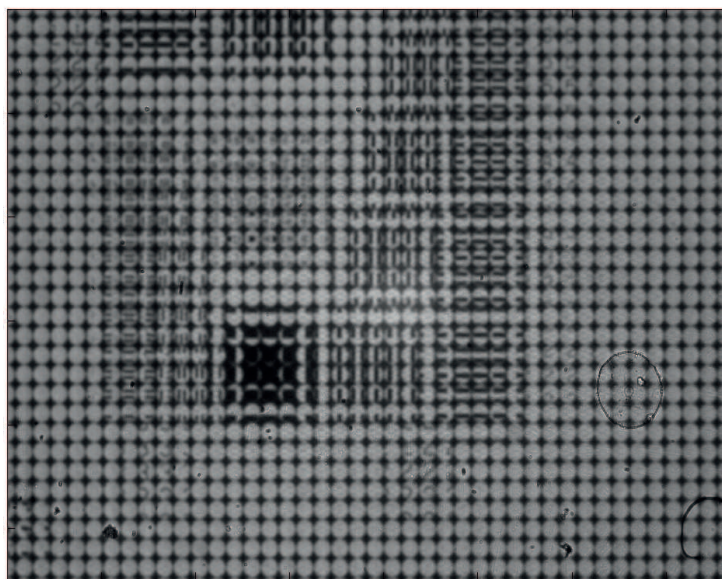
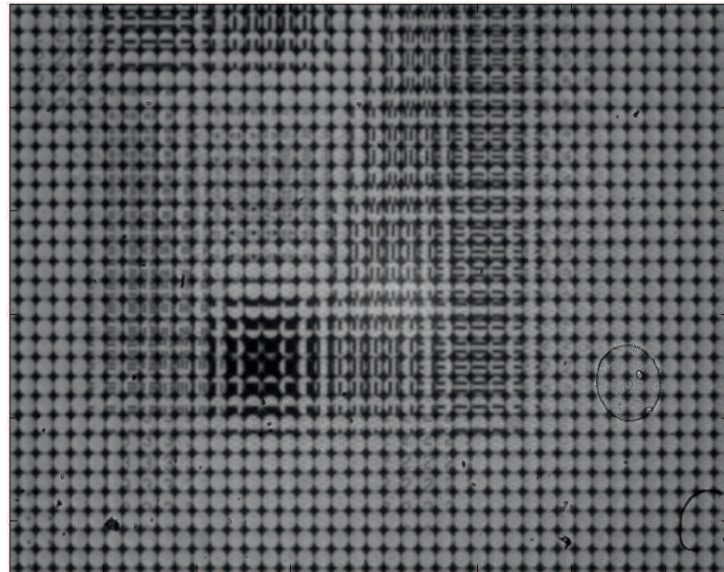


Figure 5.9: Raw plenoptic 2.0 image of the USAF resolution target obtained by the real system built in lab. The top image has a magnification of 0.5, the bottom 0.4.

Magnification: 0.3



Magnification: 0.25

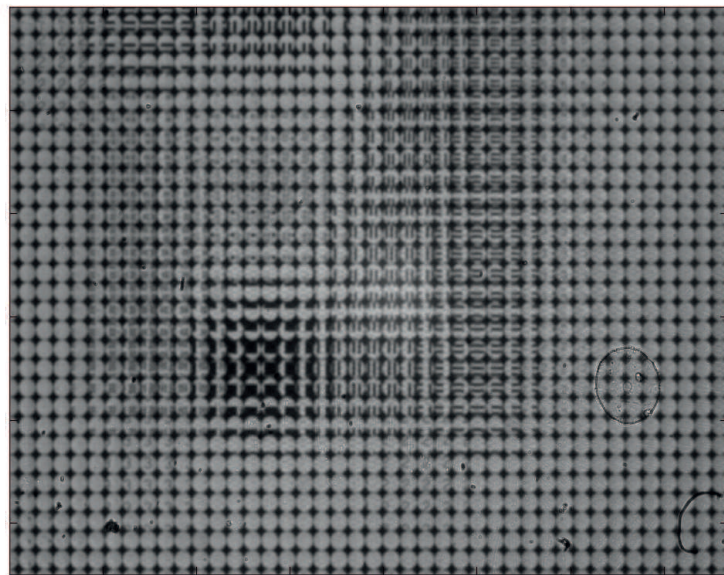


Figure 5.10: Raw plenoptic 2.0 image of the USAF resolution target obtained by the real system built in lab. The top image has a magnification of 0.3, the bottom 0.25.

From this raw images it is evident how the different features of the target object are decomposed into sub images. The number of the sub images for each point imaged increases with the decrease of the magnification. The algorithm to extract the rendering grid will by the calibration image will be explained in the next section.

## 5.5 Rendering of experimental data

Rendering images from raw data acquired by a real light field microscope is more complicated than the case of the simulated raw data. While in a simulation the lens let array is perfectly aligned with the other optical components, in a real system this is not true any more. The lens let array can have a small tilt with respect to the plane perpendicular to the optical axis, causing small differences in magnification along the sub image grid. When this happens the sub images will have different sizes along the grid, generating a distortion that is not predictable or quantifiable like in the case of the computer generated raw data in section 4.1.1. For this reason an algorithm to extract the information on the position of the sub images from the calibration image has been elaborated. It consists of the following steps as shown in figure :

- The user selects a row and a column of sub images in the calibration image
- the intensity profile of the row and the column are displayed and the user sets a threshold that will be used by the software to discriminate the boundaries of the sub images.

- a grid is formed in correspondence with the detected sub images
  - the grid is shown superimposed to the calibration image. Usually offsets are present and are removed manually by the user.
  - the image is rendered as explained in section 4.1 using the grid created from the calibration image.

The final rendered images can be seen in figure 5.12 .

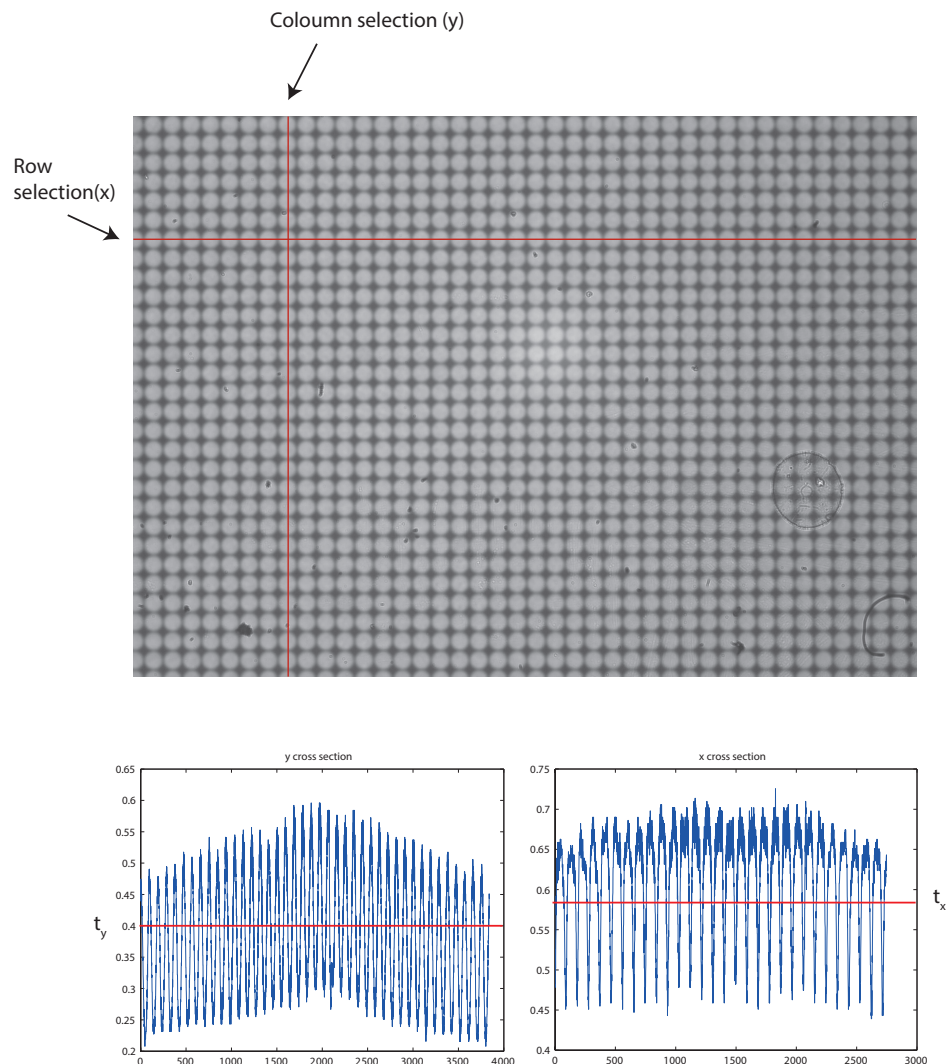


Figure 5.11: The sub images grid generated selecting a row and a column from the calibration image and setting a threshold to that allows the software to know when a sub image ends and the other end.

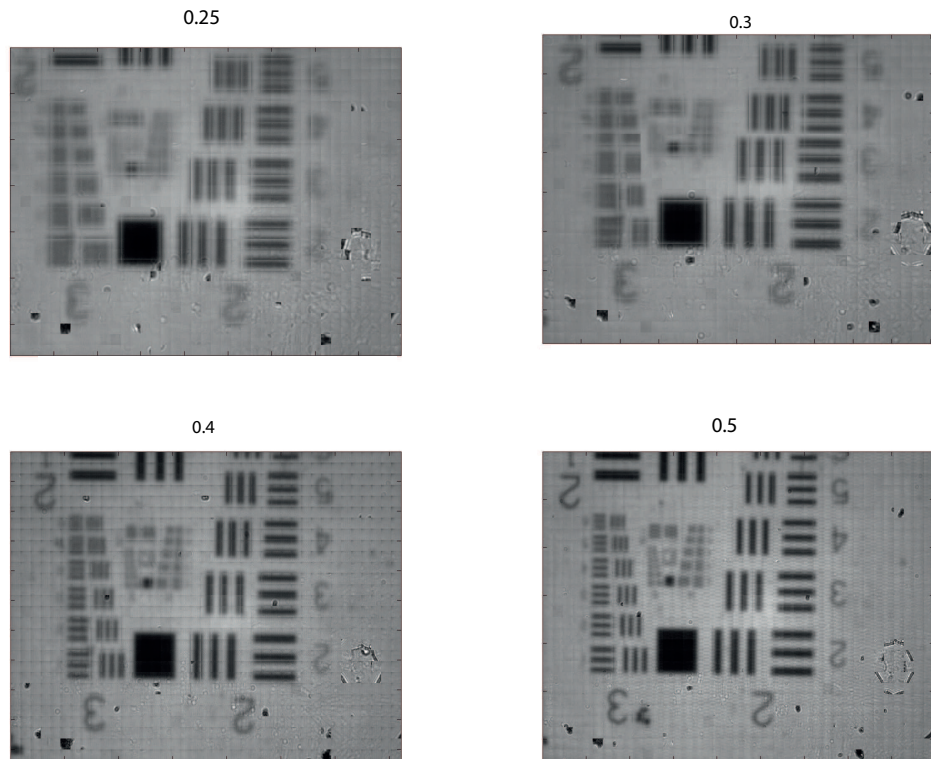
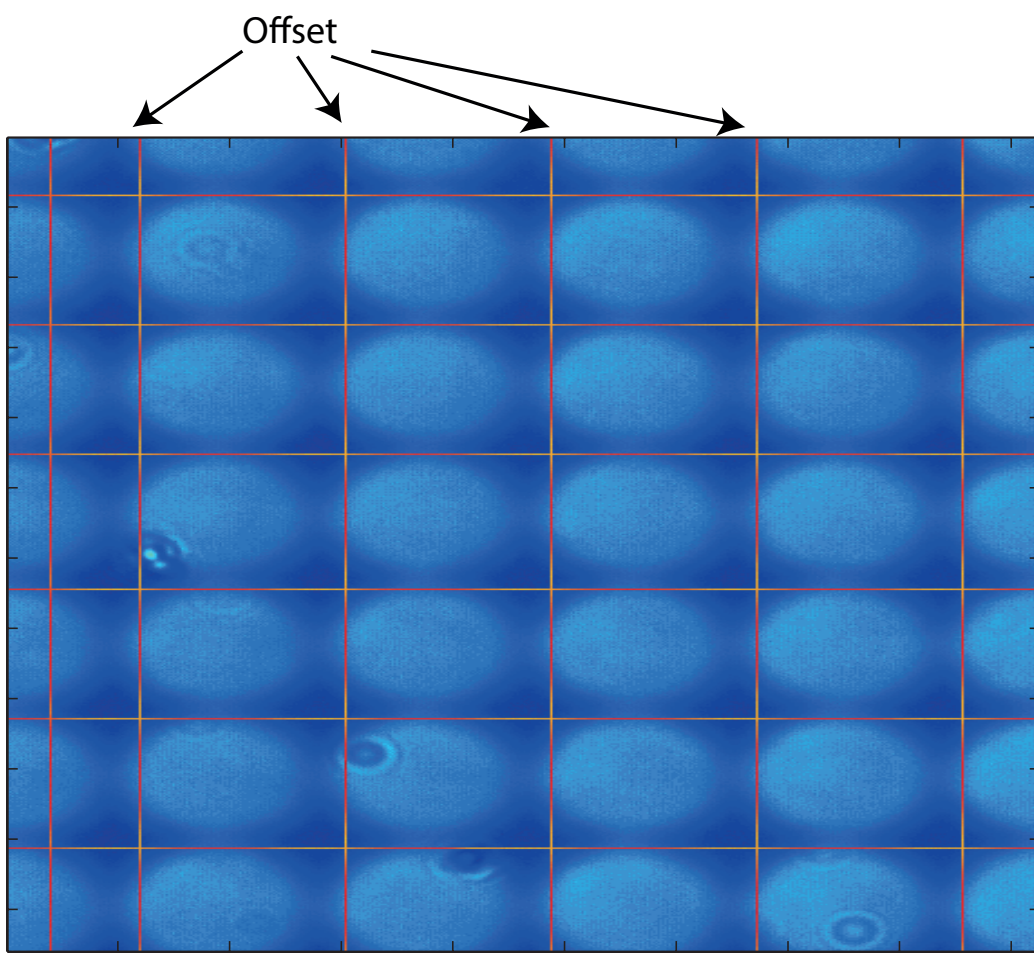
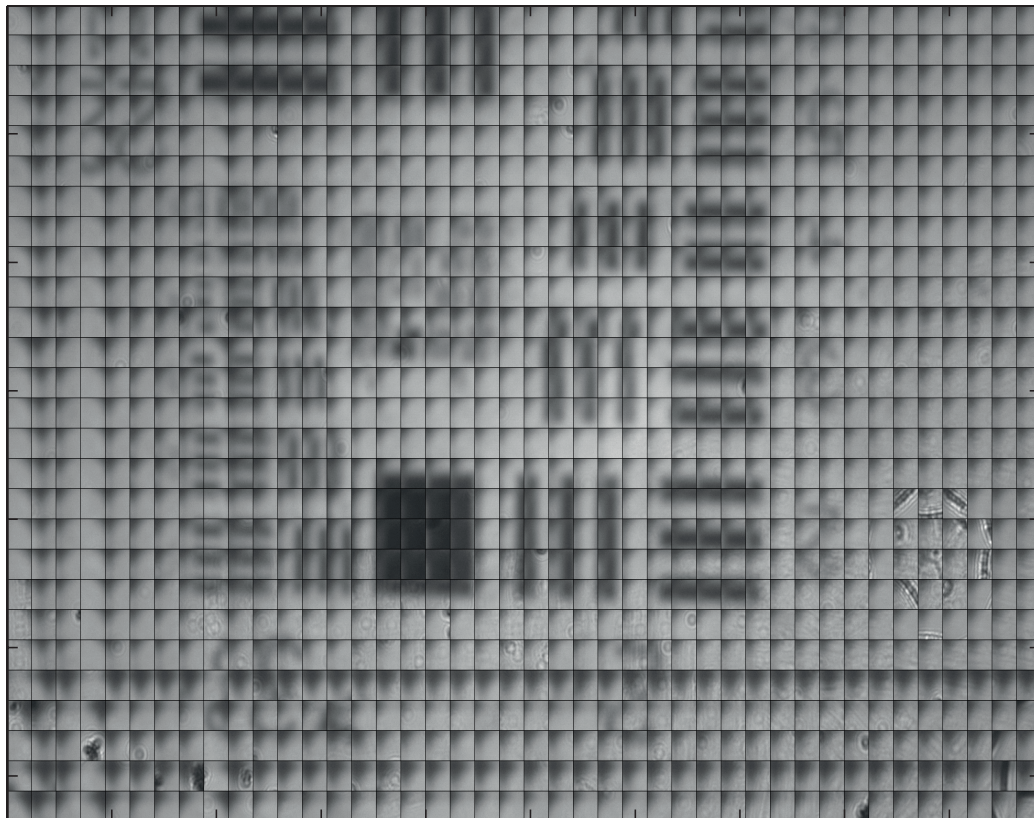


Figure 5.12: Rendered images of a 1951 USAF resolution target. the raw data shown in figures 5.9 and 5.10. Magnifications are from top left to bottom right: 0.25 0.3 0.4 and 0.5.

As expected from the simulated data and the theory of diffraction, resolution drops dramatically with the magnification. From a qualitative analysis, the image gets more blurred for low magnification values, in agreement with what seen in previous chapters. This is due to the loss of resolution due to the dependence of the optical cut-off frequency form the This matches the simulations results of section. If the grid is not correctly set the results is a rendered image with a great number of artefacts. In particular the edges of the tiled sub images will not match as figure shows.

## Wrong rendering example



Artefacts are still present in the rendered image even if the grid is set correctly.

# Appendix A

## 5.6 Optical Phase Space

Before analysing the different configurations of plenoptic cameras, it is important to define an useful tools that allows to better represent the light field, in order to understand and manage it better. This is the optical phase space. In the representation of light field explained in section 1.2, each ray of the light field is defined by a set of four coordinates, two spatial coordinates  $x$  and  $y$ , and the directional coordinates  $\theta_x$  and  $\theta_y$ . Referring to figure we define momentum the quantity:

$$\vec{p} = \frac{\partial \vec{q}(s)}{\partial s} \quad (5.3)$$

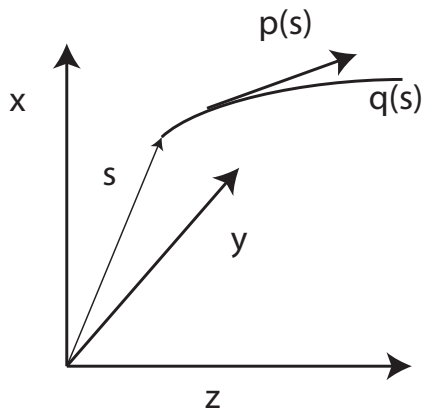


Figure 5.14: The optical momentum correspond to the direction of the ray of light.

where  $\vec{q}(s)$  is a vector describing the trajectory of a ray of light in the three dimensional space and  $s$  is the position respect the origin of the axis  $x, y$  and  $z$ . Because of the Fermat principle, considering the trajectory of the ray  $\vec{q}(s)$  as a straight line, its derivative is proportional to its angular coefficient. So we can approximate the momentum  $\vec{p}$  with the direction of the ray  $(\theta_x, \theta_y)$ . It is defined as a four dimensional manifold of the positions  $(x, y)$  and momentum  $(p_x, p_y)$  of the rays in a certain volume [72] [38]. Each point in the phase space correspond to a unique ray. We will consider the phase space as a four dimensional manifold of the positions  $(x, y)$  and the directions  $(\theta_x, \theta_y)$ . For more details regarding the phase space refer to appendix A.

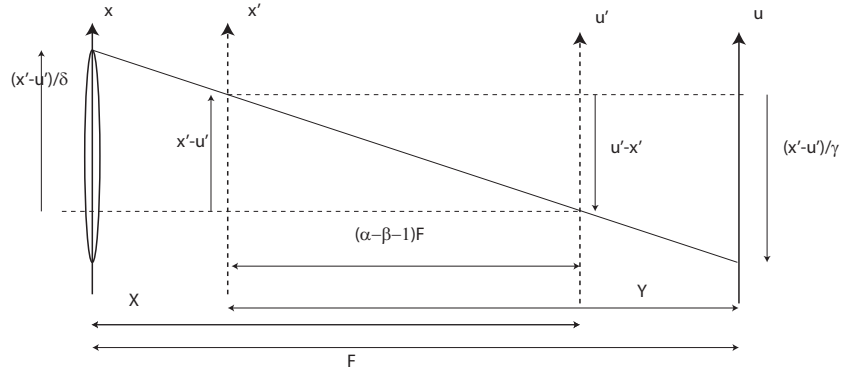


Figure 5.15: .

Referring to figure 5.15 we define

- $F$  as the distance between the main lens and the micro lens plane.
- $X$  as the distance between the lens plane  $u$  and the synthetic image plane  $u'$ .
- $Y$  as the distance between the lens plane  $u'$  and the synthetic image plane  $x$ .

- $\alpha$  and  $\beta$  are defined respectively as:  $\alpha = X/F$  and  $\beta = Y/F$
- the distance between the plane  $x'$  and  $u'$  is given by:

$$F - [F - (\beta F)] - [F - (\alpha F)] = (\alpha + \beta - 1)F \quad (5.4)$$

- We define two further quantities for notation convenience:

$$\begin{cases} \gamma = \frac{\alpha + \beta - 1}{\alpha} \\ \delta = \frac{\alpha + \beta - 1}{\beta} \end{cases} \quad (5.5)$$

Looking at figure 5.15 we note that the rays crossing the planes  $x'$  and  $u'$ , cross also the plane  $x$  at the coordinates  $u' + \frac{(x' - u')}{\delta}$  and the plane  $u$  at the coordinate  $x' + \frac{(u' - x')}{\gamma}$  and considering the fact that the light field is conserved during the propagation in the optical system, we can write:

$$L'(x, y, u, v) = L \left( u' + \frac{(x' - u')}{\delta}, v' + \frac{(y' - v')}{\delta}, x' + \frac{(u' - x')}{\gamma}, y' + \frac{(v' - y')}{\gamma} \right) \quad (5.6)$$

and the intensity at the synthetic planes is given integrating the light field at the synthetic planes:

$$I(x, y) = \iint L \left( x' + \frac{(x' - u')}{\delta}, y' + \frac{(y' - v')}{\delta}, u' + \frac{(u' - x')}{\gamma}, v' + \frac{(v' - y')}{\gamma} \right) A(x', y') dudv \quad (5.7)$$



# **Chapter 6**

## **Conclusions and Future work**

This work explored the characteristics of plenoptic imaging using a wave optics simulations platform to understand and evaluate its performances at the diffraction limit.

The first part of this research involved the design and the development of a piece of code to simulate light propagating into an optical system using the under a wave optics approach. The Fresnel simulation toolbox was developed using MATLAB and by the time this research started represented the first attempt to apply wave optics propagation to a plenoptic imaging system.

The second part of this research involved the design of the simulation experiments to understand and test the response of a plenoptic imaging system before realising a working prototype. The information collected during this second section were useful to determine the potentiality and the drawback of this technique and to design a real plenoptic microscope.

The theory and the basic characteristics of plenoptic imaging were described in chapter one, that gives an overview of this technology describing the work made by other research groups. A detailed description of the geometric optics principles that describes the behaviour was given. The light collected by the

optical system can be described using the concept of phase space that is a representation of the rays distribution on the image plane. The phase space has the property that all the linear operations on its elements are invertible. Therefore once the distribution of that ray of light is known on the sensor it is possible to apply operators on the rays distribution to recover the status of the light at any point of the propagation. These operation such as the synthetic refocus, allow to manipulate the information included into the raw image at the image plane in order to enable several interesting post processing features. For this operator like nature of the phase space, an operator approach was followed also in developing the simulation toolbox.

The second chapter describes the wave optics simulation software designed and developed in MATLAB. This approach represents an important innovation for the plenoptic imaging research since at the time this project started all simulation works on plenoptic imaging were made using ray tracing techniques. Since ray tracing uses geometrical optics principles some all the information regarding the effects of diffraction are lost in the simulation results. The tool box had the requirement to be a flexible tool, that could give accurate estimation of the optical resolution of the optical properties of a plenoptic imaging system, especially at its diffraction limit. Each step of the propagation was modelled as an operator with its characterising transfer function. Starting form Maxwell equation, chapter two describes how a particular solution of the Helmholtz equation gives an expression to compute the optical field after a propagation of a distance  $z$ . This first method of propagating light in free space is the Fresnel approximation approach. Its drawback is that the output field has a different resolution than the input

field. To overcome this fact a multi step Fresnel method was described and analysed. It consists in dividing the overall propagation distance  $z$  in sub interval  $\Delta z$  so that the resolution of the output field is the same as the one of the input field. Its drawback is the computational time since the number of Fourier transform to run is more than one, and the noise that keeps on adding at every step. Therefore the propagation was implemented with the angular spectrum of plane waves method. It consist in computing the Fourier transform of the input field, multiplying it for a transfer function whose bandwidth depends on the propagation distance and then inverse transform the product obtained. Although it requires two Fourier transform, it gives accurate results and removes the scaling factor between the input and output fields. Its drawback consist in the fact that aliasing arise in the propagation transfer function in case of large propagation distance due to the under sampling of its rapid phase oscillations. A solution to this issue consists in implementing a bandwidth limitation applying the Nyquist theorem to the transfer function oscillations. This provides accurate results, but it could cause loss of information in case the bandwidth limitation becomes so big that some of the input field frequency components are lost. In this case an original method was designed consisting in correcting the band limited angular spectrum method truncating the bandwidth of the transfer function to a value of optical frequency obtained considering the amplitude of the input field sampling window and the propagation distance. This method provides a better signal to noise ratio since the noise due to the aliasing is still less than the loss of information due to the excessive limitation of the transfer function bandwidth. The main result of chapter the implementation

of the corrected band limited angular spectrum method and the evaluation of its performances in comparison with the other three methods. The output is a robust simulation platform that allows to investigate plenoptic imaging systems from a physical point of view, propagating light without the approximation of geometrical optics and ray tracing. The third chapter is a description of the simulations of a plenoptic 1.0 system. After describing the simulation set up, some experiments to validate the results found in literature on the optical performances of plenoptic 1.0 were run. One important result is the definition of a threshold on the micro array design in order to avoid cross talk between sub images due to diffraction. This result would have been impossible with a conventional ray tracing approach. Another important result is the validation of the post processing rendering algorithms described by Ng *et.al.* The simulation also helped in understanding the physical meaning of this post processing operations, such as digital refocus, since it was possible to change the experiments parameters in order to analyse the differences in the raw images and the phase space. These results lead to the development of a home made refocusing algorithm, based on Ng work, that is implemented by a shearing operator acting on the four dimensional array representing the light field in Matlab obtained rearranging the pixels in the raw data. This matrix-operator approach is not intuitive but it is very efficient from a computational point of view because of the matrix oriented nature of the language Matlab and because operating a single shearing operator on a four dimensional array is computationally more efficient than obtaining the same results with nested for loops on the two dimensional raw data. For this reason all the raw plenoptic data obtained by the simulation of

a plenoptic 1.0 imaging system were rearranged in form of a four dimensional array. Another algorithm developed is a depth estimation method based on the creation of a stack of focal planes and on the evaluation of sharpness of each rendered image corresponding to the focal plane since the focal depth. Sharpness is a good estimator for the depth of an image since when it is in focus its spectrum spreads for a wider range of spatial frequencies, giving the opportunity to evaluate it in an automatic algorithm that integrates the total energy contained by the high frequency components of the images spectra after an high pass filtering operation on each one of them. The test run of this methods show that depth is estimated with a relative error between 1% and 10%. Future works should focus on finding ways to optimise the accuracy of this method and to develop more efficient and automatised algorithms.

The fourth chapter is about applying the simulation platform developed in chapter two to a plenoptic 2.0 system. Plenoptic 2.0 was designed to improve the poor lateral resolution of a plenoptic 1.0 system. In a plenoptic 2.0 system the micro array is placed between the main lens image plane and the sensor. Each micro lens produces an image of part of the main lens image plane on the sensor. Therefore each micro lens sub image correspond to a point of view of the object. Some simulation of imaging a point source were made to validate what the fact that the number of points of view present on the sensor depends by the magnification of the micro array stage. The more the point of views, the more directional information is present in the raw data. Like in chapter three, starting from the theoretical basics was developed an algorithm to render an image from the plenoptic raw data. In this case the image is rendered directly from the raw data. The basic rendering consists in

tiling sub sections of each micro image one next to each other. The amount of pixel extracted by each sub image for the rendering depends by the optical configuration of the micro array. After validating the functionalities of the rendering algorithm a detailed analysis of the resolution achieved in the rendered images was made. In particular one important result is the link between the magnification of the micro lens array and the optical resolution in the rendered image. The lower is the magnification, therefore a high number of directional samples, the lower is the optical resolution. This has been proven analysing the impulse response of the system with different configurations of the micro lens array. A further confirmation of this effect came from the simulation of the Rayleigh criterion of resolution and by simulating a varying frequency sinusoidal pattern. The main result of this section is a quantification of the trade-off between directional and optical resolution in a plenoptic 2.0 imaging system. This has never been formalised in such a detail in previous literature works.

The fifth chapter describes an real optical setup designed and realised using the experience and the understanding of plenoptic imaging achieved with the simulation platform. The result is a plenoptic microscope whose optical and directional resolution can be changed varying the position of the micro lens array. The experimental results matched the simulation results, providing a further proof of the robustness and reliability of the Fresnel propagation simulation toolbox.

This work shows the characteristic of plenoptic imaging devices under a wave optics point of view. It represents an important milestone in the field of computational imaging since it provides a complete view of the behaviour of this

class of instrument at their diffraction limit. When wave optics is taken into account a the trade off between spatial and angular resolution typical of plenoptic imaging system must be expanded including the optical resolution as well. The effects of diffraction in plenoptic 1.0 cameras are cancelled by the low resolution of the final rendered image. The only effect that comes in play when wave optics is taken into account regards the cross talk between the lenslets, effect that can be avoided using the design requirements explained in chapter three. Regarding plenoptic 2.0 diffraction effects have a bigger influence on the final rendered image. The angular resolution is linked to the directional resolution. Therefore research should be focused in finding ways to improve the optical resolution without limiting too much the set of directional coordinates sampled by the device. This can be achieved operating on the optics of the device or on the computational rendering algorithms. most of the literature up to date describe methods to recover the full sensor resolution, even pushing to sub pixel resolution. But the problem of loosing information adding a micro lens array between the main lens and the sensor plane remains. This is an intrinsic characteristic of plenoptic imaging. The finite dimensions of the lenslets together with the wave nature of light produce a physical limit to the amount of information that can be achieved sampling the optical fields with those kind of devices. This is also a natural consequence of the method used to codify the information carried by the rays of light. The rays of light collected by the plenoptic camera are composed by a set of directions that describes all the possible features of the object imaged. When collected by the main optics of the camera some of these directions are lost because of the finite aperture of the main lens and diffraction. When these

rays are sampled and ordered by the micro array, a second set of directions is lost, leaving the raw data frequency content much smaller than the object one. In addition to that there is the trade off between spatial and directional resolution. In Plenoptic 1.0 spatial resolution depends by the number of lens lets, and directional by their size. Bigger lens lets give better directional resolution and poor spatial resolution. On the other hand small lens lets would give higher spatial resolution and a very poor number of directional samples. To this well known fact this work added the cross talk between lens let, that becomes bigger for small lens let since light experience more diffraction the smaller is the aperture of the lens. In plenoptic 2.0 spatial resolution is not linked any more to the number of lens let, and therefore high resolution rendered images are possible even with a small number of lens let in the micro array. Problems arise when evaluating the optical field at the diffraction limit becomes important, like in microscopy applications. A way to overcome this intrinsic limitations is to remove the micro array stage and sampling the light field with other methods, such as compressive imaging. To conclude this work a few words should be spend on the future direction that research in plenoptic imaging should go. An interesting feature of plenoptic imaging is the capability to record the direction of the rays of light. Since a wave front is defined as the surface perpendicular to the direction of the rays, it could be possible to reconstruct the wave front of the propagating optical field along all the propagation path. This would enable application in aberration evaluation and correction. Due to the non linearity of aberration in this case it is not possible to simply define an operator to recover the non unaberrated wave front from raw data of an aberration affected one. A

more complex analysis should be performed and further investigation on the mathematical instruments needed to perform such a transformation should be carried on. The benefit form this work will be the possibility to perform a digital adaptive optics loop, where the same instrument measure the wave front and the image, estimates an appropriate transformation of the set of rays in the phase space and perform this transformation directly on the four dimensional array. In conclusion, plenoptic imaging is a very complex and mostly un explored field. This work still resides in the family of the preliminary studies and its purpose is to give a general view of the effects of diffraction on it. From creating the tools to do this investigation, the Matlab toolbox, some important results has been achieved on the effects of wave optics and especially in quantifying how diffraction represents a limitation in plenoptic imaging performances.



# Bibliography

- [1] Shree K Nayar. Computational cameras: Redefining the image. *Computer*, (8):30–38, 2006.
- [2] Ren Ng. *Digital light field photography*. PhD thesis, stanford university, 2006.
- [3] Todor Georgiev and Andrew Lumsdaine. Focused plenoptic camera and rendering. *Journal of Electronic Imaging*, 19(2):021106–021106, 2010.
- [4] Levoy Mark. Stanford light field microscope project, 2005.
- [5] Joseph Carroll, David B Kay, Drew Scoles, Alfredo Dubra, and Marco Lombardo. Adaptive optics retinal imaging-clinical opportunities and challenges. *Current eye research*, 38(7):709–721, 2013.
- [6] Gordon Wetzstein, Ivo Ihrke, Douglas Lanman, and Wolfgang Heidrich. Computational plenoptic imaging. In *Computer Graphics Forum*, volume 30, pages 2397–2426. Wiley Online Library, 2011.
- [7] Edward H Adelson and James R Bergen. *The plenoptic function and the elements of early vision*. Vision and Modeling Group, Media Laboratory, Massachusetts Institute of Technology, 1991.

- [8] Edward H Adelson and John Y. A. Wang. Single lens stereo with a plenoptic camera. *IEEE Transactions on Pattern Analysis & Machine Intelligence*, (2):99–106, 1992.
- [9] Plato and Francis Macdonald Cornford. *The republic of Plato*, volume 30. Oxford University Press New York, 1945.
- [10] Herbert E Ives. Parallax panoramagrams made with a large diameter lens. *J. Opt. Soc. Amer*, 20:332–342, 1930.
- [11] Frederic E Ives. Parallax stereogram and process of making same., April 14 1903. US Patent 725,567.
- [12] Lippmann Gabriel. La photographie intégrale. *Comptes-Rendus, Académie des Sciences*, 146:446–551, 1908.
- [13] Marc Levoy and Pat Hanrahan. Light field rendering. In *Proceedings of the 23rd annual conference on Computer graphics and interactive techniques*, pages 31–42. ACM, 1996.
- [14] Yuichi Taguchi, Amit Agrawal, Srikumar Ramalingam, and Ashok Veeraraghavan. Axial light field for curved mirrors: Reflect your perspective, widen your view. In *Computer Vision and Pattern Recognition (CVPR), 2010 IEEE Conference on*, pages 499–506. IEEE, 2010.
- [15] Steven J Gortler, Radek Grzeszczuk, Richard Szeliski, and Michael F Cohen. The lumigraph. In *Proceedings of the 23rd annual conference on Computer graphics and interactive techniques*, pages 43–54. ACM, 1996.

- [16] Bennett S Wilburn, Michal Smulski, Hsiao-Heng K Lee, and Mark A Horowitz. Light field video camera. In *Electronic Imaging 2002*, pages 29–36. International Society for Optics and Photonics, 2001.
- [17] Jason C Yang, Matthew Everett, Chris Buehler, and Leonard McMillan. A real-time distributed light field camera. *Rendering Techniques*, 2002:77–86, 2002.
- [18] Yoshikuni Nomura, Li Zhang, and Shree K Nayar. Scene collages and flexible camera arrays. In *Proceedings of the 18th Eurographics conference on Rendering Techniques*, pages 127–138. Eurographics Association, 2007.
- [19] Todor Georgiev, Ke Colin Zheng, Brian Curless, David Salesin, Shree Nayar, and Chintan Intwala. Spatio-angular resolution tradeoffs in integral photography. *Rendering Techniques*, 2006:263–272, 2006.
- [20] Massimo Turola and Steve Gruppetta. Wave optics simulations of a focused plenoptic system. In *Frontiers in Optics*, pages JTU3A–24. Optical Society of America, 2014.
- [21] Ren Ng, Marc Levoy, Mathieu Brédif, Gene Duval, Mark Horowitz, and Pat Hanrahan. Light field photography with a hand-held plenoptic camera. *Computer Science Technical Report CSTR*, 2(11), 2005.
- [22] Kensuke Ueda, Takafumi Koike, Keita Takahashi, and Takeshi Naemura. Adaptive integral photography imaging with variable-focus lens array. In *Electronic Imaging 2008*, pages 68031A–68031A. International Society for Optics and Photonics, 2008.

- [23] Ashok Veeraraghavan, Ramesh Raskar, Amit Agrawal, Ankit Mohan, and Jack Tumblin. Dappled photography: Mask enhanced cameras for heterodyned light fields and coded aperture refocusing. *ACM Trans. Graph.*, 26(3):69, 2007.
- [24] Douglas Lanman, Ramesh Raskar, Amit Agrawal, and Gabriel Taubin. Shield fields: modeling and capturing 3d occluders. *ACM Transactions on Graphics (TOG)*, 27(5):131, 2008.
- [25] Kshitij Marwah, Gordon Wetzstein, Yosuke Bando, and Ramesh Raskar. Compressive light field photography using overcomplete dictionaries and optimized projections. *ACM Transactions on Graphics (TOG)*, 32(4):46, 2013.
- [26] Yu Ji, Jinwei Ye, and Jingyi Yu. Depth reconstruction from the defocus effect of an xslit camera. In *Computational Optical Sensing and Imaging*, pages CM4E–3. Optical Society of America, 2015.
- [27] Todor Georgiev and Andrew Lumsdaine. The multifocus plenoptic camera. In *IS&T/SPIE Electronic Imaging*, pages 829908–829908. International Society for Optics and Photonics, 2012.
- [28] Todor Georgiev and Chintan Intwala. Light field camera design for integral view photography. *Adobe System, Inc*, 2006.
- [29] Tom E Bishop, Sara Zanetti, and Paolo Favaro. Light field superresolution. In *Computational Photography (ICCP), 2009 IEEE International Conference on*, pages 1–9. IEEE, 2009.

- [30] Sapna A Shroff and Kathrin Berkner. Image formation analysis and high resolution image reconstruction for plenoptic imaging systems. *Applied optics*, 52(10):D22–D31, 2013.
- [31] Todor Georgiev and Andrew Lumsdaine. Superresolution with plenoptic camera 2.0. *Adobe Systems Incorporated, Tech. Rep*, 2009.
- [32] Todor Georgiev. Plenoptic camera resolution. In *Computational Optical Sensing and Imaging*, pages JTh4A–2. Optical Society of America, 2015.
- [33] Changyin Zhou and Shree K Nayar. Computational cameras: Convergence of optics and processing. *Image Processing, IEEE Transactions on*, 20(12):3322–3340, 2011.
- [34] Andrew Lumsdaine and Todor Georgiev. Full resolution lightfield rendering. *Indiana University and Adobe Systems, Tech. Rep*, 2008.
- [35] Andrew Lumsdaine and Todor Georgiev. The focused plenoptic camera. In *Computational Photography (ICCP), 2009 IEEE International Conference on*, pages 1–8. IEEE, 2009.
- [36] Tom E Bishop and Paolo Favaro. Full-resolution depth map estimation from an aliased plenoptic light field. In *Computer Vision–ACCV 2010*, pages 186–200. Springer, 2011.
- [37] Todor G Georgiev and Andrew Lumsdaine. Resolution in plenoptic cameras. In *Computational Optical Sensing and Imaging*, page CTuB3. Optical Society of America, 2009.

- [38] Victor Guillemin and Shlomo Sternberg. *Symplectic techniques in physics*. Cambridge University Press, 1990.
- [39] Todor Georgiev, Andrew Lumsdaine, and Sergio Goma. Plenoptic principal planes. In *Imaging Systems and Applications*, page JTuD3. Optical Society of America, 2011.
- [40] Sapna Shroff and Kathrin Berkner. High resolution image reconstruction for plenoptic imaging systems using system response. In *Computational Optical Sensing and Imaging*, pages CM2B–2. Optical Society of America, 2012.
- [41] Gabriel C Birch, J Scott Tyo, and Jim Schwiegerling. Depth measurements through controlled aberrations of projected patterns. *Optics express*, 20(6):6561–6574, 2012.
- [42] Joyce E Farrell, Peter B Catrysse, and Brian A Wandell. Digital camera simulation. *Applied Optics*, 51(4):A80–A90, 2012.
- [43] Brian S Thurow and Timothy Fahringer. Recent development of volumetric piv with a plenoptic camera. In *PIV13; 10th International Symposium on Particle Image Velocimetry, Delft, The Netherlands, July 1-3, 2013*. Delft University of Technology, Faculty of Mechanical, Maritime and Materials Engineering, and Faculty of Aerospace Engineering, 2013.
- [44] Kyle Lynch. *Development of a 3-D fluid velocimetry technique based on light field imaging*. PhD thesis, Auburn University, 2011.

- [45] Kyle Lynch, Tim Fahringer, and Brian Thurow. Three-dimensional particle image velocimetry using a plenoptic camera. In *AIAA Aerospace Sciences Meeting*, 2012.
- [46] Arnold Sommerfeld. Optics lectures on theoretical physics, vol. iv. *Optics Lectures on Theoretical Physics, Vol. IV by Arnold Sommerfeld* New York, NY: Academic Press INC, 1954, 1, 1954.
- [47] Joseph W Goodman. *Introduction to Fourier optics*. Roberts and Company Publishers, 2005.
- [48] Maciej Sypek. Light propagation in the fresnel region. new numerical approach. *Optics communications*, 116(1):43–48, 1995.
- [49] Rafael C Gonzalez, Richard Eugene Woods, and Steven L Eddins. *Digital image processing using MATLAB*. Pearson Education India, 2004.
- [50] Kyoji Matsushima and Tomoyoshi Shimobaba. Band-limited angular spectrum method for numerical simulation of free-space propagation in far and near fields. *Optics express*, 17(22):19662–19673, 2009.
- [51] Maciej Sypek. Reply to the comment on “light propagation in the fresnel region–new numerical approach”. *Optics Communications*, 282(6):1074–1077, 2009.
- [52] Frank L Pedrotti and Leno S Pedrotti. Introduction to optics 2nd edition. *Introduction to Optics 2nd Edition by Frank L. Pedrotti, SJ, Leno S. Pedrotti* New Jersey: Prentice Hall, 1993, 1, 1993.

- [53] Joseph W Goodman and Randy L Haupt. *Statistical optics*. John Wiley & Sons, 2015.
- [54] Leonard Mandel and Emil Wolf. *Optical coherence and quantum optics*. Cambridge university press, 1995.
- [55] Max Born and Emil Wolf. *Principles of optics: electromagnetic theory of propagation, interference and diffraction of light*. Cambridge university press, 1999.
- [56] Emil Wolf. *Introduction to the Theory of Coherence and Polarization of Light*. Cambridge University Press, 2007.
- [57] Kensuke Ueda, Dongha Lee, Takafumi Koike, Keita Takahashi, and Takeshi Naemura. Multi-focal compound eye: liquid lens array for computational photography. In *ACM SIGGRAPH 2008 new tech demos*, page 28. ACM, 2008.
- [58] Todor G Georgiev and Andrew Lumsdaine. Super-resolution with the focused plenoptic camera, November 20 2012. US Patent 8,315,476.
- [59] Christian Perwass and Lennart Wietzke. Single lens 3d-camera with extended depth-of-field. In *Proc. SPIE*, volume 8291, page 829108, 2012.
- [60] Michael Hansen and Eric Holk. Depth map estimation for plenoptic images. 2011.
- [61] Ole Johannsen, Christian Heinze, Bastian Goldluecke, and Christian Perwass. On the calibration of focused plenoptic cameras. In *Time-of-*

- Flight and Depth Imaging. Sensors, Algorithms, and Applications*, pages 302–317. Springer, 2013.
- [62] Hans Peter Herzig. *Micro-optics: elements, systems and applications*. CRC Press, 1997.
- [63] Todor Georgiev, Georgi Chunev, and Andrew Lumsdaine. Superresolution with the focused plenoptic camera. In *IS&T/SPIE Electronic Imaging*, pages 78730X–78730X. International Society for Optics and Photonics, 2011.
- [64] Todor G Georgiev, Andrew Lumsdaine, and Sergio Goma. High dynamic range image capture with plenoptic 2.0 camera. In *Signal recovery and synthesis*, page SWA7P. Optical Society of America, 2009.
- [65] Paolo Favaro. A split-sensor light field camera for extended depth of field and superresolution. In *SPIE Photonics Europe*, pages 843602–843602. International Society for Optics and Photonics, 2012.
- [66] Tom E Bishop and Paolo Favaro. The light field camera: Extended depth of field, aliasing, and superresolution. *Pattern Analysis and Machine Intelligence, IEEE Transactions on*, 34(5):972–986, 2012.
- [67] Chien-Hung Lu, Stefan Muenzel, and Jason Fleischer. High-resolution light-field microscopy. In *Computational Optical Sensing and Imaging*, pages CTh3B–2. Optical Society of America, 2013.
- [68] Vivek Boominathan, Kaushik Mitra, and Ashok Veeraraghavan. Improving resolution and depth-of-field of light field cameras using a hybrid

- imaging system. In *Computational Photography (ICCP), 2014 IEEE International Conference on*, pages 1–10. IEEE, 2014.
- [69] Photonics for Innovations Quioptiq. *The Linos Catalog*. 2015.
- [70] August Köhler. A new system of illumination for photomicrographic purposes. *Z. Wiss. Mikroskopie*, 10:433–440, 1893.
- [71] August Kohler and Walter Bauersfeld. Device for light-field and dark-field illumination of microscopic objects, January 16 1934. US Patent 1,943,510.
- [72] Kurt Bernardo Wolf. *Geometric optics on phase space*. Springer Science & Business Media, 2004.